INVESTIGATION OF CRYOGENIC ENERGY STORAGE FOR AIR CONDITIONING APPLICATIONS

By

Abdalqader Y. H. Ahmad

Thesis submitted to the University of Birmingham for the

Degree of Doctor of Philosophy

School of Engineering
College of Engineering and Physical Sciences
Mechanical Engineering Department
The University of Birmingham
Edgbaston, Birmingham, UK
April - 2018

UNIVERSITYOF
BIRMINGHAM

University of Birmingham Research Archive

e-theses repository

ABSTRACT

Global demands for residential air conditioning systems (A/C) have increased significantly during the last few decades and most of this growth is located in the developing countries. This growth is forecasted to continue at the same rate until the end of this century. This air conditioning demand contributes to significant amount of power consumption in the domestic sectors and CO_2 emissions particularly during the electricity peak time where most of electricity suppliers face difficulties to meet the user's demands and to cope with this significant growth. Thus there is a need to enhance the current commonly used air conditioning systems (vapour compression system) that consume a major part of the energy consumed by the residential sector particularly during the summer season. This enhancement can reduce energy consumption and shift the cooling load to off peak times (night-time) where power plants operate effectively and cheaper electricity is available.

This research aims to develop an efficient air conditioning technology that exploits cold energy storage to reduce energy consumption and CO_2 emissions and shift the cooling load to off peak times to achieve better national electricity grid stability. The investigation includes the use of commonly used cold storage materials (ice, Phase Change Materials PCM) to enhance the existing air conditioning systems where a mathematical model was developed using MATLAB software. Also using cryogenic cold storage namely, liquid nitrogen/air (LN2/LAir), which could produce using surplus electricity or renewable energy sources, was thermodynamically investigated to provide air conditioning for domestic and office buildings. Computational Fluid Dynamic (CFD) modelling of the main two components in the cryogenic cooling system namely, cryogenic heat exchanger and expander were also carried out. An

I

experimental test facility was developed to validate the CFD modelling of the liquid nitrogen (LN2) evaporation process and assess its potential to provide cooling.

Results showed that integrating existing A/C systems with cold storage tank can lead to energy saving and shifting the cooling load to off peak times, but this energy saving is highly dependent on the storage medium and its storage temperature. When Hydrate (HC-290) which has phase change temperature of 5.6 °C was used the system showed an energy saving of up to 26% compared with conventional A/C system depending on operating strategy. However, when ice the most commercially available PCM is used, the chiller capacity was reduced by 30-40 % leading to higher power consumption compared to the conventional system. Regarding using cryogenic fluids (LN2/LAir), five different cycle configurations of cryogenic cooling systems were investigated and the results showed that, up to 94% of the energy stored in LAir and up to 78% of the energy stored in LN2 can be recovered. Based on LN2 prices of 3.5 pence per kg the system showed cost saving of the energy consumption of up to 73% when LAir is used and 67% when LN2 is used compared with the conventional system. LN2 systems showed slightly higher (less than 4%) specific power and specific cooling capacity than LAir, however, LAir showed 21-25% higher Recovery Efficiency and COP than LN2 due to its lower energy production cost. The CFD modelling of evaporation/boiling process of LN2 showed good agreement with the experimental data with maximum deviation less than 10%, thus it was used to investigate effect of fin configurations on heat transfer coefficient showing an enhancement of 79% -167% compared with the smooth tube. Results of the CFD modelling of LAir driven reciprocating engine showed that, there is a potential of using LAir to provide cooling and power for domestic applications where a mass flow rate of 0.0239 kg/s of LAir at inlet pressure of 20 Bar can generate 10 kW of cooling and 2.2 kW of electricity which is enough to meet their cooling and power demands.

Experimental results of the cryogenic heat exchanger were compared to those predicted by the CFD modelling showing good agreement with maximum deviation of 7.6%. Also, using a metal mesh to enhance the heat transfer coefficient in the gas region of the LN2 carrier tube increases the heat exchanger effectiveness and the heat transfer rate by more than 10%. This work has shown that cryogenic energy storage technology can be used for A/C applications where energy consumption and CO_2 emissions can be reduced and the cooling load can be shifted to off peak times.

ACKNOWLEDGEMENT

All praises are due to Allah (whom we praise, seek his help and asking for his forgiveness) for his guidance, blessing and helping me to complete this thesis. May his mercy and blessing be upon the noble Prophet Mohamed (SAWA), his households and his companions.

My honest gratitude goes to my supervisor Dr. Raya Al-Dadah, for her continuous support throughout this work, her guidance, her patience, her motivation and her immense knowledge. Her guidance helped me in the entire time of my research, writing research papers, and writing my thesis.

My honest gratitude is also to my second supervisor Dr Saad Mahmoud for his invaluable suggestions, novel ideas, support and encouragement through the period of my PhD research and my work.

Besides my supervisors, I have to thank Mr Simon Rowan for helping me to build my experimental test facility Also I have to thank Miss Jackie Deans for lending me the required facility to carry on the experimental work.

My gratitude is to all my friends and colleagues in the department of Mechanical Engineering as well as other departments in the University who helped me during this research project.

My truthful appreciations go to my parents; Youssef Ahmad (May Allah has mercy on him), to my Mother for her prayers, my Wife for her patience and my friends for their moral support during my PhD study.

PUBLICATIONS

A. Journal papers

1- Ahmad, A., Al-Dadah, R. and Mahmoud, S., 2016. Liquid nitrogen energy storage for air conditioning and power generation in domestic applications. Energy Conversion and Management, 128, pp.34-43.

2- Ahmad, A., Al-Dadah, R. and Mahmoud, S., 2016. Air conditioning and power generation for residential applications using liquid nitrogen. Applied Energy, 184, pp.630-640.

3- Ahmad, A., Al-Dadah, R. and Mahmoud, S., 2017. Liquid air utilization in air conditioning and power generating in a commercial building. Journal of Cleaner Production, 149, pp.773-783.

4- Khalil, K.M., Ahmad, A., Mahmoud, S. and Al-Dadah, R.K., 2017. Liquid air/nitrogen energy storage and power generation system for micro-grid applications. Journal of cleaner production, 164, pp.606-617.

5- Daabo AM, Mahmoud S, Al-Dadah RK, Ahmad A. Numerical investigation of pitch value on thermal performance of solar receiver for solar powered Brayton cycle application. Energy. 2017 Jan 15;119:523-39.

6- Daabo, A.M., Ahmad, A., Mahmoud, S. and Al-Dadah, R.K., 2017. Parametric analysis of small scale cavity receiver with optimum shape for solar powered closed Brayton cycle applications. Applied Thermal Engineering, 122, pp.626-641.

7- Badawy T, Hamza M, Ahmad A, Mansour MS, Abdel-Hafez AH, Imam H. New developed burner towards stable lean turbulent partially premixed flames. Fuel. 2018 May 15;220:942-57.

B. Conference Papers

1- Ahmad, A., Al-Dadah, R. and Mahmoud, S., 2016. Liquid Nitrogen Air Conditioning System for Domestic Application. Accepted in ICSAE 2016, IEEE

2- Ahmad, A., Al-Dadah, R. and Mahmoud, S., energy and exergy analysis of using liquid air for generating air conditioning and power for domestic buildings, the 14th cryogenics 2017, IIR International Conference & Exhibition, Dresden, Germany

3- Hassan Ahmed, Ahmad K Almajri, Saad Mahmoud, Raya Al-Dadah, Abdalqader Ahmad, CFD modelling and parametric study of small scale Alpha type Stirling Cryocooler 9th International Conference on Applied Energy, ICAE2017, 21-24 August 2017, Cardiff, UK

4- Ahmad, A., Al-Dadah, R. and Mahmoud, S., CFD modelling of a novel liquid Nitrogen/Air engine and cryogenic heat exchanger for small scale applications, 9th International Conference on Applied Energy, ICAE2017, 21-24 August 2017, Cardiff, UK

5- Manraj S., Ahmad, A., Al-Dadah, R. and Mahmoud, S CFD modeling of Direct-Contact of Water Freezing Desalination (Heat Powered Cycles Conference 2018)

CONTENTS

LIST OF FIGURES

XIII

LIST OF TABLES

NOMENCLATURE

H_{char}	Number of is charging hours
CR_{char}	Capacity ratio when charging
H_{dirct}	Number of direct cooling hours
CR_{dirct}	Capacity ratio when direct cooling
Q_c	Storage capacity
C_{chil}	Nominal chiller capacity
TC_{char}	Total cooling load during charging times
η_{st}	Thermal efficiency of storage system
V_{ST}	Volume of storage tank
A_{ST}	Storage tank surface area
$Q_{I,ch}$	Heat loses during charging processes
$Q_{I,dc}$	Heat loses during discharging processes
ρ_w	Water density
$C_{p,w}$	Water specific heat
T_{dc}	Discharge temperature
$T_{FP,w}$	Feeding water temperature
h_{fe}	Latent heat of fusion
ρ_{ice}	Ice density
$C_{p,ice}$	Ice specific heat
T_{ST}	Storage tank temperature
t_{ch}	Charging time
T_{amb}	Ambient temperature
$\dot{Q}_{Ev}$	Evaporator heat transfer rate

$\dot{m}_r$	Refrigerant mass flow rate
η_{comp}	Compressor efficiency
$\dot{W}_{comp}$	Compressor input power
m_{CT}	Cooling tower mass flow rate
Q_{cond}	Condenser heat rejected rate
COP	Coefficient of performance
NTU	Number of heat transfer units
ΔT_{LMTD}	Logarithmic mean temperature difference
U_{Ev}	Evaporator overall heat transfer coefficient
A_{EV}	Evaporator surface area
A_{Cond}	Condenser surface area
Nu	Nusselt number
K_l	Liquid thermal conductivity
h_{TP}	Two phase heat transfer coefficient
Re_l, Re_{lo}	Liquid phase Reynolds number
Pr_l	Liquid Prandtl number
G	Grashof number
x	Vapour quality
μ_l	Liquid viscosity
d	Tube diameter
F_1, F_2	Coefficient
X_{tt}	Martinelli parameter
Re_{eq}	Equivalent Reynolds number for two phase flow
Re_v	Vapour phase Reynolds number

ρ_l	Liquid density
ρ_v	Vapour density
μ_l	Liquid viscosity
μ_v	Vapour viscosity
$\dot{m}_a$	Air mass flow rate
Bo	Boiling number
q	Heat flux
h_{fg}	Vaporization energy
AHU	Air handle unit
ω	Humidity
$C_{p,a}$	Air specific heat
Z_{AHU}	Air handle unit capital cost
Z_{ST}	Storage tank capital cost
Z_{EV}	Evaporator capital cost
Z_{Comp}	Compressor capital cost
Z_{EX}	Heat exchanger capital cost
Z_{Cond}	Condenser capital cost
$Z_{Chiller}$	Chiller capital cost
$Q_{Chiller}$	Chiller capacity
A_{Cond}	Condenser surface area
A_{Ev}	Evaporator surface area
A_{AHU}	Air handle unit surface area
h	Enthalpy
CC	Specific cooling capacity

$\dot{m}$	Mass flow rate
s	Entropy
m_r	Closed Brayton or Rankine cycles mass flow rates to LAir mass flow rate
m_{r1}	The first closed Rankine cycle mass flow rate to LAir mass flow rate
m_{r2}	The second closed Rankine cycle mass flow rate to LAir mass flow rate
W	Specific power
η_{RE}	Recovery efficiency
$coeff$	Coefficient
$\vec{F}$	Body force
$\dot{m}_{lv}$	Rates of mass transfer due to evaporation and condensation, respectively
n	Number of phases
v	Vapor phase
$V_{dr,k}$	Secondary phase drift velocity for phase k
$\overrightarrow{V_m}$	Mass-averaged velocity
$\overrightarrow{V_v}$	Vapor phase velocity
T_l	Liquid temperature
T_{sat}	Saturated temperature
μ_m	The mixture viscosity
ρ	Density
ρ_m	Mixture density
ρ_v	Vapor density
$\alpha, \propto_q, \alpha_k$	Phase volume fraction
ρ_q	Phase q density
$\overrightarrow{v_q}$	Phase q velocity

$\dot{m}_{pq}$	Mass transfer from phase p to phase q
$\dot{m}_{qp}$	Mass transfer from phase q to phase p
α_v	Vapor volume fraction
S_q	Phase q source term
$\vec{F}_q$	Phase external body force
$\vec{F}_{lift,q}$	Lift force
$\vec{F}_{wl,q}$	Wall lubrication force
$\vec{F}_{vm,q}$	Virtual mass force
$\vec{F}_{td,q}$	Turbulent dispersion force
$\overrightarrow{R_{pq}}$	Interaction force between phases p and q
$\overrightarrow{v_{pq}}, \overrightarrow{v_{qp}}$	Interphase velocities
h_q	Specific enthalpy of phase q
h_{qp}	Interphase enthalpy
$\overrightarrow{q_q}$	Heat flux of phase q
Q_{pq}	Intensity of heat exchange between the phases q and p
ρ_{rq}	Reference density of phase q
A_i	Interfacial area concentration
C_l	Lift coefficient
ρ_q	Density of primary phase
$\propto_p$	Volume fraction of the secondary phase
$\overrightarrow{v_p}$	Secondary phases velocity
Eo	Modified Eotvos number based on the long axis of the deformable bubble
	d_h

G	Gravity
σ	Surface tension
d_b	Bubble diameter.
C_{wl}	Wall lubrication coefficient
$\left| \vec{v_q} - \vec{v_p} \right|$	Relative velocity component tangential to the wall surface
$\vec{n}_w$	Unit normal pointing away from the wall
$C_{w1}, \ C_{w2}$	Non-dimensional coefficients
y_w	Distance to the nearest wall
h_{pq}	Multiphase heat transfer coefficient
K_q	Thermal conductivity
Nu_p	Nusselt number
d_p	Bubble diameter
$\mu_{t,m}$	mixture turbulent viscosity
$G_{k,m}$	Turbulence kinetic energy
$\Pi_{\varepsilon_m}, \ \Pi_{k_m}$	Source terms
$\propto_i$	Phase volume fraction
μ_i	Viscosity
ρ_i	Density
$\vec{v_l}$	Liquid phase velocity
$\dot{q_w}$	Total heat flux from the surface to liquid
$\dot{q_C}$	Convective heat flux
$\dot{q_Q}$	Quenching heat flux
$\dot{q_V}$	Convective heat flux of the vapour phase
$\dot{q_E}$	Evaporative heat flux

$\dot{q}_G$	Heat flux to any other gas phases in the domain
h_C	Heat transfer coefficient
T_W	Wall temperature
A_b	Area of influence
k_l	Liquid thermal conductivity
T_l	Liquid temperature.
V_d	The bubble volume
N_W	Nucleate site density
ρ_v	Vapour density
h_{fv}	Latent heat of evaporation
f	Bubble departure frequency
h_V	Vapour heat transfer coefficient
T_V	Vapour temperature
h_G	Heat transfer coefficient of any other gases in the domain
T_G	Temperature of any other gases in the domain
ΔH	Latent heat.
h_{ref}	Reference enthalpy
T_{ref}	Reference temperature
C_p	Specific heat
Θ	Angle of incline
L	Fluid level reading on the inclined scale
$U_{Overall}$	Overall uncertainty
U_{sys}	Systematic
U_{random}	Random errors

$t_{N-1,95\%}$	Student distribution coefficient
N-1	Degree of freedom
N	Number of samples
$\sigma_{\bar{S}}$	The mean deviation
β	Accommodation coefficient

Subscripts

A	Liquid air cycle
B	Brayton cycle
Ad	Adiabatic expansion
Iso	Isothermal expansion
R	Closed Rankin cycle/first closed Rankin cycle
R'	Second closed Rankin cycle
tank	Cooling tank

CHAPTER ONE

INTRODUCTION

1.1   Background

Global demands for residential air conditioning systems (A/C) have increased rapidly over the last few decades, with most of this growth occurred in the developing countries and lead to significant power consumption particularly in the residential sector. Approximately, 87% of US households have air conditioning [1-3]. In urban cities of China, for example, the A/C demands increased from 2.3% in 1993 to 61% in 2003 with yearly growth rate of 39%, while in 2010 alone about 50 million units were sold [4, 5]. A forecast for the air conditioning growth rate (2005- 2030) across different regions in the world is shown in Figure **1**-**1** where Mexico and Middle East show the highest growth rates while Centrally-Planned Asia (CPA) shows the lowest growth rate. The abbreviations used in Figure **1**-**1** are explained in Table **1**-**1**.
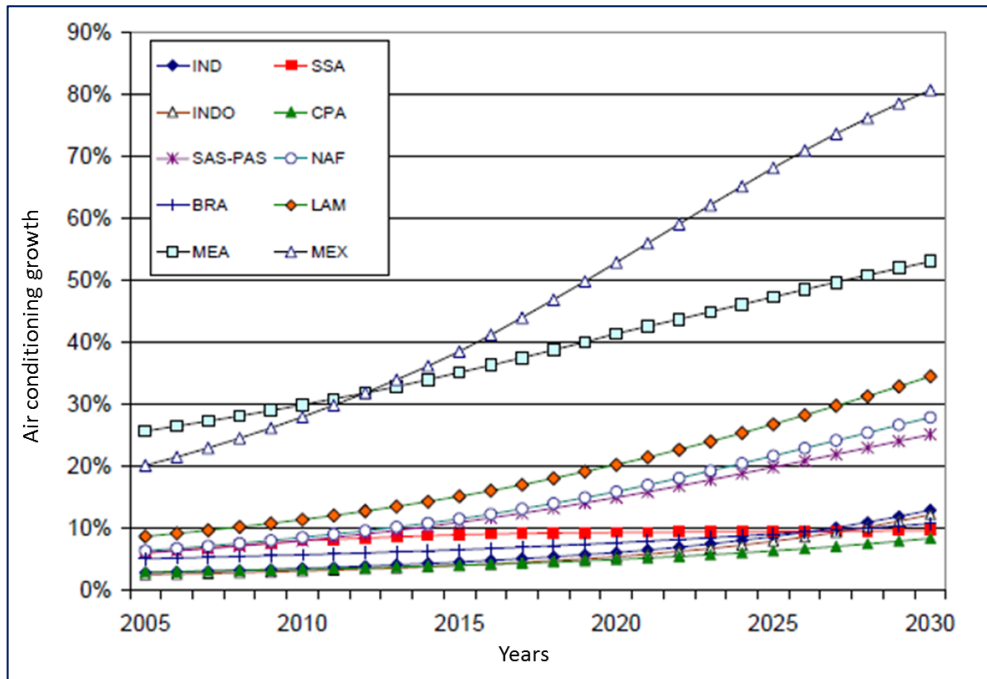
Figure 1-1: Air Conditioner growth rate for different region 2005-2030 [3]

Table 1-1 Abbreviations [3]

Region	Code
India	IND
Sub-Saharan Africa	SSA
Indonesia	INDO
Middle East	MEA
Mexico	MEX
Centrally-Planned Asia	CPA
Other Asia	SAS-PAS
North Africa	NAF
Latin America	LAM
Brazil	BRA

Air conditioning systems form a major part of the residential power consumption which vary from one place to other. For instance, the residential A/C units in Australia and India in the summer season consume approximately 40% of the total power consumption [2]. In UK and China, space cooling consumes about 17% and 20%, respectively, of the total power consumption. A/C systems consume more than half of the total power consumption in Saudi Arabia during the peak times in summer season [1, 4]. Studies have shown that, space cooling demands in Europe will significantly increase by 72% over the next 15 years and by 2100 will be 30 times its current value. By the end of this century the expectations of the global power consumption for air conditioning alone will be 33-fold [5, 6]. Figure **1-2** shows the forecast results of the power consumption of AC systems in Tera Watt hour from 2005 to 2030 for different regions across the world. Figure **1-3** compares the global energy demands for air conditioning and heating until the end of this century. This figure clearly shows that the energy demand for air conditioning is increasing significantly every year since 2011 and continues until the end of this century. Whereas for the heating remains almost constant and the peak will be 2030 [6].
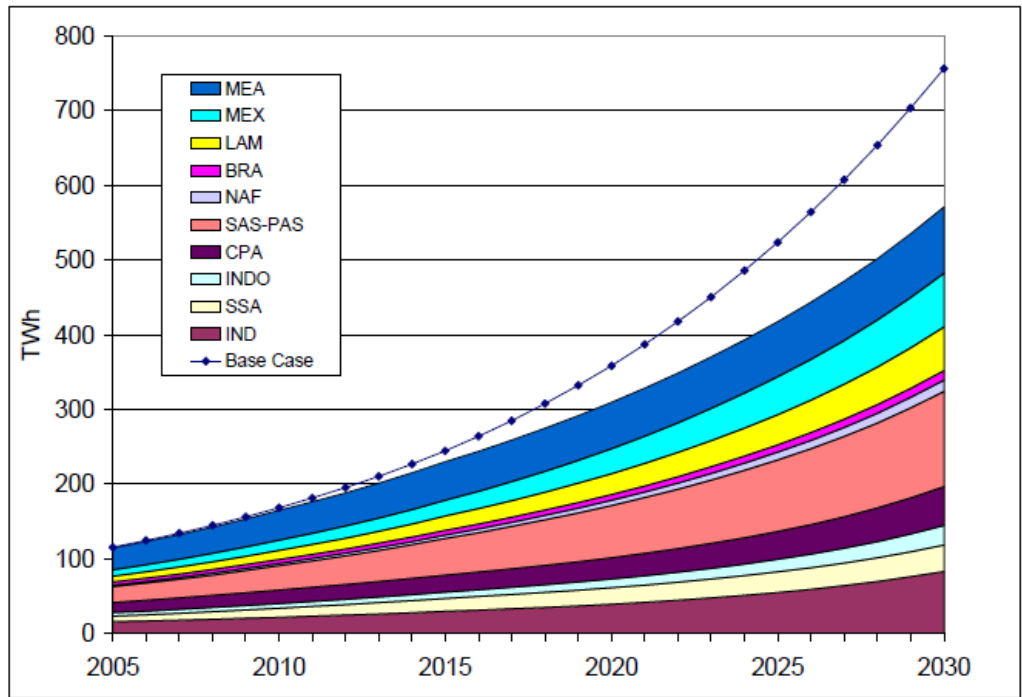
Figure 1-2: Air Conditioner in the residential sector for different region in the world [3]
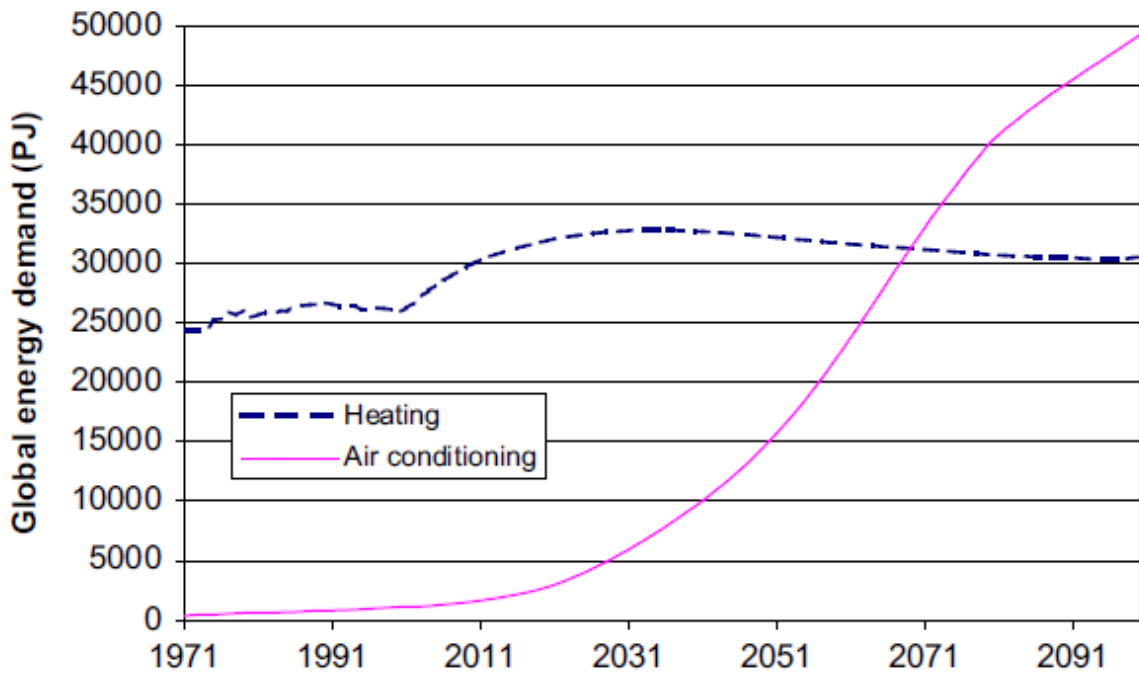
Figure 1-3: Global energy demands for residential air conditioning [5]

The above described energy consumption have a major impact on national electricity grids particularly during peak times. Also, it contributes to global warming as a result of CO_2 emissions associated with fossil fuel combustion and the leakage of the Chlorofluorocarbon (CFC) and Hydrochlorofluorocarbons (HCFC) refrigerants used in conventional A/C systems. According to the National Institute for Public Health and the Environment in Netherlands, leakage from refrigeration systems will contribute 25% of the total emissions by the middle of this century [1]. Figure **1**-**4** presents the global CO_2 emissions of air conditioning and heating systems until the end of this century showing similar trends to their energy demands shown in Figure **1**-**3** [3, 6].
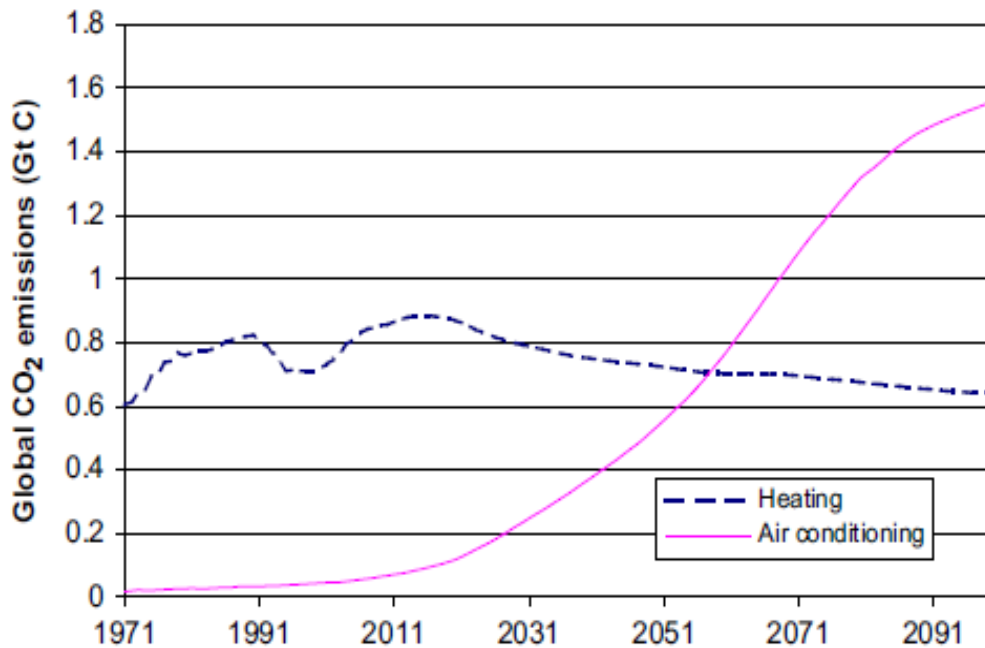
Figure 1-4: Contributions of the residential air conditioning and heating system to the global CO_2 emissions [6]

Many electricity suppliers face difficulties to overcome this significant growth of the energy demands particularly during peak times where the ambient temperature is at highest level. Thus there is a need to enhance the performance of the commonly used air conditioning

systems (vapour compression system) by reducing their power consumption and CO_2 emissions which will lead to better electric network balance and cleaner environment.

The performance of the AC systems is assessed based on the well-known factor called Coefficient of Performance (COP). Different techniques are used to enhance the air conditioning system COP by either reducing the compressor input power or increasing the cooling output by using sub-cooling or superheating the refrigerant in the evaporator [7].

Various enhancement technologies are discussed in the literature such as reducing the condenser temperature using water cooled condenser or water spray [8-10], or by reducing the compressor power input through using efficient compressors or by having an efficient control system particularly during partial load operating conditions [11-13].

Other researchers have investigated advanced method to enhance the system COP by shifting the cooling load to the off peak times (at night where the ambient temperature and the electricity prices are lower than that during the day) through integrating cold storage devices into existing air conditioning systems. This technique has many advantages in terms of: reducing the energy demands during peak times, reduction in system size, and enhancement in the A/C system performance by running at lower ambient temperature (night-time) [14-24].

However, the published work showed contradictory results regarding the energy saving of such systems with some researchers reporting energy saving of 27% to 46% while others reported no energy saving particularly when the storage medium is ice [25-29]. Therefore the integration of energy storage with A/C systems needs further research to identify the operating conditions or storage materials that will lead to energy saving.

Due the fact that the current A/C systems consume large amount of energy during compression process, other researchers have developed new methods to generate cooling and power using cryogenic fluids for different applications. Different cryogenic fluids can be used for such approach such as liquid natural gas (LNG), liquid carbon dioxide (CO_2), liquid

oxygen (LO_2), liquid nitrogen (LN2) and liquid air (LAir) [30-35]. Many of them have reported that LN2 and LAir are the most attractive energy storage cryogenic fluids due to their high energy density, availability, low cost and environment friendly [35-40].

Surplus electricity at off peak times or renewable sources such as wind turbines, geothermal, biomass and solar PV can be used to generate LN2/LAir. Most of the published work regarding using cryogenic fluids for cooling and power generation is for refrigerated transport vehicles. However, using cryogenic fluids for air conditioning and/or power generation for domestic or office buildings have not been investigated. To assess the performance of the integration system or the proposed cryogenic system a cooling load of typical dwelling in Sebha city, Libya was selected as a case study.

To recover most of the energy stored in LN2/LAir an efficient cryogenic heat exchanger where boiling/evaporating process of LN2/LAir (which considered as one of the most complex two phase flow system) takes place needs to be developed. CFD simulation using Ansys Fluent software is used to develop highly efficient cryogenic heat exchangers. The simulation will take into account evaporating/boiling process of liquid nitrogen flowing in the heat exchanger. There is very limited published work that investigated such process either experimentally or mathematically [41-55]. Moreover the CFD simulation tools will also be used to assess the expander performance at various input conditions.

1.2   Aims and objective

The aim of this work is to investigate the feasibility of using LN2/LAir air conditioning for domestic and commercial applications that leads to energy saving and reduction in the peak electricity demands and CO2 emissions. This aim can be achieved through the following objectives:

- Carry out detailed literature review regarding (i) the growth of global demands of air conditioning systems, their types, their energy consumption and their global contribution to the CO2 emissions, (ii) the methods used to enhance their performance including integrating them with cold energy storage systems to determine the key components or parts that have the major impact on their performance

- Develop a mathematical model using MATLAB combined with REFPROP software to find the key parameters, operating conditions and storage mediums that lead to significant improvement.

- Investigate the possibility of using other cooling systems including cryogenic fluids such as LN2/LAir.

- Develop a mathematical model using MATLAB combined with REFPROP for various LN2/Air cooling and power cycles to investigate the potential of using such fluids not only to generate cooling but also to generate power for domestic and commercial applications at peak times.

- Develop CFD models for the main components (cryogenic heat exchanger and LN2 engine) to find out the best configuration that extracts most of the energy stored in LN2/Air.

- Construct the prototype for the developed cryogenic heat exchanger and build the test facility required to assess its performance and to validate the CFD model.

1.3   Thesis outline

This thesis presents detailed investigation regarding the feasibility of using cryogenic energy storage for air conditioning of domestic and commercial buildings. The overall thesis structure and how the chapter links to each other is presented in the flowchart shown in Figure **1**-**5**.

CHAPTER ONE: INTRODUCTION
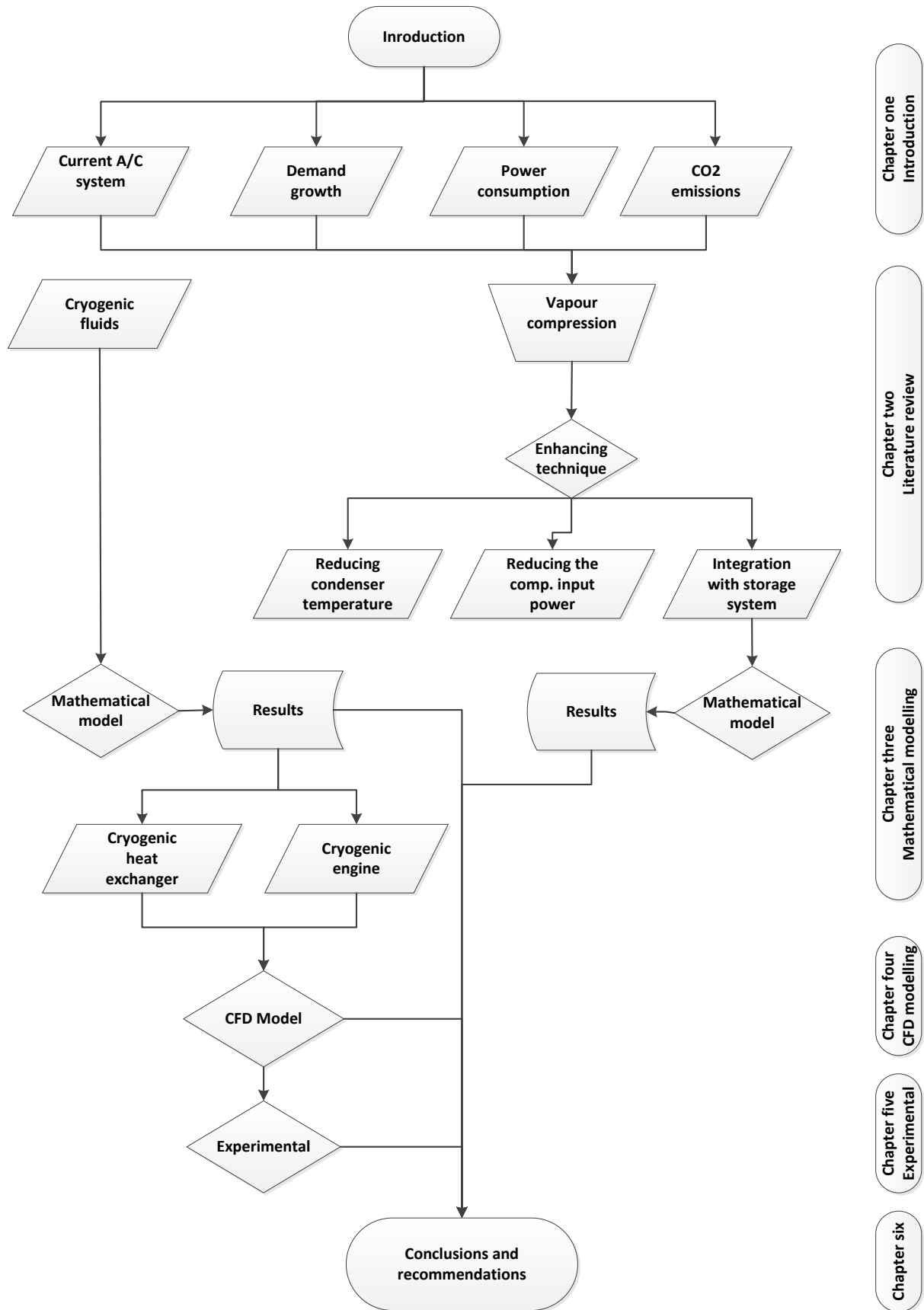
Figure 1-5: Thesis structure flow chart

The thesis is divided into six chapters as following:

Chapter one provides a brief introduction about the significant growth in demands for air conditioning systems and their effect on the national electricity grid. Also it presents a brief description of various methods used to enhance the performance of AC systems. This chapter also includes the research aim and objectives as well as thesis outline.

Chapter two presents a comprehensive literature review regarding the most commercially available and used air conditioning systems and their global demands. Also it highlights their impact on the national electricity grid and the environment. Then the chapter gives detailed review about the most commercially used methods to enhance their performance including lowering condenser temperature, using water cooled condense or water spray, reduce the compressor input power by controlling flow rate and integration of cold storage in the Air Conditioning systems. A review about other used methods to provide cooling such as cryogenic fluids is also presented.

Chapter three describes the development of a thermodynamic model for assessing the performance of air conditioning system and investigating the effect of including energy storage using phase change materials. The chapter is divided into two sections; the first one investigates the energy saving of integrating various cold storage technologies with the conventional AC systems using MATLAB software. While the second section proposes a new air conditioning system that uses the cold storage energy in the form of Liquid Nitrogen/Air to generate cooling and power for domestic and commercial applications using MATLAB and REFPROP software.

Chapter four presents the CFD modelling for the cryogenic cooling and power system components using ANSYS FLUENT V18.2 software. The CFD models are divided into different sections including the modelling of LN2 evaporation process, modelling of

cryogenic heat exchanger, modelling of solidification process and modelling of LN2/Air engine. the

Chapter five describes the developed LN2 facilities with detailed description of each component and the measuring devices. Also it presents the calibration of measuring instruments and uncertainty analysis. Finally the chapter presents a comparison between the CFD model and the experimental results.

Chapter six presents the project conclusions and recommendations for future work. The chapter highlights the main outcomes from this research and provide some suggestions for future work.

CHAPTER TWO

LITERATURE REVIEW

2.1 Introduction

This chapter presents a detailed literature review regarding the commonly used residential air conditioning systems and the commonly used techniques to enhance their performance including reducing the condensing temperature by using water spray or water cooled condenser, controlling the refrigerant flow rate and integration with cold storage systems. Other cooling systems that use cryogenic fluids have also been described in this chapter.

2.2 Current AC system

Electrically driven mechanically vapour compression cycle is the most commonly used technology for air conditioning applications. The cycle consists of four components namely; compressor, condenser, expansion valve and evaporator (see Figure **2-1**). The cycle works between two pressures; the lower pressure is in the evaporator where the working fluid (refrigerant) is evaporated and superheated by absorbing heat from the space to be cooled. The superheated gas is pumped to the condenser, which is located outside the building, to reject the absorbed cooling load and the heat generated by the compression process to the ambient. The condensed refrigerant returns to the evaporator after passing through an expansion valve that reduces its pressure and temperature as shown in Figure **2-1** [56]. The actual system coefficient of performance COP vary from 2 to 2.9 depending on the type and the condenser cooling method [57].
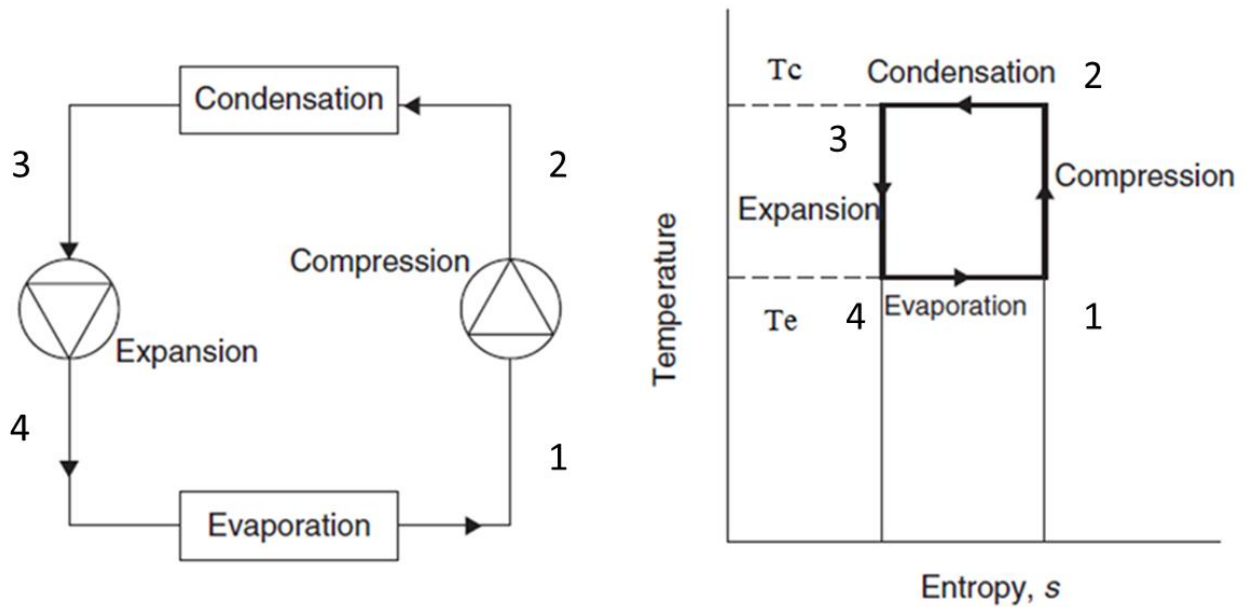
Figure 2-1: Air conditioning cycle[56]

2.3 Enhancing A/C performance

The performance of the A/C systems is assessed based on the well-known factor called Coefficient of Performance (COP) defined as the ratio of load to (h_1-h_4) to the compressor input power (h_2-h_1). Thus most enhancement methods/techniques were focused on either reducing the compressor input power or increasing the cooling effect by reducing the evaporator inlet temperature using sub-cooling technique and/or increasing the evaporator temperature by superheating the refrigerant in the evaporator [7].

2.3.1 Lowering condenser temperature (using water cooling)

Air conditioning system uses a condenser to reject the heat absorbed at the evaporator cooling load and the heat generated through the compression process. Condensers are classified based on the selected cooling medium as air-cooled, water cooled or evaporative where the two mediums (air and water) are mixed. Due to their lower initial cost and less maintenance requirement, air cooled condensers are commonly used in small and medium sizes (up to

capacity 20 refrigeration tonnes) which include most air conditioning and refrigeration systems used in the residential sector. However, input power for air conditioning or refrigeration systems which use air-cooled condensers are higher than other types due to their high condensing temperature (15-20 degrees) above the ambient. This high condensing temperature increases the compressor pressure ratio which increases the compressor input power and decreases the system COP as well as the compressor life [10]. Using Ph diagram, Figure **2**-**2** shows how reducing the condensing temperature will lead to reduction in the compressor input work (1-2) without significant reduction in the cooling effect (4-1) which enhances the system COP. Youbi-Idrissi et al. [10] developed a mathematical model for using a water spray on an air cooled condenser and found that the cooling capacity and the COP have increased by 13 % and 55 % respectively. Hosoz et al. [9] have experimentally tested three different types of air conditioning condensers; air cooled, water cooled and evaporative condensers. They found that in terms of the system capacity and the COP, water-cooled system had higher cooling capacity and higher COP and they were 2.9–14.4% and 1.5–10.2% higher than that of the evaporative condenser. The cooling capacity and the COP of the evaporative condenser system were 31% and 14.3% respectively higher than air-cooled condenser. Hsiao et al. [8] have developed air conditioning system using a cold storage material that stored surplus cold energy when the cooling load is lower than the nominal capacity. The cold storage system was used to cool the condenser at the full load time to enhance the system performance. They have tested the system at various cooling loads and results showed that within the tested range the system COP was improved by 15.3% compared with the conventional one.
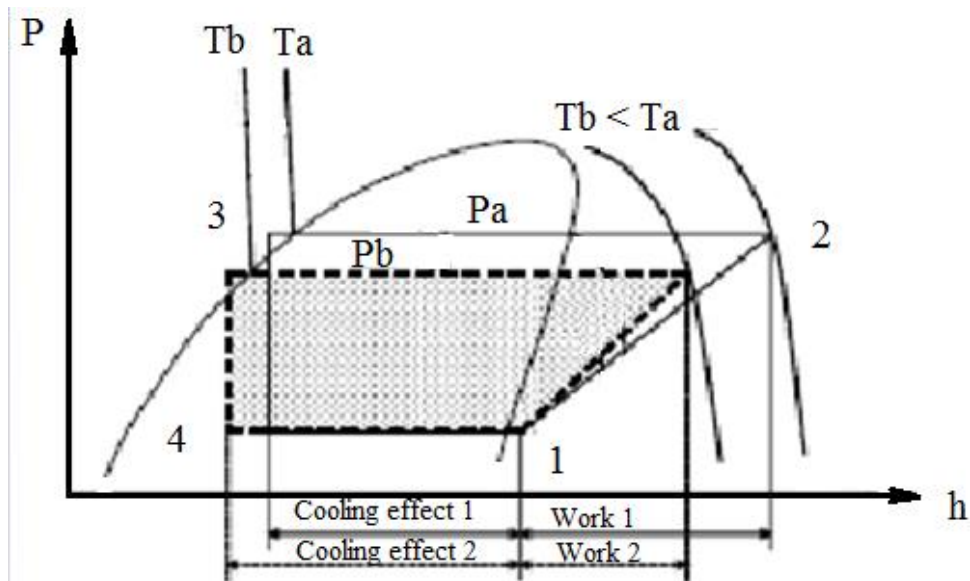
Figure 2-2: Reducing the condenser temperature using water spray [10]

2.3.2 Controlling flow rate

The vapour compression systems are normally designed for full load operation, however, most of the time they work under partial load due to the variation of cooling demand due to changing the ambient temperature during the day or the season or any other conditions. Different methods/techniques are used to meet the required cooling load without significant reduction in the system performance. Meeting these various loads need an efficient control system to be integrated to the A/C system to maximize the system COP and the comfort in the cooling space.

As the condenser and the evaporator are static devices and they are designed for the maximum load thus most of the control systems are fitted to the compressors or the expansion valves to control the refrigerant flow rate to match the load variation.

At part load, different techniques are used to reduce the input compressor work and enhance the air conditioning system performance [13].

Regarding reducing the compressor input power, different techniques have been used such as using inverter to control the compressor speed with respect the cooling load, control the

refrigerant flow rate by adjusting the compressor displacer or by using electronic expansion valve that can change the refrigerant flow rate according to the load. These techniques are mainly control the refrigerant flow rate, which leads to reducing the compressor input power [13].

Aprea et al. [12] have developed a test facility identifying the optimum compressor frequency/speed that gives the maximum energy and exergy saving for a given cooling/heating load. Two different types of compressors (scroll and reciprocating) were used and the results showed that, compared with the traditional thermostat control this system achieved 15% energy saving when a reciprocating compressor was used and 25% when a scroll compressor was used. Similar work has been reported by Hu et al. [11] however, they have used a digitally controlled scroll compressor to provide various refrigerant volume flow rates. The proposed system was flexible and controlled the compressor pressure ratio and the expansion valve to meet the exact load particularly during the partial load. At partial load (83% of the full load) the system showed energy saving up to 75% compared with the conventional system, and its cost is 20% less than the AC inverter system.

2.3.3 Integrating Air Conditioning with storage systems

The maximum cooling load normally happens during the peak times where most of the electricity suppliers have difficulties to meet the user's demand. Also, the outdoor temperature where the compressor and the condenser are normally located is highest at peak time which lowers the system performance. Energy storage technologies have the advantages of storing the surplus electricity at off peak times to be used during the peak hours to meet various demands. So shifting the cooling to off-peak times using cold storage is another technique that can be used not only to enhance the air conditioning performance but also to provide a better stability of national electricity grid [24].

The use cold energy storage has many advantages such as reducing the energy consumption, increasing the system cooling capacity without changing the chiller size, enhancing the system performance by working at lower ambient temperature and working at the design load (full chiller capacity). A schematic diagram of the integration of cold storage with A/C system is shown in Figure **2**-**3**. At off-peak hours where there is no or little cooling load, the system stores the surplus cold energy in the storage tank. While at the peak times the stored energy is used to meet the full or the part of the cooling demand [3, 23, 29].
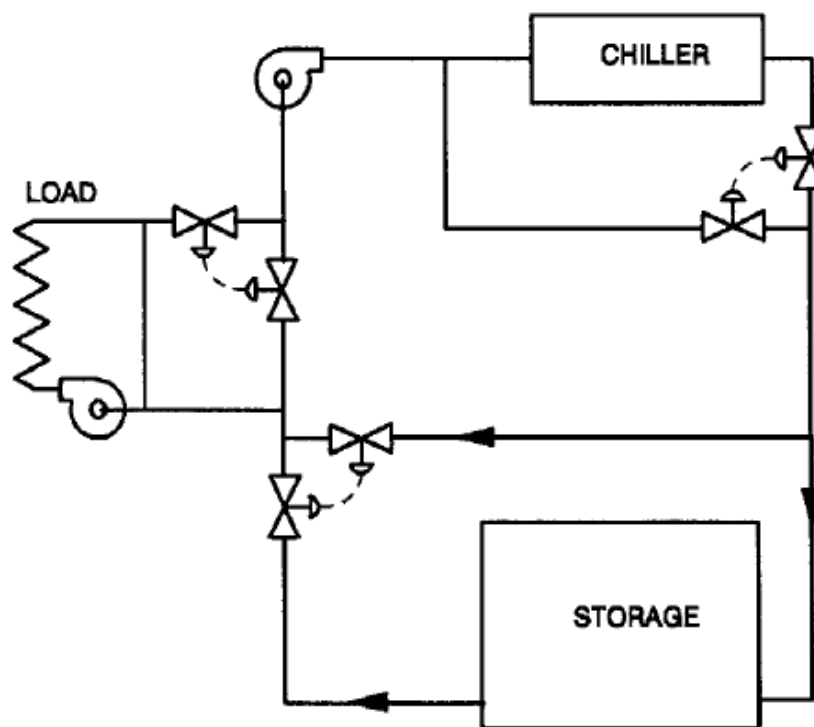
Figure 2-3: Integrating A/C with storage system [23]

There are several arrangements of integrating the cold storage devices with the conventional A/C system space [22] and several operating strategies for charging and discharging cold storage tanks to meet the cooling demand [16-21, 28].

These strategies are classified as Full Storage and Partial Storage. In the Full Storage strategy the A/C system is turned off at the peak times and the storage system is used to meet the cooling load while at the off peak times the A/C system is used to meet the cooling load and

for charging the storage system as shown in Figure **2-4** (a). In the Partial Storage scenario the storage system is used continuously to meet part of the cooling load and the rest is met by the A/C system. This scenario can be divided into two sub categories; Load Levelling where the chiller is running at the same capacity at all times to charge the storage system or meet the cooling load as in Figure **2-4** (b). The other sub category is Demand Limiting where the chiller capacity is lowered to certain level (20%, 30%, 50% and so on) at the peak times and it runs at the full capacity in the rest of the time as in Figure **2-4** (c) [16-21, 28].
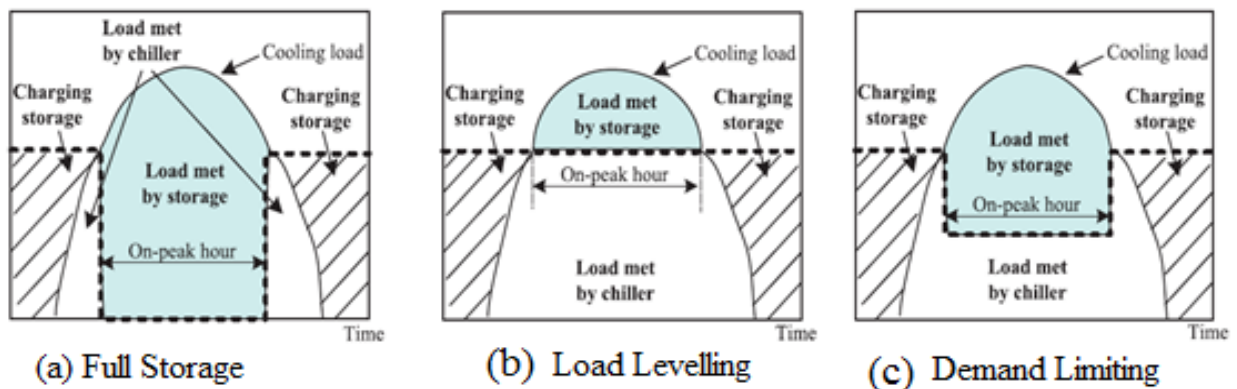
Figure 2-4: Different operating strategies [17]

The system performance is affected by the storage temperature and the storage medium. Most commonly used storage substances are chilled water, ice and phase change materials (PCMs) which can be classified to two main categories; sensible heat (chilled water or brine) and latent heat or phase change materials (PCMs). The PCMs have many advantages compared to sensible heat materials such as: higher storage capacity and it is 5-14 times of that sensible heat storage mediums depending on the storage medium [15]; a wide range of materials giving flexibility to choose the phase change temperature according to A/C requirements; enhancing the system performance when a higher evaporating temperature is used; and less temperature variation. On the other hand, PCMs have some disadvantages such as low

thermal conductivity; density variation; unstable under long term cycling and phase segregation [14].

The above mentioned published work and others have reported some achievements of integrating the A/C with the cold storage technique such as a considerable reduction in the energy consumption due to the lower rate of electricity during the off peak times, reduction in the system capacity particularly chiller capacity and enhancing the system performance due to working at lower ambient temperature (night time) [16-21, 28]. However, there was a great debate about the energy saving. Parameshwaran and Kalaiselvam [27] have experimentally investigated the effect of integrating PCM (hybrid nanocomposites-based) with a conventional A/C system on the system performance during full year. They achieved significant reduction in the nominal capacity of chiller by 40% and 46% at peak and partial loads, respectively. Compared with the convectional system 27% and 30% energy saving were achieved at peak times in summer and winter respectively [25-27]. Another PCM (Clathrate Hydrate Slurry), which has energy storage density 2-3 times that of chilled water and phase change temperature ranging from 5-12 °C, was used by Hidemasa et al. [58] showing that the integrated system showed energy saving of up to 36% and reduction in the yearly power consumption by 46% compared with the conventional system. The effect of integrating a chilled water storage system with existing air cooled chillers in Kuwait on the chillers performance was studied by Sebzali and Rubini [59]. Three different operating strategies, namely full load, load levelling and demand limiting, were applied and the results showed saving of up to 4% when full load strategy is used.

Nassif et al. [60] have developed a model to design an optimum system for integrating the PCM with the A/C system using ice as storage medium. The model took into account the charging and discharge times and the whole system size. Their results showed that, although there was 50% reduction in the annual energy cost due to the lower electricity rates during the

night compared to those during the day; the annual energy consumption increased by 11%. Sebzali et al. [60] integrated storage system using ice as storage medium to a clinic building in Kuwait where there were no differences in electricity prices during the day and night. They have used different operating strategies; Full Load, Load Levelling. Demand Limiting 50%, Demand Limiting 60% and Demand Limiting 70%. Despite of the benefits achieved by integrating the storage system in all operating strategies compared to the traditional A/C system, the system was showing no energy saving as shown in Table **2-1** [61, 62].

Table 2-1 Energy saving at different operating strategies [61, 62]

	Conventional	Partial (Load Levelling)	Partial (50% Demand Limiting)	Partial (60% Demand Limiting)	Partial (70% Demand Limiting)	Full
Chiller size (kW)	613	531	610	610	563	813
Charging storage Capacity (kWh)	0	656	1116	990	887	2264
Discharging Storage Capacity (kWh)	0	-273	-1028	-787	-666	-2261
Power at Peak Load (kW)	321	259	160	178	209	0
Chiller Energy Consumption (kWh)	4416	4506	4792	4756	4692	4785
Maximum Power (kW)	321	260	317	317	278	414
Increase in Chiller size (%)	0	-13	0	0	8	33
Cool Storage Used (%)	0	42	92	79	75	100
Increase in Peak Power (%)	0	-19	-50	-45	-35	-100
Increase in Energy Consumption (%)	0	2	8	7	6	8

Chaichana et al. [63] developed a mathematical model of integrating ice storage system with A/C system. The model considered different operating strategies and investigated the effect of the ambient temperature. Their results showed that the energy consumption was reduced by 5% when the Full load strategy was used where cooling system run at lower ambient temperature at night, however, for the other operating strategies the energy consumption has increased by up to 18%. Both strategies were showing reduction in the energy cost by 55% and 15% for the Full load and the Partial load respectively. Yang and You [64] tested and analysed the integration of ice storage with the A/C system using a Partial load strategy. Their results showed that about 45% of the peak load was cut off whereas the system consumed 13% an extra energy. The system could achieve some reduction in the energy cost if the electricity tariff at night was reduced to $0.035/ kWh from $0.090 /kWh.

2.4   Cryogenic energy storage

Cryogenic fluids such as Liquid Air (LAir) and Liquid Nitrogen (LN2) have recently been acknowledged as attractive energy carriers due to their high energy density and availability. These two energy storage medium have almost similar thermal properties due to the high percentage of nitrogen 78% in the air composition. The energy density can be defined as the maximum useful work that can be achieved to change the LAir/LN2 from the storage conditions to the ambient conditions. Renewable energy sources or surplus electricity at night can be used to liquefy atmospheric air and storing it in a liquid form [33-35, 40]. Comparison of LN2 energy density with some common cryogenic fluids is shown in Table **2-2** where it is clearly shown that, the energy density per kg of liquid nitrogen is higher than all other fluids except Methane which has 40% higher energy density however taking into consideration the energy density per volume (liter for example) Methane has 25% less energy storage per unit volume than LN2 [38, 39].

Table 2-2 Energy density of commonly used cryogenic fluids

fluid	Storage temperature K	Density kg/m³	Energy density		
			kJ/kg	W-hr/kg	W-hr/L
Liquid Nitrogen	77.4	809	768	213	173
Liquid Air	78.9	886	737	205	181
Liquid Oxygen	90.2	1140	635	176	201
Methane (without burning)	111.6	423	1093	304	128
Ethane (without burning)	184.6	545	352	97.7	53.2
Compressed air at 200 bar [bar]	300	233	258	715	16.7

The low boiling/evaporating temperature of the cryogenic fluids encouraged many researchers not only to use them to generate cooling for different applications but also to generate power. Regasification process of Liquid Natural Gas LNG where sea water is normally used to evaporate LNG and increases its temperature to be close to the ambient is one of the processes that encouraged many researchers to study the possibility of using that cold energy to recover part of the energy consumed to liquefy it or to reduce the energy input for new nearby liquefaction plant. In such systems, the LNG is used to run an open Rankine power cycle to generate power and cooling for liquefaction plant [30-32, 65-67].

These studies have concluded that recovering the cold energy stored in LNG during the regasification process to generate cooling and power is possible and promising, however, these plants are normally located in specific places and considering the safety aspects which add difficulties to use the system for domestic applications. Taken into account the environment and safety issues, the above mentioned advantages of using LN2/LAir as energy carrier, several studies investigated the potential of using these energy storage carriers to provide either cooling [36, 37, 68-72] or power [73-77] or both [78-84] for domestic applications as discussed in the following section.

2.4.1 Using cryogenic fluids for cooling applications

Regarding using liquid nitrogen for cooling applications, a cooling system for food transport vehicle was developed by Place [72]. The system generated cooling by evaporating LN2 in tubes/channels fitted around the cooling space as shown in Figure **2**-**5**. The LAir flow rate was controlled using a control valve connected to a thermostat fitted in the cooling space to provide the required amount of LN2. The system was simple, provided a uniform distribution of the temperature in the cooling space and kept the cooling space dry. Also the proposed

system showed a significant reduction in the car weight by replacing the traditional refrigerator or the ice that was used at that time.
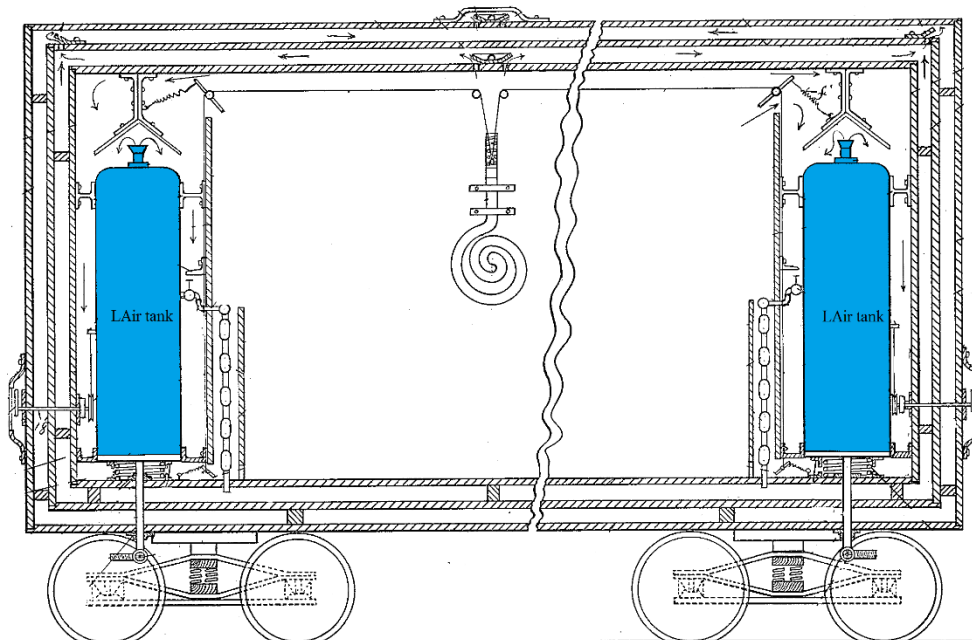
Figure 2-5: Liquid air cooling system[72]

LAir or liquid oxygen air conditioning system was presented by Harold . The system was quite and simple as shown in Figure **2**-**6** where LAir passes through a heat exchanger fitted in the path of a hot air flow. The hot air was cooled by means of evaporating and superheating of the LAir. The system had no moving parts, it was relatively lightweight and suitable for closed or partially closed space such as an airplane or spaceship [68].
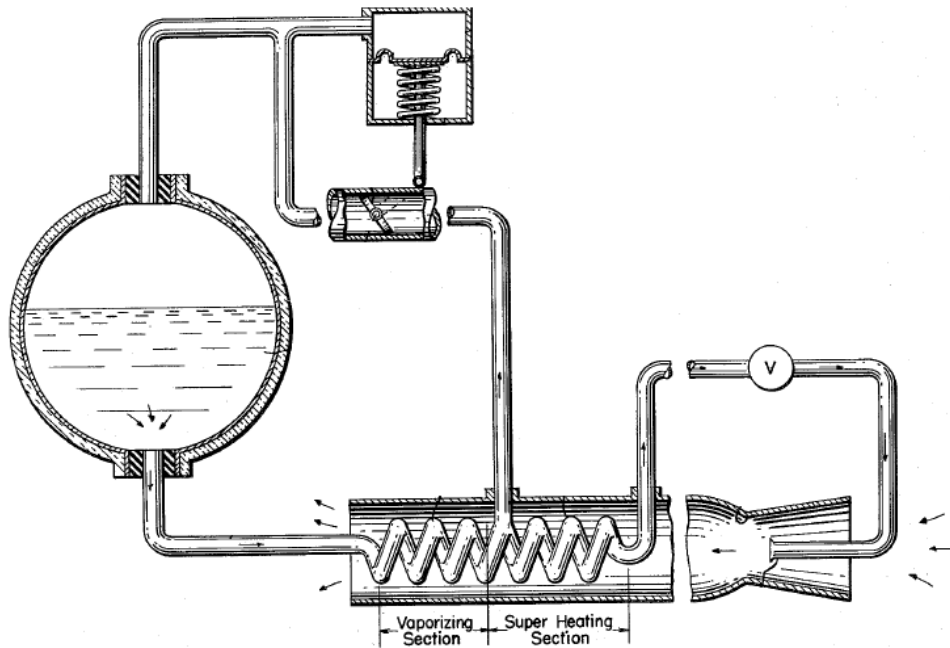
Figure 2-6: Liquid air/oxygen air conditioning systems [68]

Another cooling system using liquefied carbon dioxide to cool a frozen food transport lorry was developed by Saia et al. [71]. The system uses a finned heat exchanger with circulating fan fitted in the food space roof to evaporate the liquid carbon dioxide as shown in Figure **2-7**. A temperature regulator valve was used to control discharging the CO2 from its container which was also fitted in the cooling space roof. Ignoring the safety issues of the CO_2 in a closed space, the system reduced the lorry weight and provided wide range of freezing temperatures (below zero) suitable for various foods [71].
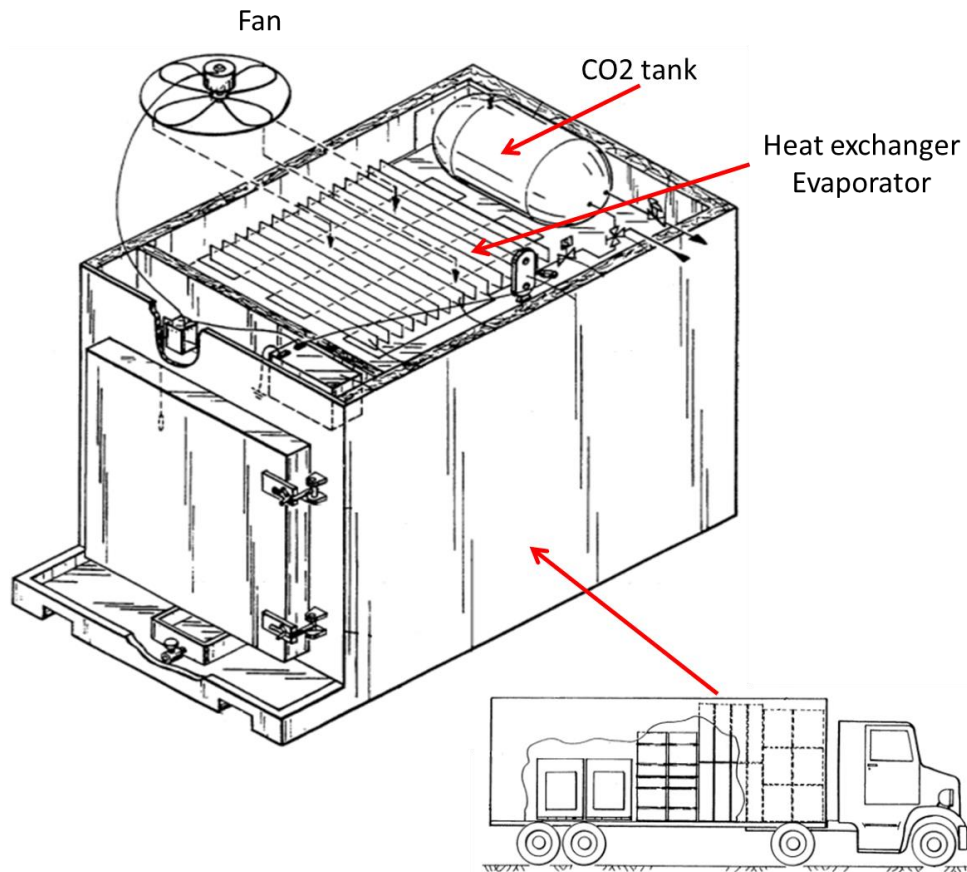
Figure 2-7: Liquid CO2 cooling system [71]

An air conditioning system using the direct release of LN2 from a high pressure vessel was reported by Dakhil [37]. The system is very simple as shown in Figure **2-8** where the LN2 vessel inserted in a small cabinet where the LN2 will be released to evaporate. Using a small fan fitted into the cabinet forces hot air to enter the cabinet space to be mixed with the released and evaporated LN2 then left the room space as cold air [37].
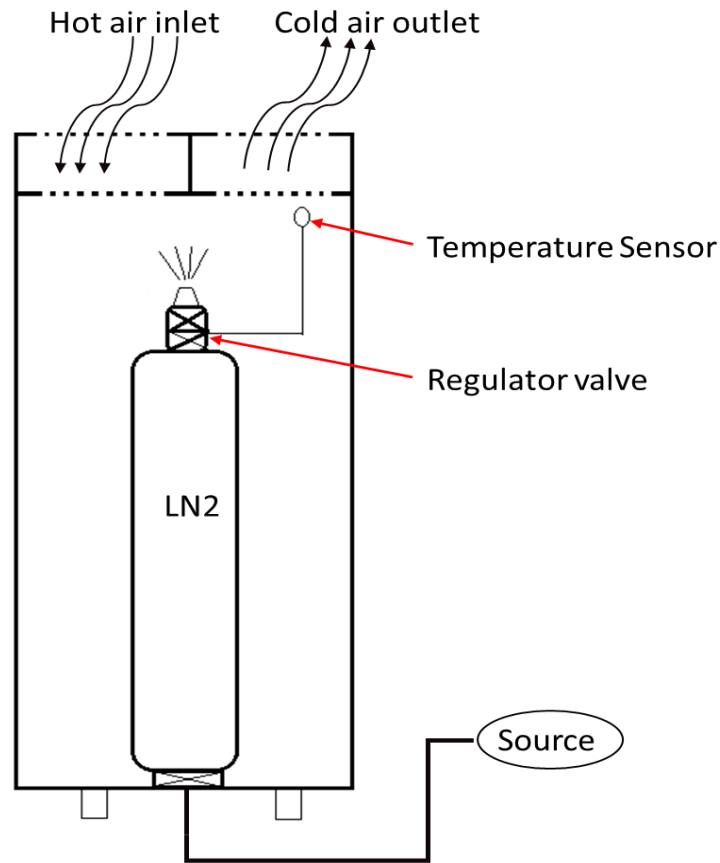
Figure 2-8: Liquid Nitrogen spray air conditioning system [37]

Garlov et al. [70] used a similar system for cooling a food transport vehicle where LN2 is directly sprayed into the food space in the lorry to maximize the extracted heat as shown in Figure **2-9**. During the loading/unloading of the vehicle, LN2 is directed through a heat exchanger fitted to the cooling space roof and a fan forced the fresh air into the cooling space through the heat exchanger. This make the environment inside the container breathable and cold during the loading/unloading processes [70].
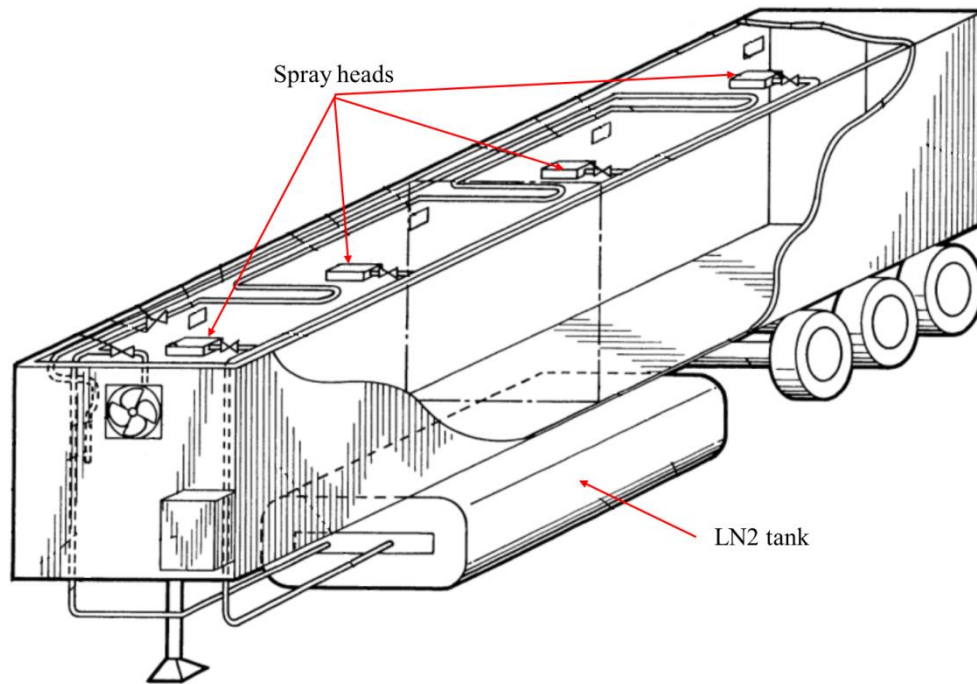
Figure 2-9: Liquid Nitrogen direct spray refrigerator [70]

Skobel et al. [36] invented a compact and remote refrigerator system for a beverage dispenser using LN2. The system as shown in Figure **2**-**10** consists of two heat exchangers to maximize extracting the cooling energy from the LN2. The first heat exchanger cools the beverage to a certain level while the second one cools it to the required freezing temperature. A flow control system was used to control the LN2 and the beverage flow rate to achieve the required temperature of the beverage and to extract cold energy as much as possible from the LN2 before venting it to the ambient. The device was relatively fast and efficient in producing cooling, quiet, suitable for the remote areas where there is no electricity and environment friendly.
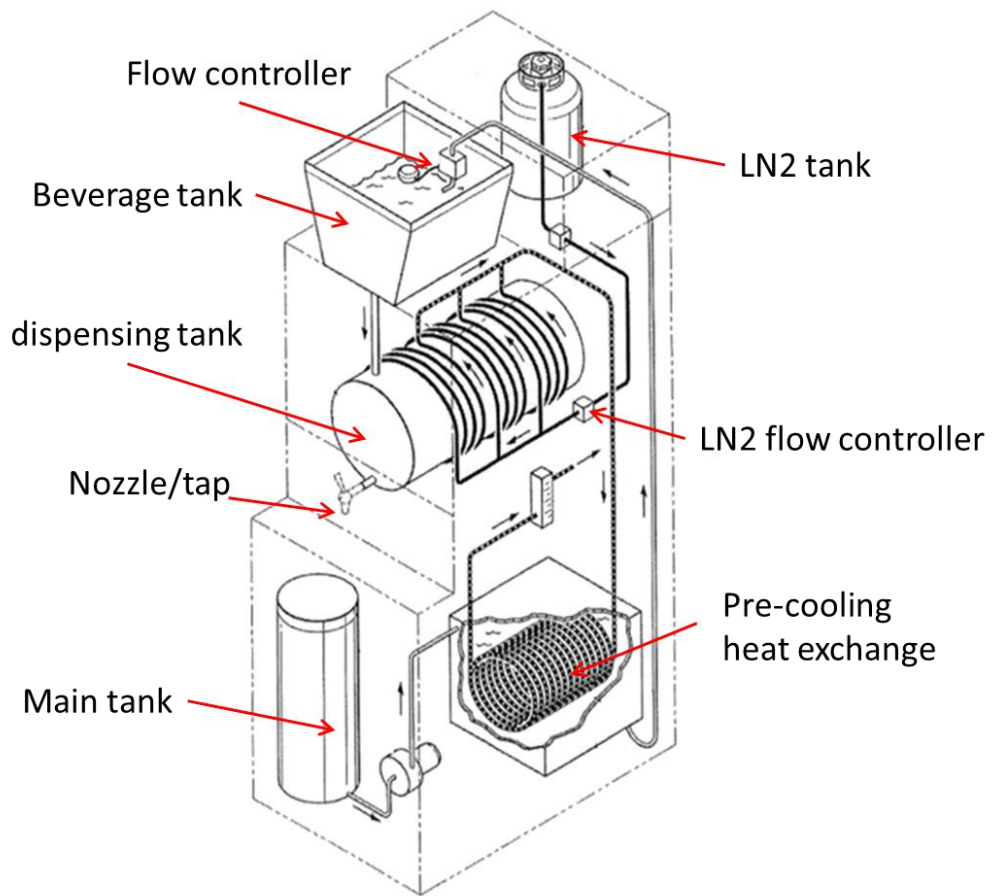
Figure 2-10: LN2 beverage refrigerators [36]

Watanabe et al. [69] have tested new cooling system that uses liquid nitrogen to cool high-temperature superconductor (HTS) cables to maintain them at superconducting state. There were different configurations as shown in Figure **2-11** where the cables have two paths allowing circulating LN2 to go and return.
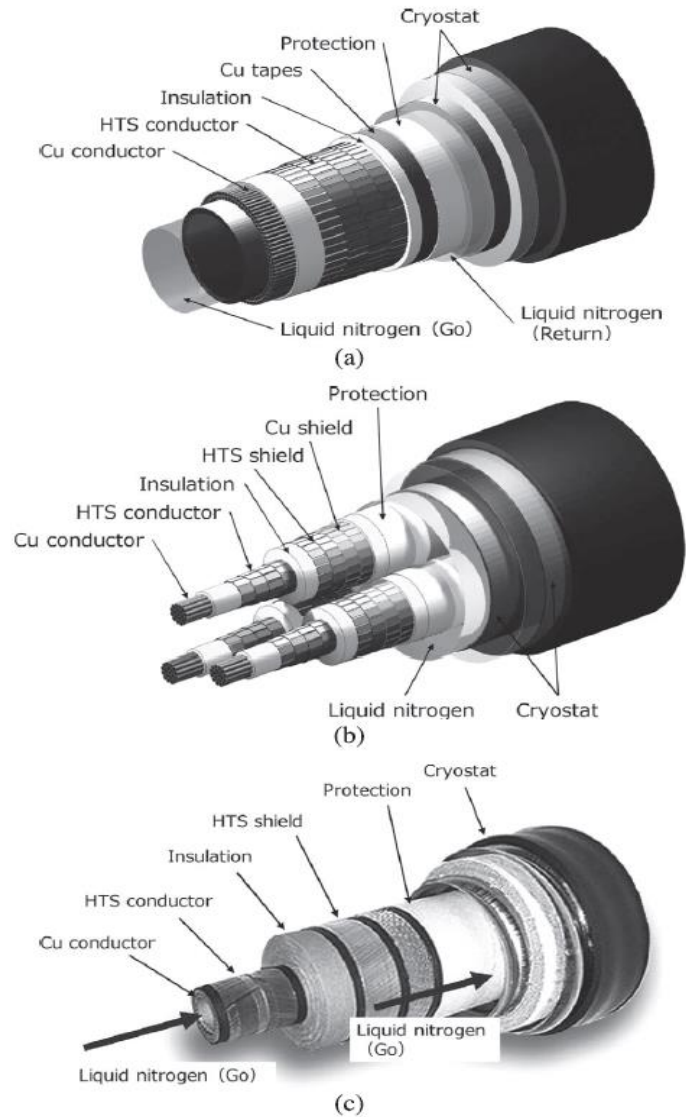
Figure 2-11: HTS cables LN2 cooling system [69]

2.4.2 Using cryogenic fluids for generating power

Regarding using cryogenic fluids for power generation, Manning and Schneider, [77] have patented an efficient liquid nitrogen engine. The engine runs close to isothermal expansion process by passing the high pressure gas (nitrogen) through three expanders with reheating between the first and the second stage. Schematic diagram of their engine is shown in Figure **2-12** (a) where the LN2 is pumped from the cryostat to a high pressure heat exchanger

where it evaporates and superheats by the ambient temperature. Then the superheated nitrogen passes through the three expanders to generate power. To approach isothermal expansion process, nitrogen passes through two heat exchangers after the first and the second stages respectively to return the gas temperature to the ambient as show on the T-S diagram in Figure **2-12** (b).
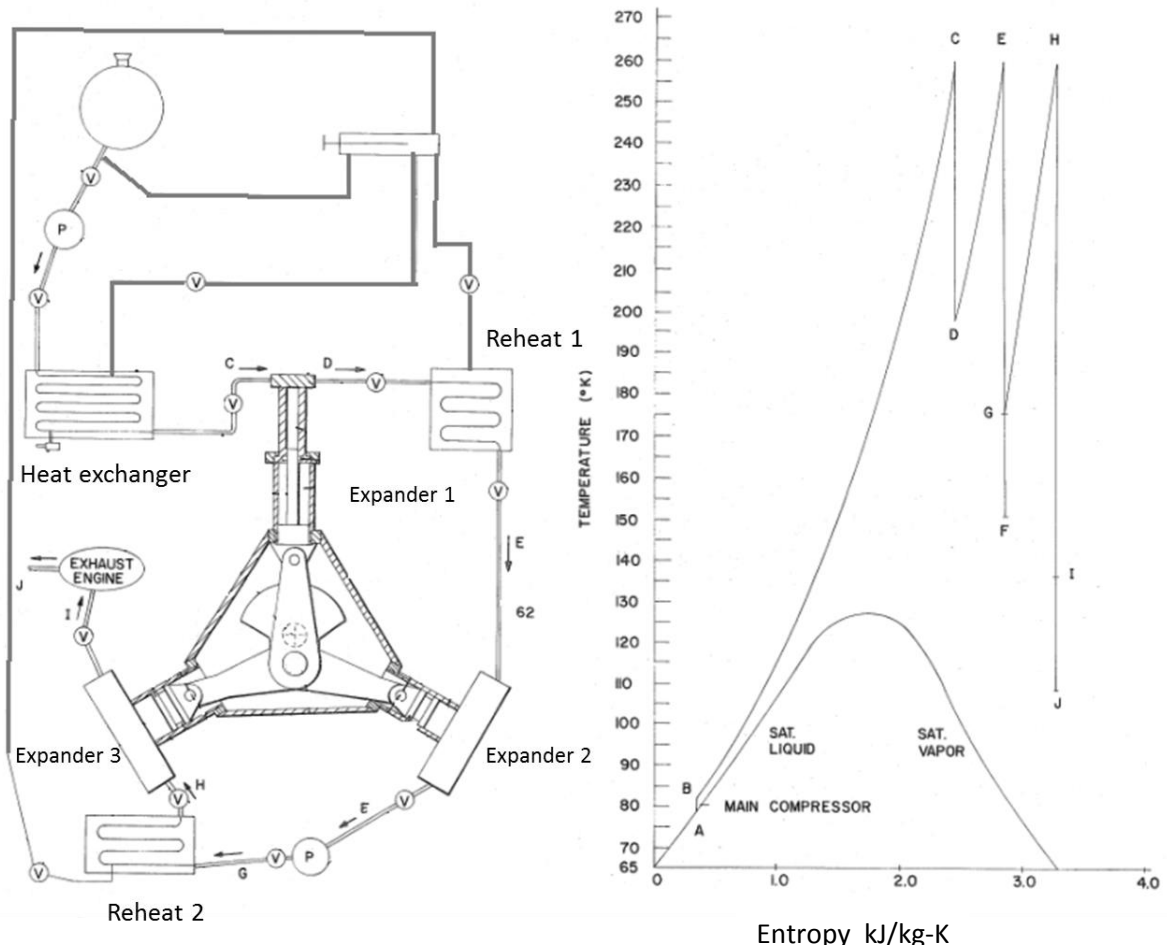
Figure 2-12: LN2 engine with three stage expanders and reheat [77]

Ordonez et al. [76] analysed and tested different cryogenic fluids (including He, Ne, N2 and Air) to investigate their feasibility to generate power to derive a small car. The result showed that LN2 is the most attractive fluid to fuel such engine with high energy density of 0.75 MJ/kg [3, 75, 76].

Knowlen et al. [74] investigated the feasibility of using LN2 to fuel a car engine. The engine used the ambient temperature as heat source and different near isothermal expansion approaches were intensively studied. A schematic diagram of the engine is shown in Figure **2**-**13** where the ambient heat evaporates a pressurized LN2 in a heat exchanger before expanding it in an isothermal expander that uses a secondary warming fluid to add heat to the nitrogen during the expansion process to maintain it at almost constant temperature. A comparison between the isothermal expansion and the adiabatic expansion was also made showing significant difference as depicted in Figure **2**-**14**. The figure shows that as the inlet pressure to the expander increases both expansion processes show increase in the specific output work, however, after certain level of pressure the adiabatic expansion shows no significant change while the isothermal expansion process continue to show an increase in the specific work output with the increase of the inlet pressure. They also reported that using LN2 to drive cars is promising where 15 kW power can be generated using a two-cylinder engine with inlet pressure of 60 Bar and at RPM of 850. This output power is enough to drive a small car 140 km consuming only 200 litres. Practically using a three-stage expander with reheat in-between or a reciprocating engine with high surface-to-volume ratio can achieve 85% of the isothermal expansion process [3, 74].
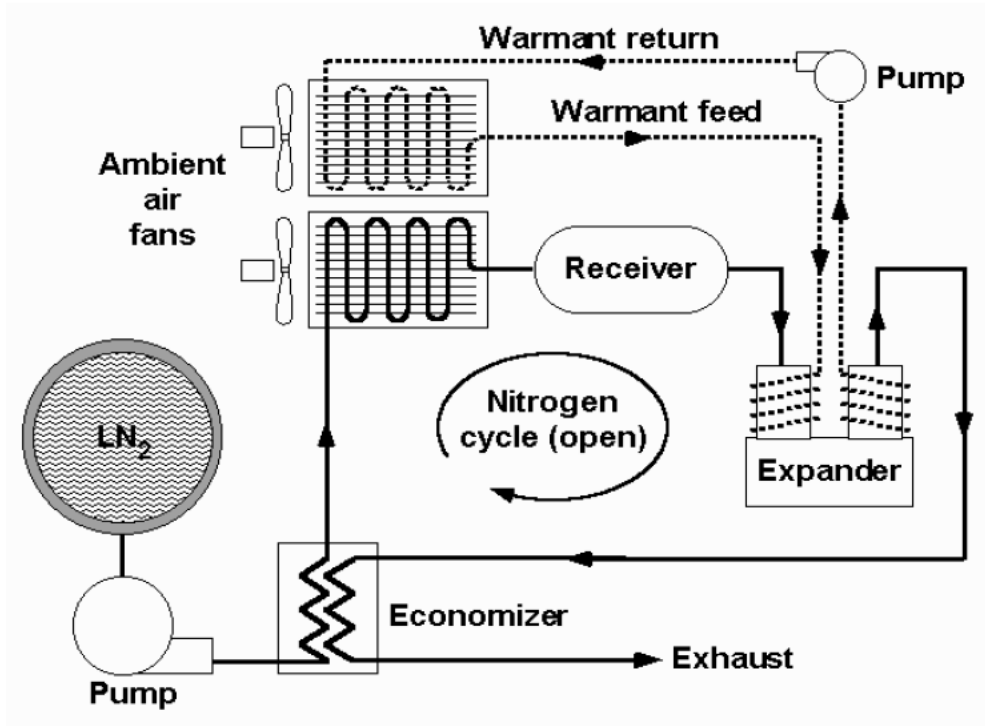
Figure 2-13: LN2 engine [74]
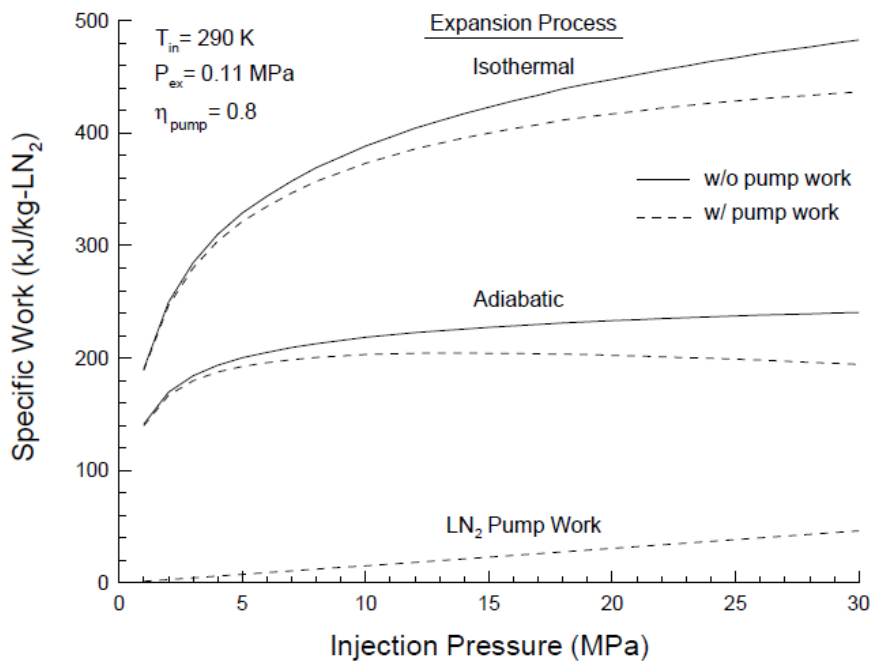
Figure 2-14: Specific work output from isothermal and adiabatic expansions [74]

Chen et al. [73] developed a mathematical model to compare the performance of compressed

air and a LAir for fuel zero emission engines. The engine was proposed for driving a typical

small car and the comparison was based on the energy density, the output work, cooling capacity and the efficiency. Figure **2**-**15** (a, b) show schematic diagram of the compressed air and the LAir engines, respectively, while Figure **2**-**16** (a, b) shows the T-S diagram of the power cycle of each engine. The study investigated wide range of working pressure (0-400 Bar) and ambient temperature (270-320 K). Both fluids showed an increase in the output work and the cooling capacity (coolth) with increasing the ambient temperature and the working pressure as shown in Figure **2**-**17**. For a given temperature and pressure (300 K and 300 Bar for example) the output work and the efficiency of the compressed air engine is slightly higher than the liquid air engine due to the pump input power, however, the volumetric energy density of the compressed air is about 2.5 times less than that of LAir which produce higher cooling capacity [73].
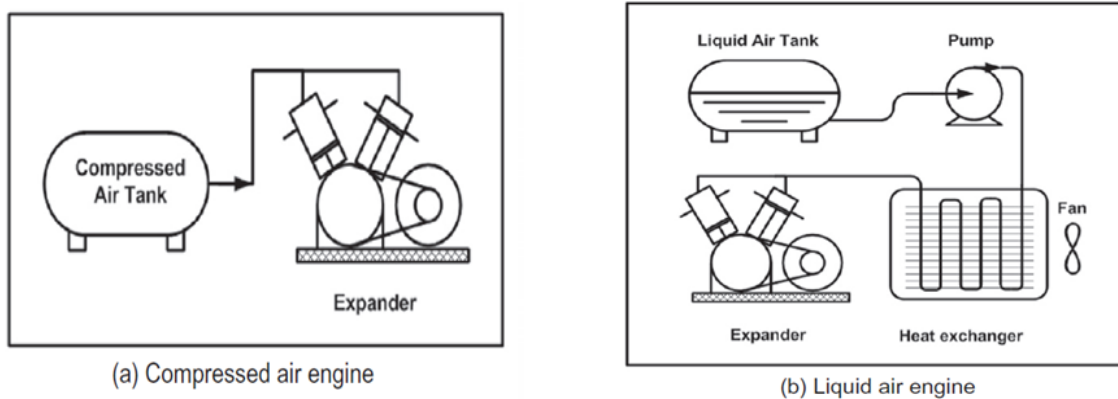
Figure 2-15: (a) compressed air engine, (b) LAir engine [73]
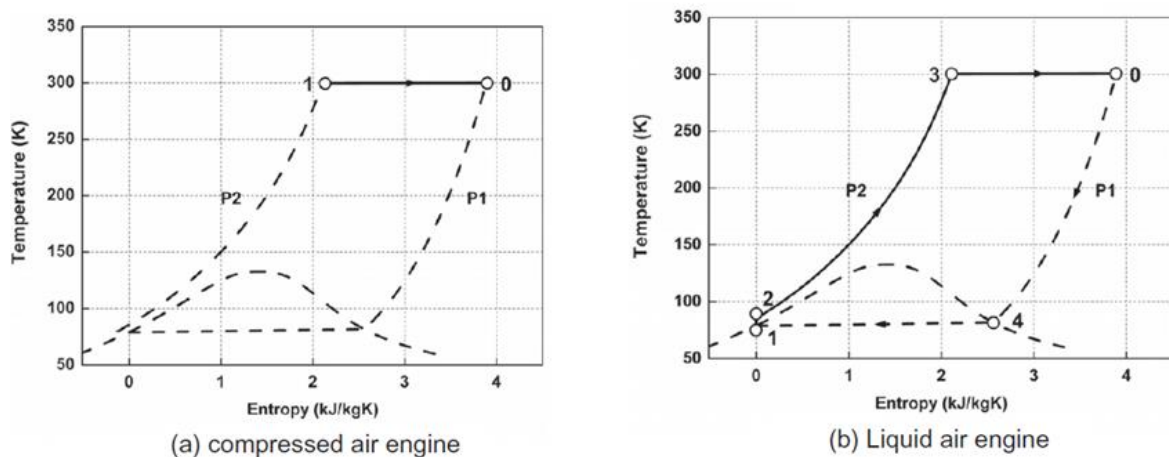
Figure 2-16: (a) compressed air engine, (b) LAir engine [73]
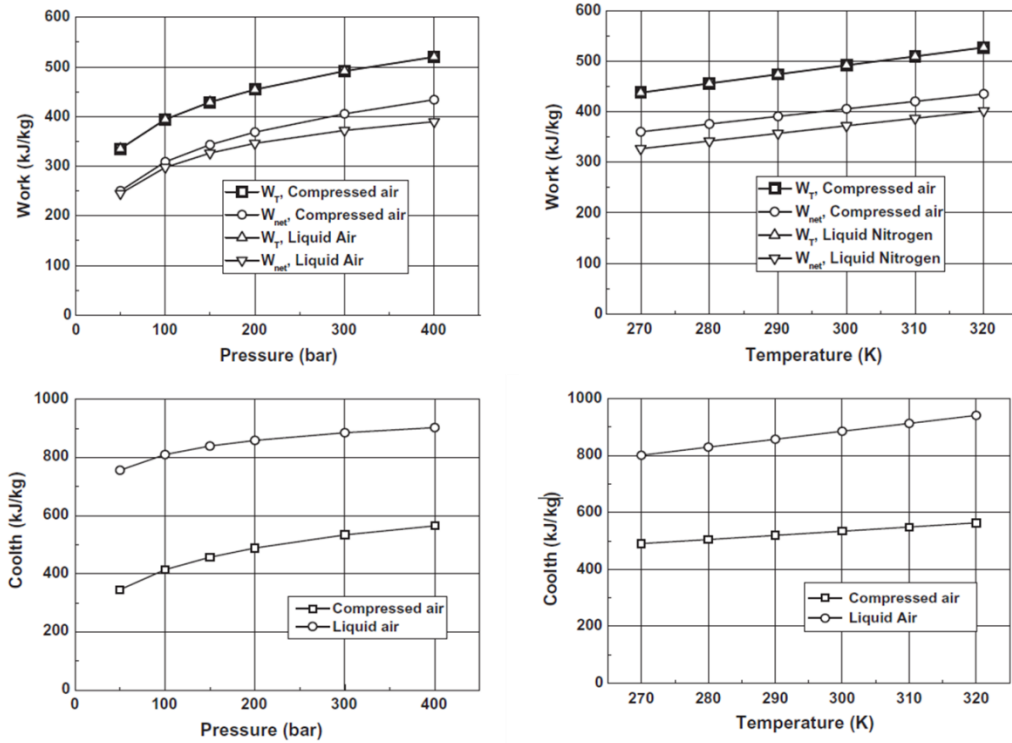
Figure 2-17: specific work output and coolth [73]

2.4.3 Cryogenic fluids for generating cooling and power

To recover all or most of the stored energy in the cryogenic fluid, systems for simultaneously generating power and cooling were reported by some researches. Ordonez, et at [84] developed a mathematical model of integrating an open LN2 power cycle to drive a closed Brayton cycle. The dual power output was used to drive a zero emission vehicle. The working principle of the system can be explained using the schematic diagram shown in Figure **2-18** where the system can be split into two parts (a) and (b). The numbers 1, 2, 3, 4, 5 and 6 in part (a) are referred to the cooling, compression, heat recovery, heat input, expansion and precooling processes of the closed Brayton cycle. While a, b, c, d, and e are referred to the LN2 open power cycle where a-b, b-c, c-d, d-e are evaporation, compression, heat input and expansion processes. Their results showed that the specific output energy of the proposed combined system was ten times higher than that of a prototype LN2 car (CooLN2Car) and more cost effective than the commonly used electric batteries [84].
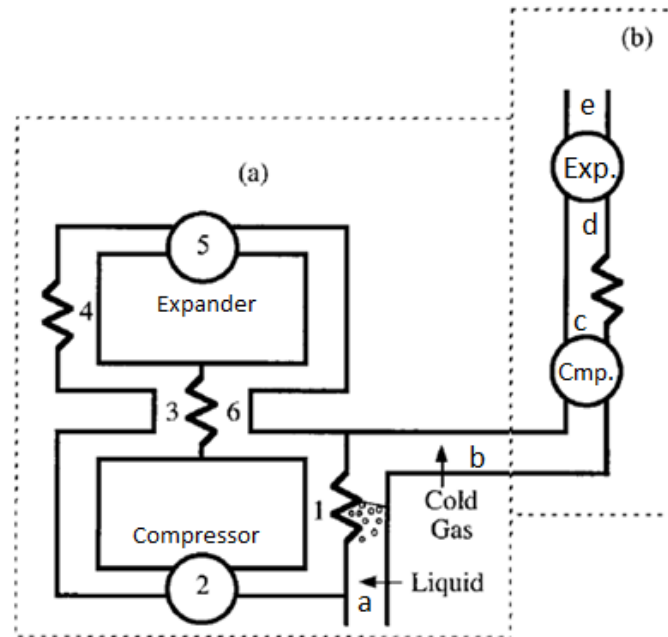
Figure 2-18: LN2 fueled a closed Brayton cycle [84]

Dearman [83] developed LN2 cooling and power generation system for food transport vehicles. A schematic diagram of such system is shown in Figure **2-19** where LN2 is pumped to an evaporator fitted in the roof of the vehicle then the high pressure gas/vapour is used to run a reciprocating engine. The engine works at near isothermal expansion using a novel concept of directly spraying a heavy fluid simultaneously with N_2 gas during the expansion process to maintain the gas at the same inlet temperature. A separator is used to separate the cold heavy fluid, which will be used to cool a conventional A/C condenser in order to enhance its performance. The output power from the LN2 engine is used to drive a conventional A/C system. The capital cost of the proposed system is much lower than commercially available battery systems. Compared with the commercially used diesel engine, the total cost over five year is slightly higher (9%), but 32% and 22% less fuel consumption and CO2 emissions respectively [82, 83].
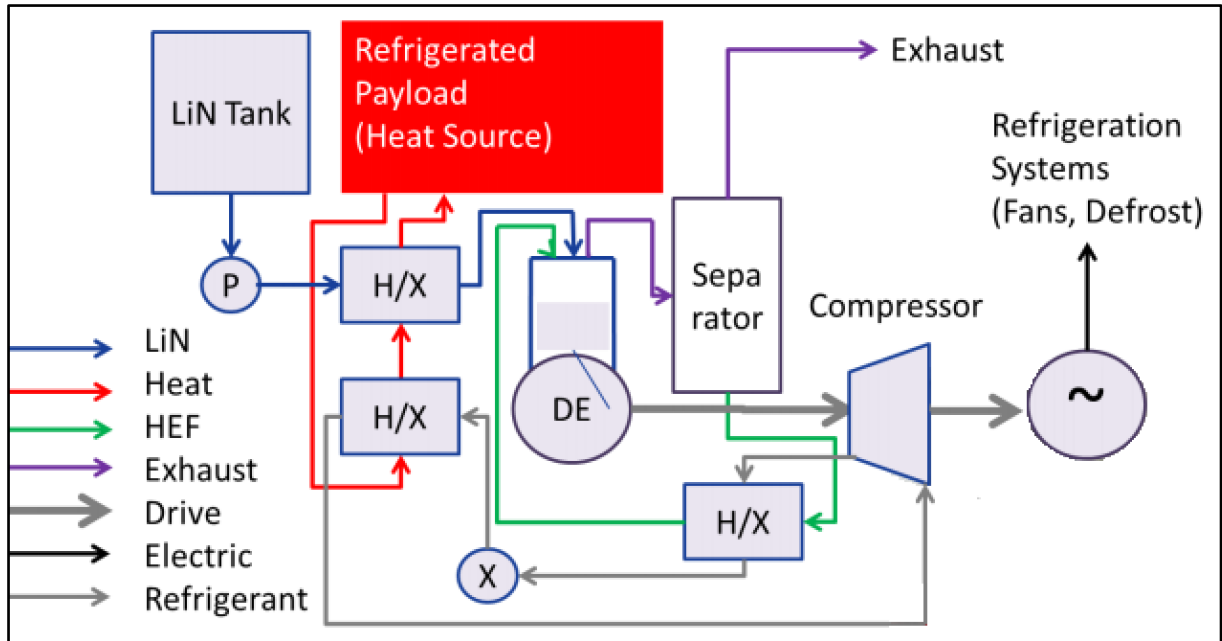
Figure 2-19: Dearman cooling and power system [83]

Ameel et al. [81] developed a mathematical model of a combined system for storing and recovering energy using LAir as storage medium and low temperature heat source as input heat. The system uses the low boiling temperature of LAir to provide cooling for a liquefaction plant and generating power as shown in Figure 2-20. Compressed air passes through a heat exchanger where it is significantly cooled by evaporating LAir after being precooled. Then the extremely cold air passes through a throttling device to the storage tank to yield LAir. An open LAir power cycle is used to generate power and drive the compressor. The results showed an improvement in the recovery efficiency by 17% compared with the open Rankine cycle [81].
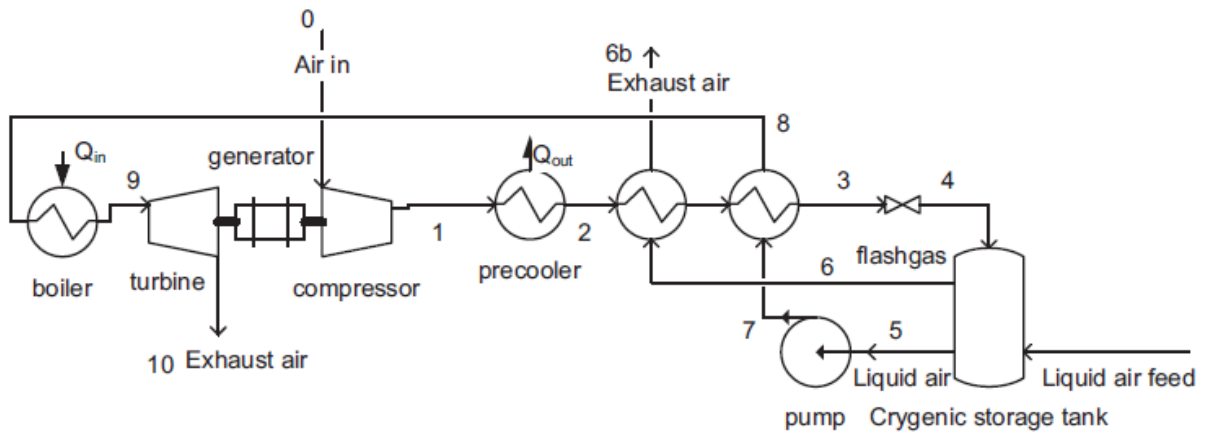
Figure 2-20: Combined LAir power cycle with liquefaction system [81]

Newman and McCormick [80] have patented the use of both LN2 and LNG fluids to cool and power a food transport vehicle. Figure **2-21** shows the proposed system where two separate cryogenic tanks (for LN2 and LNG) are fitted under the vehicle body. Both fluids are evaporated, superheated and mixed in an extended fin heat exchanger fitted in the cooling space roof to refrigerate the products, then the mixture of nitrogen and natural gas is used to fuel the vehicle engine.
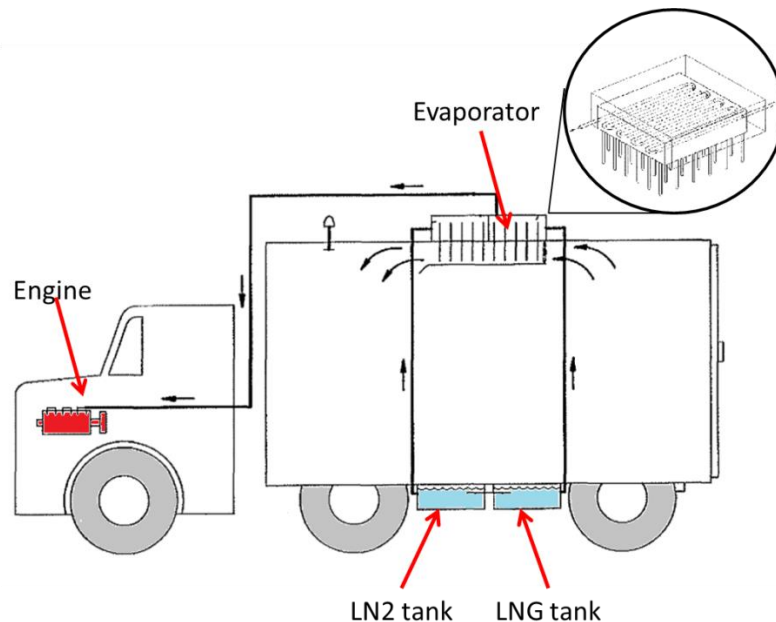
Figure 2-21: LNG and LN2 cooling and power generation system [80]

Another cooling and power system uses the open LN2 Rankine cycle to drive Stirling engine was mathematically modelled by Wang et al. [78]. The system uses the very low boiling temperature of LN2 to cool the cold space of a Stirling engine as shown in Figure **2-22**. Their results showed that decreasing the cold side temperature increases the hot/cold temperature difference resulting in significant improvement in the engine efficiency [78, 79].
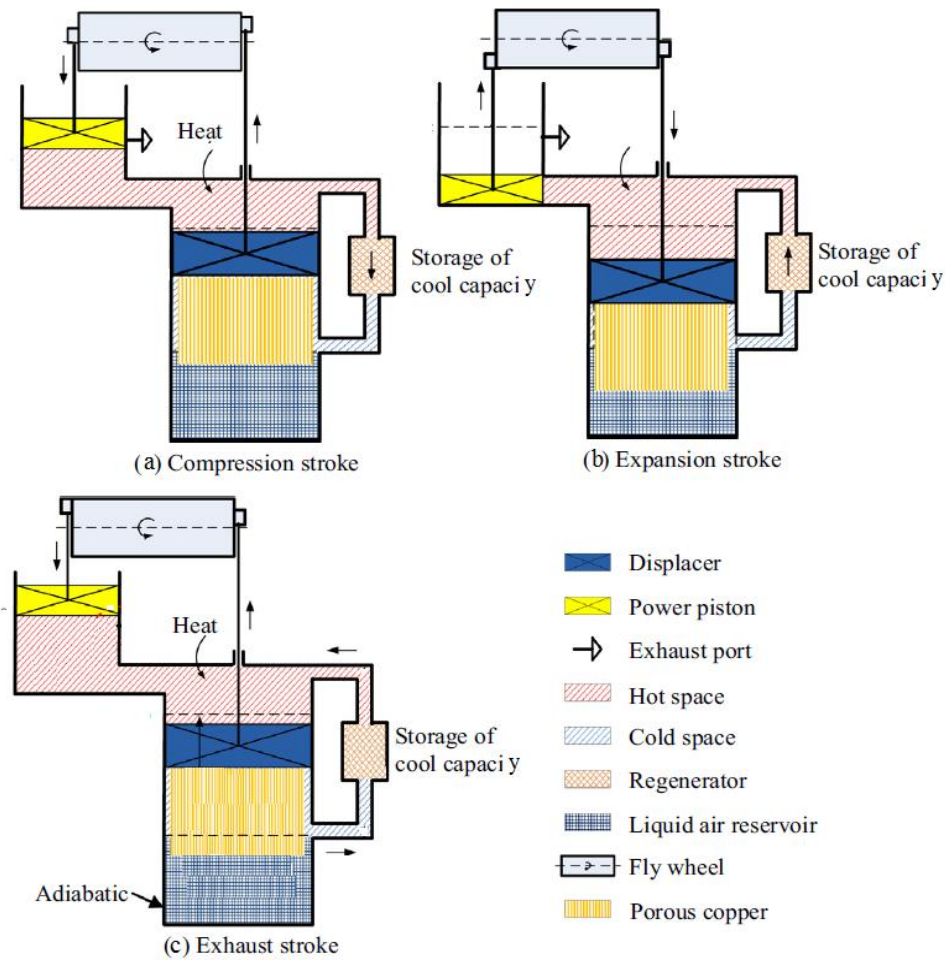
Figure 2-22: LN2 integrated with Stirling engine [78, 79]

2.5 Flow Boiling of liquid nitrogen

Several researchers have experimentally studied the boiling process of LN2 during chilldown processes, used to cool down the cryogenic transport pipes or system from the ambient temperature to the fluid temperature. During chilldown, the boiling of LN2 involves a

complex and unsteady two phase flow where different type of boiling occurs (film boiling, transient boiling and nucleate boiling) [51-55].

Hong Hua et al. [55] carried out an experimental work studying chilldown processes of liquid nitrogen pipelines. In their study, liquid nitrogen was used as working fluid and various mass flow rates were used to investigate its effect on the heat transfer rate and the movement of the interface. Figure **2-23** shows schematic diagram of their test facility where a vacuum chamber was used to provide high quality insulation of the test section. The test section was made of Pyrex glass tube with 8 mm ID and 254 mm length. The tube was fitted vertically and upward and downward flow directions were studied. 15 thermocouples at five positions with equal distance from each other were fitted on the surface. A high speed camera was used to monitor the flow pattern in the glass tube during the experiment. It is clear that the wall temperature in the case of downward flow reduce faster than that of the upward flow however the three type of boiling regions (film, transient and nucleate boiling) are clearer in the upward flow as shown Figure **2-24**.
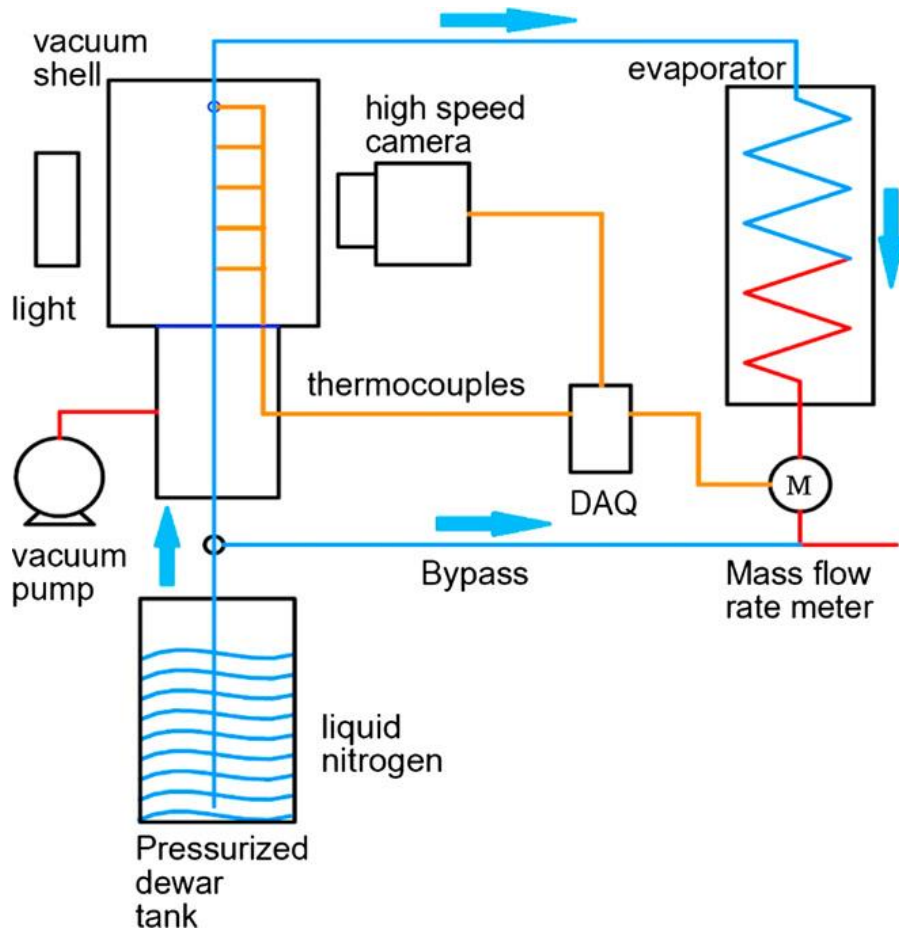
Figure 2-23: LN2 Cilldown test facility [55]
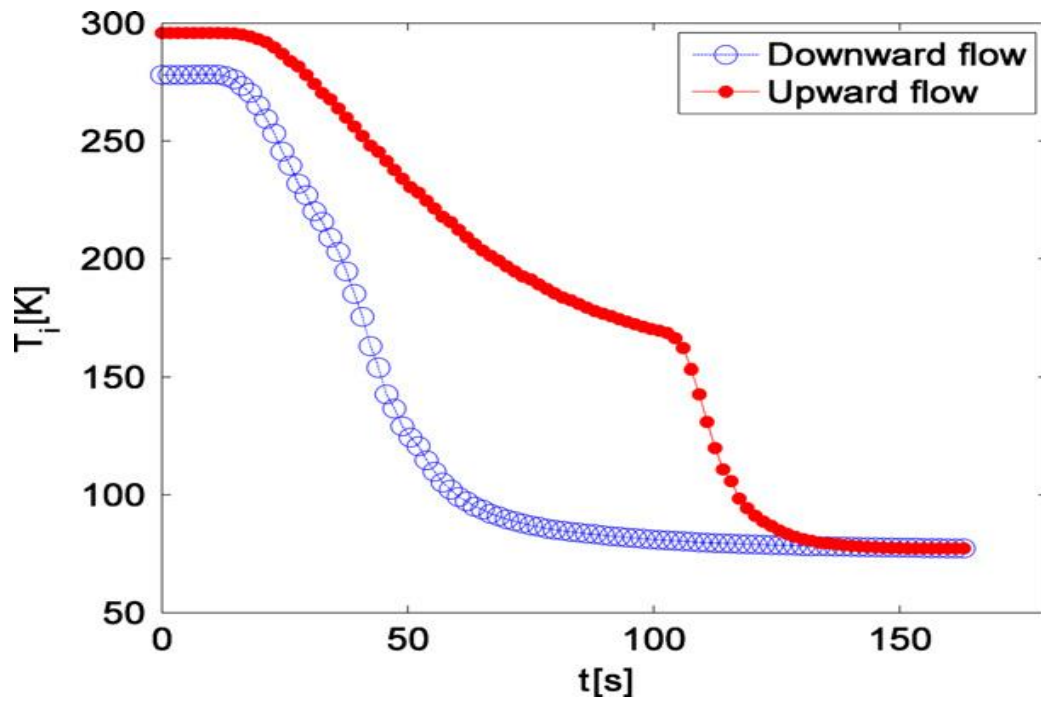
Figure 2-24: Tube temperature at Upward and downward flow directions [55]

Jason [53] et al. also experimentally tested the flow boiling of liquid nitrogen during the chilldown process at Reynolds number ranging from 1000 to 4000 and compared with boiling flow of liquid hydrogen at Reynolds number ranging from 1.84×10^4 to 4.33×10^5. Their results of heat flux, wall temperature and heat transfer coefficient, showed that; the low surface tension and viscosity of hydrogen led to very rapid move from the film boiling to nucleate boiling which significantly increases the chilldown process of LH2 compared to LN2.

Samuel et al. [50] developed numerical model to simulate the chilldown of liquid nitrogen in a vertical tube with downward flow. The available correlations of the film, transient and nucleate boiling heat transfer coefficient, critical heat flux and departure from nucleate temperature were used in their model. The results were compared with an available data base from 55 recent experimental studies. At the mass flux of 61.2-1150 kg/m^2-s, subcooled inlet temperature of 0-14 K and pressure inlet of 0-14 kPa, the model was able to predict the time to onset of nucleate boiling.

Simin et al. [49] also developed a 3D numerical model to predict the subcooled boiling of LN2 in a vertical tube with upward flow taking into consideration the bubble flow and the void fraction distribution patterns. Their results showed that along the flow direction the void fraction increased nonlinearly with applied heat flux and it decreased with decreasing the subcooled temperature and the mass flow rate. The heat transfer coefficient showed good agreement with published experimental work.

Hisashi et al. [48] experimentally studied the heat transfer characteristics of downward flow of liquid nitrogen. Figure **2-25** shows a schematic diagram of their test facility where LN2 passes through a subcooler to ensure that it enters as liquid phase to the test section. The test section was made of Stainless Steel 304 tube with dimensions of 5 mm ID, 0.5 mm thickness

and 900 mm length, and was insulated using a vacuum chamber. An electric heater was used to provide the required heat flux and temperature sensors were fitted on the tube surface to monitor its temperature. The results were compared with available published correlations showing that the experimental heat transfer coefficients were in good agreement with Steiner and Polomik correlations [46, 48].

1. LN$_2$tank
2. Head column
3. Subcooler
4. Test section
5. Pressure gauge
6. D.P.cell
7. Vacuum pump
8. Turbine flowmeter
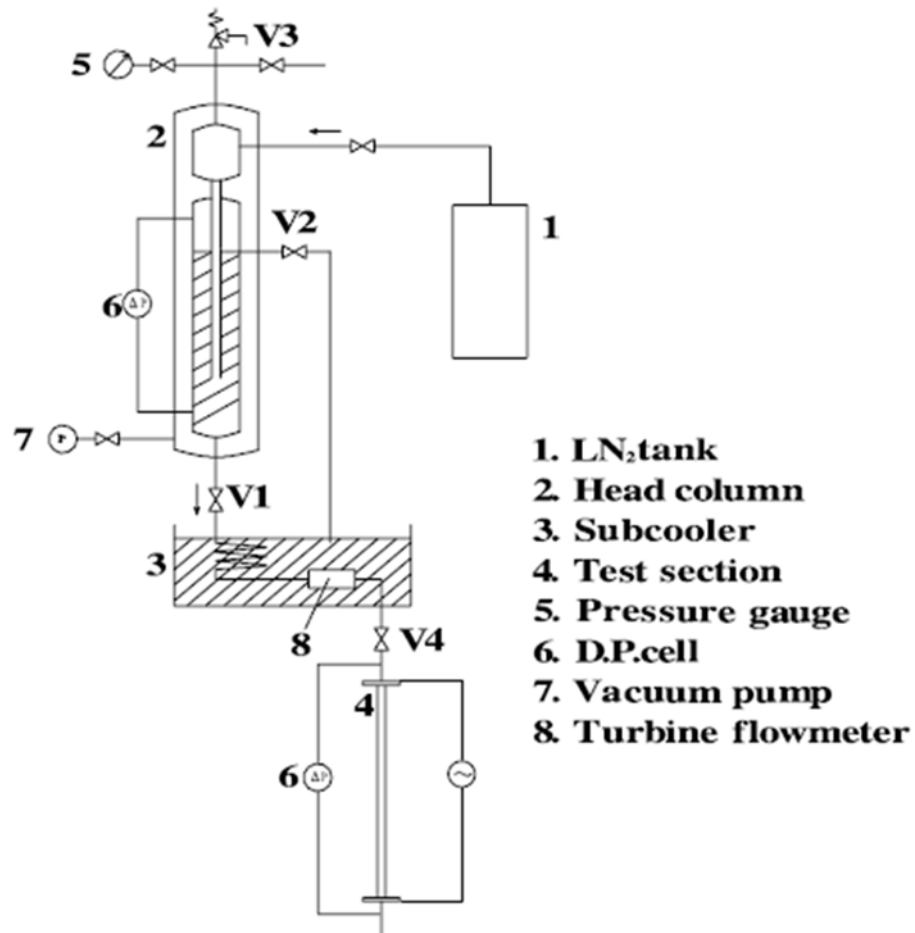
Figure 2-25: Experimental apparatus [48]

Steiner [45] has experimental studied the boiling heat transfer coefficient of cryogenic fluids and compared his results with the developed correlations for determining the boiling heat transfer coefficient of various cryogenic fluids including nitrogen, oxygen, argon, neon, hydrogen and helium. The study considered upward and downward flow, however, only subcooled and nucleate boiling were considered. His results showed that at low heat flux there

is a large deviation in the experimental data and this due to the low accuracy of measurements that have been used.

Klimenko and Sudarchikov [44] experimentally studied the forced flow boiling of liquid nitrogen in a vertical long tube. The tube length and inner diameter were 1800 mm and 10 mm respectively. Various inlet pressure, mass flux and heat flux were used and they were (0.7-1.8 Bar), 170-750 kg/m^2-k) and (10.2- 42.72 kW/m^2), respectively. Their results showed moving from subcooled boiling to nucleate boiling has no significant impact on the applied heat flux. Also the effect of heat flux and pressure is not significant when compared with pool boiling.

Liu et al. [43] used Computational Fluid Dynamic CFD to model pool boiling of liquid nitrogen using Ansys Fluent software. The model was 2D of small tank of LN2 with dimensions of 4.59 X 13.76 mm. Various wall temperatures was applied on the tank bottom surface (80, 90, 100, 110, 120, 150, 200 and 300 K) to include different types of boiling process. Heat flux was predicted at each temperature and the curve showed a similar trend to the standard boiling curve available in [42]. Also the model was good for predicting the critical heat flux point however it slightly over predicted the heat flux for the film boiling and significantly under predicted for the nucleate boiling heat flux.

Ciclo [41] developed CFD modelling of flow boiling of liquid nitrogen in slug flow region. VOF multiphase model in the Ansys fluent software was used and 2D axisymmetrical geometry was used to reduce the computational time. Also in the laminar flow the liquid and gas phases were treated as incompressible flow. The CFD results showed a satisfactory improvement when compared with a published experimental work. Compared with a single phase flow, the two phase flow showed 20% enhancement in the heat transfer rate.

2.6   Summary

The reported literature have indicated that, the global demands of the residential air conditioning systems increased significantly over the last few decades, and the forecasts showed this growth will continue at the same rate until the end of this century. Moreover, in many countries across the world, a major part of the residential power consumption is used by the air conditioning systems which contribute to significant CO_2 emissions. Many electricity suppliers have difficulties to overcome this significant growth of the energy demands particularly during the peak where the ambient temperature is at highest level. Therefore there is a need to enhance the current commonly used air conditioning systems (vapour compression system) to reduce their power consumption and CO2 emissions leading to better electric network stability and cleaner environment.

Various enhancement technologies for air conditioning systems such as reducing the condenser temperature or reducing the compressor power input by using efficient compressors or by having an efficient control system particularly during partial load were reported in the literature. Also researchers have investigating shifting the cooling load to the off peak times by integrating cold storage devices into existing air conditioning systems. This approach has many advantages such as reducing the energy demand during the peak times, reducing the system size and enhancing the A/C system performance by running at lower outside temperature (night-time). However, there were disagreements regarding the energy saving of such systems where some researchers have reported significant energy saving whereas others reported no energy saving particularly when the storage medium is ice. Therefore the integration of energy storage into A/C systems needs further research to identify the operating conditions/scenarios that produce energy saving.

Due to the fact that vapour compression system consumes a large amount of energy during compression process, researchers have used different techniques for providing not only

cooling but also generating power using cryogenic fluids. Such systems used different cryogenic fluids such as LNG, liquefied CO_2, LO_2, LN_2 and LAir, and for different applications. Many researchers have reported LN2 and/or LAir are the most attractive fluids due to their high energy density, availability, low cost and environment friendly.

LN2 and LAir have been recently acknowledged as the most attractive energy storage fluids where they can be generated using the surplus electricity at off peak times or using renewable sources like wind turbines and solar PV. Most of published work regarding the use of LN2/LAir for cooling and power generation are for refrigerated transport vehicles. However, using LN2/LAir for air conditioning of domestic or office buildings have not been investigated [85].

Therefore this thesis will investigate the feasibility of using the cold energy storage in the form of LN2/LAir to provide air conditioning and power for domestic applications at peak times. Mathematical modelling will be carried out to develop an efficient system that extract all or most of the energy stored in the LN2/LAir. Also, the system performance will be affected by the used heat exchanger (s) performance therefore CFD simulation using Ansys Fluent software will be used to develop highly efficient cryogenic heat exchangers. The simulation will take into account evaporating/boiling process of liquid nitrogen flow in the heat exchanger where most of published works have studied the process either experimentally or mathematically but very limited literature on CFD simulation of such process. Moreover the CFD tools will also be used to assess the expander performance at various input conditions.

CHAPTER THREE

MATHEMATICAL MODELLING

3.1 Introduction

As reported in the literature review, the global energy demands have increased continuously over the last few decades and in many countries the national electricity grid face difficulties to meet the user's demand. For example Libya, which is a North African country with area of 1.7 million m^2 and 6.2 million people, the demand has grown steadily over the last years as reported by the General Electricity Company of Libya GECL Figure 3-1 [86]. As a result, the country is facing shortage in its electricity supply and GECL has difficulties to meet the user's demand which caused GECL to start a programme of power cuts since 2010 [86]. This data was the most recent available date at the time where the author has started his research and at 2011 the data was not continually recorded due to revolution year. About 50% of the power generated is consumed by domestic and public utilities sectors. Air conditioning, space heating and water heater consume more than 70% of the residential electrical load. The demand of air conditioning systems in Libya has been increasing rapidly in the last few years as a result of long hot summers and poor building insulation materials. This has a negative impact on the national grid as shown in Figure **3**-**2** where the summer months have the highest power consumptions.
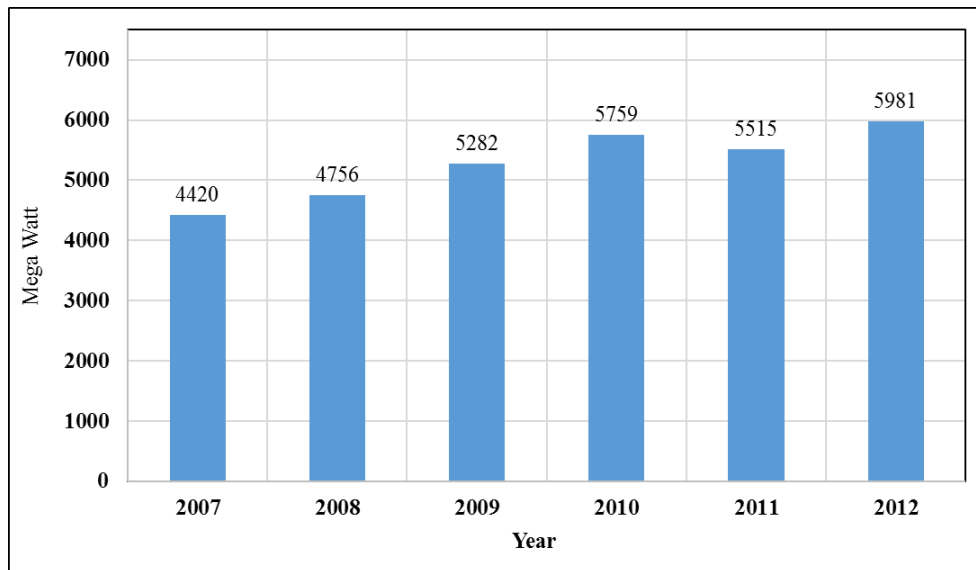
Figure 3-1: Electricity demand growth in Libya [86]
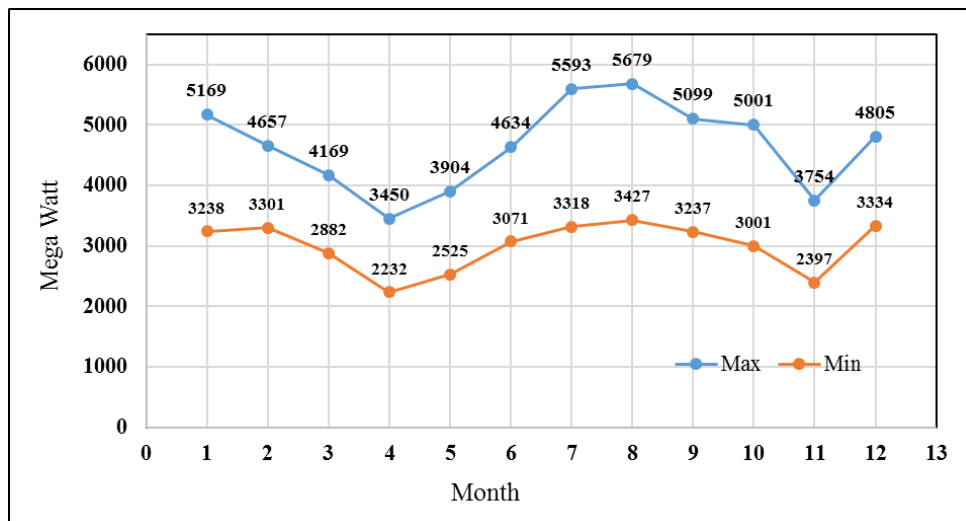
Figure 3-2: Monthly electricity demand in 2012 [86]

Figure **3-3** shows the daily percentage of the power consumption in Brack, Libya as an example [87]. The figure presents the percentage of the power consumption to the average of the yearly power consumption. Shifting the cooling load to off peak times seems a promising technique to reduce the peak electricity demands which will reflect positively on the national grid. The literature highlights many advantages of integrating storage systems in the current A/C systems including reducing the gap between the peak and the off peak demands, operating power generation systems at its best efficiency and ensuring the availability of A/C

services. However, there were contradictory reports regarding the energy saving achieved using this technique. This chapter describes the development of a thermodynamic model for assessing the performance of A/C system to investigate the effect of including energy storage using phase change materials (PCM). It is divided into two sections; the first one investigates the energy saving of integrating the cold storage system with the conventional A/C systems. While the second section proposes new air conditioning system that uses the cold storage energy in form of liquefied gases to generate cooling and power for domestic and commercial applications. All the work presented in this section has been published by the author in different journals and conferences papers [3, 41, 85, 88-92].
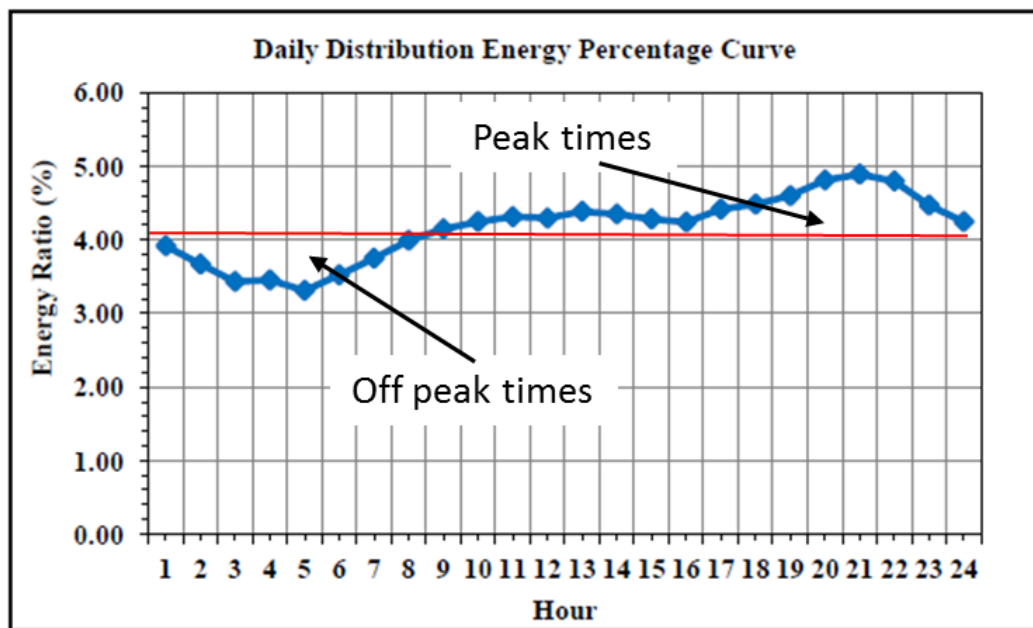
Figure 3-3: Daily energy percentage distribution [87]

A typical dwelling in Sebha city, Libya with an overall area of 170 m^2 was selected as a case study and the house schematic diagram is shown in Figure 3-4. Figure **3-5** shows the cooling load profile with 25° C indoor design temperature and the variation of outdoor ambient temperature on 21st July as reported by Mohamed et al. [93].
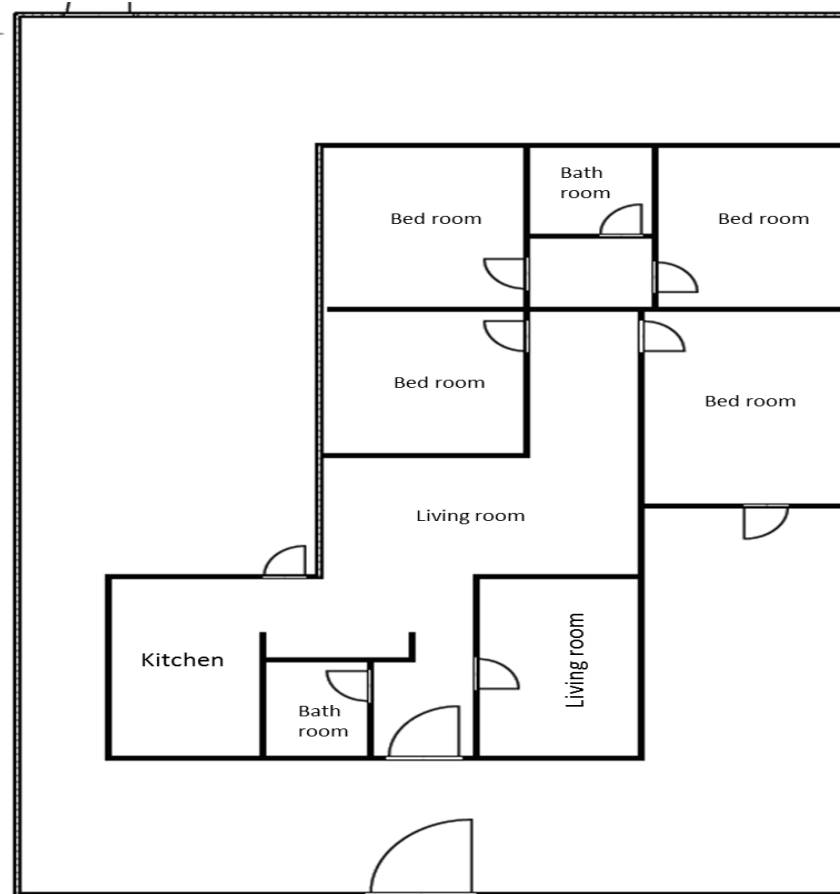
Figure 3-4: Typical house sketch that selected as case study [93].
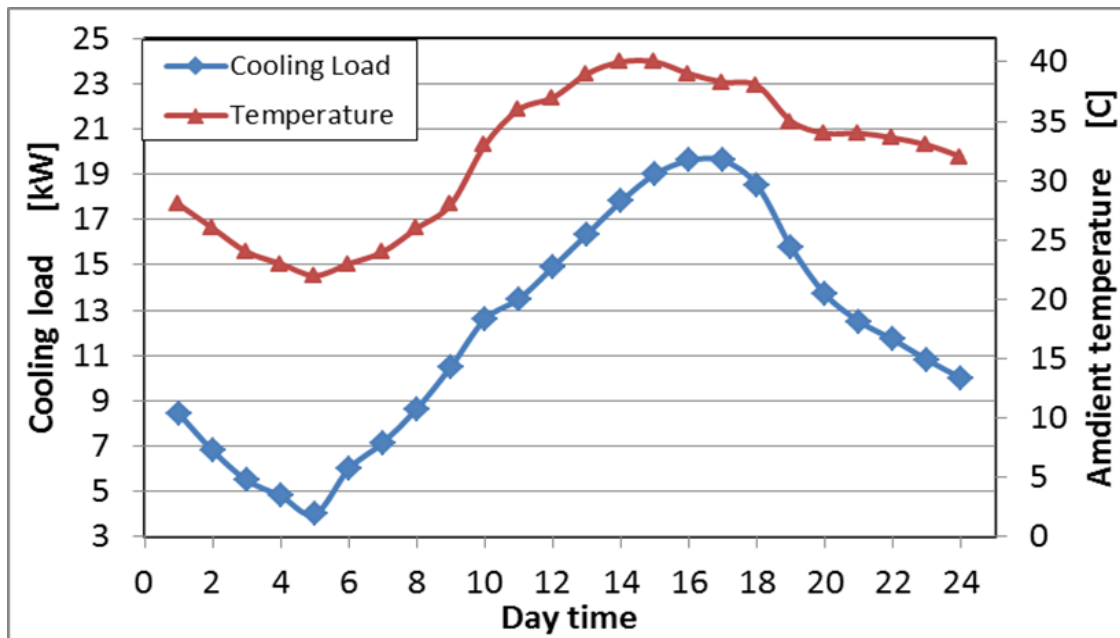
Figure 3-5: Cooling load profile and outdoor ambient temperature [93].

3.2 Integrating air conditioning with cold storage system

This section presents a detailed description and modelling of integration the existing A/C systems with cold storage systems which is one of the commonly used techniques to enhance their performance.

3.2.1 System description

This section presents a mathematical model of integrating cold storage system to a conventional A/C system using the commonly used storage medium (ice) and other PCMs. The system performance was investigated in terms of the power consumption, the system size and cost compared to the case with no storage. Schematic diagrams of the two systems are shown in Figure **3**-**6** and Figure **3**-**7** where in the conventional system the chiller cools a secondary coolant that is circulated to meet the cooling load. While in Figure **3**-**7**, a cold storage system integrated to a conventional system where the evaporator is immersed in the storage tank. Both systems were used to meet the same cooling load as shown in Figure **3**-**5**.
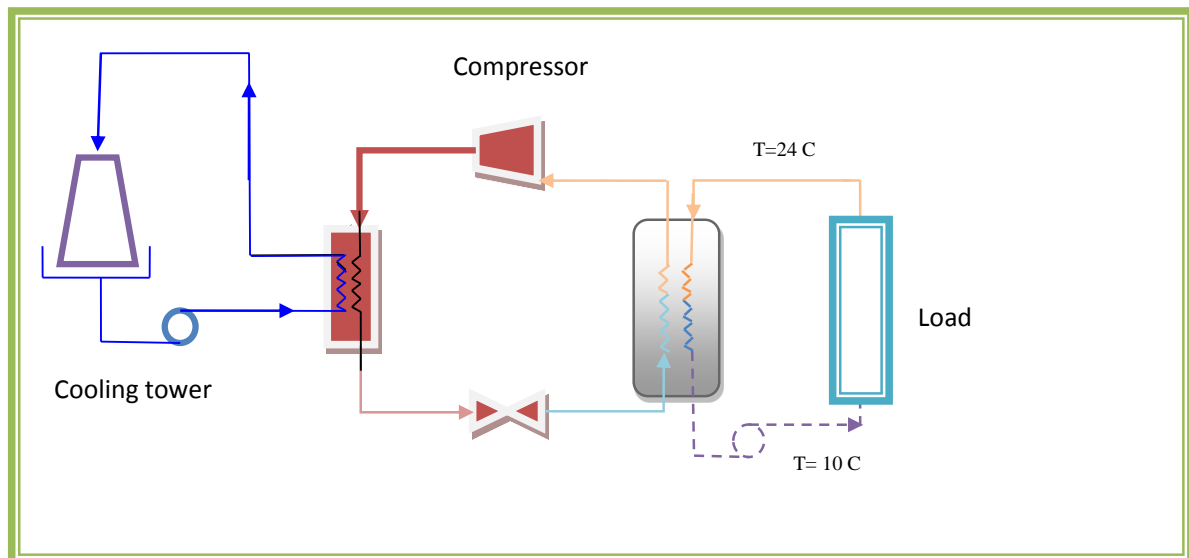
Figure 3-6: Conventional AC system.
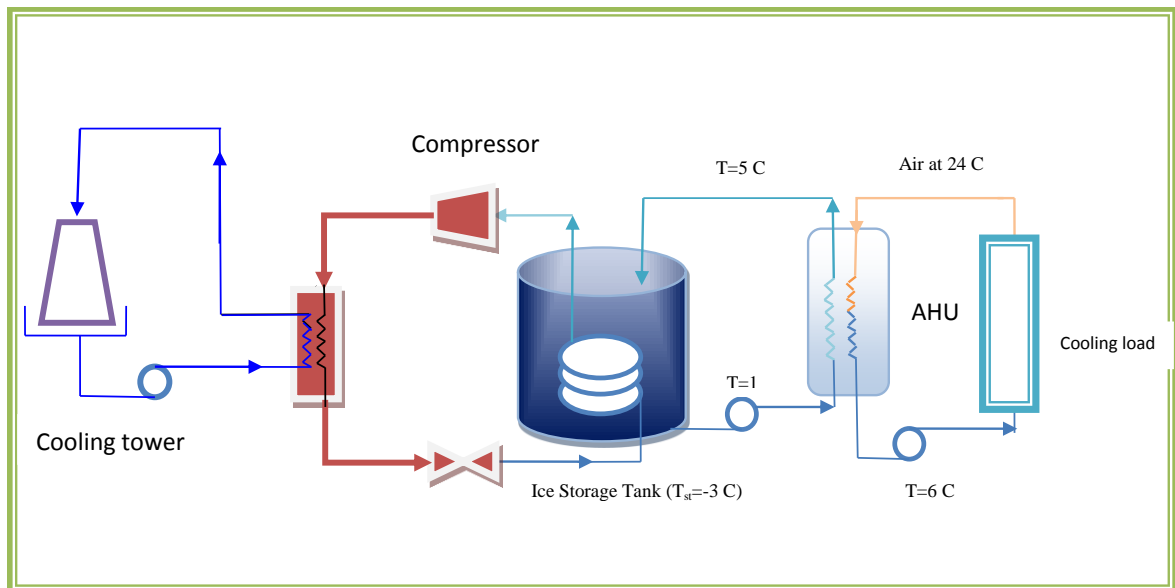
Figure 3-7: Chiller with cold storage system.

Generally the weather in Libya is relatively dry especially in the area where the case study has been selected, with ambient temperature around 30-35° C, the AC units are typically turns on at 11:00 am and off at 9:00 pm. Figure **3-8** shows the cooling load profile where the maximum house's load reaches 19.6 kW which occurs at about two hours after maximum outdoor temperature shown in Figure **3-5** (at 4:00 and 5:00 pm) because of the thermal capacity of the building structure materials. The overall cooling load is 168.73 kWh/day.

3.2.2 Operating strategies

In this study three different operating strategies namely; Full Storage, Load Levelling and Demand Limiting strategies were used to assess the system performance compared with the conventional system. For the conventional system, the chiller is normally designed to meet the maximum cooling load which is 19.6 kW, while for the system with energy storage; the chiller capacity is varied depending on the operating strategy. For each strategy, the chiller initial capacity depends on the total cooling load, charging hours, the chiller capacity ratio during charging period (which is defined as the ratio of the actual chiller capacity during the charging/discharging processes to the nominal capacity, for example, during charging process

of ice energy storage the chiller capacity is about 30-40% less than its nominal capacity which means the capacity ratio is 60-70%) and the direct cooling period as in Equation **3.1** [17-21, 28].
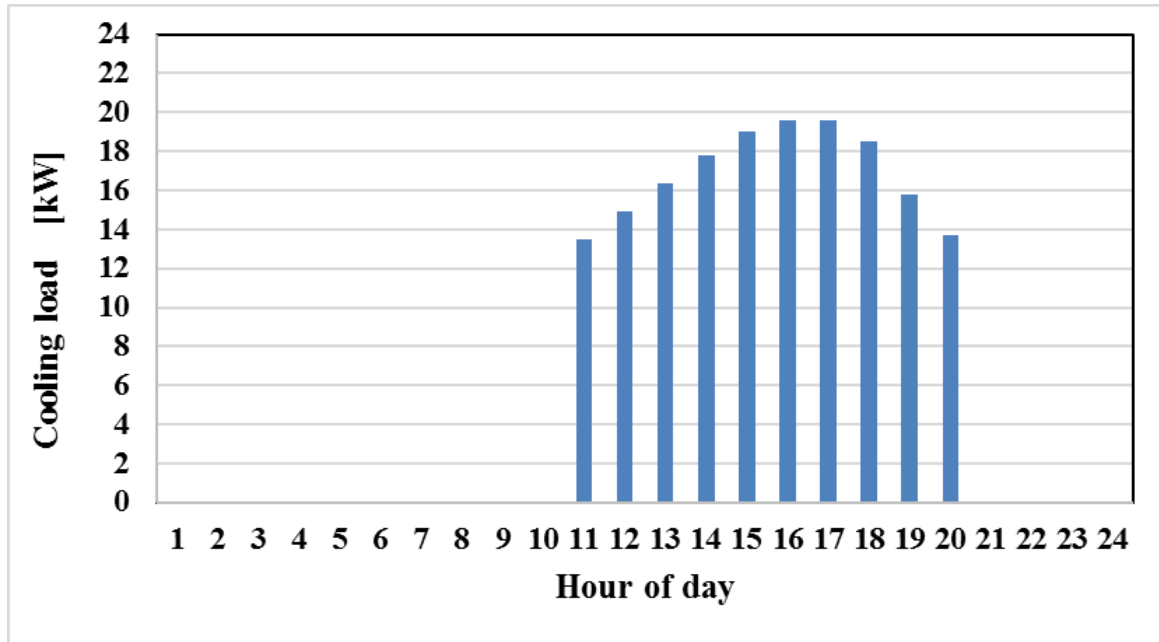
Figure 3-8: Designed cooling load in kW [93].

$$\text{Nominal chiller capacity} = \frac{\text{Total cooling load [kWh]}}{H_{char} \times CR_{char} + H_{dirct} \times CR_{dirct}} \qquad 3.1$$

Where H_{char} number of charging hours, CR_{char} is capacity ratio during charging, H_{dirct} is number of direct cooling hours and CR_{dirct} is capacity ratio when direct cooling is used.

3.2.2.1 Full Storage strategy

In Full Storage operation strategy the chiller is running for 18 hours charging the storage tank at off peak times and the partial load times, and it switches off during the peak times. In this mode the storage tank meets the whole cooling load at the peak period. The chiller capacity during the operating times and the cooling load calculated using Equation **3.1** is presented in

Figure **3-9**. The following is an example how to calculate the nominal chiller capacity for the Full Storage Strategy.

$$\text{Nominal chiller capacity} = \frac{168.73}{14*0.7+4*1} = 12.226 \; kWh$$

The result shows that the chiller capacity at hours 11, 12, 19 and 20 is less than the cooling loads which means the chiller meets part of the load and the storage system will be used to meet the remaining load.
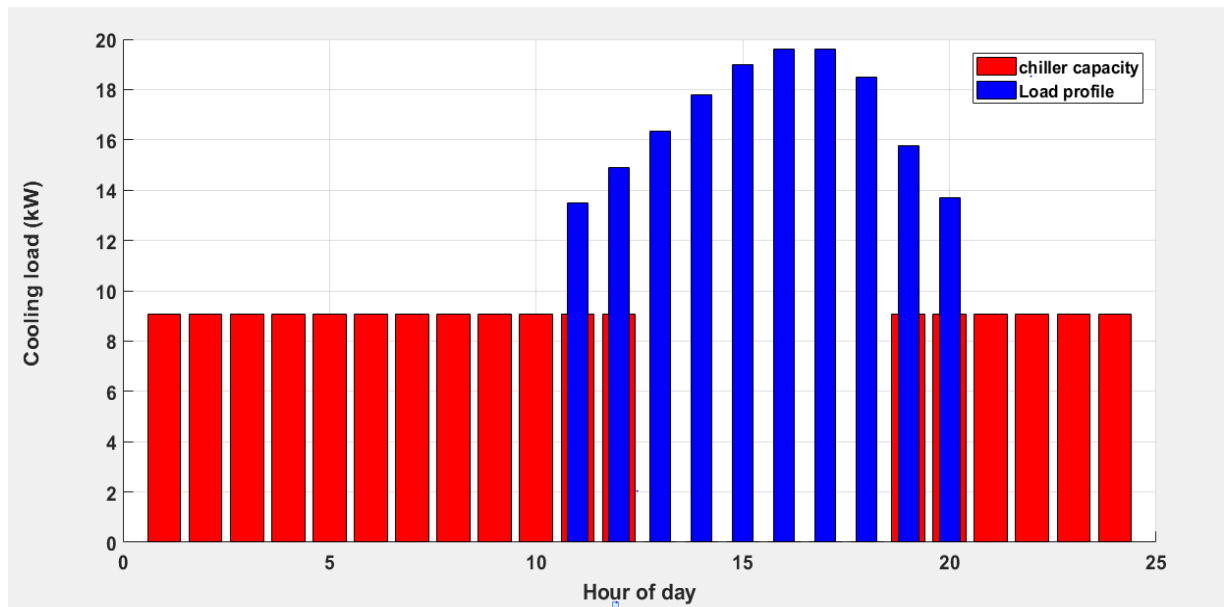
Figure 3-9: Chiller and load variation in full storage strategy operation.

3.2.2.2 Load Levelling strategy

In Load Levelling strategy the chiller runs for 24 hours charging the storage tank at off peak and non-load period and meets cooling load at the peak period. When the chiller capacity is lower than the cooling load, the storage system is used to meet the additional load. Figure **3-10** shows the chiller capacity as calculated using Equation 3.1 and the cooling load during the day for this strategy.
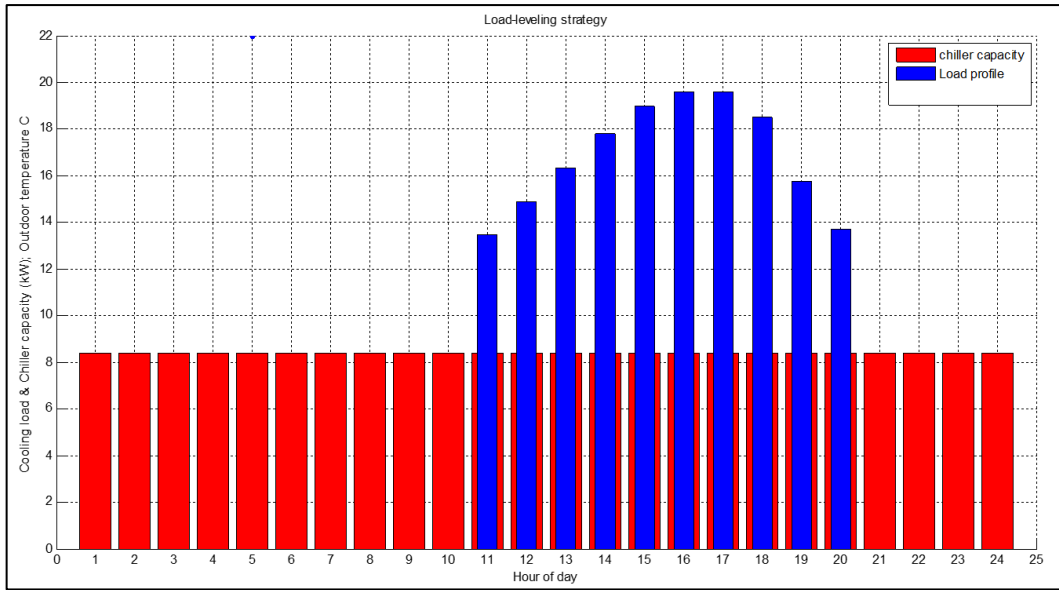
Figure 3-10: Chiller and load variation in Load Levelling storage strategy.

3.2.2.3 Demand-Limiting strategy

In Demand-Limiting strategy the chiller runs for 24 hours charging or meeting the cooling load but with lower capacity during the peak times. In this study during the peak times the chiller capacity is lower than other times. Figure **3-11**, Figure **3-12** and Figure **3-13** show the chiller capacity during the day for different Demand-Limiting modes of 40%, 50% and 60%, respectively.
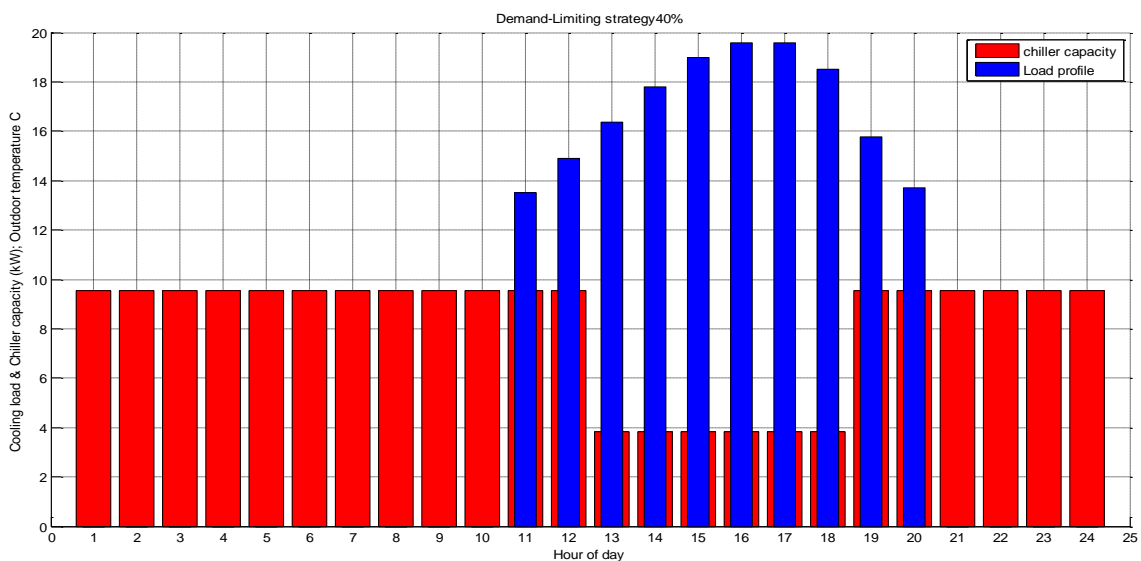
Figure 3-11: Chiller and load variation in Demand Limiting storage strategy 40%
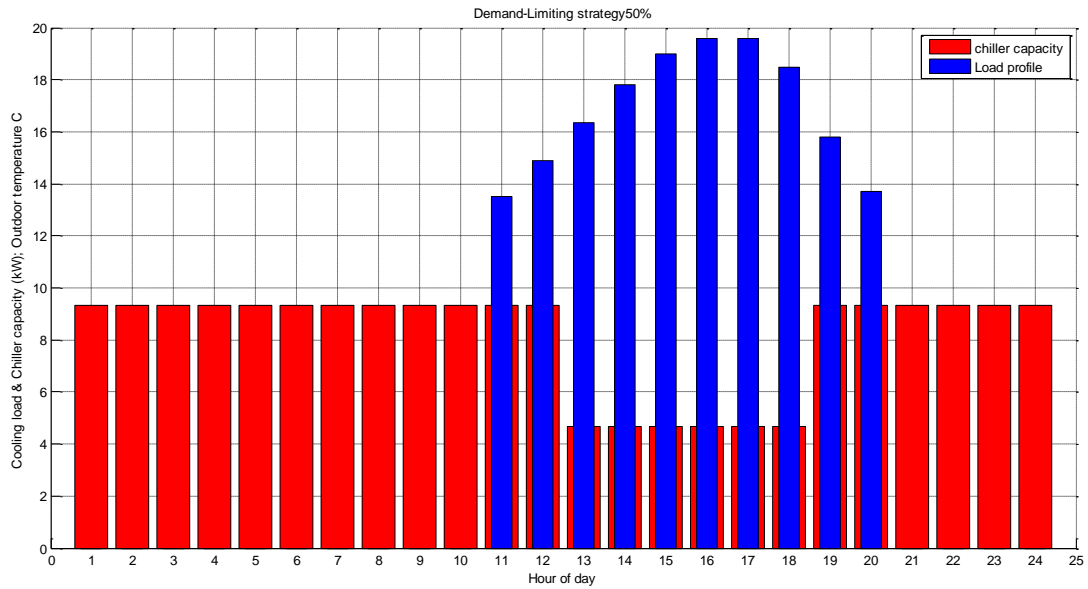
Figure 3-12: Chiller and load variation in Demand-Limiting strategy 50%.
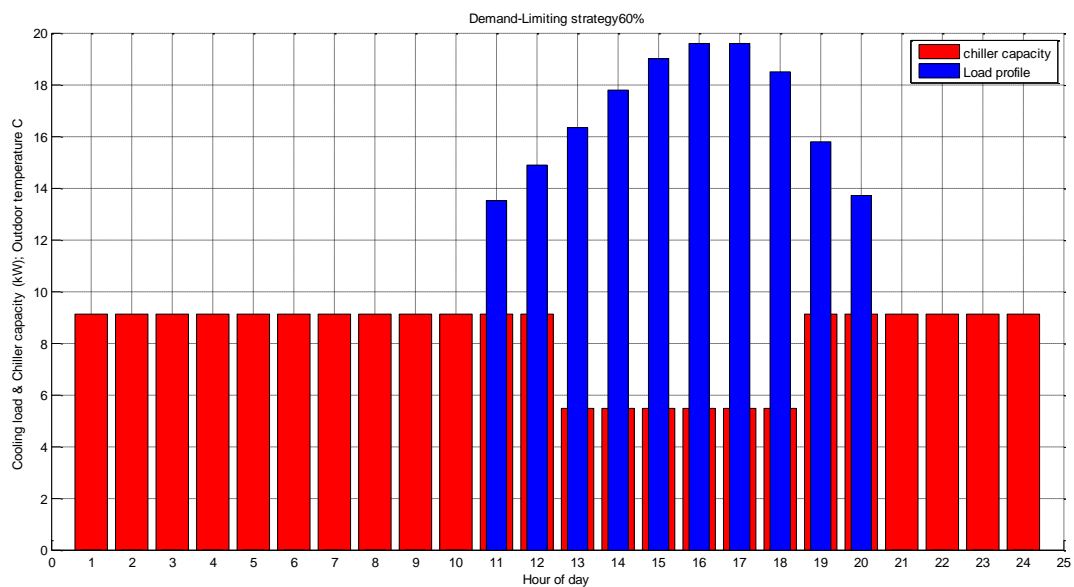
Figure 3-13: Chiller and load variation in Demand-Limiting strategy 60%.

3.2.3 System modelling

The operating strategies not only affect the chiller capacity but also the storage tank and the whole system size. The storage tank size depends on the storage medium and temperature. The initial capacity of the storage tank depends on the chiller capacity, charging period,

capacity ratio during the charging time and total cooling load during the charging period as in

Equation **3.2** [23].

Storage capacity $(Q_c) = C_{chil} \times H_{char} \times CR_{char} - TC_{char}$ 3.2

Where:

C_{chil} is nominal chiller capacity, and TC_{char} is the total cooling load during charging period

only.

For Full Storage strategy as an example, the normal storage capacity can be calculated as:

Noninal storage capacity $= 168.73 - 12.226 \times 4 = 119.8228$ kWh

Using ice the most commonly used cold storage medium for such applications as an example,

storage tank capacity can be calculated using Equation **3.2** assuming storage tank temperature

ranging from -6 to -3 °C, and capacity ratio at this range varying from 0.6 to 0.7 of the

nominal chiller capacity. During the direct cooling period, the outlet temperature from the

chiller is 6°C and the capacity ratio is 1.0.

The initial estimations of the chiller and the storage system capacities are used to develop a

thermodynamic model for the whole system as described below where MATLAB software

was used to solve the equations.

The initial storage capacity calculated using Equation **3.2** was used to calculate actual storage

capacity Q_{st} using Equation **3.3**. The actual capacity is higher than the initial one because it

takes into consideration the heat loses during charging $(Q_{I,ch})$ and discharging $(Q_{I,dc})$

processes. Equation **3.4** was used to estimate the initial volume of the storage tank which was

then used to calculate the charging and discharging heat losses using Equations **3.5** and **3.6**

[94].

$Q_{st} = \frac{Q_c}{\eta_{st}}$ 3.3

Where Q_c and η_{st} are initial storage capacity and thermal efficiency

$$V_{ST} = \frac{3600 Q_{st}}{\rho_w C_{p,w}(T_{dc} - T_{FP,w}) + \rho_w h_{fe} + \rho_{ice} C_{p,ice}(T_{FP,w} - T_{ST})} \qquad 3.4$$

$$Q_{I,ch} = A_{ST} * t_{ch} \frac{T_{amb} - T_{ST}}{R_{th}} \qquad 3.5$$

$$Q_{I,dc} = A_{ST} * t_{dc} \frac{T_{amb} - T_{dc}}{R_{th}} \qquad 3.6$$

Where, A_{ST} is the storage tank surface area which can be calculated for cylindrical tank as:

$$A_{ST} = 6\pi \left(\frac{V_{ST}}{2\pi}\right)^{\frac{2}{3}} \qquad 3.7$$

The initial storage efficiency η_{st} can be calculated using Equation **3.8** then the above calculations are repeated to get accurate storage capacity and the storage tank size [94].

$$\eta_{st} = \frac{Q_{st} - Q_{I,ch} - Q_{I,dc}}{Q_{st}} = 1 - \frac{Q_{I,ch} + Q_{I,dc}}{Q_{st}} \qquad 3.8$$

For the charging process Equation **3.9** is used to calculate the evaporator heat transfer rate.

$$\dot{Q}_{Ev} = \frac{Q_{st}}{t_{ch}} \qquad 3.9$$

Where: t_{ch} is charging time.

A vapour compression cycle is used to generate the required cooling in the storage tank. The cycle operates between evaporator and condenser temperatures of -7 and 46 respectively. Thus the mass flow rate of the working fluid (refrigerant) can be calculated using Equation **3.10**. Also the compressor efficiency calculated using equations **3.11** which is an empirical equation and the power consumption calculated using equations **3.13** [28, 94].

$$\dot{m}_r = \frac{Q_{Ev}}{h_1 - h_4} \qquad 3.10$$

$$\eta_{comp} = 0.85 - 0.46667 \left(\frac{p_2}{p_1}\right) \qquad 3.11$$

$$\eta_{comp} = \frac{h_{2s} - h_1}{h_2 - h_1} \qquad 3.12$$

$$\dot{W}_{comp} = \dot{m}_r (h_2 - h_1) \qquad 3.13$$

The heat rejected from condenser and the cooling water flow rate were calculated using Equations **3.14** and **3.15**, respectively [94].

$$\dot{Q}_{Cond} = \dot{m}_r(h_2 - h_3)$$ 3.14

$$m_{CT} = 43.2 * 10^{-3}Q_{cond}$$ 3.15

The system coefficient of performance COP was calculated using Equation **3.16**.

$$COP = \frac{\dot{Q}_{Ev}}{\dot{W}_{comp}}$$ 3.16

After finding the overall heat transfer coefficient of the evaporator and the condenser (U_{Ev}, U_{Cond}), NTU and ΔT_{LMTD} approaches were used to calculate the surface area of the evaporator and the condenser using Equations **3.17**, and **3.18**, respectively [94].

$$A_{EV} = \frac{NTU*(\dot{m}c_p)_{min}}{U_{Ev}}$$ 3.17

$$A_{Cond} = \frac{\dot{Q}_{Cond}}{U_{Cond}*F*\Delta T_{LMTD}}$$ 3.18

In this system evaporative condenser and helical coil evaporator were used. The forced convection heat transfer coefficient inside and outside the condenser tubes can be found by using the following equations [95-97].

For the two phase flow, Nusselt number can be calculated using equation (**3.19**).

$$Nu = \frac{h_{TP}\,d}{K_l}$$ 3.19

Where h_{TP} is two phase heat transfer coefficient, d is the hydraulic diameter and K_l is the liquid thermal conductivity.

For the liquid phase Nusselt number Nu_l can be calculated using equation (3**3.20**).

$$Nu_l = Pr_l Re_l^{0.9}\frac{F_1}{F_2}$$ 3.20

Where; Re_l is liquid Reynolds which can be calculated using equations (**3.21**), and Pr_l is liquid Prandtl numbers.

$$Re_l = \frac{G(1-x)d}{\mu_l}$$ 3.21

Where G is Grashof number, x is the vapour quality and F_1 and F_2 are coefficient can be computed as various Reynolds number range as following:

$$F_1 = 0.15 \left[\frac{1}{X_{tt}} + \frac{2.85}{X_{tt}^{0.476}} \right] \qquad\qquad 3.22$$

Where X_{tt} is Martinelli parameter and it can be calculated using Equation (**3.23**) [95-97].

$$X_{tt} = \left(\frac{1-x}{x} \right)^{0.9} \left(\frac{\rho_v}{\rho_l} \right)^{0.5} \left(\frac{\mu_l}{\mu_v} \right)^{0.1} \qquad\qquad 3.23$$

$$F_2 = 0.7 Pr_l Re_l^{0.5} \quad for \ Re_l \leq 50 \qquad\qquad 3.24$$

$$F_2 = 5 Pr_l + 5 ln \left[1 + Pr_l (0.09636 Re_l^{0.585} - 1) \right] \quad for \ 50 < Re_l \leq 1125 \qquad 3.25$$

$$F_2 = 5 Pr_l + 5 \ln(1 + 5 Pr_l) + 2.5 \ln(0.00313 Re_l^{0.812}) \quad for \ Re_l > 1125 \qquad 3.26$$

The two phase flow heat transfer coefficient can be calculated using Equation (**3.27**).

$$h_{TP} = 0.05 \, Re_{eq}^{0.8} \, Pr_l^{0.33} \, \frac{k_l}{d} \qquad\qquad 3.27$$

Where Re_{eq} is the equivalent Reynolds number for two phase flow and it can be calculated using Equation (**3.28**).

$$Re_{eq} = Re_v \left(\frac{\rho_l}{\rho_v} \right)^{0.5} \left(\frac{\mu_v}{\mu_l} \right) + Re_l \qquad\qquad 3.28$$

Where Re_v is vapour phase Reynolds number which can be calculated using Equation (**3.29**), and ρ_l, ρ_v, μ_v and μ_l and are liquid and gas densities and viscosities

$$Re_v = \frac{Gxd}{\mu_v} \qquad\qquad 3.29$$

Water spray is used to enhance the condenser performance therefore the condenser outside flow will be mixture of air and water spray and the heat transfer coefficient can be calculated using Equation (**3.30**) [95-97].

$$\bar{h}_{m\,a} = 5.028 * 10^{-8} Re_a^{0.9} Re_{spray}^{0.15} d_o^{-2.6} \qquad\qquad 3.30$$

$$\bar{h}_{m\,a} = C(\dot{m}_a)^n \qquad\qquad 3.31$$

Where $\dot{m}_a$ is air mass flow rate, C is a factor lies between 0.049 and 0.076, and n lies between 0.77 and 0.905.

$$h_{c,a} = C_{pa} * \bar{h}_{m\,a} \qquad\qquad 3.32$$

$$h_{c,w}^{film} = C \left(\frac{\dot{G}_{spray}}{d_o}\right)^n \qquad\qquad 3.33$$

Where C=2100 and n=1/3

For a coil the evaporator immersed in a tank, the heat transfer of the two phase flow of refrigerant inside the evaporator can be calculated using the following equations [97, 98]:

$$\frac{h_{TP}}{h_{lo}} = \left[\left(2.6(\frac{1}{X_{tt}})^{0.95}\right)^3 + \left(4*10^4 Bo Re_{lo}^{-0.12}\right)^3\right]^{\left(\frac{1}{3}\right)} \qquad 3.34$$

Where Bo is Boiling number and the subscript which can be calculated using Equation (**3.37**) lo refers to liquid phase only.

$$Bo = \frac{q}{G h_{fg}} \qquad\qquad 3.35$$

Where q is the heat flux and h_{fg} is the vaporization energy

$$Re_{lo} = \frac{G d_i}{\mu_l} \qquad\qquad 3.36$$

The liquid phase Nusselt number calculated using Equation (**3.37**).

$$Nu_{lo} = \frac{1}{41} Re_{lo}^{5/6} Pr_l^{0.4} \left(\frac{d_i}{d_{coil}}\right)^{\frac{1}{12}} \left(1 + \frac{0.061}{\left(Re_{lo}(\frac{d_i}{d_{coil}})^{2.5}\right)^{1/6}}\right) \qquad 3.37$$

The heat transfer coefficient outside the coil can be calculated using the following Nusselt number equation:

$$Nu = \frac{(0.6+0.387*Re^{1/6}}{\left[(1+(\frac{0.559}{Pr})^{\frac{9}{16}})^{8/27}\right]^2} \qquad\qquad 3.38$$

Regarding air handling unit AHU the external air flow rate ($\dot{m}_a$) varies with the cooling load, but its size was considered at maximum load. For simplifying the analysis, the dwelling house was assumed to have five equal sizes of AHU and each of them can cover one fifth of the maximum load.

$$\dot{m}_a = \frac{\dot{Q}_c}{h_i - h_o} \tag{3.39}$$

Where $\dot{Q}_c$ is the cooling load, and h_i, h_o are inlet and outlet enthalpies.

$$h_i - h_o = C_{p,a}(T_i - T_o) + (\omega_i h_{ig} - \omega_o h_{og}) \tag{3.40}$$

Where ω is air humidity which can be calculated using Equation (**3.41**), and $C_{p,a}$ is air specific heat [97, 98].

$$\omega = 0.622 * \frac{\emptyset * p_{ws}}{p_{atm} - \emptyset * p_{ws}} \tag{3.41}$$

Where:

$$p_{ws} = \frac{C_1}{T} + C_2 + C_3 T + C_4 T^2 + C_5 T^3 + C_6 \ln(T) \tag{3.42}$$

The heat transfer coefficient inside the AHU can be calculated using Equations (**3.43**) or (**3.45**) [98].

$$Nu_b = \frac{\left(\frac{f}{2}\right) Re_b Pr_b}{1.07 + 12.7 \left(\frac{f}{2}\right)^{0.5} \left(Pr_b^{\frac{2}{3}} - 1\right)} \tag{3.43}$$

Where:

$$f = (1.58 \, lnRe_b - 3.28)^{-2} \tag{3.44}$$

$$Nub = 0.27 * Re_b^{0.36} * \left(\frac{Pr_b}{Pr_w}\right)^{0.25} \tag{3.45}$$

Capital cost of each component was calculated using the following equations [99-104]

$$Z_{AHU} = 24202 * A_{AHU}^{0.4162} \tag{3.46}$$

$$Z_{ST} = 8.67 * 10^{(2.9211\exp(0.1416*logV_{ST}))} \qquad 3.47$$

$$Z_{EV} = 16648.3 * A_{EV}^{0.6123} \qquad 3.48$$

$$Z_{Comp} = \frac{39.5*\dot{m}_r}{0.9-\eta_{Comp}} * \left(\frac{p_{dc}}{p_{suc}}\right) \ln\left(\frac{p_{dc}}{p_{suc}}\right) \qquad 3.49$$

$$Z_{EX} = 114.5 * \dot{m}_r \qquad 3.50$$

$$Z_{Cond} = 268.45 + (516.621 * A_{Cond}) \qquad 3.51$$

$$Z_{Chiller} = 150.2 * Q_{Chiller} \qquad 3.52$$

Figure 3-14 shows a flowchart of the procedure used in the modelling of cooling system with ice storage where the following assumption was made to simplify the system analysis;

1- Negligible pressure drops in piping system and negligible the heat losses from refrigeration system components.

2- The states of the refrigerant at evaporator and condenser outlets were assumed as ideal refrigeration cycle (saturated vapour and saturated liquid respectively) .

3- The temperature gradient inside the storage tank is negligible.
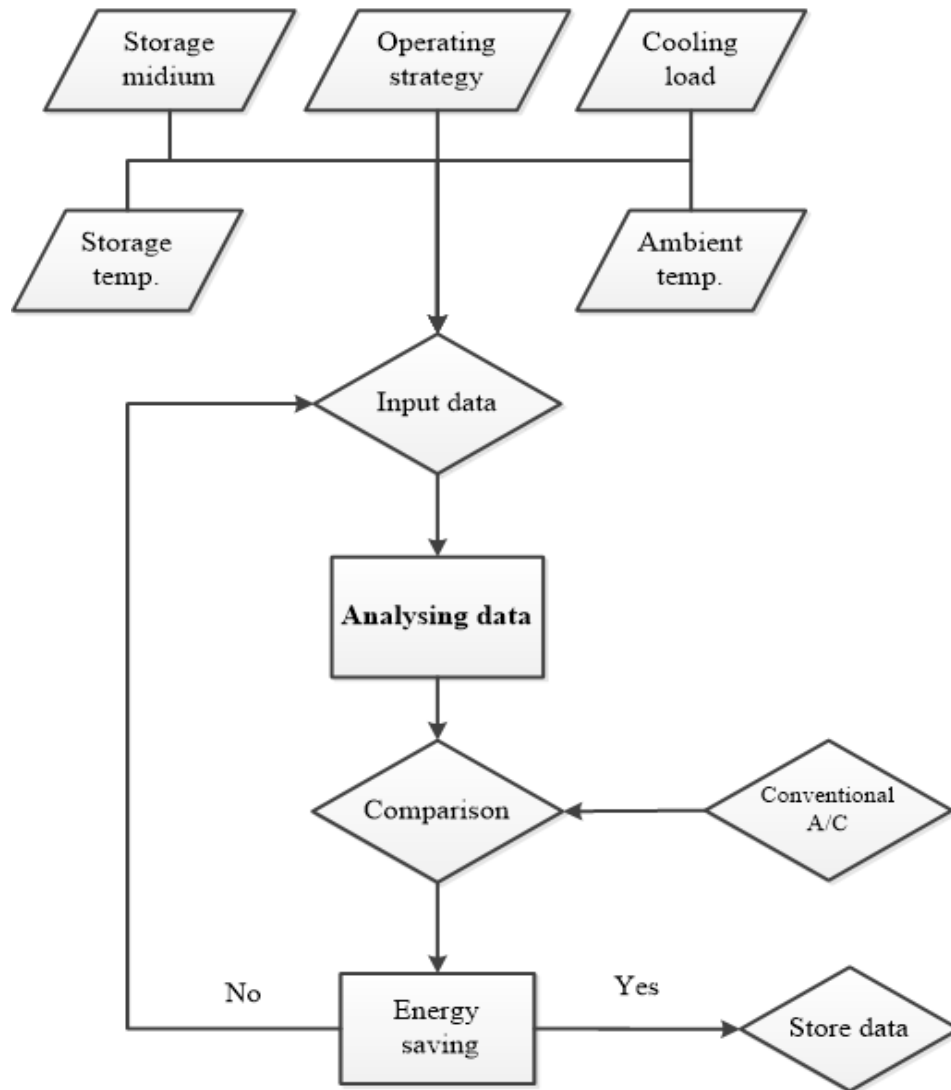
Figure 3-14: MATLAB procedure flow chart.

3.2.4 Results of using ice as storage medium

Table **3-1** presents the chiller capacity, the storage capacity and the storage tank size for three different strategies described in section (3.2.2) compared with conventional A/C system. The results show that the conventional AC system has the largest chiller capacity compared with other operating strategies. And among the three strategies, Full Storage mode has the highest chiller and storage capacities whereas Load Levelling mode has the lowest chiller and storage capacities. The Demand Limiting strategy has values in between and its performance depends

on the percentage of the peak load that is met by chiller. Also at the different strategies, ice storage tank size was calculated and the results show that the Full Storage mode showed the highest tank size of 2 m^3 and the lowest size was for the Load Levelling mode of 1.47 m^3. The tank size mainly depends on the storage medium and if a PCM with higher latent heat is used lower tank size can be achieved. Compared with chilled-water storage system, ice storage system has significant reduction in the volume of the storage tank at the same capacity. This reduction ranges between four to six times depending on the system design temperatures. For example with 10 degree temperature difference (from -2 °C to 8 °C), the storage capacity of chilled-water system it is about 41 kJ/kg while for the ice it is about 370 kJ/kg which is approximately 9 times higher than that of chilled-water.

Table 3-1 Caparison between the operating systems

System strategy	Chiller capacity [kW]	Storage capacity [kW]	Tank volume [m^3]
Conv. system	19.6	0	0
FSS	12.2268	119.8228	2.0908
DLS 40%	9.5436	96.1990	1.6786
DLS 50%	9.3324	94.0707	1.6414
DLS 60%	9.1304	92.0345	1.6059
LLS	8.4029	84.7011	1.4779

DLS: Demand-Limiting strategy; FSS: Full Storage Strategy; LLD: load levelling strategy.

Compared with conventional AC system, ice storage uses lower evaporation temperature which means it can provide a lower temperature to the AHU. Lowering the AHU temperature at the same cooling load leads to higher temperature difference between the AHU and the cooling space which requires less AHU size to meet the same cooling load.

The system power consumption depends on the type of chiller, its specification, the outdoor temperature and its operating strategy. For domestic air conditioning in Libya, a split units A/C systems are commonly used. Therefore TOSHIBA air conditioning units were used to simulate real practical system and achieve more accurate results about the power consumptions. Table **3-2** presents different models with different sizes of TOSHIBA air

conditioning units and their power consumptions. Practically, the available air conditioning units have capacities different from the actual cooling load. Therefore a number of units were selected to meet the required cooling capacity for the various operating strategies as shown in Table **3**-**3**.

Table 3-2 TOSHIBA air conditioning units

Chiller name	Chiller cooling capacity	Power consumption W
13	3.5	1070
15	4.396	1150
16	4.62	1350
17	4.75	1285
18a	5	1420
18b	5.3	1640
21	6	1995
22	6.27	2200

Table 3-3 Chiller capacity at the various operating strategies

System strategy	Chiller designed capacity	Number of units	Available capacity	Peak power consumption kWh	Daily power consumption kWh
Con. sys.	19.6	2*17+2*18b	19.84	5.980	54.80
FSS	12.23	2*22	12.27	4.195	75.51
DLS 40%	9.54	1*16+1*18a	9.62	2.770	57.96
DLS 50%	9.33	15+18a	9.40	2.570	54.78
DLS 60%	9.13	2*16	9.24	2.700	64.80
LLS	8.40	13+18a	8.50	2.490	59.76

Table **3**-**4**, 3-5, 3-6 and 3-7 present at each hour of the day the power consumption, type of units used, its cooling capacity and charging and discharging time for all scenarios namely: conventional AC system (no storage system), Full Storage System (FSS), Load Levelling System (LLS) and Demand Limiting system (DLS) 50%, respectively.

Although the conventional AC system has the largest units' capacity among the studied systems, it has lowest daily power consumption. Many researchers obtained similar results [61, 63] which mean there is no energy saving of using ice as storage medium for air conditioning applications. This would be explained as:

1) Cooling load is directly met by the A/C units thus reducing the amount of energy losses associated with the charging and discharging processes of the storage system system.

2) Lowering the evaporator temperature to generate ice for storage scenarios reduces the chiller capacity by 30% which means the chiller consumes more energy to meet the same cooling load.

Table 3-4 Conventional system (Non Storage System)

Hour	Utility Period	Required Cooling load kW	Number and size of units			Units capacities kWh	Power cons. kWh
			2*18b	1*16	1*16		
1	Off peak	0	0	0	0	0	0
2	Off peak	0	0	0	0	0	0
3	Off peak	0	0	0	0	0	0
4	Off peak	0	0	0	0	0	0
5	Off peak	0	0	0	0	0	0
6	Off peak	0	0	0	0	0	0
7	Off peak	0	0	0	0	0	0
8	Off peak	0	0	0	0	0	0
9	Off peak	0	0	0	0	0	0
10	Off peak	0	0	0	0	0	0
11	Off peak	13.5	10.6	4.62	0	15.22	4.29
12	Off peak	14.9	10.6	4.62	0	15.22	4.78
13	Peak	16.35	10.6	4.62	4.62	19.84	5.29
14	Peak	17.8	10.6	4.62	4.62	19.84	5.80
15	Peak	19	10.6	4.62	4.62	19.84	6.22
16	Peak	19.6	10.6	4.62	4.62	19.84	6.43
17	Peak	19.6	10.6	4.62	4.62	19.84	6.43
18	Peak	18.5	10.6	4.62	4.62	19.84	6.05
19	Off peak	15.78	10.6	4.62	4.62	19.84	5.09
20	Off peak	13.7	10.6	4.62	0	15.22	4.36
21	Off peak	0	0	0	0	0	0
22	Off peak	0	0	0	0	0	0
23	Off peak	0	0	0	0	0	0
24	Off peak	0	0	0	0	0	0
SUM		168.73 kWh					54.80316 kWh

Table 3-5 Full Storage System

Hour	Utility Period	Cooling load kW	Chiller capacity kWh	Number and size of units		Units capacities kWh	System mode	Power cons. kWh
				1*18b	2*16			
1	Off-P	0	12.226	5.3	4.62	14.54	charging	4.07
2	Off-P	0	12.226	5.3	4.62	14.54	charging	4.07
3	Off-P	0	12.226	5.3	4.62	14.54	charging	4.07
4	Off-P	0	12.226	5.3	4.62	14.54	charging	4.07
5	Off-P	0	12.226	5.3	4.62	14.54	charging	4.07
6	Off-P	0	12.226	5.3	4.62	14.54	charging	4.07
7	Off-P	0	12.226	5.3	4.62	14.54	charging	4.07
8	Off-P	0	12.226	5.3	4.62	14.54	charging	4.07
9	Off-P	0	12.226	5.3	4.62	14.54	charging	4.07
10	Off-P	0	12.226	5.3	4.62	14.54	charging	4.07
11	Off-P	13.5	12.226	5.3	4.62	14.54	D & D	4.07
12	Off-P	14.9	12.226	5.3	4.62	14.54	D & D	4.07
13	Peak	16.35	0	0	0	0	Discharging	0
14	Peak	17.8	0	0	0	0	Discharging	0
15	Peak	19	0	0	0	0	Discharging	0
16	Peak	19.6	0	0	0	0	Discharging	0
17	Peak	19.6	0	0	0	0	Discharging	0
18	Off-P	18.5	0	0	0	0	Discharging	0
19	Off-P	15.78	12.226	5.3	4.62	14.54	D & D	4.07
20	Off-P	13.7	12.226	5.3	4.62	14.54	D & D	4.07
21	Off-P	0	12.226	5.3	4.62	14.54	charging	4.07
22	Off-P	0	12.226	5.3	4.62	14.54	charging	4.07
23	Off-P	0	12.226	5.3	4.62	14.54	charging	4.07
24	Off-P	0	12.226	5.3	4.62	14.54	charging	4.07
SUM		168.73 kWh						73.24421 kWh

Where: D & D = Discharging and direct cooling; Off-P = Off peak

Table 3-6 Load Levelling System

Hour	Utility Period	Cooling load kW	Chiller capacity kWh	Number and size of units			Units capacities kWh	System status	Power cons. kWh
				1*18b	1*16	Part load (1*16)			
1	Off-P	0	8.4029	5.3	4.62	3.1029	9.92	charging	2.728
2	Off-P	0	8.4029	5.3	4.62	3.1029	9.92	charging	2.728
3	Off-P	0	8.4029	5.3	4.62	3.1029	9.92	charging	2.728
4	Off-P	0	8.4029	5.3	4.62	3.1029	9.92	charging	2.728
5	Off-P	0	8.4029	5.3	4.62	3.1029	9.92	charging	2.728
6	Off-P	0	8.4029	5.3	4.62	3.1029	9.92	charging	2.728
7	Off-P	0	8.4029	5.3	4.62	3.1029	9.92	charging	2.728
8	Off-P	0	8.4029	5.3	4.62	3.1029	9.92	charging	2.728
9	Off-P	0	8.4029	5.3	4.62	3.1029	9.92	charging	2.728
10	Off-P	0	8.4029	5.3	4.62	3.1029	9.92	charging	2.728
11	Off-P	13.5	8.4029	5.3	4.62	3.1029	9.92	D & D	2.728
12	Off-P	14.9	8.4029	5.3	4.62	3.1029	9.92	D & D	2.728
13	Peak	16.35	8.4029	5.3	4.62	3.1029	9.92	D & D	2.728
14	Peak	17.8	8.4029	5.3	4.62	3.1029	9.92	D & D	2.728
15	Peak	19	8.4029	5.3	4.62	3.1029	9.92	D & D	2.728
16	Peak	19.6	8.4029	5.3	4.62	3.1029	9.92	D & D	2.728
17	Peak	19.6	8.4029	5.3	4.62	3.1029	9.92	D & D	2.728
18	Peak	18.5	8.4029	5.3	4.62	3.1029	9.92	D & D	2.728
19	Off-P	15.78	8.4029	5.3	4.62	3.1029	9.92	D & D	2.728
20	Off-P	13.7	8.4029	5.3	4.62	3.1029	9.92	D & D	2.728
21	Off-P	0	8.4029	5.3	4.62	3.1029	9.92	charging	2.728
22	Off-P	0	8.4029	5.3	4.62	3.1029	9.92	charging	2.728
23	Off-P	0	8.4029	5.3	4.62	3.1029	9.92	charging	2.728
24	Off-P	0	8.4029	5.3	4.62	3.1029	9.92	charging	2.728
SUM		168.73 kWh							65.489 kWh

Table 3-7 Demand-Limiting strategy 50%

Hour	Utility Period	Cooling load kW	Chiller capacity kWh	Number and size of units		Full units capacities	System status	Power cons. kWh
				1*18b	Part load (1*16)			
1	Off-P	0	9.3324	5.3	4.0324	9.92	charging	3.054
2	Off-P	0	9.3324	5.3	4.0324	9.92	charging	3.054
3	Off-P	0	9.3324	5.3	4.0324	9.92	charging	3.054
4	Off-P	0	9.3324	5.3	4.0324	9.92	charging	3.054
5	Off-P	0	9.3324	5.3	4.0324	9.92	charging	3.054
6	Off-P	0	9.3324	5.3	4.0324	9.92	charging	3.054
7	Off-P	0	9.3324	5.3	4.0324	9.92	charging	3.054
8	Off-P	0	9.3324	5.3	4.0324	9.92	charging	3.054
9	Off-P	0	9.3324	5.3	4.0324	9.92	charging	3.054
10	Off-P	0	9.3324	5.3	4.0324	9.92	charging	3.054
11	Off-P	13.5	9.3324	5.3	4.0324	9.92	D & D	3.054
12	Off-P	14.9	9.3324	5.3	4.0324	9.92	D & D	3.054
13	Peak	16.35	4.6662	5.3	0	9.92	D & D	1.640
14	Peak	17.8	4.6662	5.3	0	9.92	D & D	1.640
15	Peak	19	4.6662	5.3	0	9.92	D & D	1.640
16	Peak	19.6	4.6662	5.3	0	9.92	D & D	1.640
17	Peak	19.6	4.6662	5.3	0	9.92	D & D	1.640
18	Peak	18.5	4.6662	5.3	0	9.92	D & D	1.640
19	Off-P	15.78	9.3324	5.3	4.0324	9.92	D & D	3.054
20	Off-P	13.7	9.3324	5.3	4.0324	9.92	D & D	3.054
21	Off-P	0	9.3324	5.3	4.0324	9.92	charging	3.054
22	Off-P	0	9.3324	5.3	4.0324	9.92	charging	3.054
23	Off-P	0	9.3324	5.3	4.0324	9.92	charging	3.054
24	Off-P	0	9.3324	5.3	4.0324	9.92	charging	3.054
SUM		168.73 kWh						64.827 kW/day

Regarding the system size, the results show that there is a reduction in the size of the system components when storage is included compared with the conventional system as shown in Table **3**-**8**. However the storage tank is the most expensive part which makes the system with storage more expensive than the conventional system.

Table 3-8 Comparison of components sizes

component	Full storage system		Conventional system	
	Capital cost $	Area in m^2	Capital cost $	Area in m^2
Storage tank	7787.3	6.2356	0	NA
Evaporator	4024.2	0.0984	7750.3	0.2869
Condenser	1056.2	1.5249	1514.9	2.4126
Compressor	169.8	NA	105.4	NA
Expansion valve	7.7	NA	16.4	NA
Total	13045.2		9387	

3.2.5 Using Phase Change Materials (PCM)

There are many PCMs that have phase change temperature above zero degree Celsius which can be used as storage medium for air conditioning applications. This means there is no need to make any changes or modifications to the conventional A/C system to provide lower evaporator temperature. Table **3**-**9** presents some of these materials which have melting temperature of 4-7 °C, which allow the system to operate at the same conventional system temperature.

Table 3-9 PCMs for air conditioning

No	Composition	Type	Melting point	Heat of fusion
1	50:50 Tetradecane [105]	Paraffin wax mixture	4-6	154.839
2	Bulk 100% tetradecane [106]	Organic	5.5	215
3	Bulk 94% tetradecane + 6% tetradecanol [106]	Organic	5.5	202.1
4	Bulk 96% tetradecane + 4% tetradecanol [106]	Organic	5.5	206.4
5	C14, C15, C16, C17, C18 (33.4:47.3:16.3:2.6: 0.4 by quality) [14]	Organic	7	158.32
6	C14H30 (n-Tetradecane) [105, 107]	Single paraffin wax	6	230
7	Caprylic acid–Palmiticacid(9:1byquality) [14]	Organic	6.54	116.5
8	Dodecanol and Octanoic acid (2:3) [108]		6.2	173.2
9	Formic Acid [106]	Organic	7.8	247
10	HC-290 [105]	Hydrate	5.7	382
11	Hexadecane (vol.%) [105]	Paraffin wax mixture	4.9	154.839
12	HS-1, HS-4,HS-8,HS-9 [14]	Organic	6.48–8.14	143.2–147.0
13	K2HPO4_6H2O [106]	Salt hydrates	4	109
14	KF 4H2O [106]	Paraffin	4.5	165
15	Lauryl alcohol–Capry licacid (2:3by quality) [14]	Organic	6.2	173.2
17	Microencapsulated 100% tetradecane [106]	Organic	5.2	215
18	Microencapsulated 94% tetradecane + 6% tetradecanol [106]	Organic	5.1	202.1
19	Microencapsulated 96% tetradecane + 4% tetradecanol [106]	Organic	5.2	206.4
20	MPCM 6D [105]		6	157-167
21	Na2SO4+NaCl+KCl+H2O [106]	eutectics	4	234
22	No. of carbon atoms:14 [106]	Paraffin	5.5	228
23	N-Tetradeca [106]	Organic	5.5	226
24	n-Tetradecane [106]	Single paraffin wax	6	230
25	Paraffin C14 [106]	Organic	5.5	228
26	Pentadecane + heneicosane [106]	Eutectic organic	6.23–7.21	128.25
27	Rubitherm RT5 [105]	Paraffin wax mixture	4-6	158.332
28	SbCl5 [106]	Inorganic	4.0	33
29	Tetradecane [106]		5.5	211.47
30	Tetradecane + geneicosane Eutectic	organic	3.54–	200.28

	[106]			5.56	
31	Tetrahidrofurano (THF) [106]	Eutectic organic		5	280
32	The mixture of 50% tetradecane [106]			4–6	154.839
33	THF 17 [105]	TBAB/TBAC/THF hydrate crystals		4.4	260
Commercial PCMs available in the market					
1	Name	Type	Company		
2	ClimSel C 7	n.a.		7	130
3	Rubitherm RT5	Paraffin		5	198
4	Microencapsulated RT6 slurry (RT6) [105, 107]	Paraffin		6	175
5	MPCM 6[105]	Paraffin		6	157–167
6	Type 41 [105]		Transphase	5.0-5.5	123.3
7	Microencapsulated RT3 slurry (RT3)	Paraffin		4	198
8	Microencapsulated RT4 slurry (RT4)	Paraffin		4	182
9	S7 [105]		PCM products	7	150

These PCMs have many advantages which can be summarized as following:

1- PCMs have storage density 5-14 times higher than sensible heat storage

2- Wide ranges of melting temperature which help to choose the suitable one for the system.

3- By avoiding the decrease of the evaporator temperature, high system efficiency can be achieved.

4- Low temperature swing compared with sensible heat storage.

The selected PCM for such application should have good thermal properties such as: large latent heat of fusion, high thermal conductivity, high density, the phase change temperature within the range of the chiller's evaporator temperature to avoid any modifications, high freezing and melting rate, small volumetric change between solid and liquid phases, minimum supercooling, long term stability, chemically stable, non-toxic, low cost and non-corrosive.

Hydrate (HC-290) with the highest heat of fusion of 382 kJ/kg was selected as storage medium instead of ice in the proposed system. This material has a phase change temperature 5.7 °C which in within the range of the conventional A/C system evaporator temperature 5-7

°C. The same model described in section (3.2.3) was applied with additional assumptions that simplify the analysis such as:

a- The delay time during charging/discharging processes due to the low thermal conductivity of the PCM is negligible.

b- The evaporator has constant evaporating temperature which is 5 °C.

c- The refrigerant entering the compressor is saturated vapour and leaving the condenser as saturated liquid.

d- Condensing temperature changes with the ambient temperature.

e- Pumping power is negligible due to its low power consumption compared with the compressor.

Two operating strategies namely Full Storage and Load Levelling were studied and compared with the conventional system. Comparison was made in terms of compressor power consumption as shown in Table 3-10. Both storage strategies Full Storage and Load Levelling have consumed less power with energy saving of 20.5% and 26%, respectively compared to the conventional system. These results indicate that, reduction in the energy consumption can be achieved using storage medium where there is no significant reduction in the evaporator temperature.

Table 3-10 Comparison between three systems

Day hour	Compressor power consumption kWh		
	Conve. S	FSS	LLS
1	0	1.4594	0.9099
2	0	1.3853	0.8388
3	0	1.3647	0.8009
4	0	1.3271	0.7664
5	0	1.2896	0.7321
6	0	1.3271	0.7664
7	0	1.3647	0.8009
8	0	1.3853	0.8388
9	0	1.4594	0.9099
10	0	1.6609	1.1072
11	3.2882	1.739	1.2026
12	3.3775	1.7649	1.2352
13	3.6339	0	1.329
14	3.8392	0	1.4041
15	3.8392	0	1.4041
16	3.6339	0	1.329
17	3.4728	0	1.2701
18	3.4306	0	1.2546
19	3.2004	1.7128	1.1704
20	3.0041	1.6771	1.1319
21	0	1.6712	1.1279
22	0	1.6726	1.1233
23	0	1.6609	1.1072
24	0	1.6553	1.0893
Total power kWh	34.71	27.57	25.65
Energy saving	0	20.5 %	26%

3.3 Using cryogenic fluids to generate air conditioning and power

As reported in the literature review (chapter 2), storage systems in the form of liquefied gases are a promising techniques not only for providing cooling during the peak times but also generating power. Recently, LAir and LN2 have been acknowledged as the most attractive mediums for energy storage systems due to their availability, high energy storage density,

cost effective and environment friendly [33-35, 40]. They can be generated using the surplus electricity at night (off peak times) or renewable energy sources. The very low boiling temperature (about -200 °C) of these cryogenic fluids can be used to generate air conditioning and power with relatively low mass flow rate. This section presents a comprehensive study investigating the feasibility of providing air conditioning and power generation for domestic and/or commercial applications using LAir/LN2. The following proposed systems, methodologies and results have been published by the author in the following papers [3, 41, 85, 88-92].

3.3.1 System description

Figure **3**-**15** shows a schematic diagram of the cryogenic cooling and power generation system where the surplus electricity or renewable energy powers a liquefier machine. Liquefied air/nitrogen is stored in a tank to be used to provide cooling and generate power when needed.

The proposed system aims to use the stored energy in the form of LN2/LAir to provide air conditioning and power generation in domestic buildings. It consists of two circuits; the first one provides cooling for the house using a secondary coolant that is cooled by the cryogenic fluid by means of heat exchanger. The second circuit is a power cycle where the extracted heat from the house is used to evaporate a pressurized LN2 which then expands in an expander to generate power. Thermodynamic analysis of five different cryogenic cooling and power cycles were modeled using MATLAB integrated with REFPROP software [109, 110]. These cycles were compared in terms of their cooling capacity, output power, recovery efficiency and Coefficient of Performance (COP), and also were compared with the conventional AC system. The Cooling load of the typical dwelling in Libya described in section (3.2) was also used as case study. The effect of changing the LN2/LAir input pressure

on the consumption of LN2/LAir, cooling effect and the power generation were also investigated [3, 91].

The model was developed for each configuration to calculate the properties of working fluids at each point in the cycle, solve the energy and mass balance equations for LN2 and other working fluids, the cooling capacity and the power output. The results will be used to identify the best cycle configuration that achieves minimum amount of LN2/LAir and maximum power output and cooling capacity for the selected application [3, 91].
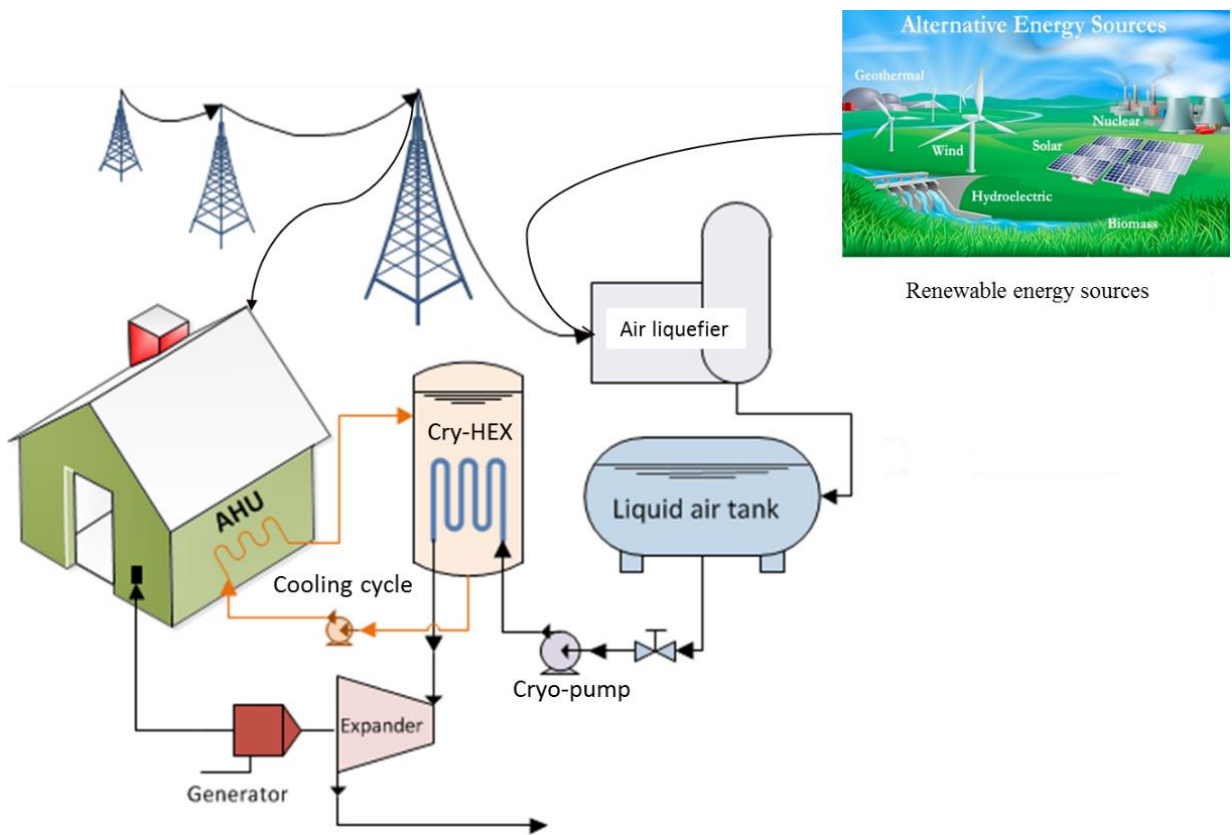
Figure 3-15 Schematic diagram of the cryogenic cooling and power system [85]

3.3.2 Cryogenic air conditioning and power generation cycles

3.3.2.1 First configuration (Cycle 1) cooling only

Figure **3-16** shows the simplest configuration (Cycle 1) that generates cooling using LN2/LAir which evaporates in a heat exchanger using a secondary coolant to meet the building cooling load with no power generation. A T-s diagram of this configuration is shown

in Figure 3-17 where the LN2 is evaporated and superheated in the process 1N-3N at atmospheric pressure.
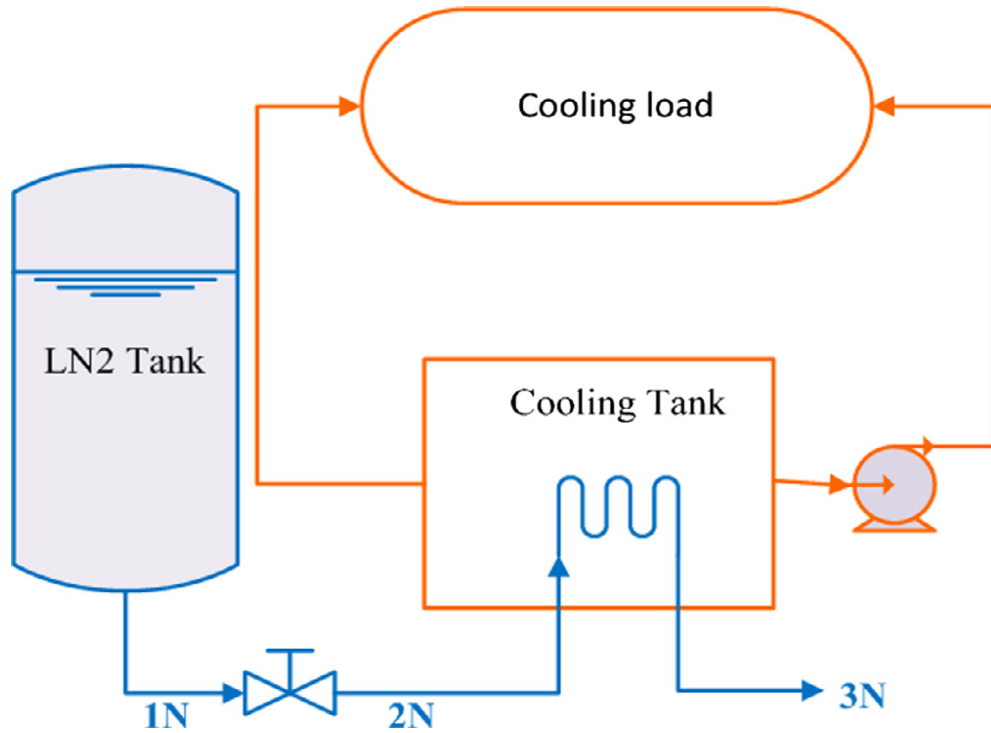
Figure 3-16: First cycle, using LN2 to generate cooling [3]
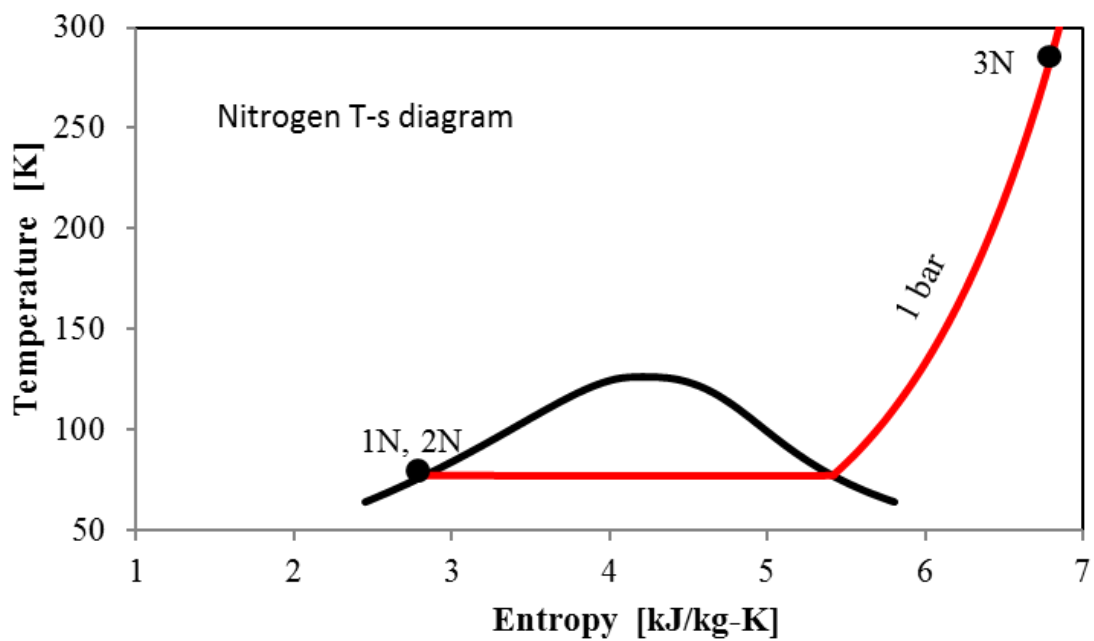
Figure 3-17 First cycle T-s diagram [92]

3.3.2.2   Second configuration (Cycle 2)

The second configuration is (Cycle 2) shown in Figure 3-18 where the liquid nitrogen/air is pumped through a coil immersed inside the cooling tank to be evaporated and superheated by the secondary coolant fluid before passing through an expander to generate power. The expansion process can be assumed either adiabatic as shown on the left hand side of Figure **3-19** or isothermal processes as shown on the right hand side of Figure **3-19**. In the adiabatic expansion scenario (3A-4A), the expansion process reduces the air outlet temperature so it can be returned to the cooling tank in order to increase the system cooling capacity (4A-5A). However, for the isothermal expansion scenario (3A-5A), the expanded air leaves the turbine at the secondary coolant temperature, so it vents directly to the atmosphere. This later scenario has the advantage of absorbing heat in the expansion process which will lead to increase the output power. Also the inlet pressure (P2A) can be increased to more than 500 bar whereas this value cannot exceed 100 bar in the first scenario due to lowering the exit temperature below saturated line as shown by the expansion process (a-b) in Figure **3-19**. More than 80% of the isothermal expansion can be practically achieved by gaining heat from the surrounding using secondary fluid or using an expander with high surface area to volume ratio or using three stage expander with reheat after the first and the second stage [3, 74, 76, 82, 83, 89, 111, 112].
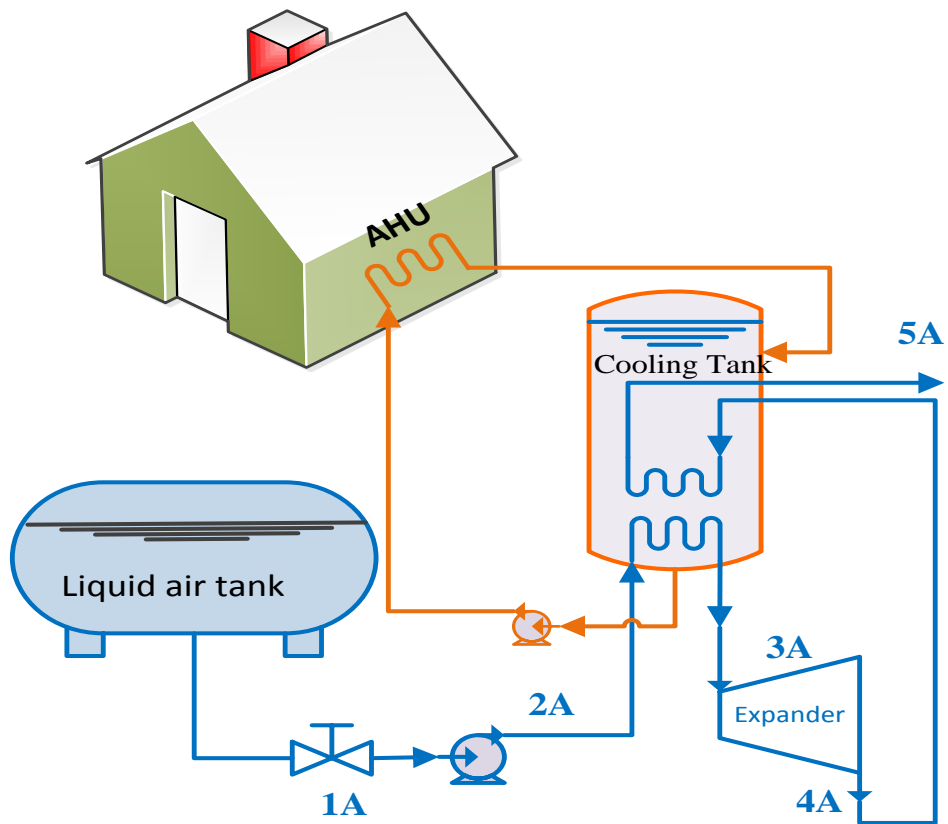
Figure 3-18 Second cycle, LN2 cooling and power cycle [92]
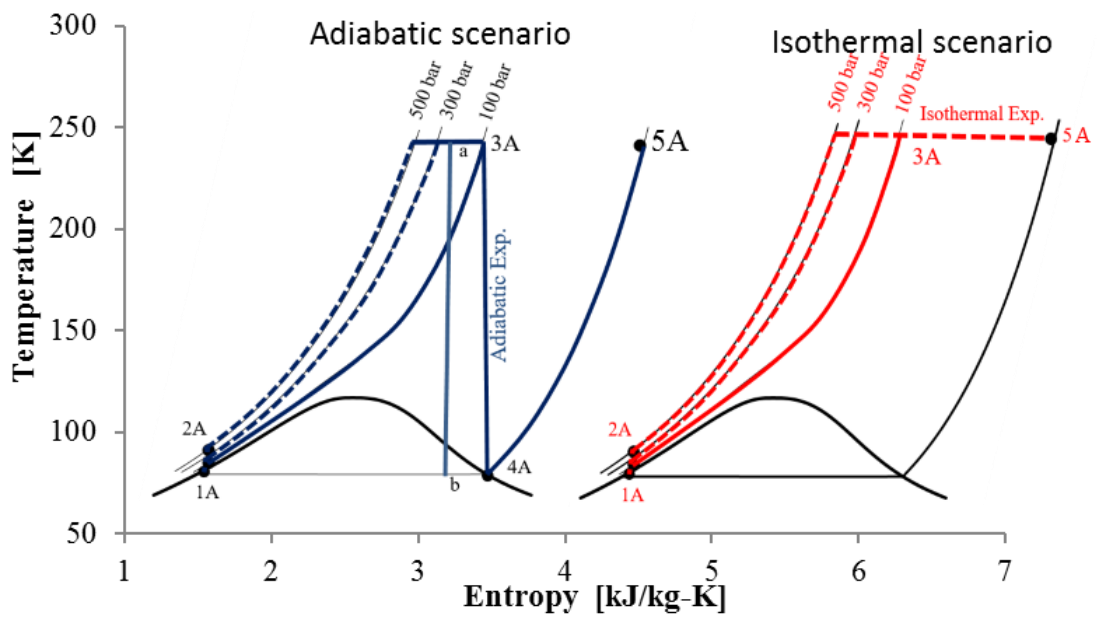
Figure 3-19: Second cycle's T-s diagram [89, 92]

3.3.2.3 Third configuration (Cycle 3)

The third configuration (Cycle 3) is presented in Figure **3-20** and Figure **3-21** where liquid nitrogen is used to run a closed Brayton cycle where 1B, 2B, 3B and 4B are representing its working fluid states. The left-hand cycle shown in Figure **3-21** is the LN2 cycle; whereas that on the right-hand side is the Brayton cycle and the X axis represents only the nitrogen entropy. The pressurized LN2 is evaporated and superheated (2A–3A) while cooling down the Brayton cycle fluid (4B–1B) in the evaporator before returning to the compressor. The superheated nitrogen/air and the compressed Brayton cycle fluid pass through the expanders after being heated by the secondary fluid in the cooling tank. The output power of the Brayton cycle expander depends on its pressure ratio and mass flow rate. Increasing the pressure ratio leads to an increase in the compressor's outlet temperature (T2B); this should not exceed that of the secondary fluid in the cooling tank. The mass flow rate depends on the selected evaporator outlet temperature (T3A), where increasing this temperature leads to increasing the mass flow rate; however, it decreases the temperature difference between the cooling tank and the evaporator leading to a reduction in the power output. This temperature, pressure ratio and the Brayton cycle working fluid should be carefully selected to maximize the output power and to avoid any possibility of condensation occurring in the evaporator. Various gases, such as Xenon, Neon, Helium or Hydrogen, which have a boiling temperature lower than LN2, can be used as a working fluid for the Brayton cycle to meet cycle requirements; the first working fluid (Xenon) was selected for the current study considering the safety aspects and availability [3].
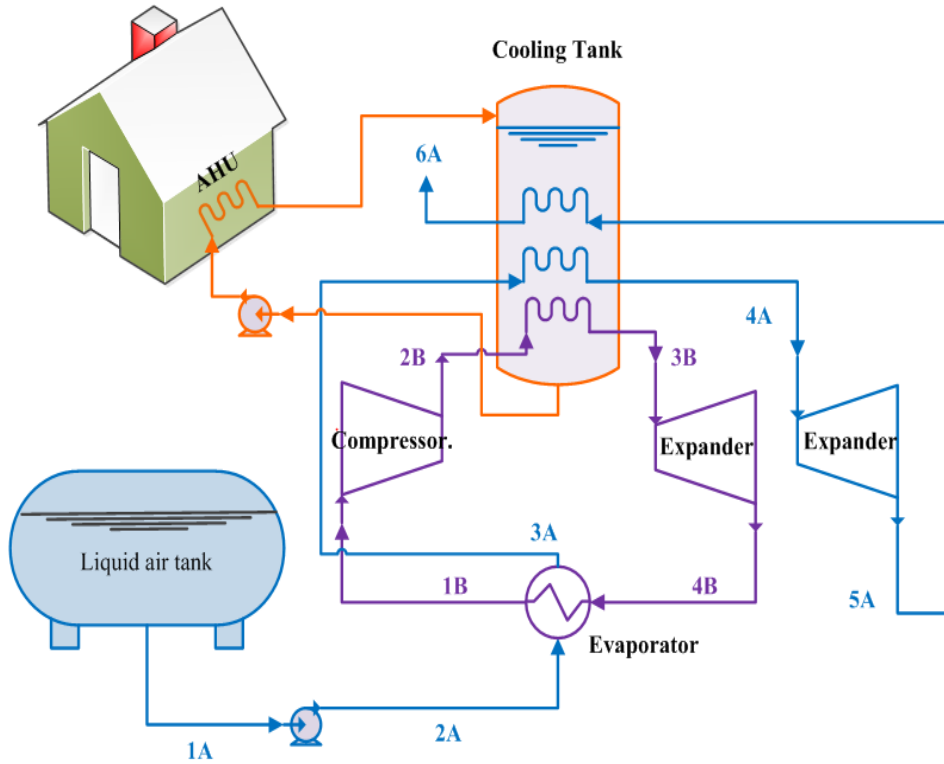
Figure 3-20: Third cycle, LN2 drives closed Brayton cycle [89]
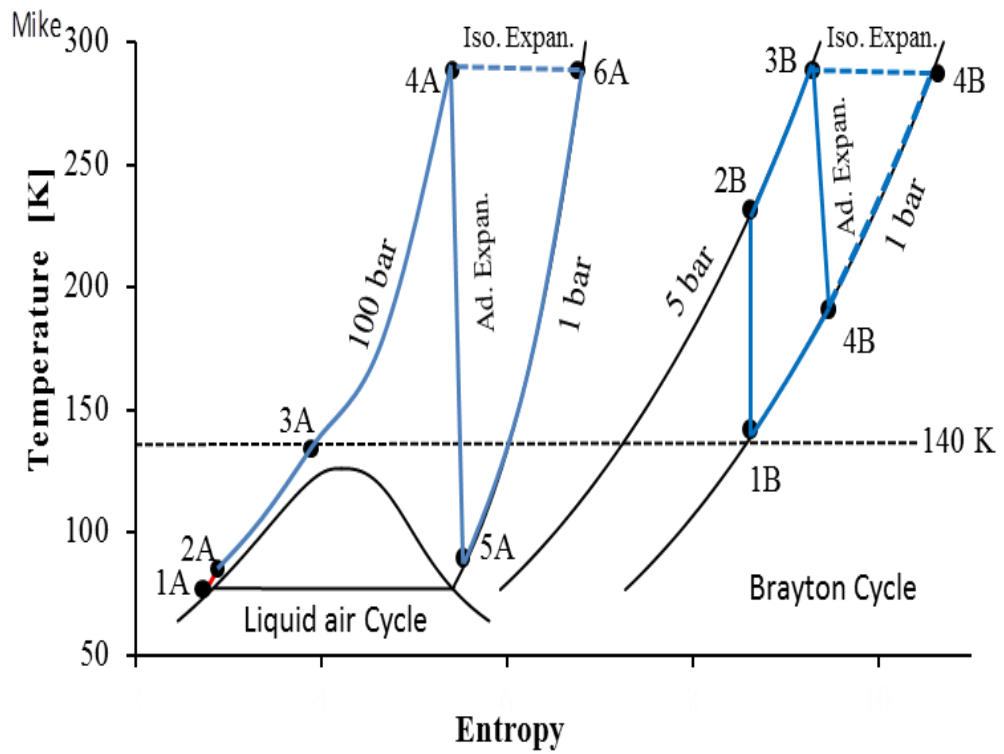
Figure 3-21: Third cycle's T-s diagram [89]

3.3.2.4   Fourth configuration (Cycle 4)

Compared with the Brayton cycle, Rankine cycle is a more efficient power cycle; therefore using liquid nitrogen to drive such a cycle will lead to generating more cooling and power from liquid nitrogen. Figure 3-22 and Figure **3**-**23** show the fourth cycle where the liquid nitrogen cycle run the closed Rankine cycle, and the symbols 1R, 2R, 3R and 4R are representing the state of its working fluids. The right-hand cycle shown in Figure **3**-**23** is the LN2 cycle; whereas the left hand side shows the closed Rankine cycle. The X axis in this figure represents only the nitrogen entropy. The high pressure LN2/LAir evaporates and superheats by absorbing heat from Rankine cycle fluid in HE1 which condenses during the process (4R-1R). The condensed Rankine cycle fluid is then pumped to the secondary fluid cooling tank to be evaporated and then expanded in the expander. The LN2 is passed through a separate expander after further superheating in the cooling tank. The condensing and the LN2 inlet pressures are chosen to be atmospheric and Xenon was selected as the working fluid for the closed Rankine cycle. Xenon boils at −108 °C at atmospheric pressure and it has a relatively high boiling temperature, but it does not freeze at the Rankine cycle condenser HE1. For this combined cycle, as mentioned above, there is a limitation on the value of the expander inlet pressure of the adiabatic expansion process for the open LN2 and the closed Rankine cycles; while high pressure values can be used in the isothermal expansion as long as the fluid boiling temperature is less than the temperature in the cooling tank [3, 91].
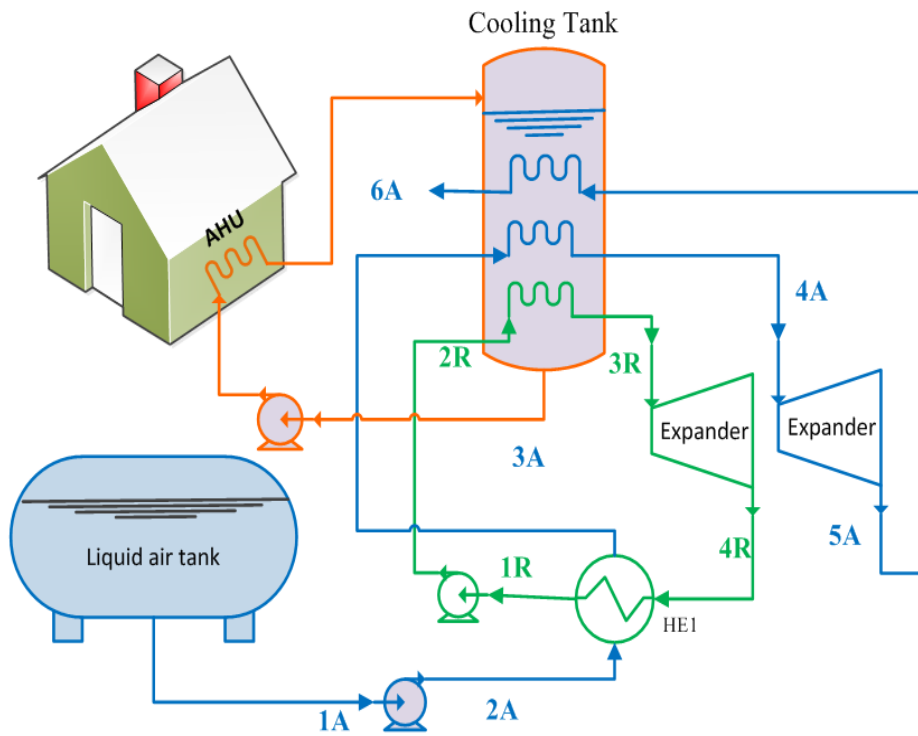
Figure 3-22: Fourth cycle, LN2 drives closed Rankine cycle [89]
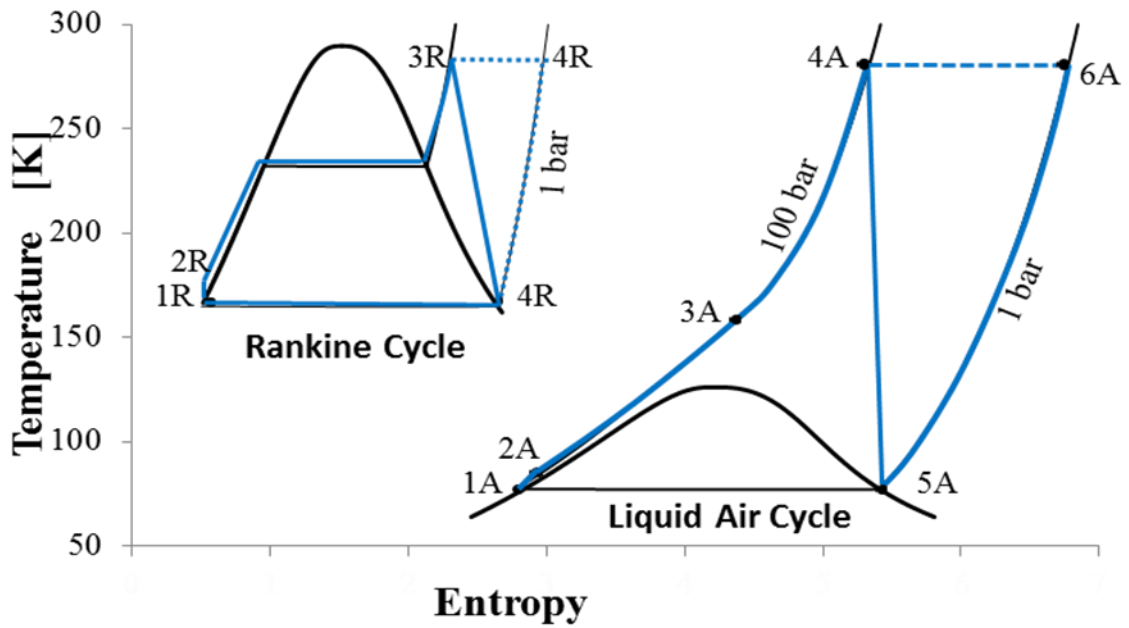
Figure 3-23: Fourth cycle's T-s diagram [89]

\

3.3.2.5   Fifth configuration (Cycle 5)

Figure 3-24 and Figure 3-25 show the last configuration (Cycle 5) which is also uses Rankine cycle; however, the LN2/Air cycle drives two cascaded closed Rankine cycles, and 1R, 2R, 3R, 4R, 1R´, 2R´, 3R´ and 4R´ are representing the state of the first and the second closed Rankine cycles respectively. The right-hand cycle that is shown in Figure 3-25 is the LN2 cycle; while the middle and the left-hand cycles are the first and the second closed Rankine cycles respectively. The X axis in this figure represents only the nitrogen entropy. This will further increase the amount of cold energy recovered from the LN2. In this cycle, the pressurized LN2 is evaporated and superheated in HE1 while condensing the working fluid of the first closed Rankine cycle. Then the condensate fluid is pumped to another heat exchanger (HE2) where it evaporates while condensing the working fluid of the second closed Rankine cycle, which has a higher boiling temperature. All outlets from HE2 pass though individual expanders after gaining heat from the secondary fluid in the cooling tank as shown in Figure 3-24 and Figure 3-25. The two working fluids of the Rankine cycles should be carefully selected to meet the cycle's and the application's requirements such as boiling/condensing temperature at the operating conditions and avoiding freezing the working fluid at the operating conditions. Tetrafluoromethane (R14) and Chlorotrifluoromethane (R13) with boiling temperatures at an atmospheric pressure of -127.8 °C and -81.5 °C were selected, respectively in the first and second closed Rankine cycles. The outlet temperatures from HE2 are assumed to be three degrees lower than the secondary fluid temperature in the cooling tank for all working fluids [3].
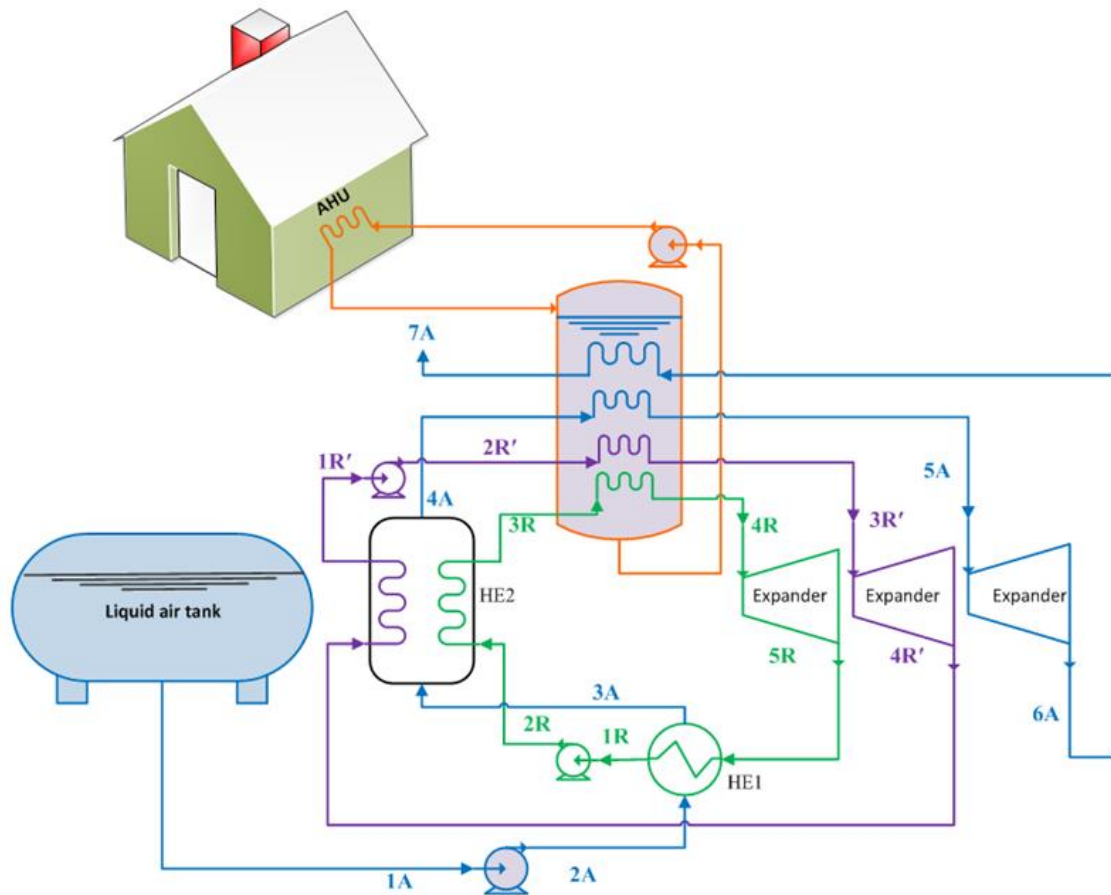
Figure 3-24: Fifth cycle, LN2 drives two closed Rankine cycles [89]
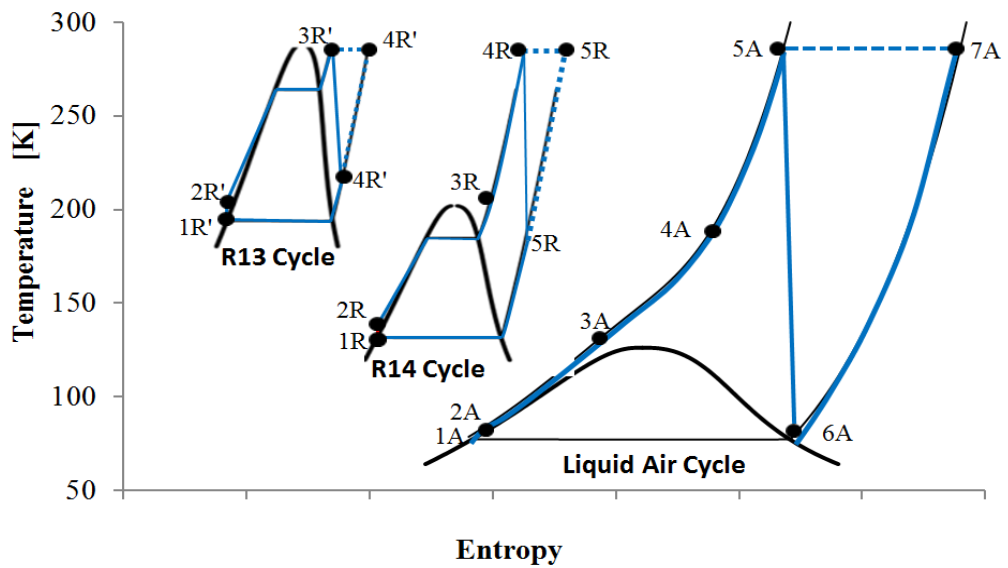
Figure 3-25: Fifth cycle's T-s diagram [89]

3.3.3 Thermodynamic modelling

The proposed cycles were analysed from thermodynamic point view to determine the most effective system which recovers most of the energy stored in LAir, and provide higher output power and cooling capacity for the selected application. A mathematical model was developed for each of the above cycles using MATLAB combined with REFPROP software to (a) calculate the properties of all working fluids at each state in the cycle, (b) solve the energy and mass balance equations, (c) calculate LN2 mass flow rate, power output, cooling capacity, efficiency and the cycle COP and (d) optimize the operating conditions. Adiabatic and isothermal expansion processes were considered in the current study with wide range of inlet pressure (P_{2A}) investigated. The modelling was carried out using the following assumptions [3, 91]:

- Liquid nitrogen enters to the system at liquid 77 K and atmospheric pressure, and leaves as gas at 283 K.

- Heat transfer from/into the surroundings is negligible.

- LN2 inlet pressure of all pumps is atmospheric pressure.

- For the Brayton cycle the compressor inlet pressure is atmospheric pressure.

- The pumps, expanders and compressors isentropic efficiency are 90%, 90% and 85%, respectively.

- The pressure drop in all cycle's components is negligible.

For the first configuration where there is no power generation the LN2 mass flow rate can be calculated by applying the energy balance equation between the cooling load and the specific enthalpy at the inlet and the outlet of the secondary coolant tank Equation **3.53** [92].

$$\dot{m}_N = \frac{\text{Cooling Load}}{(h_{3N} - h_{2N})} \qquad\qquad 3.53$$

For the second cycle shown in Figure **3-19**, the specific work output was calculated using Equations **3.54** when adiabatic expansion process is considered and Equation (**3.55**) when isothermal expansion process is considered.

$$W_{Ad} = [(h_{3A} - h_{4A}) - (h_{2A} - h_{1A})]$$ 3.54

$$W_{Iso} = [T_{tank}(s_{4A} - s_{3A}) - (h_{2A} - h_{1A})]$$ 3.55

Where; *W* is specific work in kJ/kg, *h* is the specific enthalpy [kJ/kg], *s* is specific entropy [kJ/kg.K] and *T* is temperature [K]. Whereas the subscripts *Ad, Iso, A* and *tank* refer to adiabatic expansion, isothermal expansion, LN2 cycle and cooling tank, respectively. The specific cooling capacity was calculated using Equation **3.56** for the adiabatic expansion and using Equation **3.57** for the isothermal expansion process.

$$CC_{Ad} = [(h_{3A} - h_{2A}) + (h_{5A} - h_{4A})]$$ 3.56

$$CC_{Iso} = [(h_{3A} - h_{2A})] + [T_{tank}(s_{5A} - s_{3A})]$$ 3.57

Where; *CC* is specific cooling capacity in kJ/kg.

Regarding the third cycle shown in Figure **3-20**, the ratio of the closed Brayton cycle mass flow rate to the LN2 mass flow rate was first calculated by applying energy balance to the fluids passing through the evaporator using Equation **3.58**.

$$m_r = \frac{\dot{m}_B}{\dot{m}_A} = \frac{(h_{3A} - h_{2A})}{(h_{4B} - h_{1B})}$$ 3.58

Where; $\dot{m}_B$ is the mass flow rate in kg/s for the closed Brayton cycle, and $\dot{m}_A$ is the mass flow rate of the LN2 cycle in kg/s. The specific work output was calculated using Equations (**3.59**), (**3.60**) and (**3.61**) for the adiabatic expansion and Equations (**3.62**), (**3.63**) and (**3.64**) for the isothermal expansion processes.

$$(W_A)_{Ad} = [(h_{4A} - h_{5A}) - (h_{2A} - h_{1A})] \qquad\qquad 3.59$$

$$(W_B)_{Ad} = m_r[(h_{3B} - h_{4B}) - (h_{2B} - h_{1B})] \qquad\qquad 3.60$$

$$W_{Ad} = (W_A)_{Ad} + (W_B)_{Ad} \qquad\qquad 3.61$$

$$(W_A)_{Iso} = [T_{tank}(s_{5A} - s_{4A}) - (h_{2A} - h_{1A})] \qquad\qquad 3.62$$

$$(W_B)_{Iso} = m_r[T_{tank}(s_{4B} - s_{3B}) - (h_{2B} - h_{1B})] \qquad\qquad 3.63$$

$$W_{Iso} = (W_A)_{Iso} + (W_B)_{Iso} \qquad\qquad 3.64$$

Where; the subscript A refers to the LN2 cycle, and the subscript B refers to the closed Brayton cycle. The specific cooling capacity was calculated using Equation **3.65** for when adiabatic expansion case and Equation **3.66** for the isothermal expansion case.

$$CC_{Ad} = [(h_{4A} - h_{3A}) + (h_{6A} - h_{5A})] + m_r(h_{3B} - h_{2B}) \qquad\qquad 3.65$$

$$CC_{Iso} = \qquad\qquad 3.66$$
$$[(h_{4A} - h_{3A})] + m_r(h_{3B} - h_{2B}) + [T_{tank}(s_{5A} - s_{4A})] + m_r[T_{tank}(s_{4B} - s_{3B})]$$

The modelling of the fourth cycle shown in Figure Figure 3-22 is similar to that of the third cycle. The ratio of the LN2/LAir mass flow rate to the closed Rankine cycle mass flow rate was calculated by applying energy balance to the fluids passing through HE1 using the Equation **3.67**.

$$m_r = \frac{\dot{m}_R}{\dot{m}_A} = \frac{(h_{3A} - h_{2A})}{(h_{4R} - h_{1R})} \qquad\qquad 3.67$$

Where; $\dot{m}_R$ is the mass flow rate of the working fluid in the closed Rankine cycle in kg/s and subscript R is referred to the closed Rankine cycle. The specific work output was calculated using Equations (**3.68**), (**3.69**) and (**3.70**) for the adiabatic expansion case and Equations **3.71**), (**3.72**) and (**3.73**) for the isothermal expansion case [3, 89, 92].

$$(W_A)_{Ad} = [(h_{4A} - h_{5A}) - (h_{2A} - h_{1A})] \qquad\qquad 3.68$$

$$(W_R)_{Ad} = m_r[(h_{3R} - h_{4R}) - (h_{2R} - h_{1R})] \qquad\qquad 3.69$$

$$W_{Ad} = (W_A)_{Ad} + (W_R)_{Ad} \qquad\qquad 3.70$$

$$(W_A)_{Iso} = [T_{tank}(s_{6A} - s_{4A}) - (h_{2A} - h_{1A})] \qquad\qquad 3.71$$

$$(W_R)_{Iso} = m_r[T_{tank}(s_{4R} - s_{3R}) - (h_{2R} - h_{1R})] \qquad\qquad 3.72$$

$$W_{Iso} = (W_A)_{Iso} + (W_R)_{Iso} \qquad\qquad 3.73$$

The specific cooling capacity was calculated using Equation **3.74** for the adiabatic expansion case and Equation **3.75** for the isothermal expansion case.

$$CC_{Ad} = [(h_{4A} - h_{3A}) + (h_{6A} - h_{5A})] + m_r(h_{3R} - h_{2R}) \qquad\qquad 3.74$$

$$CC_{Iso} = [(h_{4A} - h_{3A})] + m_r(h_{3R} - h_{2R}) + [T_{tank}(s_{5A} - s_{4A})] + m_r[T_{tank}(s_{4R} - s_{3R})] \qquad\qquad 3.75$$

Regarding the fifth cycle shown in Figure 3-24 where the LN2 cycle derives two cascaded Rankine cycles, the ratio of mass flow rate of the first closed Rankine cycle working fluid to the LN2 mass flow rate (m_{r1}) was calculated using the energy balance applied to HE1 as in Equation **3.76**, and ratio of mass flow rate of the second closed Rankine cycle working fluid to the LN2 mass flow rate (m_{r2}) was calculated using the energy balance applied to HE2 as in Equation **3.77** [3].

$$m_{r1} = \frac{\dot{m}_R}{\dot{m}_A} = \frac{(h_{3A} - h_{2A})}{(h_{5R} - h_{1R})} \qquad\qquad 3.76$$

$$m_{r2} = \frac{\dot{m}_{R'}}{\dot{m}_A} = \frac{m_{r1}(h_{3R} - h_{2R}) + (h_{4A} - h_{A3})}{(h_{4R'} - h_{1R'})} \qquad\qquad 3.77$$

Where; $\dot{m}_R$ is the mass flow rate in kg/s of the working fluid in the first closed Rankine cycle

and $\dot{m}_{R'}$ is the mass flow rate in kg/s of the working fluid in the second closed Rankine cycle.

The subscripts R is referring to the first closed Rankine cycle, while the subscript R' is

referring to the second closed Rankine cycle.

The specific work output was calculated using Equations (**3.78**-**3.81**) when the adiabatic

expansion process is considered and Equation (**3.82**-**3.85**) when the isothermal expansion

process is considered.

$$(W_A)_{Ad} = [(h_{5A} - h_{6A}) - (h_{2A} - h_{1A})] \tag{3.78}$$

$$(W_R)_{Ad} = m_{r1}[(h_{4R} - h_{5R}) - (h_{2R} - h_{1R})] \tag{3.79}$$

$$(W_{R'})_{Ad} = m_{r2}[(h_{3R'} - h_{4R'}) - (h_{2R'} - h_{1R'})] \tag{3.80}$$

$$W_{Ad} = (W_A)_{Ad} + (W_R)_{Ad} + (W_{R'})_{Ad} \tag{3.81}$$

$$(W_A)_{Iso} = T_{tank}(s_{7A} - s_{5A}) - (h_{2A} - h_{1A}) \tag{3.82}$$

$$(W_R)_{Iso} = m_{r1}[T_{tank}(s_{5R} - s_{4R}) - (h_{2R} - h_{1R})] \tag{3.83}$$

$$(W_{R'})_{Iso} = m_{r2}[T_{tank}(s_{4R'} - s_{3R'}) - (h_{2R'} - h_{1R'})] \tag{3.84}$$

$$W_{Iso} = (W_A)_{Iso} + (W_R)_{Iso} + (W_{R'})_{Iso} \tag{3.85}$$

The specific cooling capacity was calculated using Equation **3.86** for the adiabatic expansion

case and Equation **3.87** for the isothermal case.

$$CC_{Ad} = [(h_{5A} - h_{4A}) + (h_{7A} - h_{6A})] + m_{r1}[(h_{3R} - h_{2R})] + m_{r2}[(h_{3R'} - h_{2R'})] \tag{3.86}$$

$$CC_{Iso} = [(h_{5A} - h_{4A})] + m_{r1}[(h_{3R} - h_{2R}) + m_{r2}[(h_{3R'} - h_{2R'}) +$$

$$\tag{3.87}$$

$$[T_{tank}(s_{6A} - s_{5A})] + m_{r1}[T_{tank}(s_{5R} - s_{4R})] + m_{r2}[T_{tank}(s_{4R'} - s_{3R'})]$$

The above cycles provide cooling and power which makes the system neither heat engine nor heat pump, so assessing the system performance seems different from normal systems. Therefore two factors were used to evaluate the system performance; the first one is Coefficient of Performance COP where the whole system was consider as a heat pump, in this case, the output power was converted to an equivalent cooling capacity (cooling produced using this output power to run a conventional AC system that has a COP of 3.5). Then the system COP was calculated based on the total cooling capacity and the energy consumed to produce LN2 (which is 1080 kWh/kg for LAir and 1350 kWh/kg for LN2) as in Equation **3.88** [81].

$$COP = \left[\frac{Total\ cooling\ capacity}{1080}\right]_{LAir} \quad or \quad COP = \left[\frac{Total\ cooling\ capacity}{1350}\right]_{LN2} \qquad 3.88$$

The second factor is *Recovery Efficiency* (η_{RE}) where the whole system was considered as heat engine. In this case, the output cooling capacities were converted to an equivalent power (which is the input power needed to run a conventional AC system that has a COP of 3.5 to provide the same cooling capacity). Then the system *Recovery Efficiency* was calculated based on the total output power and the energy consumed to produce LAir or LN2 as in using Equation **3.89**.

$$\eta_{RE} = \left[\frac{Total\ output\ power}{1080}\right]_{LAir} \quad or \quad \eta_{RE} = \left[\frac{Total\ output\ power}{1350}\right]_{LN2} \qquad 3.89$$

3.3.4 Results and discussion

3.3.4.1 Mathematical modeling

The proposed cycles were investigated to assess their feasibility to provide cooling and power to domestic and commercial buildings at peak times leading to energy saving and reduction of the electricity peak demands using more environment friendly solution [3, 85, 88-92]. Two different clod storage mediums LAir and LN2, which have similar physical and

thermodynamic properties but different energy production requirements, were investigated. LAir consumes 20% less energy that of LN2.

The typical dwelling described in section (3.1) was also selected as a case study to determine the amount of LN2 needed to meet its cooling load. Figure 3-26 and Figure 3-27 show the consumption of LN2 with the variation of cooling load with time on the 21st June for all the investigated cycles using the adiabatic and isothermal expansion processes respectively. It is clear that, the required LN2/LAir mas flow rate is highest (more than 200 L/h at peak time) for the first cycle shown in Figure **3-16**, which is used to generate air conditioning only. As for the other cycles that produce cooling and power, it is clear that the fifth configuration (cycle 5) shows the lowest LN2 consumption. Also, when isothermal expansion process is used, the LN2 consumption is lower than that of the adiabatic expansion, with most cycles' performance being very close to each other. To determine the effect of changing the LN2 inlet pressure (P_{2A}) on the system's LN2 mass flow rate and the power output, model was solved at pressure values vary from 0 to 100 bar in the adiabatic case and from 0 to 500 bar in the isothermal cases, and the cooling load was fixed at the maximum value (19.6 kWh) where the maximum flow rate was expected [3, 91, 92]
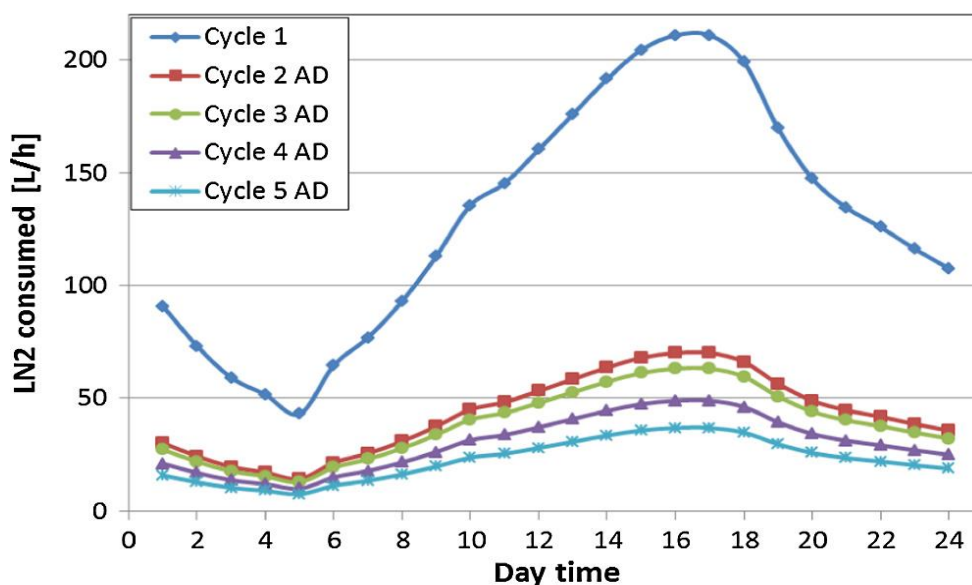
Figure 3-26: Hourly LN2 flow rate to meet the cooling load for adiabatic case [3]
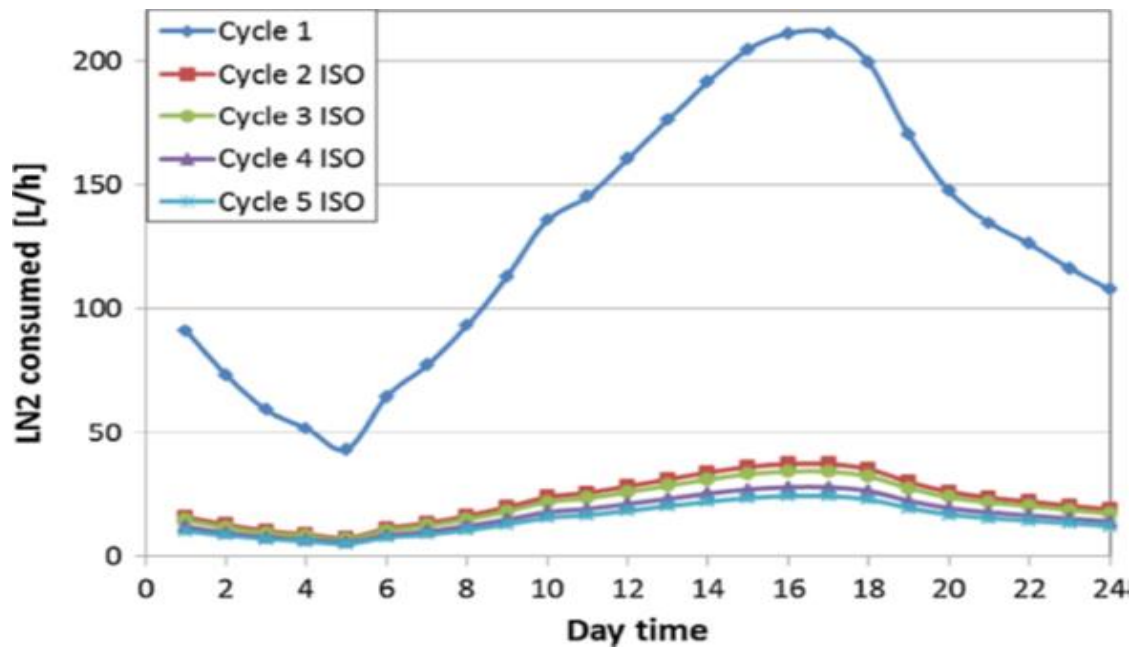
Figure 3-27:Hourly LN2 flow rate to meet the cooling load for isothermal case [3]

The following figures present the specific work output, specific cooling capacity, the system COP and the system *Recovery Efficiency* for the adiabatic and the isothermal expansion processes for all proposed cycles either using LAir or LN2 except the first one where there is no power generation.

For the adiabatic expansion scenario, Figure **3**-**28** and Figure **3**-**29** present the specific work versus the inlet pressure (P2A) for all proposed cycles when use Figure **3**-**28** LAir or LN2 respectively. The figures show that the specific work curve has the same trend for both working fluids (LAir or LN2) where there is no significant change after inlet pressure of 30 bar. The maximum specific work output for the 3rd , 4th and 5th cycles increases by 10.6%, 56.9% and 133.1% respectively compared with the 2nd cycle when LAir is used as working fluid and by 10.8% 54.8% and 129.5%, respectively, when LN2 is used as working fluid.

The specific cooling capacities followed the same specific work trend as shown in Figure 3-30 and Figure 3-31, and compared to the second cycle, the maximum values of the cooling capacities for 3rd, 4th and 5th cycles show improvement by 3.0%, 15.2% and 36.8%,

respectively, when LAir is used and by 2.8%, 7.8% and 15.3%, respectively, when LN2 is used [3, 89, 91, 92].
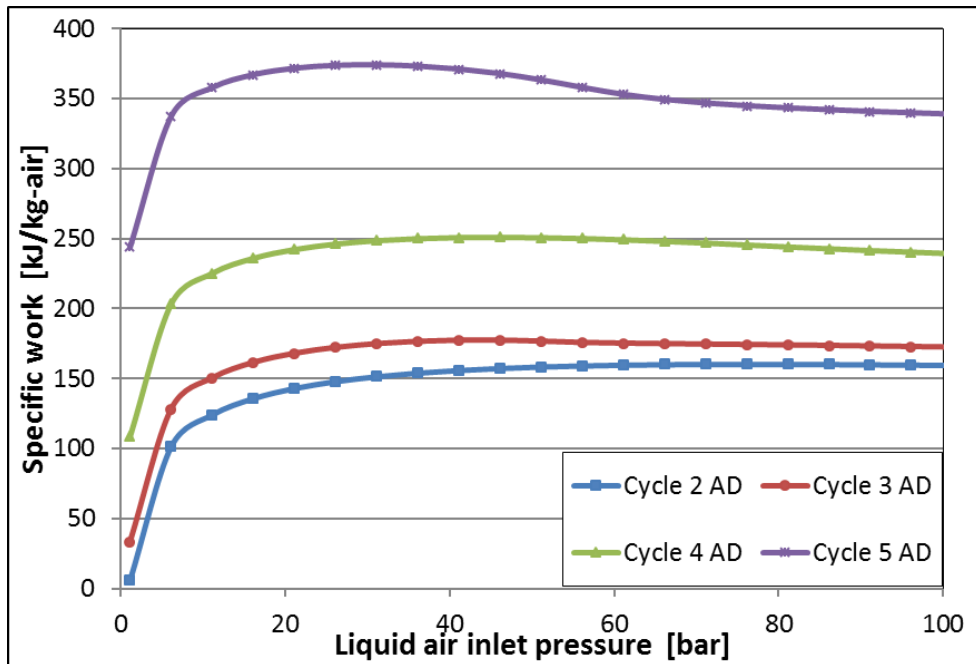
Figure 3-28: Specific output work at various inlet pressure for the adiabatic expansion [89, 92]
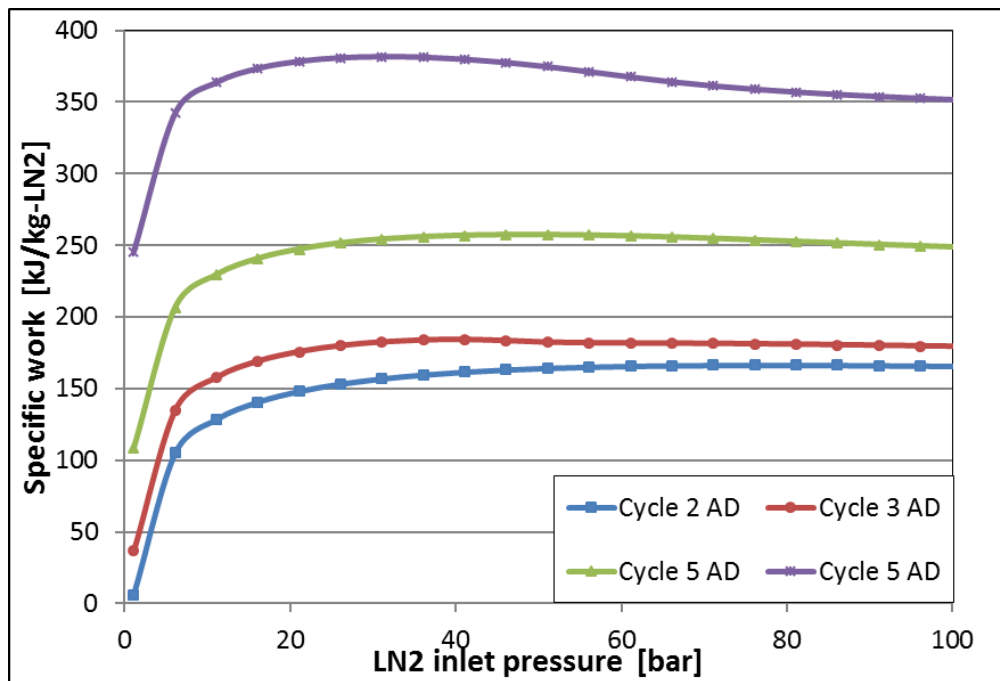
Figure 3-29: Specific output work at various inlet pressure for the adiabatic expansion [89, 92]
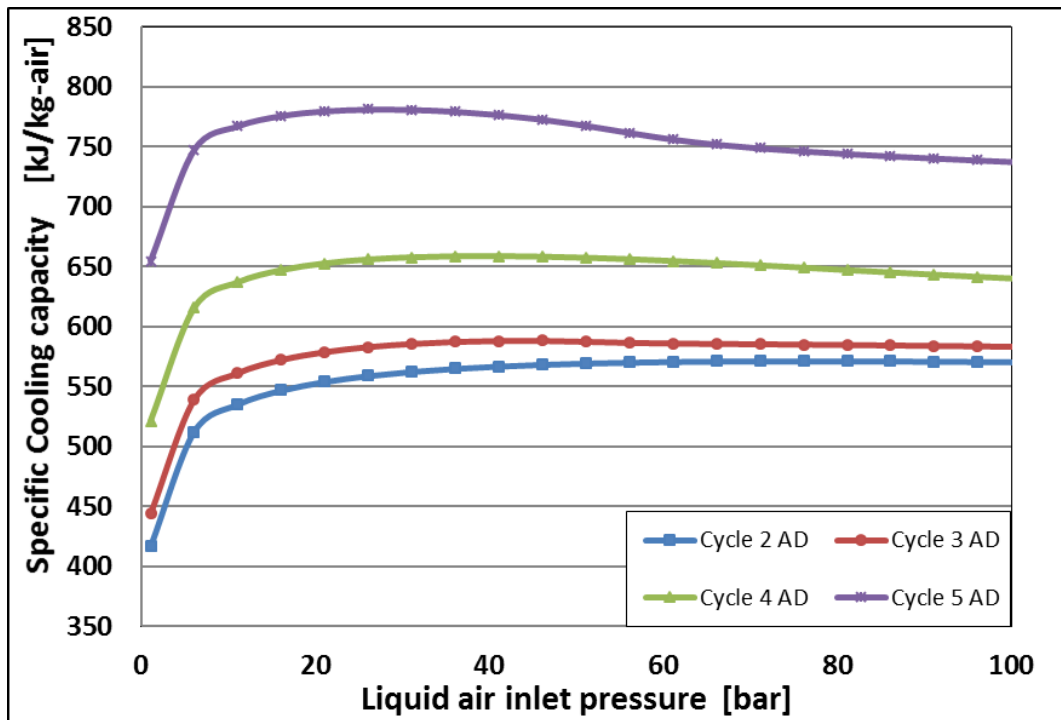
Figure 3-30: Specific cooling capacity at various inlet pressure for the adiabatic expansion [89, 92]
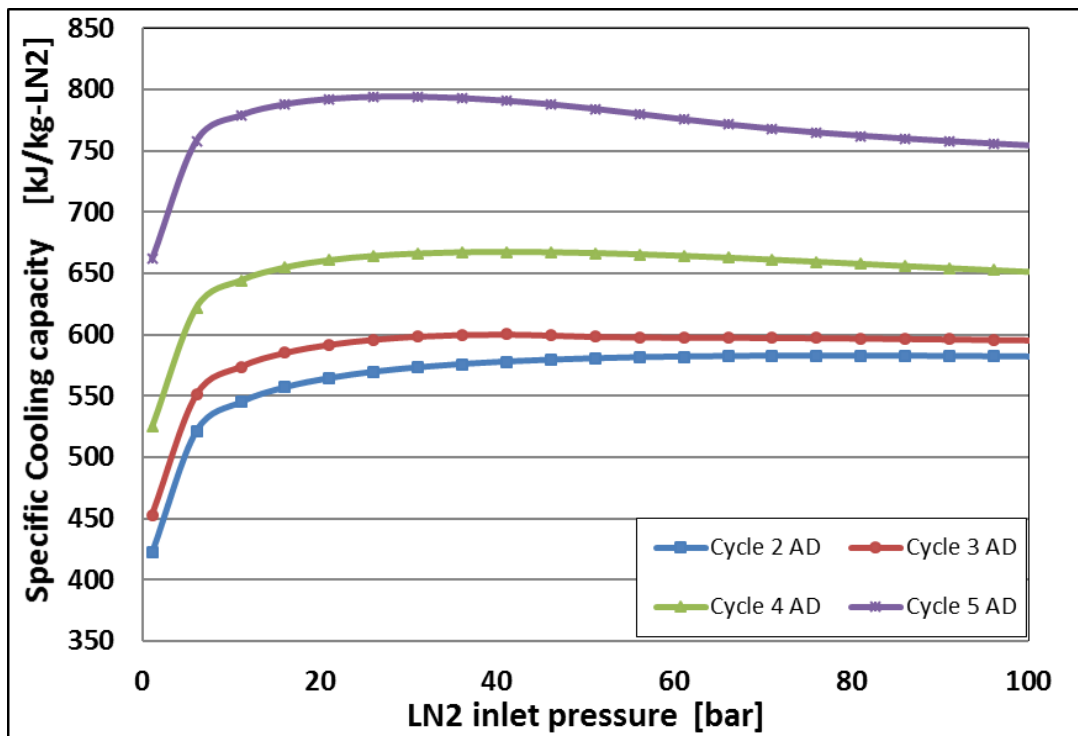
Figure 3-31: Specific cooling capacity at various inlet pressure for the adiabatic expansion [89, 92]

Regarding the isothermal expansion scenario, the specific work output and specific cooling capacity are higher than those of the adiabatic one as shown in Figure **3-32** to Figure 3-35. This expansion process allows the system to increase the inlet pressure up to 500 bar or even more. Compared with 2nd cycle the specific work output increased by 16.2%, 31.5%, 47.7% using 3rd, 4th and 5th respectively when LAir is used and by 13.7%, 32.5% and 48.4%, respectively, when LN2 is used. Also, compared with the adiabatic expansion, the specific work output is increased by about 3.1, 3.2, 2.6 and 2.0 times for the 2nd, 3rd, 4th and 5th cycles respectively, for both working fluids (LAir or LN2).
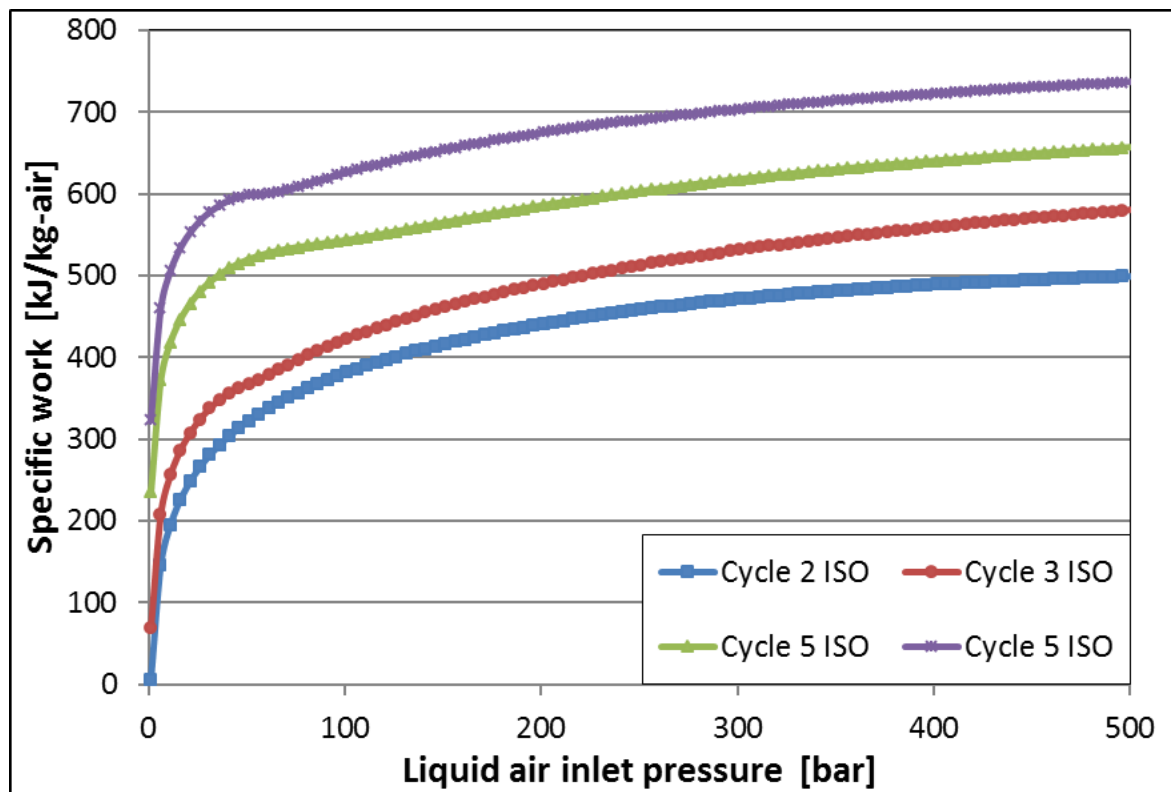
Figure 3-32: Specific output work at various inlet pressures for the isothermal expansion [89, 92]
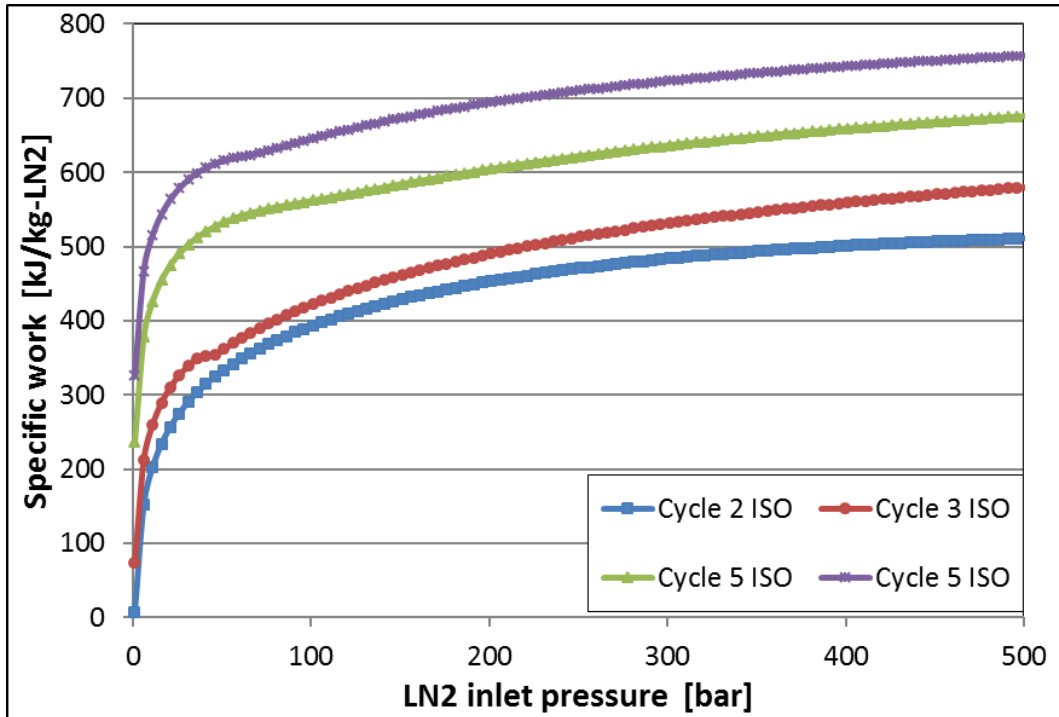
Figure 3-33: Specific output work at various inlet pressure for the isothermal expansion
[89, 92]

Figure **3-34** and Figure 3-35 show the specific cooling capacity respectively when LAir and
LN2 were used and they show almost the same trend as those of the specific work output. The
maximum values increased by 50%, 50%, 40% and 30% compared with the adiabatic
expansion for 2nd, 3rd, 4th and 5th cycles, respectively. Compared to the second cycle, the
maximum cooling capacity of the 3rd, 4th and 5th cycles showed improvement by 2.8%, 7.8%
and 15% respectively when LAir is used and by 0%, 7.6% and 15%, respectively, when LN2
is used [3, 89, 92, 94].
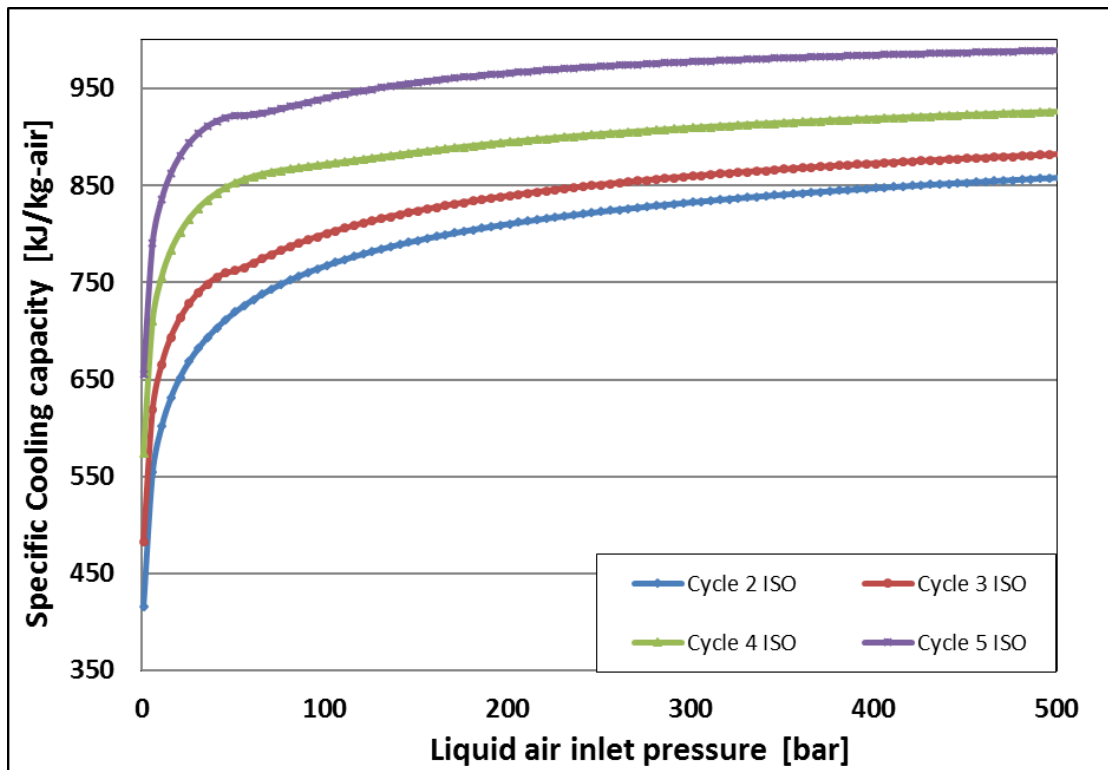
Figure 3-34: Specific cooling capacity at various inlet pressure for the isothermal expansion[89, 92]
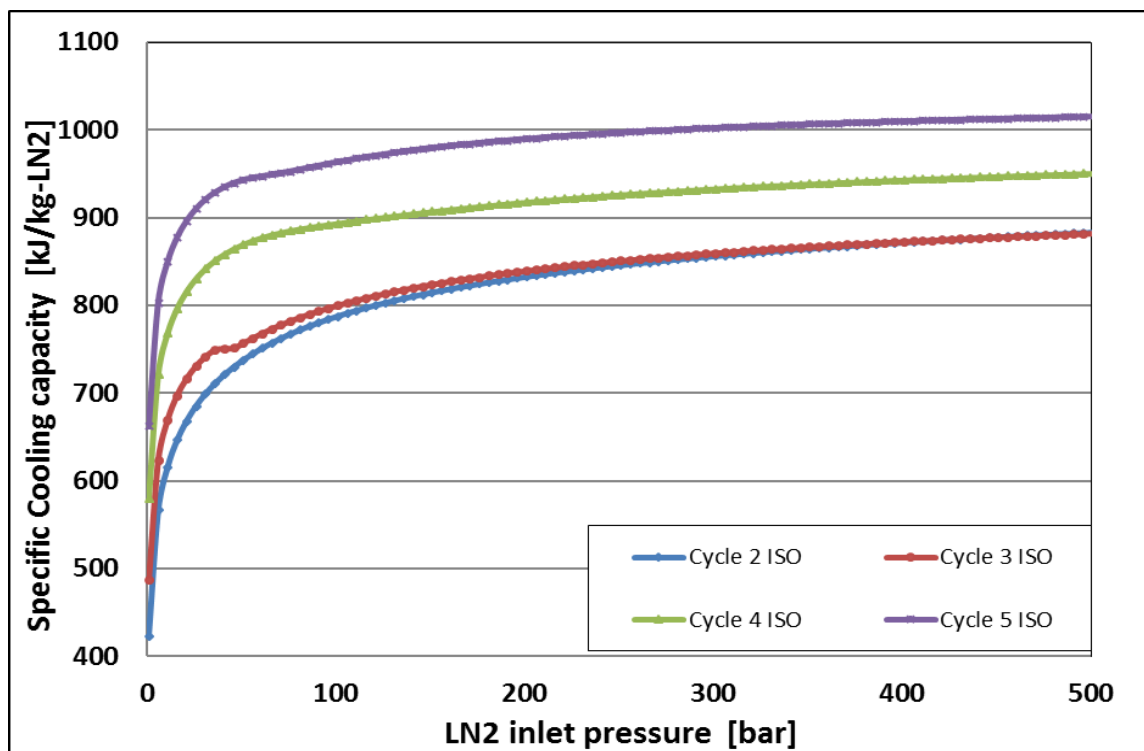
Figure 3-35: Specific cooling capacity at various inlet pressure for the isothermal expansion

[89, 92]

The performance of the various configurations was assessed based on *Recovery Efficiency* and COP as mentioned in section (3.3.3). For the adiabatic scenario, the *Recovery Efficiencies* and COPs of all proposed power cycles are presented in Figure 3-36 to Figure 3-39 and their trends are similar to those of the specific output work and cooling capacity. The figures indicate that the 5th cycle has the highest *Recovery Efficiency* and COP, reaching 55% and 2, respectively, when LAir is used and 45% and 1.6, respectively, when LN2 is used. For the isothermal expansion scenario, the Recovery Efficiencies and COPs of all proposed cooling and power cycles are presented in Figure 3-40 to Figure **3**-**43**. The figures show that, the Recovery Efficiency and COP of the lowest performing system (2nd cycle) reach 70% and 2.4, respectively, when LAir is used and 55% and 1.9, respectively, when LN2 is used. However, the 5th cycle produced *Recovery Efficiencies* and COP values reaching 94% and 3.3, respectively, when LAir is used and 78% and 2.7, respectively, when LN2 is used. The figures show clearly that, the systems *Recovery Efficiencies* and COPs when LAir is used are more than 20% higher than that of when LN2 is used. The fifth cycle shows the highest system performance while the 2nd cycle shows the lowest.
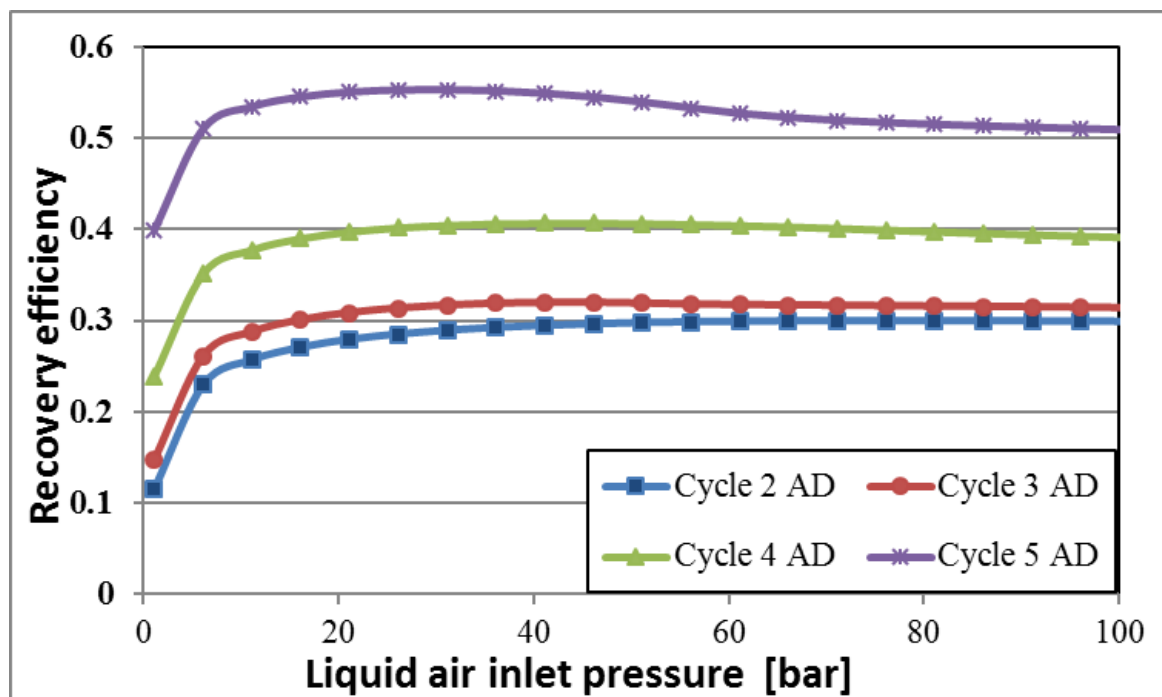
Figure 3-36: Recovery Efficiency at various inlet pressure for the adiabatic expansion [89, 92]
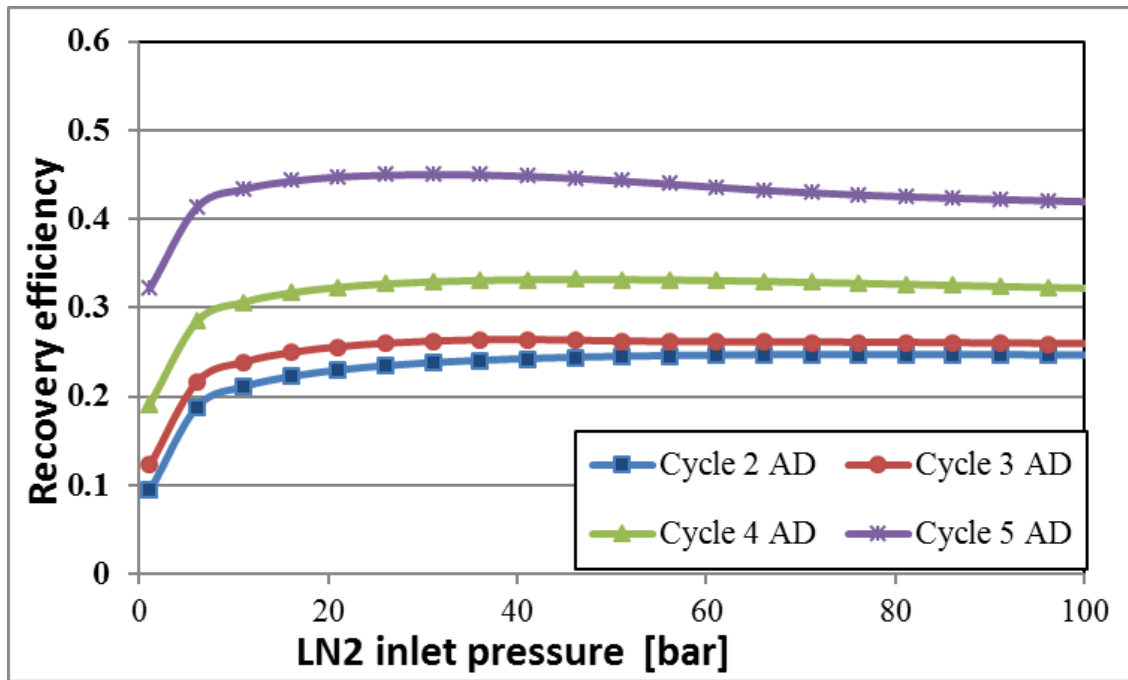
Figure 3-37: Recovery Efficiency at various inlet pressure for the adiabatic expansion [89, 92]
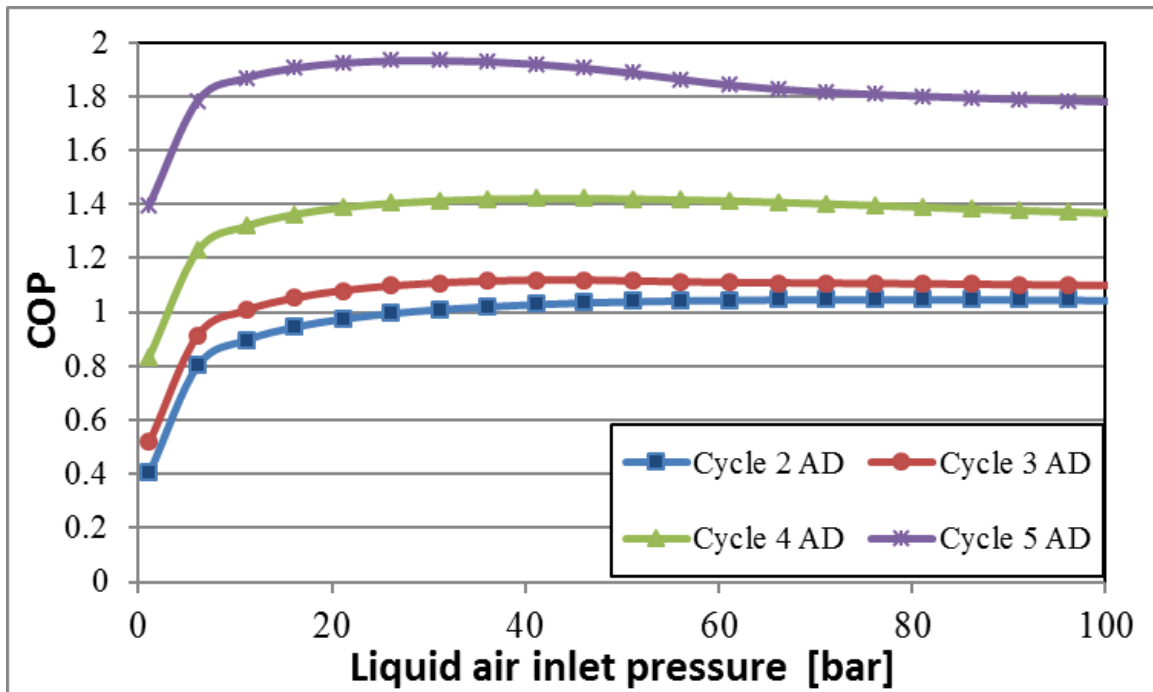
Figure 3-38: COP at various inlet pressure for the adiabatic expansion [89, 92]
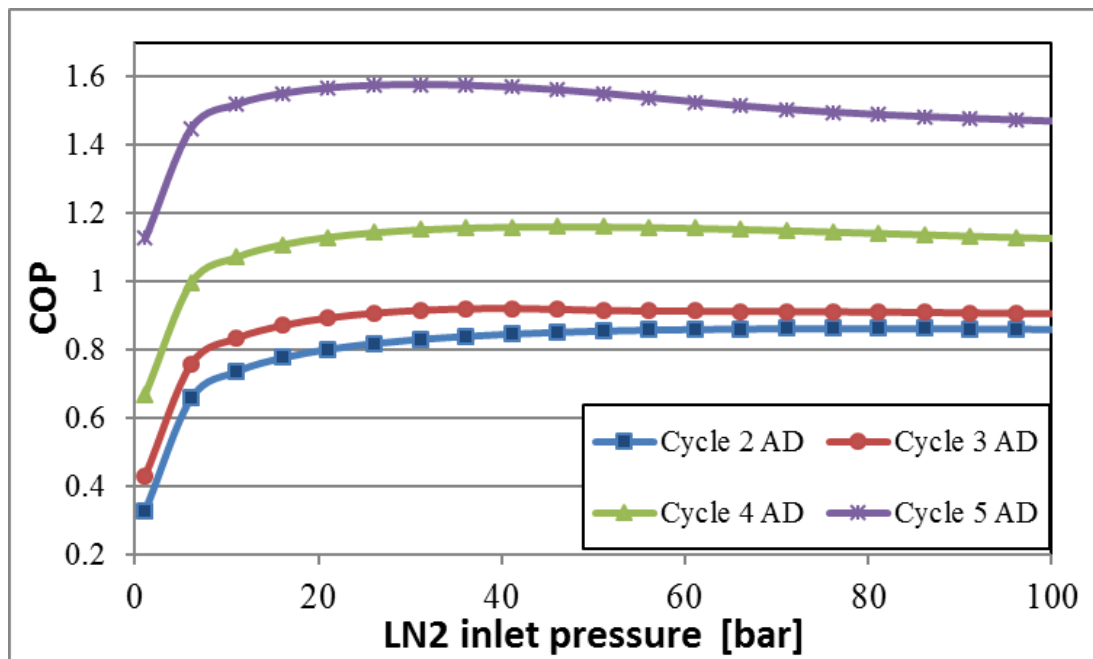
Figure 3-39: COP at various inlet pressure for the adiabatic expansion [89, 92]
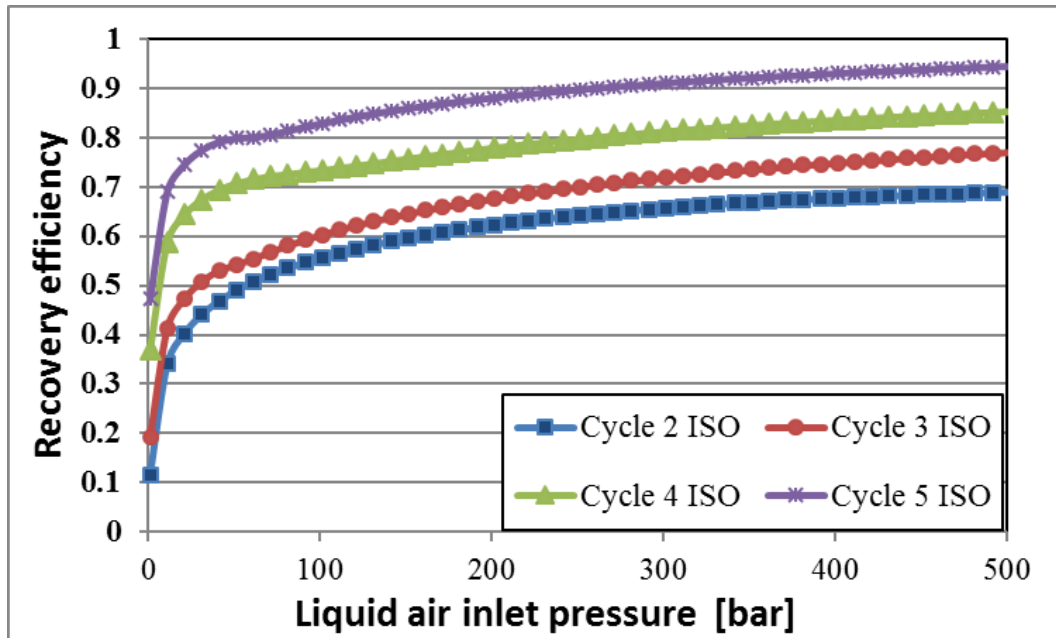
Figure 3-40: Recovery Efficiency at various inlet pressure for the isothermal expansion [89, 92]
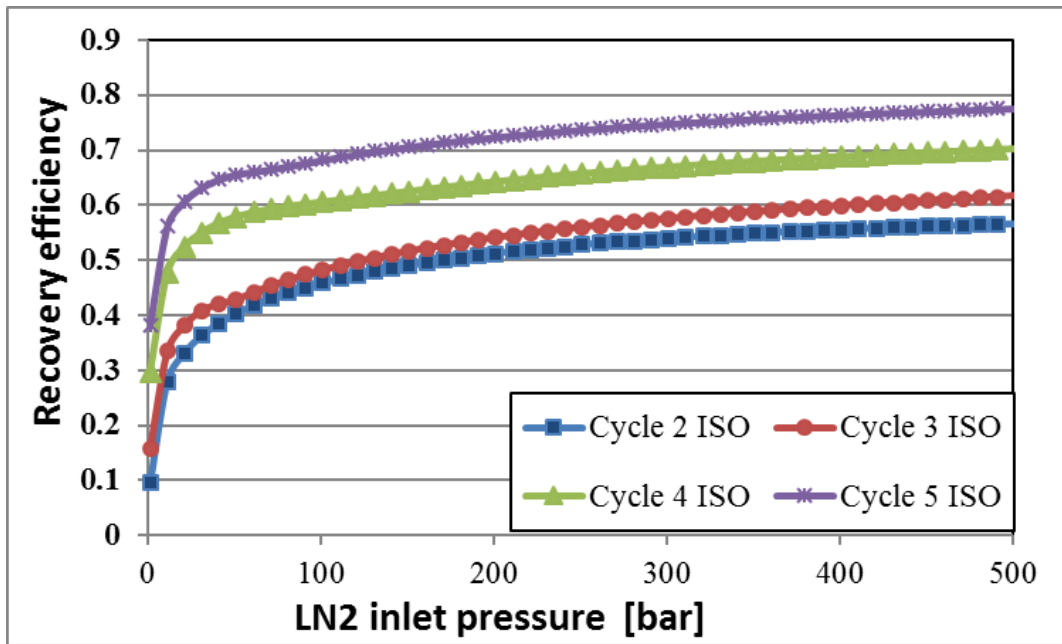
Figure 3-41: Recovery Efficiency at various inlet pressure for the isothermal expansion [89, 92]
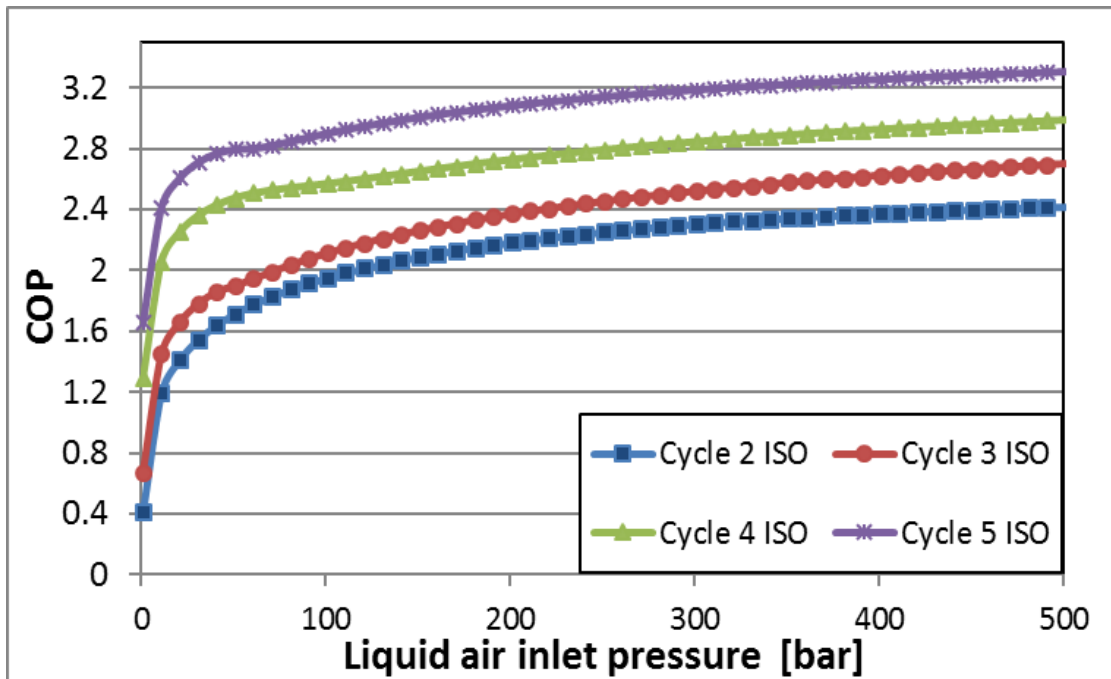
Figure 3-42: COP at various inlet pressure for the isothermal expansion [89, 92]
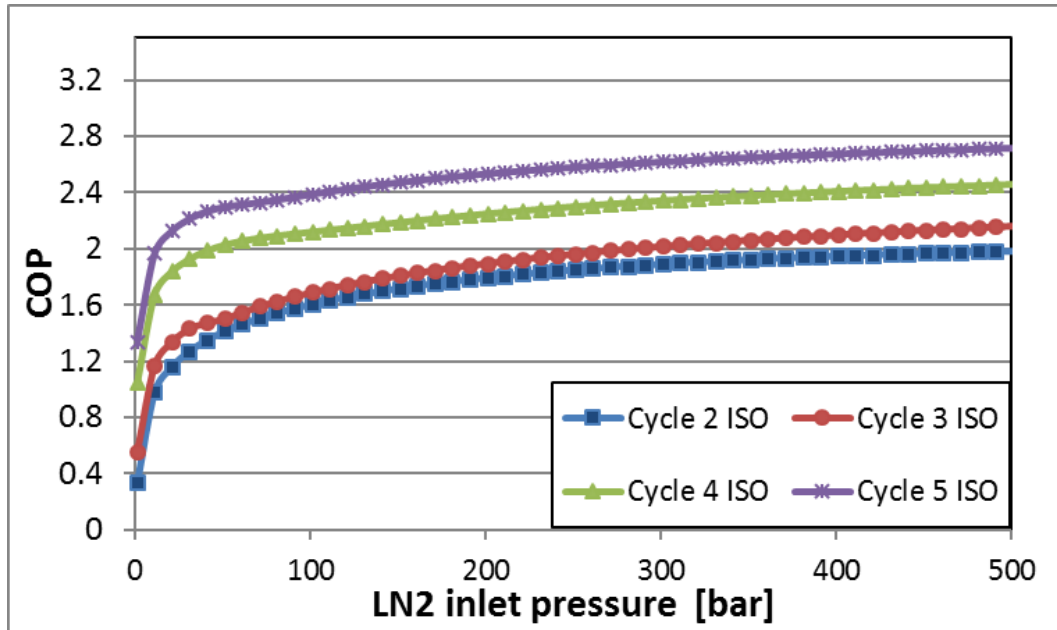
Figure 3-43: COP at various inlet pressure for the isothermal expansion [89, 92]

Table **3**-**11** presents a comparison between LAir and LN2 in the proposed systems in terms of work output, cooling capacity, Recovery Efficiency and COP. The table shows that in all proposed cooling and power cycles, the specific work output and the specific cooling capacities are slightly higher when LN2 is used with difference of less than 4%, however, the Recovery Efficiencies and the COPs are higher by 21-25% when LAir is used indicating using LAir is more efficient than LN2.

Table 3-11 Comparison between LAir and LN2

Expansion process		Adiabatic				Isothermal			
Cycle No		1	2	3	4	1	2	3	4
Max. specific power output	Air	160	177	251	373	499	580	656	737
	Nitrogen	166	184	257	381	510	580	676	757
Difference [%]		3.6	3.8	2.3	2.1	2.2	0.0	3.0	2.6
Max. specific cooling	Air	571	588	658	781	858	882	925	989
	Nitrogen	582	600	667	793	883	881	950	1015
Difference [%]		1.9	2.0	1.3	1.5	2.8	-0.1	2.6	2.6
Max. recovery efficiency [%]	Air	29.96	31.98	40.66	55.29	68.95	77.09	85.33	94.43
	Nitrogen	24.66	26.34	33.18	45.07	56.53	61.64	70.19	77.61
Difference [%]		21.5	21.4	22.5	22.7	22.0	25.1	21.6	21.7
Max. system COP	Air	1.05	1.12	1.42	1.93	2.41	2.69	2.98	3.3
	Nitrogen	0.86	0.92	1.16	1.57	1.97	2.15	2.45	2.71
Difference [%]		22.1	21.7	22.4	22.9	22.3	25.1	21.6	21.8

3.3.4.2 Cost Analysis

A cost analysis was carried out to compare the proposed systems with the conventional A/C system. For the same dwelling used in above section (3.3.4.1) using LN2/LAir as working fluid. The results are shown in Figure **3**-**44** and Figure **3**-**45** where the cost of using LN2 for air conditioning and power generation is compared to the cost of using a conventional A/C system. The investment cost and the running cost are not taken to consideration in this research. This comparison was based on a total power consumption of one day that has a cooling load of 288 kWh/day at the electricity rate during peak times (it was up to 19 pence/kWh during the peak times [113]) and with various LN2/LAir prices. The figures show clearly that, for the adiabatic scenario, only the fifth cycle showed lower energy cost than the conventional A/C system for the LN2/LAir price of 3 pence/kg; while for the isothermal scenario, all the configurations show lower energy cost than the conventional A/C system for the LN2/LAir price of less than 5.5 pence/kg. With the current price of 3.5 pence per kg [3, 82, 91, 114], the proposed system shows savings up to 11%, 21%, 29% and 36% for the second, third, fourth and fifth cycles, offering a cost effective method for using the stored energy in LN2 to produce cooling and power for domestic applications. The first configuration, which has no power generation, costs five times that of the conventional A/C system, indicating that this configuration is the worst method for the use of LN2 to provide cooling for domestic applications. Also, the Dearman report [58] showed that the market dynamics of LN2/LAir can lead to a further reduction in the cost of producing LN2/LAir, leading to a market price of 1.3 pence/kg; and with this price, the 2nd, 3rd, 4th and 5th can save up to 74, 77, 80 and 81%, respectively, compared to the conventional A/C systems. The widespread use of this technology will lead to a significant reduction in CO_2 emissions since LN2/LAir are produced using surplus electricity or renewable energy sources [85, 89, 92].
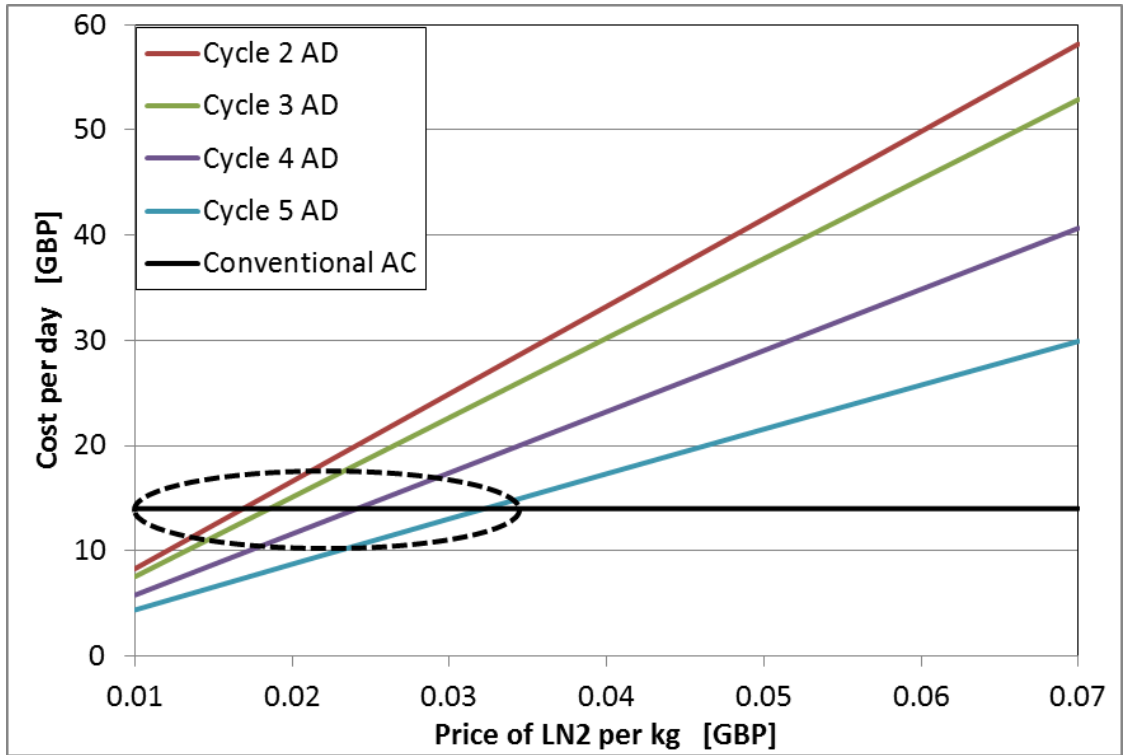
Figure 3-44: Daily power consumption at various LN2/LAir prices.
(a) Adiabatic expansion [89, 92]
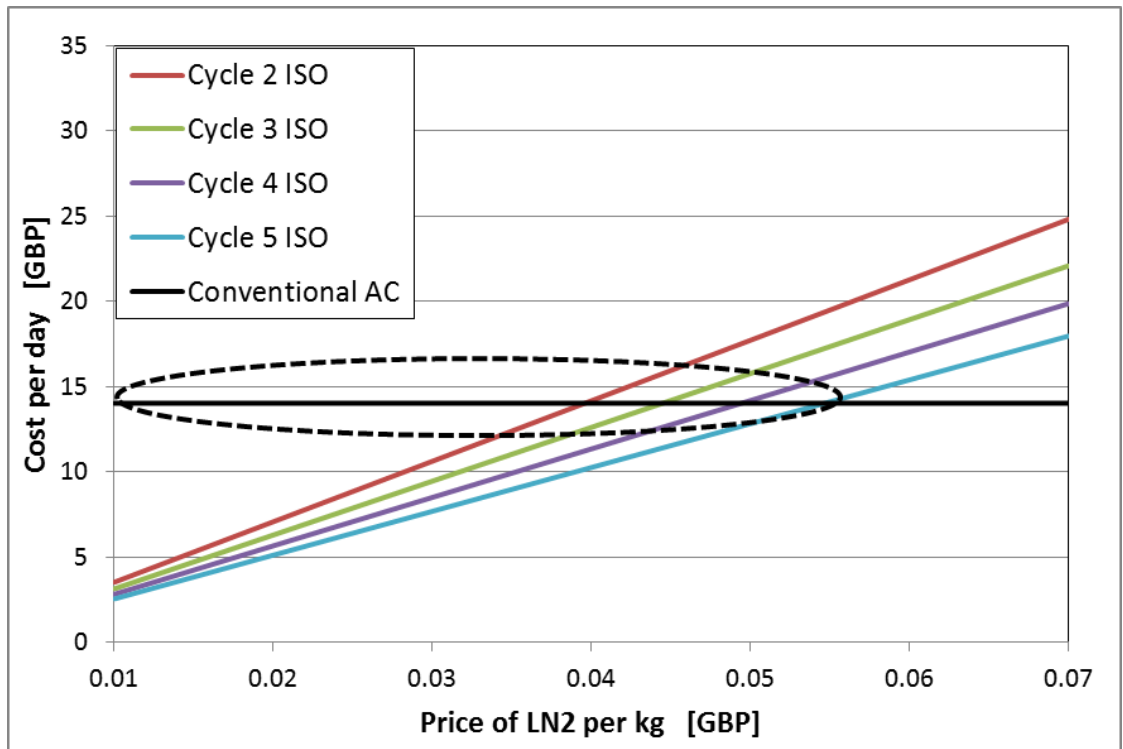
Figure 3-45: Daily power consumption at various LN2/LAir prices.
(b) Isothermal expansion [89, 92]

For commercial applications a building located in Ahwaz, Iran with cooling load as shown in Figure 3-46 was selected as case study [94]. The comparison was made based on the cost of the required LAir or LN2 compare to the conventional AC system power consumption to meet the building cooling load. The results are very sensitive to the LAir and LN2 prices and at the current prices of LAir , LN2 and kWh electricity [92], all the above proposed cycles in the isothermal expansion scenario consume less energy than the conventional system when LAir is used and only the 2nd cycle consumed more energy when LN2 is used as shown in Figure **3**-**47** and Figure **3**-**48**. The cost in these two figures was calculated based on the cooling load in Figure **3**-**45** by dividing the cooling load by the COP and multiply it by electricity price. At this level of price the 2nd , 3rd, 4th and 5th cycles show savings up to 15%, 24%, 31% and 37.5%, respectively, when LAir is used, and -3.5%, 5%, 16% and 24%, respectively, when LN2 is used. Where the negative sign indicates there is no saving achieved in this cycle and the conventional system consumes less energy with this percentage. As it was mentioned above the widespread of this technology and using the co-located systems leads to further reduction in LAir and LN2 prices leading to further energy savings and further reduction in CO_2 emissions [62]. Figure 3-49) to Figure (3-50) presents the energy cost saving of each of the above cycles at three different LAir and LN2 prices (3.5, 2.5 and 1.5 pence per kg). At the lowest LAir and LN2 prices the 2nd, 3rd, 4th and 5th cycles show savings up to 63%, 67%, 70% and 72%, respectively, when LAir is used, and 55%, 59%, 63% and 67% , consecutively, when LN2 is used. At this level of price, the 5th cycle, which is the most complex one among the investigated cycles, shows savings of only 14%, 8% and 3% higher than those of the 2nd, the 3rd and the 4th cycles, respectively, indicating there is no significant advantage of such a complex cycle [89, 92].
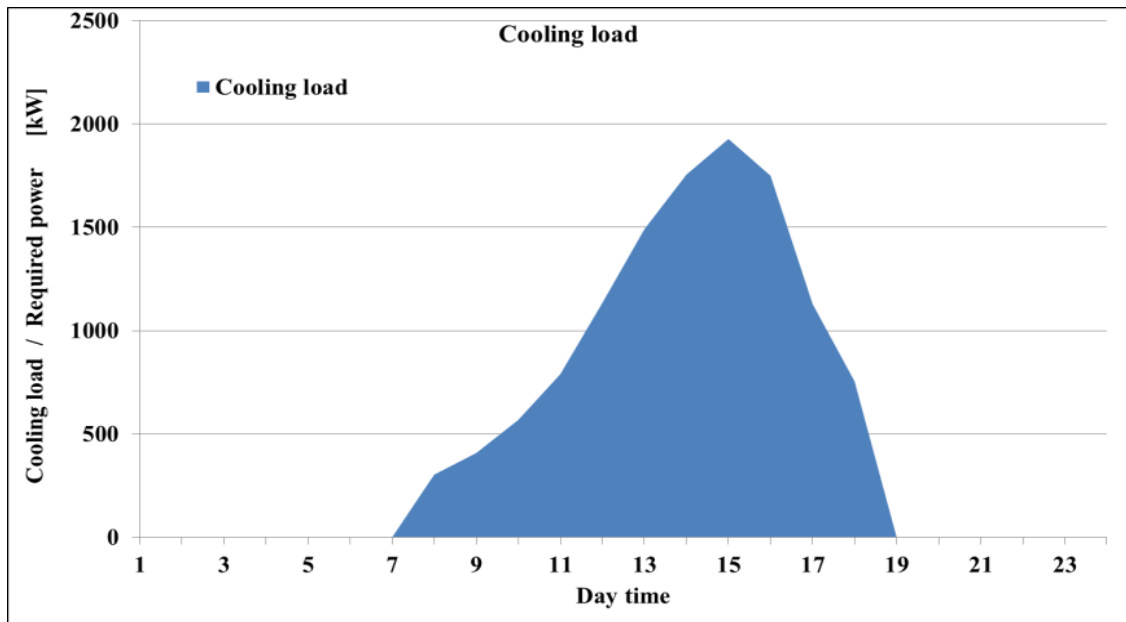
Figure 3-46: Cooling load and the required power of the selected building [94]
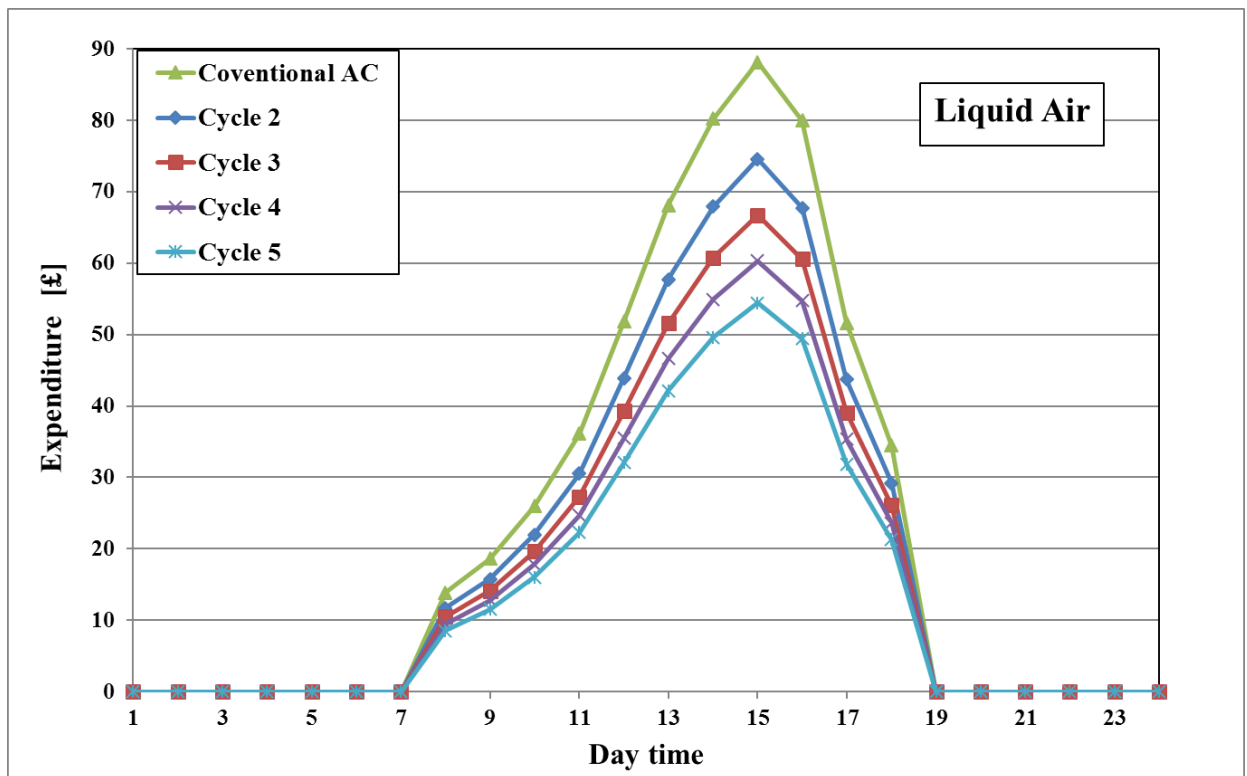
Figure 3-47: Daily energy cost for the proposed cycles and conventional AC system
(a) Liquid Air [89]
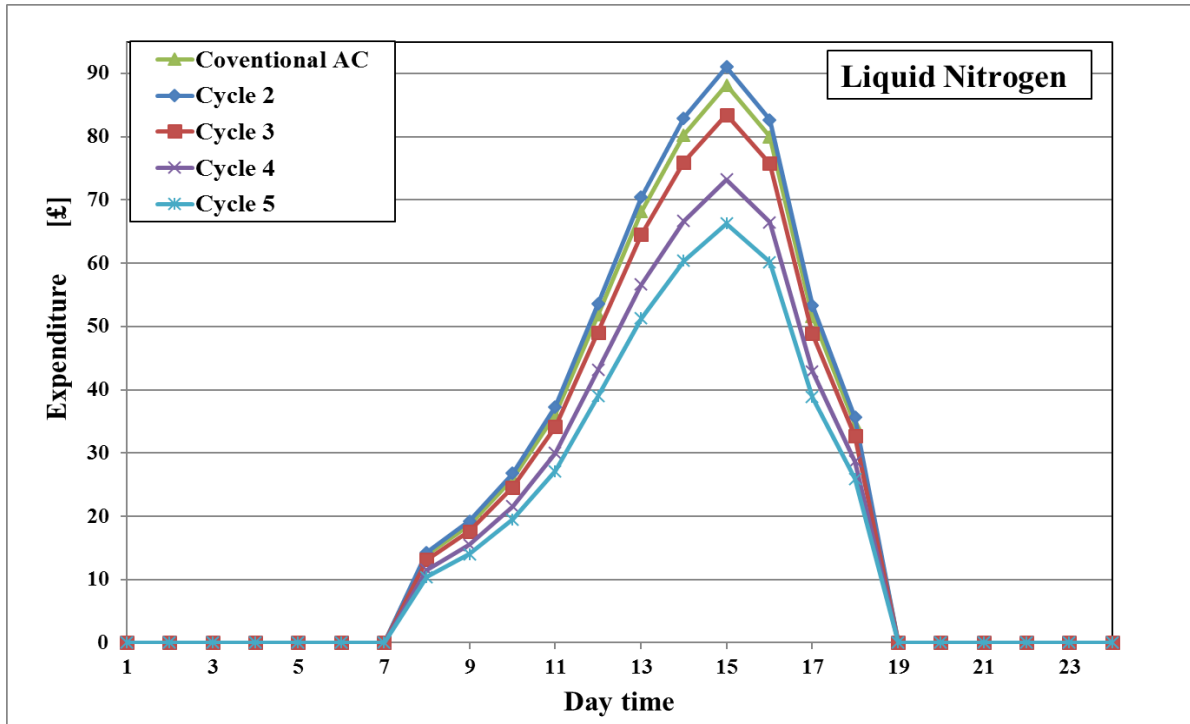
Figure 3-48: Daily energy cost for the proposed cycles and conventional AC system
(b) Liquid Nitrogen [89]
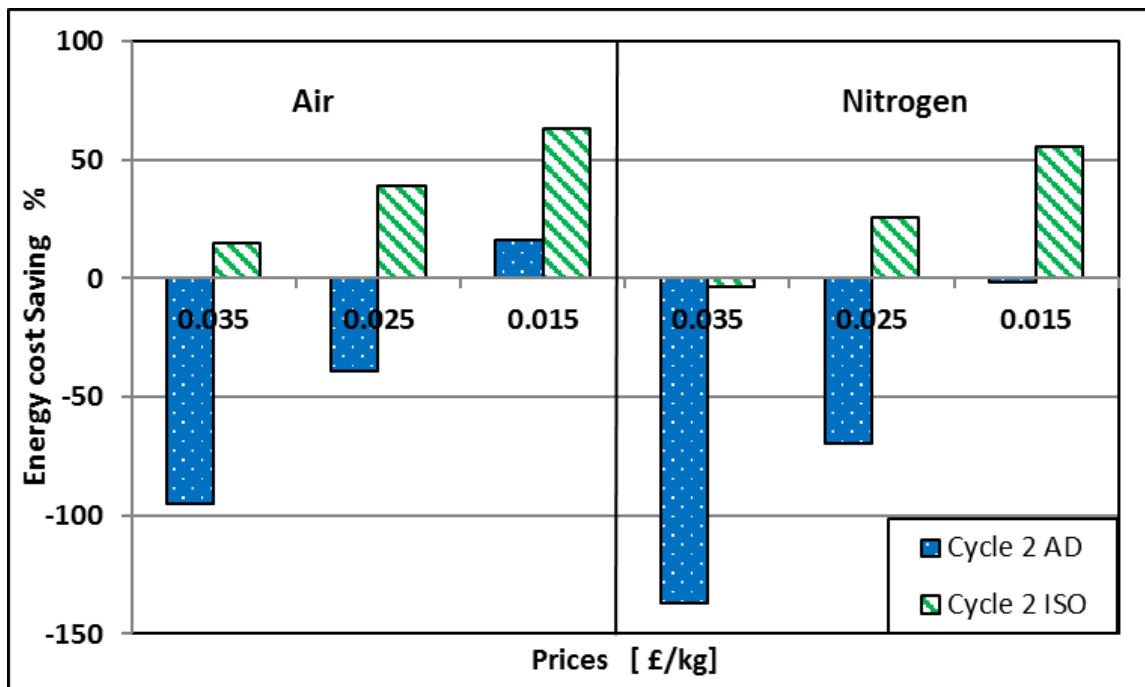
Figure 3-49: Saving of each proposed cycle against the conventional AC system [89]
(a) Cycle 2
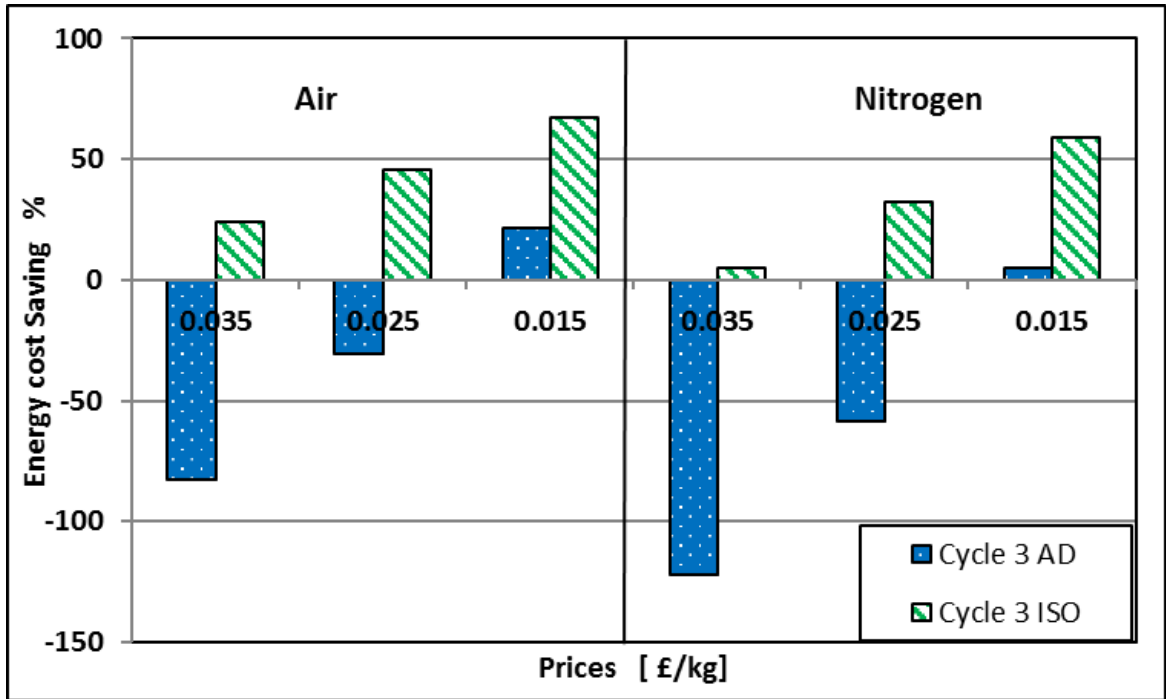
Figure 3-50: Saving of each proposed cycle against the conventional AC system [89]
(b) Cycle 3
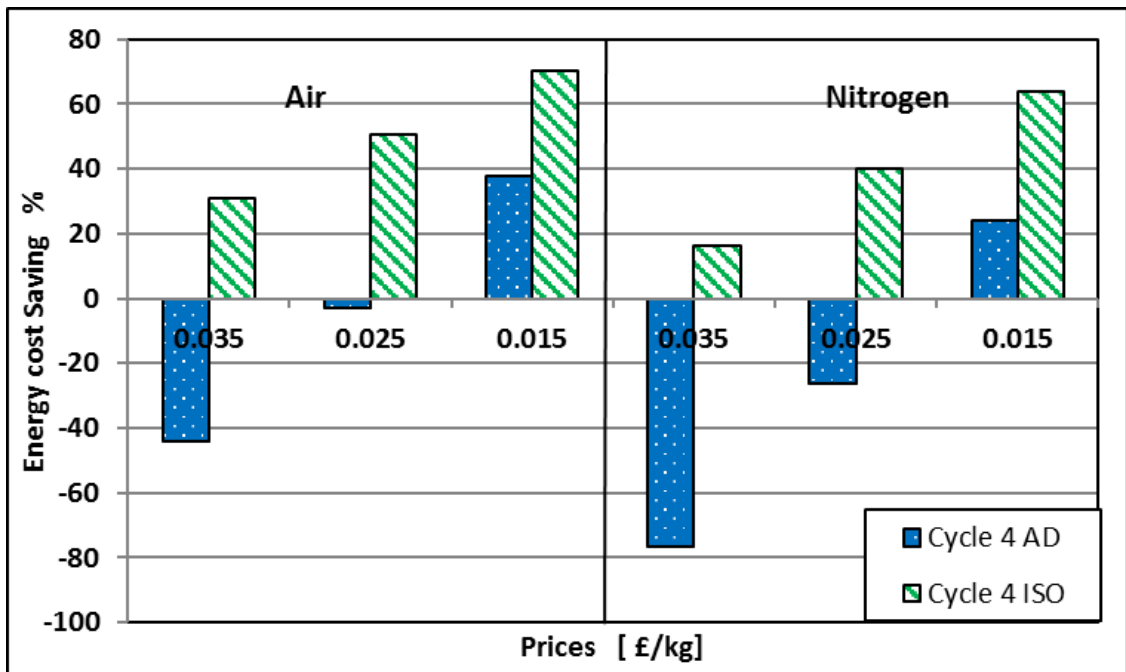
Figure 3-51: Saving of each proposed cycle against the conventional AC system [89]
(c) Cycle 4
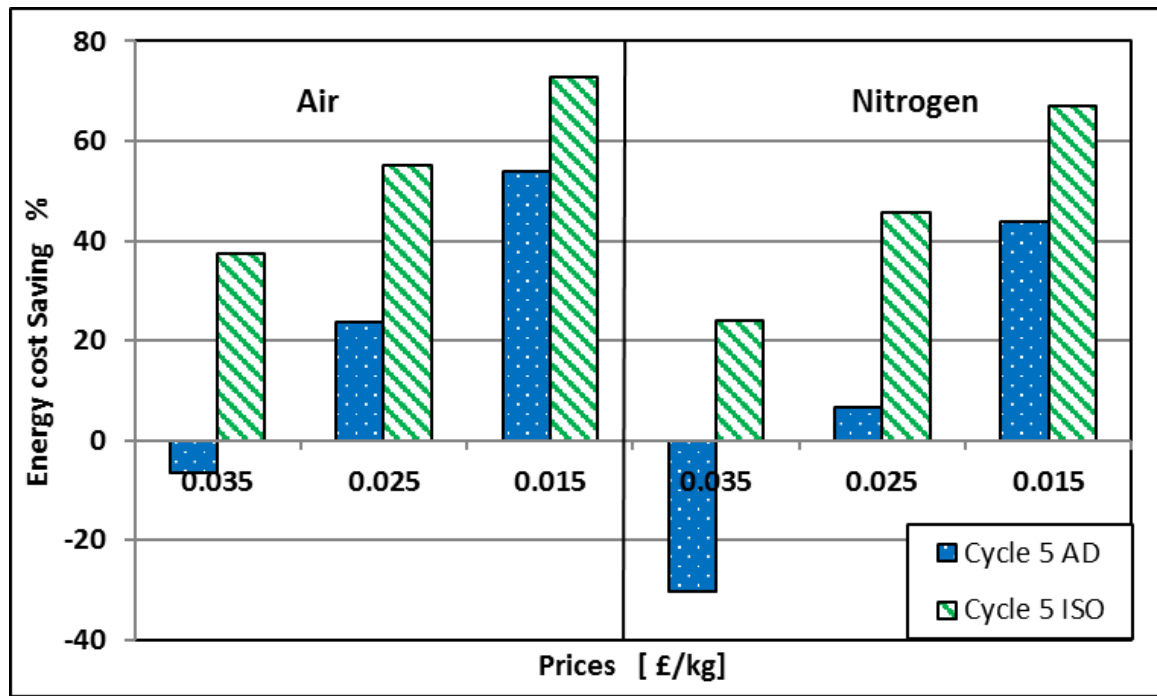
Figure 3-52: Saving of each proposed cycle against the conventional AC system [89]
(d) Cycle 5

3.4 Summary

The conventional A/C systems consume significant amount of energy particularly during the peak times where most of electricity providers are facing difficulties to meet the user's demands. Consequently there is a need to modify the conventional A/C systems or to develop new technology that leads to energy saving, reduce the peak demands and reduce the CO_2 emissions. Cold energy storage offers advantages by shifting the peak cooling demands to off peak times. In this chapter two kinds of cold storage technologies were investigated to evaluate their feasibility and their energy saving compared with the traditional systems.

The first technology investigated the effect of integrating the current A/C systems with storage system on the system performance, size and cost. Different storage mediums such as ice and other PCMs were used. A mathematical model was developed using MATLAB and REFPROP software. A cooling load of typical dwelling in Libya was used as case study. The results showed that, due to the need of lowering the evaporator temperature below zero degree

(-6 to -3) when the ice is used as storage medium, the chiller capacity reduced by 30-40 % which leads to more power consumption of the cooling system. However, when other PCMs that have higher phase change temperature (4-7 °C) such as Hydrate (HC-290) that has phase change temperature of 5.6 °C was used, the system showed an energy saving of up to 26% compared with conventional A/C system depending on the operating strategy.

The second technology is a new air conditioning system that utilises the most attractive energy storage medium in the form of Liquid Air/Nitrogen. The proposed technology was not only shifting the cooling load but also generating power during peak times. Five different cryogenic cooling and power cycles were investigated to determine their feasibilities to meet the cooling demands of domestic and commercial buildings and evaluate their energy saving compared with the conventional system. A comparison between the two cryogenic fluids (LN2 and LAir) was also made and the results showed that:

- The fifth cycle, which is the most complex one, showed the highest system performance, and it recovered up to 94% of the energy stored in LAir and up to 78% of the energy stored in LN2. Also it showed cost saving of the energy consumption of up to 73% when LAir is used and 67% when LN2 is used. However, the decisions about the selection of the most economical solution must take into consideration the complete design of the system including equipment sizing and investment costs.

- LN2 system showed slightly higher (less than 4%) specific power and specific cooling capacity than Lair and this due to its lower evaporating temperature, however, LAir showed 21-25% higher Recovery Efficiency and COP than LN2 due to its lower energy consumption during production.

- Compared to the conventional system the result of the cost saving depends on the LN2/LAir prices. At the current price of 3.5 pence per kg the 1st, 2nd, 3rd and 4th cycles

showed cost saving up to 15%, 24%, 31% and 37.5%, respectively, when LAir is used, and -3%, 5%, 16% and 24%, consecutively, when LN2 is used.

- The energy saving from LN2/LAir systems at the current prices (which can reach up to 37%) is higher than that of PCMs integrating system where it reached maximum 26%.

- Extensive use of this technology can lead to further reduction in the LAir and LN2 prices, and results showed that, at price level of 1.5 pence per kg-LAir/kg-LN2 the 1st, 2nd, 3rd and 4th cycles saved up to 63%, 67%, 70% and 72%, respectively when LAir is used, and 55%, 59%, 63% and 67%, consecutively when LN2 is used. Therefore using even the simplest cycle can result in significant cost saving.

- This technology showed promising results from the thermodynamic point view however to achieve these results an efficient cryogenic heat exchanger and efficient expander, which are the two main components in all proposed systems, need to be developed. Therefore CFD modelling of these two components were carried out and presented in the following chapter.

CHAPTER FOUR

CFD MODELLING

4.1 Introduction

Thermodynamic analysis have been carried out by many researchers showing the potential of using cryogenic energy storage to provide cooling and power for both domestic and commercial buildings [3, 85, 88-92]. Also prototypes of LN2 engine were developed and fitted in a food transport truck to provide the required cooling [82, 85, 91, 114].

The Key components in all reported systems for recovering the stored energy are cryogenic heat exchangers, which are used to evaporate the LN2/LAir to provide cooling, and the expanders, which are used to generate power. Therefore, this chapter presents CFD modeling of these two components using ANSYS FLUENT V18.2 software [115]. Literature review of LN2/LAir boiling heat transfer process showed that most of the published works focus on either mathematical modelling [42, 46, 47, 49, 50] or experimental testing [48, 51-55] and that there is limited research on CFD modelling of such phase change heat transfer process [41, 43]. Therefore, in this study an advanced computational fluid dynamic (CFD) model for the flow boiling of LN2/LAir was developed and validated using published experimental data [55]. The developed CFD model was used to investigate different heat exchanger configurations. A CFD model was also developed for a reciprocating LN2 engine and used to investigate the effect of inlet pressure and rotational speed.

4.2 CFD modelling of cryogenic heat exchanger

The investigated heat exchangers are used to evaporate LN2/LAir to cool a secondary coolant. So there will be evaporating and superheating processes of LN2/LAir on one side of the heat

exchange, and cooling with possibility of freezing of the secondary coolant on the other side. Modelling this complex heat transfer processes were challenging. Modelling the evaporation process of LN2/LAir is considered as the most difficult part in this flow system where is there very limited literature regarding simulation of such process. A specific case was built for modelling the evaporation of LN2 and validated using data from published work. Thus a detailed study was carried out regarding the simulation of boiling/evaporation process and CFD model was developed

4.2.1 Modelling and validation of evaporation process of LN2

Many researchers have studied two phase flow (evaporating/boiling process) of cryogenic fluids either experimentally or by developing mathematical models [41-55]. It is reported that; depending on the wall temperature, the boiling process can be divided into three types, nucleate boiling (when the temperature difference between the wall and the saturation temperature ranges from 5 to 30 degrees), transient boiling (when the temperature difference between the wall and the saturation temperature varies from 30 to 120 degrees) and film boiling (when the temperature difference between the wall and the saturation temperature ranges from 120 to 1000 degrees), as shown in Figure **4-1**.
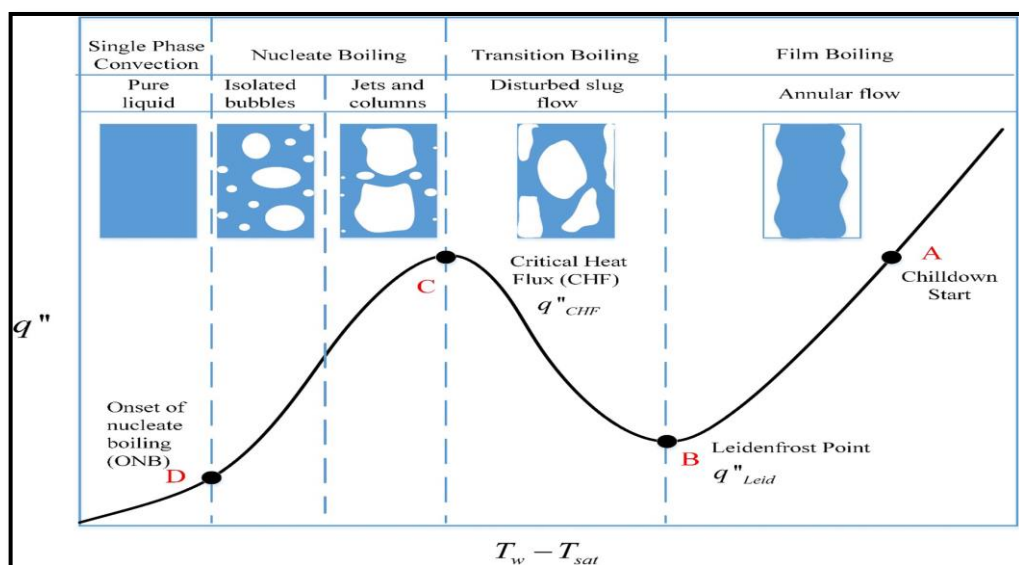
Figure 4-1: Flow boiling curve [55]

4.2.1.1 **Geometry**

The geometry used in the modeling was built based on an experimental work of studying the chilldown of LN2 transport pipes. In the chilldown process all the above mentioned boiling types occur. The tube initial temperature is room temperature so film boiling is expected then transient boiling when the tube temperature decreases and finally nucleate boiling and convective heat transfer when the wall temperature becomes close to the LN2 saturated temperature. A test rig to study this phenomena was built by Hartwig et al. [53], and vacuum chamber was used to insulate the test section thus reducing heat gain from the surroundings. The test section was 8 mm ID, 1 mm thick and 254 mm length of a Pyrex glass tube. 15 thermocouples were fitted on the tube surface as shown in Figure 4-2. Based on these information a 3D geometry was built in ANSYS workbench, however instead of monitoring only three points at each location (50, 70, 90, 110, and 130 mm from the inlet), the whole surface on these location was monitored as shown in Figure 4-3. To reduce the computational time only quarter of the test section was modelled as shown in Figure 4-3 and this will not significantly affect the results due to the small pipe diameter and the gravity effect can be negligible [85].
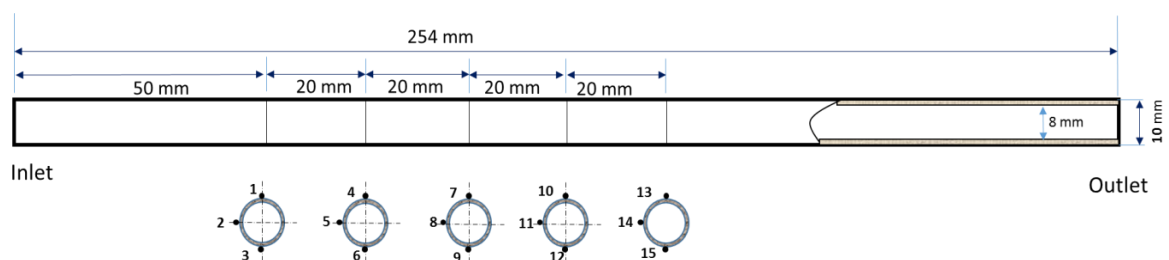
Figure 4-2: Thermocouples locations on the test section [55]
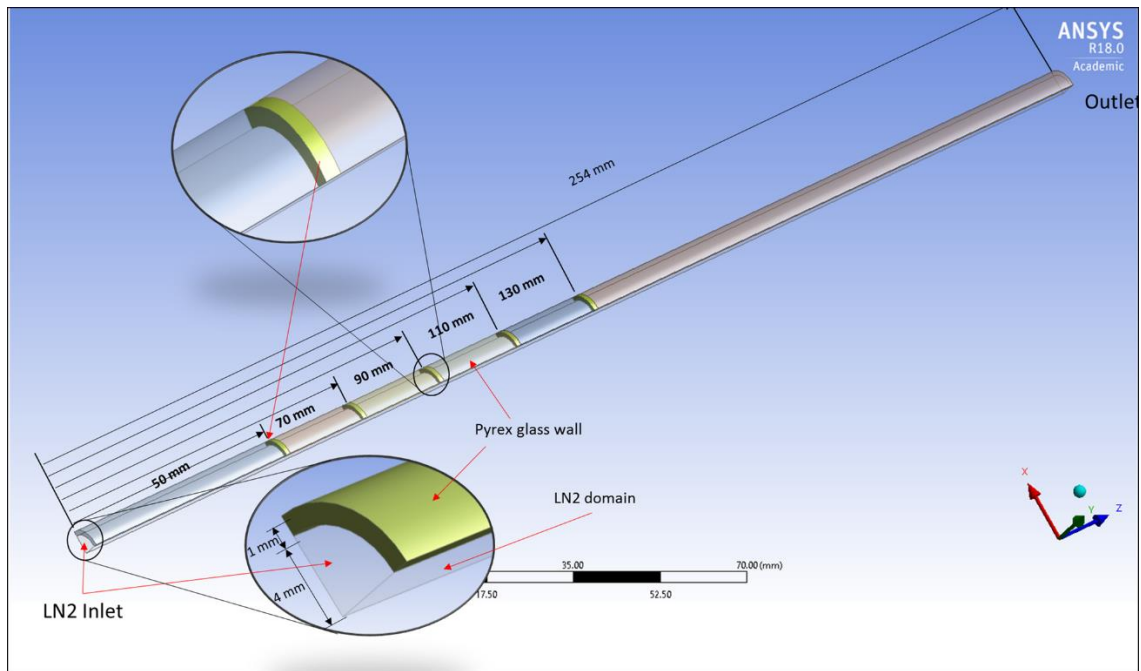
Figure 4-3: 3D tube geometry

4.2.1.2 **The model mesh**

Different mesh sizes as shown in Figure 4-4 were investigated to achieve accurate results. Quadratic and tetrahedron mesh type were selected based on the mesh guide recommendations for the wall and the fluid domain respectively. Tetrahedron mesh is the more suitable mesh type for domains with curvatures and it is leading to high mesh quality, less convergence issues and less computational time. Inflation with five layers was applied on the interface between the solid and the fluid domain to take into consideration the effect of the fluid boundary layer. The first mesh size (A) in Figure 4-4 was a fine mesh where the number of elements reached 20150 while mesh sizing control was used to reduce the element size in the other two mesh sizes (B and C) where the number of elements reached 50353 and 210460, respectively. In all cases the mesh quality was good where the average aspect ratio of the three cases A, B and C shown in Figure 4-4 were 3.5, 2.59 and 2.07 respectively, Also the average orthogonal quality of these mesh cases A, B and C were 0.82, 0.85 and 0.855, respectively.
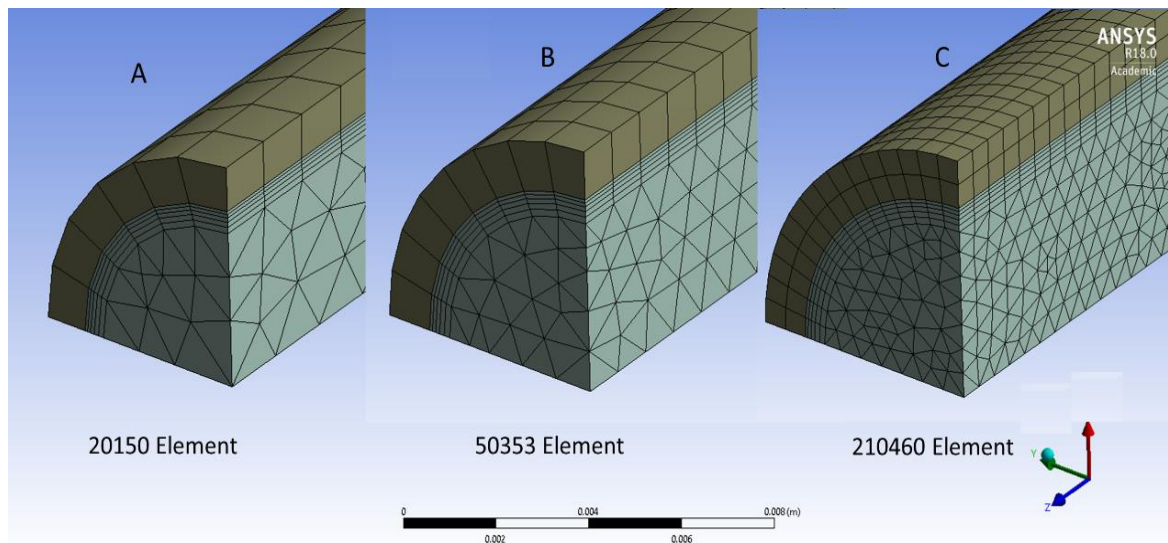
Figure 4-4: Different mesh sizes

4.2.1.3 The model setup

In the model setup window a pressure-based, time dependent (transient) and absolute velocity formulation were enabled in the solver panel for this case. As mentioned above, the wall temperature in the chilldown process varies with time so a transient solver has to be used in this case. In the boiling/evaporating process, the liquid phase change to vapour or gas phase, therefore one of the multiphase models option needs to be enabled depending on the case and the accuracy order and brief description about these models presents in the following section.

4.2.1.3.1 Ansys multiphase models

For simulating evaporating process Ansys have three different options namely; VOF model, Mixture model and Eulerian model. Each option can model the evaporation process with various results accuracy.

Eulerian model is the more complex one and it takes into the consideration the effect of most of the boiling process parameters such as lift force, drag coefficient, wall lubrication, bubble departure, heat transfer mechanism during nucleate, transient and film boiling and mass

transfer [116]. VOF model is the least complex model, accuracy and computational time [116]. This model has not been used in this research. Mixture model is less complexity compared with the Eulerian model and in most of the physical application shows acceptable results compared with experimental. The other advantage of this model is the ability to have more than one domain in the model without facing strong difficulties to run the model [116]. However, to achieve very close to experimental results, evaporation and condensation frequency needs to be turned which means repeating the solution many time.

4.2.1.3.1.1   Eulerian multiphase model

This model has the ability to include the effect of bubble departure, lift force, drag coefficient, wall lubrication, and heat transfer mechanism during nucleate, transient and film boiling and phases mass transfer. For sub-cooling and nucleate boiling non-equilibrium boiling model was used and for transient and film boiling critical heat flux was used. The energy and turbulent models were also enabled. A brief description of Eulerian multiphase model and its governing equations is presented in this section.

Eulerian multiphase model is one of the Ansys fluent multiphase models that has ability to model a multiphase flow consisting of gases, liquids or particles (solids) or a mixture of any of these phases. The secondary phase can be any number and there is no limitation. It depends on the computer capacity and convergence issues. The model solution depends on; (a) solving continuity and momentum equations for each phase; (b) all phases sharing the same pressure, (c) offering various drag coefficient equations and turbulence models suitable for various multiphase flow types.

The space occupied by each phase is called Volume fraction $\propto_q$ and the summation of the volume fraction of all phase should be equal 1 as shown in Equation **4.1** and for each phase individually the conservation of mass and momentum equations are valid. In the mixture the

volume and the effective density of phase q can be defined as V_q and $\acute{\rho}_q$ and they are

calculated using Equations 4.2 and 4.3 [117].

$$\sum_{q=1}^{n} \propto_q = 1 \qquad\qquad 4.1$$

$$V_q = \int_V \propto_q dV \qquad\qquad 4.2$$

$$\acute{\rho}_q = \rho_q \propto_q \qquad\qquad 4.3$$

For each phase the model solves the conservation equations of energy, mass and momentum

using the following equations:

For a phase q the continuity equation is

$$\frac{\partial}{\partial t}\left(\propto_q \rho_q\right) + \nabla.\left(\propto_q \rho_q \overrightarrow{v_q}\right) = \sum_{p=1}^{n}\left(\dot{m}_{pq} - \dot{m}_{qp}\right) - S_q \qquad\qquad 4.4$$

Where $\overrightarrow{v_q}$, $\dot{m}_{pq}$ and $\dot{m}_{qp}$ are the phase q velocity, the mass transfer from phase p to phase q

and the mass transfer from phase q to phase p, respectively.

For a phase q the momentum equation can be written as:

$$\frac{\partial}{\partial t}\left(\propto_q \rho_q \overrightarrow{v_q}\right) + \nabla.\left(\propto_q \rho_q \overrightarrow{v_q}\,\overrightarrow{v_q}\right) = -\propto_q \nabla_p + \nabla.\overline{\overline{\tau_q}} +\propto_q \rho_q \vec{g} + \sum_{p=1}^{n}\left(\overrightarrow{R_{pq}} + \dot{m}_{pq}\overrightarrow{v_{pq}} - \right.$$
$$\left. \dot{m}_{qp}\overrightarrow{v_{qp}}\right) + \left(\vec{F}_q + \vec{F}_{lift,q} + \vec{F}_{wl,q} + \vec{F}_{vm,q} + \vec{F}_{td,q}\right) \qquad\qquad 4.5$$

Where $\vec{F}_q$, $\vec{F}_{lift,q}, \vec{F}_{wl,q}, \vec{F}_{vm,q}$ and $\vec{F}_{td,q}$ are the phase external body force, lift force, wall

lubrication force, virtual mass force and turbulent dispersion force. $\overrightarrow{R_{pq}}$ is the interaction force

between phases p and q. $\overrightarrow{v_{pq}}$ and $\overrightarrow{v_{qp}}$ are interphase velocities [117].

For a phase q the energy equation can be written as:

$$\frac{\partial}{\partial t}\left(\alpha_q\rho_q h_q\right) + \nabla.\left(h_q\alpha_q\rho_q\overrightarrow{u_q}\right) = \alpha_q\frac{dp_q}{dt} + \overline{\overline{\tau_q}}:\nabla\overrightarrow{u_q} - \nabla.\overrightarrow{q_q} + S_q + \sum_{p=1}^{n}\left(Q_{pq} + \right.$$
$$\left. \dot{m}_{pq}h_{pq} - \dot{m}_{qp}h_{qp}\right) \qquad\qquad 4.6$$

Where h_q and h_{qp} are the specific enthalpy of phase q and the interphase enthalpy. $\overrightarrow{q_q}$ and Q_{pq} are the heat flux and intensity of heat exchange between the phases q and p. S_q is the source term [117].

The phase volume fraction $\propto_q$ can be fraction calculated using the continuity equation as :

$$\frac{1}{\rho_{rq}}\left(\frac{\partial}{\partial t}\left(\propto_q \rho_q\right) + \nabla.\left(\propto_q \rho_q \overrightarrow{v_q}\right) = \sum_{p=1}^{n}\left(\dot{m}_{pq} - \dot{m}_{qp}\right)\right) \qquad 4.7$$

Where ρ_{rq} is the reference density of phase q.

The interfacial area between two phases per the unit volume of the mixture is known as Interfacial area concentration (A_i). This is an important parameter which is used for calculating the mass, momentum and energy transfers between the two phases through the interface. There are several ways to calculate A_i depending on the flow type. For different type of boiling, Ishii correlation is used and recommended by Ansys [116] [88].

$$A_i = \frac{6(1-\propto_p)\min(\propto_p,\propto_{p,crit})}{d_p(1-\min(\propto_p,\propto_{p,crit}))} \qquad 4.8$$

Where $\propto_{p,crit}$ is equal 0.25

The model takes into account the impact of the lift force on the secondary phase bubbles and this effect will be more significant when large number of small size bubbles are generated [118].

$$\vec{F}_{lift} = -C_l\rho_q \propto_p (\overrightarrow{v_q} - \overrightarrow{v_p}) \times \nabla \times \overrightarrow{v_q} \qquad 4.9$$

Where C_l is Lift Coefficient, ρ_q is the density of primary phase, $\propto_p$ the volume fraction of the secondary phase and $\overrightarrow{v_q}$ and $\overrightarrow{v_p}$ are the primary and the secondary phases phase.

To determine the Lift Coefficient, different models are available in the Ansys fluent including Moraga, Saffman-Mei, Legendre-Magnaudet and Tomiyama. Howver, Tomiyama Lift Force Model (equations **4.10** to **4.14**) is recommended for modelling boiling processes and it is appropriate for larger-scale deformable bubbles [117, 119].

$$C_l = \begin{cases} min[0.288\, tanh(0.121Re_p), f(Eo)] & Eo \geq 4 \\ f(Eo) & 4 < Eo \leq 10 \\ -0.27 & 10 < Eo \end{cases}$$ 4.10

$$f(E\sigma) = 0.00105E\sigma^3 - 0.0159E\sigma^2 - 0.0204E\sigma^1 + 0.474$$ 4.11

$$Eo = \frac{g(\rho_q - \rho_p)d_h^2}{\sigma}$$ 4.12

$$d_h = d_b(1 + 0.163Eo^{0.757})^{1/3}$$ 4.13

$$Eó = \frac{g(\rho_q - \rho_p)d_b^2}{\sigma}$$ 4.14

Where Eo is a modified Eotvos number based on the long axis of the deformable bubble d_h, and g, σ and d_b are the gravity, surface tension and bubble diameter.

In the Eulerian multiphase model the effect of the Wall Lubrication Force on secondary phase bubbles also can be included. This force pushes the secondary phase away from the wall [117].

$$\vec{F}_{wl} = C_{wl}\rho_q \propto_p \left|(\vec{v_q} - \vec{v_p})\right|^2 \vec{n}_w$$ 4.15

Where C_{wl} is wall lubrication coefficient, $\left|\vec{v_q} - \vec{v_p}\right|$ is relative velocity component tangential to the wall surface. $\vec{n}_w$ is the unit normal pointing away from the wall.

$$C_{wl} = max\left(0, \frac{C_{w1}}{d_b} + \frac{C_{w2}}{y_w}\right)$$ 4.16

Where $C_{w1} = -0.01$, $C_{w2} = 0.05$ are non-dimensional coefficients and y_w is the distance to the nearest wall.

The energy transfer rate between the two phases is a function of the interface area and temperature difference between them.

$$Q_{pq} = h_{pq}A_i(T_p - T_q)$$ 4.17

where h_{pq} is the multiphase heat transfer coefficient and it can be found using Nusselt number as:

$$h_{pq} = \frac{K_q Nu_p}{d_p}$$
4.18

Where K_q, Nu_p and d_p are the thermal conductivity, Nusselt number and bubble diameter.

Ansys Eularian model uses various approaches to calculate the multiphase heat transfer and for the boiling process Ranz-Marshall method is recommended [117].

$$Nu_p = 2.0 + 0.15Re_p^{0.8}Pr^{0.5}$$
4.19

Where Re_p and Pr are Reynolds and Prandtl numbers respectively.

Regarding modelling turbulence of multiphase flow, Ansys fluent has three different options in the $k - \varepsilon$ and $k - \omega$ methods namely: (a) mixture turbulence model, (b) dispersed turbulence model and (c) turbulence model for each phase. The last option is the default option for the $k - \varepsilon$ which was used in this work.

$$\frac{\partial}{\partial t}(\rho_m k) + \nabla.(\rho_m \overrightarrow{v_m} k) = \nabla.\left(\left(\mu_m + \frac{\mu_{t,m}}{\sigma_k}\right)\nabla k\right) + G_{1\varepsilon} - \rho_m \epsilon + \Pi_{k_m}$$
4.20

and

$$\frac{\partial}{\partial t}(\rho_m \varepsilon) + \nabla.(\rho_m \overrightarrow{v_m} \varepsilon) = \nabla.\left(\left(\mu_m + \frac{\mu_{t,m}}{\sigma_\varepsilon}\right)\nabla \varepsilon\right) + \frac{\varepsilon}{k}\left(C_{1\varepsilon}G_{k,m} - C_{2\varepsilon}\rho_m \varepsilon\right) + \Pi_{\varepsilon_m}$$
4.21

where ρ_m, μ_m and $\overrightarrow{v_m}$ are the mixture density, molecular viscosity and velocity respectively. $\mu_{t,m}$ and $G_{k,m}$ are the mixture turbulent viscosity and the turbulence kinetic energy respectively. They are calculated using the following equations. Π_{ε_m} and Π_{k_m} are the source terms [117].

$$\rho_m = \sum_{i=1}^{N} \propto_i \rho_i$$
4.22

$$\overrightarrow{v_m} = \frac{\sum_{i=1}^{N} \overrightarrow{v_i}\propto_i\rho_i}{\sum_{i=1}^{N}\propto_i\rho_i}$$
4.23

$$\mu_m = \sum_{i=1}^{N} \propto_i \mu_i \tag{4.24}$$

$$\mu_{t,m} = \rho_m C_\mu \frac{k^2}{\varepsilon} \tag{4.25}$$

$$G_{k,m} = \mu_{t,m}(\nabla \vec{v_m} + (\nabla \vec{v_m})^T) : \nabla \vec{v_m} \tag{4.26}$$

Where $\propto_i$, μ_i, ρ_i and $\vec{v_i}$ are the phase volume fraction, viscosity, density, and velocity, respectively.

For the different boiling types Ansys fluent has different models to simulate the wall boiling process; RPI (Rensselaer Polytechnic Institute) boiling model for modelling subcooled boiling, and Non-equilibrium boiling model for modelling nucleate boiling up to the critical heat flux and dry-out state, and Critical Heat Flux (CHF) model to model transient and the film boiling.

The total heat flux from the surface to liquid $\dot{q}_w$ in the RPI model is calculated using equation (**4.27**) while Equation (**4.28**) is used for the Non-equilibrium and Critical Heat Flux boiling models [117].

$$\dot{q}_w = \dot{q}_C + \dot{q}_Q + \dot{q}_E \tag{4.27}$$

$$\dot{q}_w = \left(\dot{q}_C + \dot{q}_Q + \dot{q}_E\right) f\left(\propto_l\right) + (1 - f(\propto_l))\dot{q}_V + \dot{q}_G \tag{4.28}$$

Where $\dot{q}_C, \dot{q}_Q, \dot{q}_V, \dot{q}_E$ and $\dot{q}_G$ are the convective heat flux, quenching heat flux, convective heat flux of the vapour phase, evaporative heat flux and heat flux to any other gas phases in the domain, respectively, given as:

$$\dot{q}_C = h_C(T_W - T_l)(1 - A_b) \tag{4.29}$$

$$\dot{q}_Q = \frac{2k_l}{\sqrt{\pi T \lambda_l}}(T_W - T_l) \tag{4.30}$$

Where; h_C, T_W, A_b, k_l and T_l are the heat transfer coefficient wall temperature, area of influence, liquid thermal conductivity and liquid temperature.

$$q_E = V_d N_W \rho_v h_{fv} f \tag{4.31}$$

Where; V_d, N_W, ρ_v, h_{fv} and f are the bubble volume, nucleate site density, vapour density, latent heat of evaporation and bubble departure frequency.

$$\dot{q}_V = h_V(T_W - T_V) \tag{4.32}$$

Where h_V and T_V are vapour heat transfer coefficient and vapour temperature.

$$\dot{q}_G = h_G(T_W - T_G) \tag{4.33}$$

Where h_G and T_G are heat transfer coefficient and temperature of any other gases in the domain [117].

$f(\alpha_l)$ in Equation **4.28** depends on the local liquid volume fraction and for Non-equilibrium Subcooled Boiling model can be calculated using Equation **4.34** [117, 120]

$$f(\alpha_l) = \begin{cases} 1 - \frac{1}{2}e^{-20(\alpha_l - \alpha_{l,crit})} \\ \frac{1}{2}\left(\frac{\alpha_l}{\alpha_{l,crit}}\right)^{20\alpha_{l,crit}} \end{cases} \tag{4.34}$$

Where $\alpha_{l,crit} = 0.2$

While for the Critical Heat flux CHF model it is calculated using Equation **4.35** [117, 120]

$$f(\alpha_l) = \begin{cases} 1 - \frac{1}{2}exp\left[-20(\alpha_l - \alpha_{l,crit})\right] & \alpha_l \geq \alpha_{l,crit} \\ \frac{1}{2}\left(\frac{\alpha_l}{\alpha_{l,crit}}\right)^{20\alpha_{l,crit}} & \alpha_l < \alpha_{l,crit} \end{cases} \tag{4.35}$$

Where $\alpha_{l,crit} = 0.2$

For the vapour phase, equation (**4.36**) can be used recommended by Ansys [117] and Tentner et al. [121].

$$f(\alpha_v) = 1 - f(\alpha_l) = \begin{cases} 0 & \alpha_l \geq \alpha_{v,crit} \\ \frac{1}{2}\left[1 - \cos(\pi \frac{\alpha_v - \alpha_{v,1}}{\alpha_{v,2} - \alpha_{v,1}}\right] & \alpha_{v,1} \leq \alpha_v \leq \alpha_{v,2} \\ 1 & \alpha_v > \alpha_{v,2} \end{cases} \tag{4.36}$$

Where $\alpha_{v,crit}$ is equal to $1 - \alpha_{l,crit} = 0.8$

Regarding the Bubble Diameter, Fluent uses equation (**4.37**) to calculate the bubble diameter

as a function of local subcooled temperature [122].

$$D_w = \begin{cases} max\left[1 \times 10^{-5}, d_{min}exp\left(\frac{-K(\Delta T_{sub}-\Delta T_{max})}{d_{min}}\right)\right] & \Delta T_{sub} > 13.5\ K \\ d_{max} - K(\Delta T_{sub} - \Delta T_{min}) & \Delta T_{sub} \leq 13.5\ K \end{cases}$$

4.37

Where: $K = \frac{d_{max} - d_{min}}{\Delta T_{max} - \Delta T_{min}}$

$d_{min} = 0.00015$ m, $d_{max} = 0.001$ m, $\Delta T_{min} = 0$ K, $\Delta T_{max} = 13.5$ K

The evaporation mass transfer rate depends on the evaporative heat transfer (**4.31**) and the

evaporation energy (h_{fv}). It can be calculated using equation (**4.38**).

$$\dot{m}_E = \frac{\dot{q}_E}{h_{fv} + C_p \Delta T_{sub}}$$

4.38

Where C_p is the specific heat.

4.2.1.3.1.2 Mixture model

The mixture model can simulate evaporation processes by solving the energy, momentum and

continuity energy equations for the mixture. Also it solves the volume fraction equations for

the secondary phases, the relative velocities and uses Lee approach to calculate the mass

transfer during the evaporation and the condensation processes. The used governing equations

in this mode are briefly presented in this section.

Continuity equation in Mixture model is given as Equation **4.39**.

$$\frac{\partial}{\partial t}(\rho_m) + \nabla \cdot \left(\rho_m \overrightarrow{V_m}\right) = 0$$

4.39

Where: $\overrightarrow{V_m}$ and ρ_m are calculated using Equations (**4.40**) and (**4.41**).

$$\overrightarrow{V_m} = \frac{\sum_{k=1}^{n} \alpha_k \rho_k \overrightarrow{V_k}}{\rho_m}$$

4.40

$$\rho_m = \sum_{k=1}^{n} \alpha_k \rho_k$$

4.41

The Mixture model momentum equation can be obtained from the summation of the momentum equation of each phase individually as following [85]:

$$\frac{\partial}{\partial t}\left(\rho_m \overrightarrow{V_m}\right) + \nabla.\left(\rho_m \left(\overrightarrow{V_m}\right)^2\right) = -\nabla p + \nabla.\left[\mu_m \left(\nabla\overrightarrow{V_m} + \nabla\overrightarrow{V_m}^T\right)\right] + \rho_m \vec{g} + \vec{F} +$$

$$\nabla.\left[\sum_{k=1}^{n} \alpha_k \rho_k \left(\overrightarrow{V_{dr,k}}\right)^2\right]$$

4.42

Where:

$$\mu_m = \sum_{k=1}^{n} \alpha_k \mu_k$$

4.43

$$\overrightarrow{V_{dr,k}} = \overrightarrow{V_k} - \overrightarrow{V_m}$$

4.44

The model also solves the Energy equation as:

$$\frac{\partial}{\partial t}\sum_{k=1}^{n}(\alpha_k \rho_k E_k) + \nabla.\sum_{k=1}^{n}\left(\alpha_k \overrightarrow{V_k}(\rho_k E_k + p)\right) = \nabla.\left(k_{eff}\nabla T\right) + S_E$$

4.45

Where;

$$E_k = h_k - \frac{p}{\rho_k} + \frac{v_k^2}{2}$$

4.46

The Secondary Phases Volume Fraction Equation

$$\frac{\partial}{\partial t}(\alpha_p \rho_p) + \nabla.(\alpha_p \rho_p \overrightarrow{V_k}) = -\nabla.(\alpha_p \rho_p \overrightarrow{V_{dr,p}}) + \sum_{q=1}^{n}(\dot{m}_{qp} - \dot{m}_{pq})$$

4.47

The LN2 mass transfer equation in the Mixture Model takes into account the Evaporation and Condensation processes where Lee approach was used as given by the following equations;

$$\frac{\partial}{\partial t}(\alpha_p \rho_p) + \nabla.(\alpha_v \rho_v \overrightarrow{V_v}) = \dot{m}_{lv} - \dot{m}_{vl}$$

4.48

$$\dot{m}_{lv} = coeff * \alpha_l \rho_l \frac{(T_l - T_{sat})}{T_{sat}}$$

4.49

$$coeff = \frac{6}{d_b} \beta \sqrt{\frac{M}{2\pi R T_{sat}}} L \left(\frac{\alpha_v \rho_v}{\alpha_l - \rho_v}\right)$$

4.50

In the model LN2 was set as the primary phase while N2 gas was set as the secondary phase. The properties of the primary and secondary phases were varied depending on the temperature and the pressure based on data from ASHERA hand book (see Appendix A-C) [85, 123]. The energy and turbulent models were also enabled.

4.2.1.4 Boundary conditions

In the experimental work, the test section was fully insulated using a vacuum chamber, thus an adiabatic wall was applied on the tube outer surface and a mass flux with a value of 66 kg/s-m^2 was applied at the inlet to the pipe. LN2 enters the domain as saturated liquid at temperature of 77.34K. The flow direction was upward (A) and downward (B), and the tube was initially empty at the room temperature of 293K. The outlet boundary was set as pressure outlet at atmospheric pressure as shown in Figure **4-5**. To obtain accurate results and to avoid any convergence difficulties, small time steps is needed however decreasing the time step will increase the computational time. In this modelling the time step used was 1e-5 s which took 5-7 days depending on the number of elements using high performance computer with Intel (R) Core (TM) i7-4820K CPU @ 3.70 GHz 3.70 GHz processor and 48.0 GB Installed Memory (RAM).

Inlet   Adiabatic wall at initial temperature of 293 K   **Outlet**

$\dot{m} = 66 \frac{kg}{s \cdot m^2}$ Pressure Outlet

T=77.34 K   1 atm.
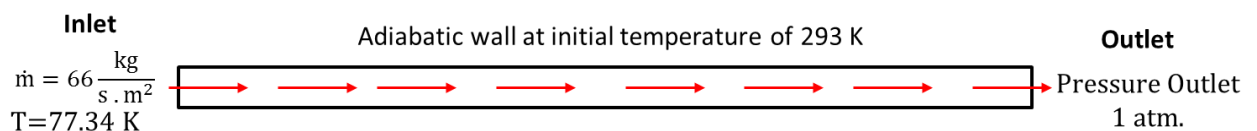
Figure 4-5: Boundary conditions

4.2.1.5 Model results

Figure **4-6** and Figure 4-7 present the variation of the tube surface temperature versus time for the experimental work [55] and the CFD modelling for the upward and downward flow respectively when the Eulerian model was used. The figures show a good agreement between the CFD model and the experimental work where the maximum deviation is less than 10 %. Figure **4-6** for the upward flow shows three regions; the first one is film boiling where the wall temperature is significantly higher than the LN2 boiling point. In the second region where the transient boiling occurs, the experimental work shows clearly that there is no significant reduction in the wall temperature due to the low heat flux in this region, however, this was not clear enough the CFD results due to its limitations. The last region is the nucleate boiling and it is clearly seen that the wall temperature decreased significantly due to the effect of the bubbles generation on heat transfer coefficient. Then subcooled boiling occurred when the surface temperature is close to the liquid saturation temperature. These regions although they exists, it hard to be seen in Figure 4-7 for the downward flow due to the fast reduction in the wall temperature.
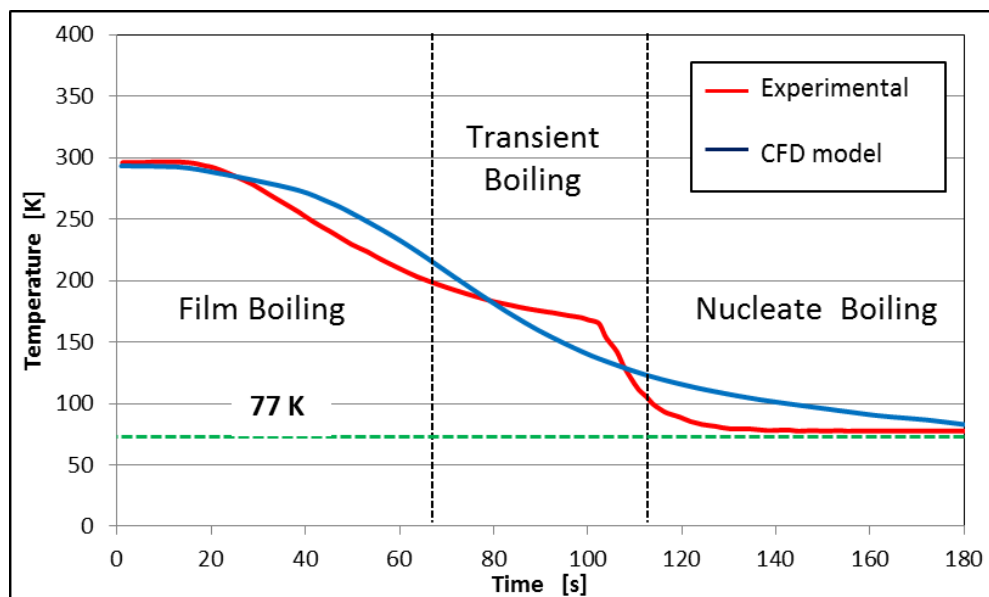
Figure 4-6: CFD results compares to experimental, upward flow
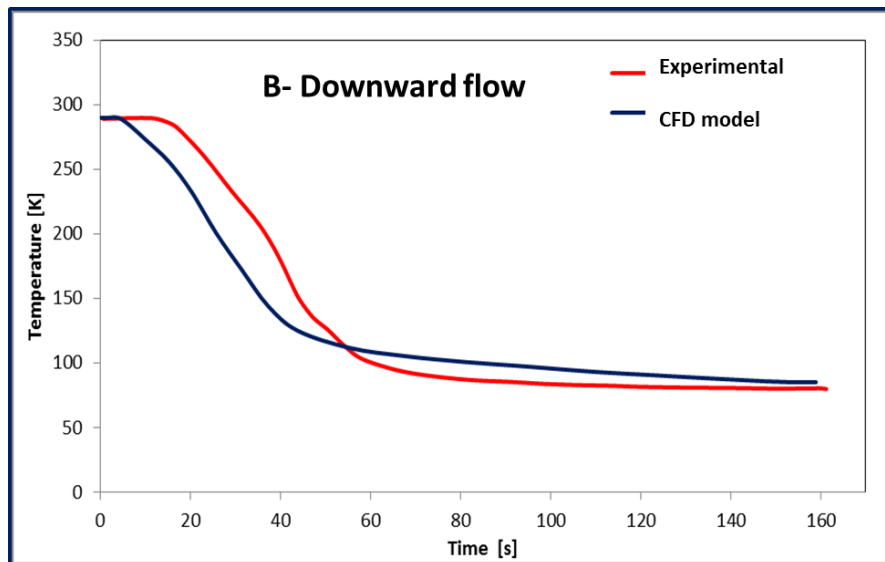
Figure 4-7: CFD results compared to experimental, downward flow

Figure **4-8** shows the predicted temperature when Mixture and Eulerian models are used compared with the experimental results where both models showing good agreement. In this results Mixture model shows good agreement with the experimental work in the first try, however, this is not always the case. In the model setup there is a factor calls evaporation and condensation frequency needs to be turned with experimental results to get it right and trial and error method is used to find the correct value. The default value of this factor in the software is 0.1 for the condensation and the evaporation however in the presented result they were 0.1 and 17.5 respectively.
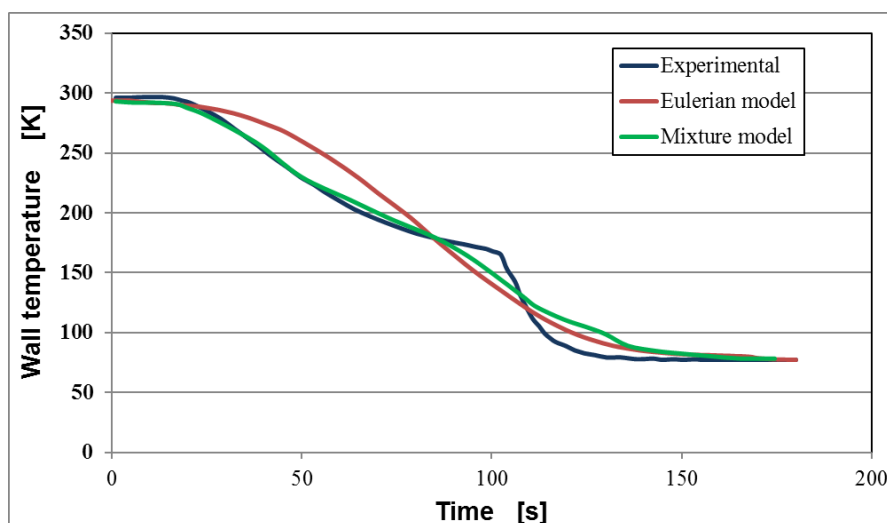
Figure 4-8: Mixture and Eulerian models versus the experimental

128

4.2.2 Different pipe configuration

In the proposed systems described in chapter three, the LN2/LAir are evaporated using a secondary coolant, where LN2/LAir flows inside the tube and the secondary coolant flows outside. In such arrangement, the heat transfer will vary along the tube depending on the nitrogen phase which will be high if N_2 phase is liquid and low if it is gas or vapour. So the heat transfer between the two fluids is dominated by the internal flow (LN2/LAir) phase. Therefore, the validated CFD technique was used to study the effect of internal fins on the heat transfer coefficient where four different cupper tubes (see Figure **4**-**9**) with different configurations were simulated.

Figure **4**-**9** (A) shows the first configuration which is smooth tube with 0.5 mm thickness. The second tube is a finned tube where the fins have a rectangular shape with 1 mm height as shown in Figure **4**-**9** (B). The third configuration also has rectangular shape fins but instead of straight fins along the pipe length, the rectangular fins were twisted as shown in Figure **4**-**9**(C). The last configuration has cylindrical shape fins with 1 mm thickness as shown in Figure **4**-**9** (D). All the tubes have an outer diameter of 8 mm, 0.5 wall thickness and 500 mm length. Only a quarter of the tube was modeled in all cases to reduce the computational time except the twisted fins configuration where modeling quarter or half of tube will change the geometry.
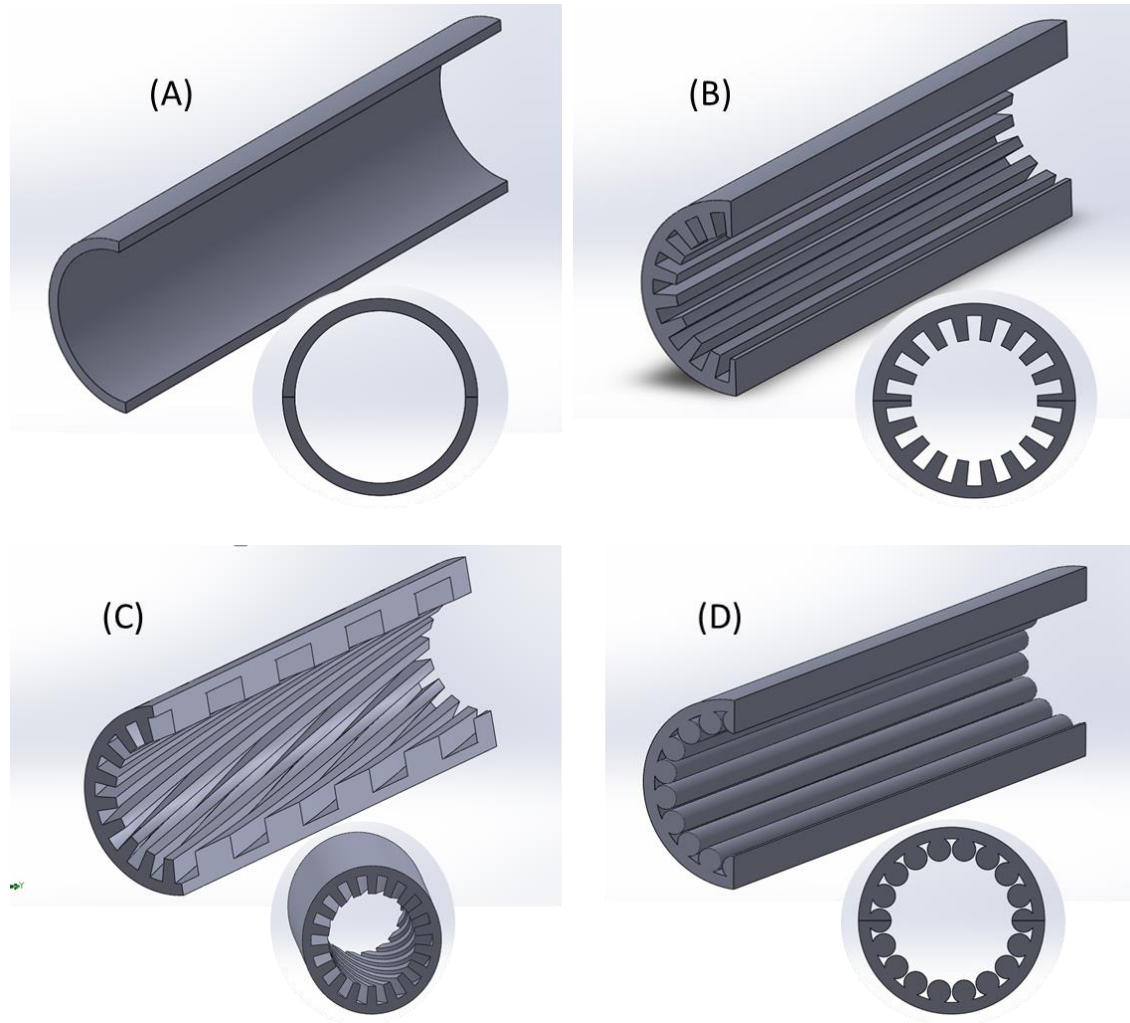
Figure 4-9: Different tube geometry

Quadratic and tetrahedron mesh type were used for the wall and the fluid domains. Inflation with five layers on the fluid domain near the wall was used to take into account the fluid boundary layer near the wall. The mesh and the number of elements are shown in Figure **4**-**10**. The smooth pipe has the lowest numbers of mesh elements of 33307 among the studied cases while cases B, C and D were having 491811, 435564 and 1195000 respectively. The mesh quality in all cases was good with average orthogonal quality ranging from 0.82 to 0.85.
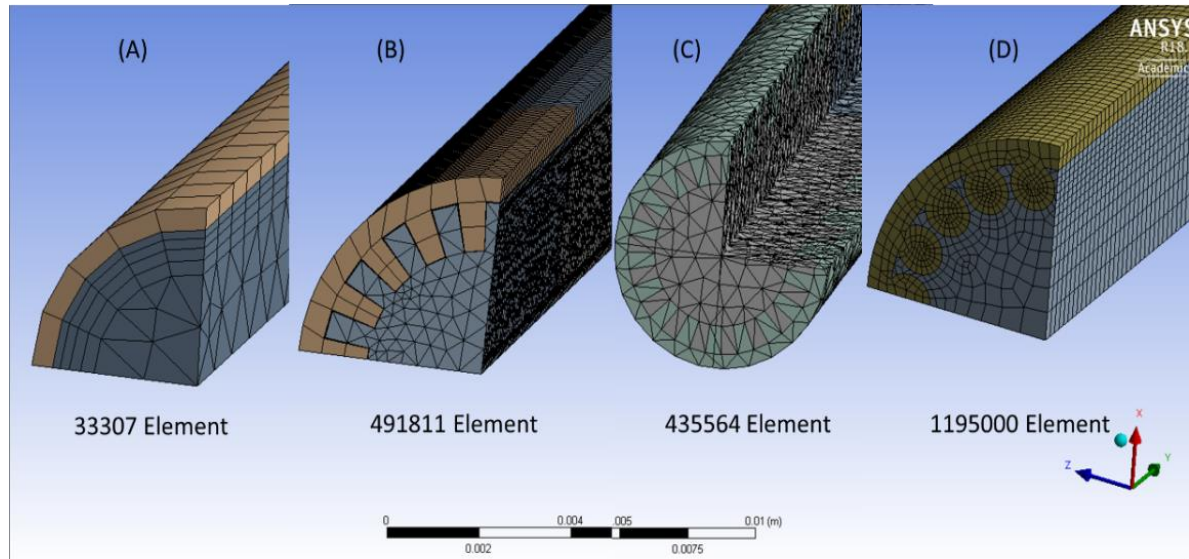
Figure 4-10: Mesh type and the number of elements of each case

The model setup was similar to the previous model where Eulerian multiphase model was used, and the same inlet and outlet boundaries were applied. The only change was on the outer tube surface where a convictive heat with value of 10 W/m^2 was applied instead of adiabatic wall in order to solve the case as steady state instead of transient state. This convective heat corresponding to natural convection was used to evaporate the LN2.

The four cases were simulated using the high performance PC described above where 4-7 days were required depending on the tube configuration. To evaluate the performance of the various configurations the result were compared in terms of heat transfer coefficient, heat flux on the outer wall and the pressure drop. Figure **4**-**11** shows the variation of heat transfer coefficient along the tube where it is clear that the highest values are at the tube inlet where most of the N2 phase is liquid and the effect of the bubbles flow enhanced the heat transfer. Once most of the liquid changes to gas phase, at about 10 cm from the inlet, the heat transfer remains constant through more than 80 % of the tube's length. Figure **4**-**11** the variation of the local heat transfer coefficient along the tube for each case where it is clear that the smooth tube has the lowest heat transfer due to its lowest contact area between the wall and the fluid

131

domain (the area of the inner tube which interface between the solid and the fluid domains) which reduces the cryogenic fluid evaporation rate. The tube with the cylindrical fins, it showed lower heat transfer enhancement compared to the rectangular finned tube where it reached 79% higher than the smooth tube. The rectangular fins enhanced the heat transfer coefficient inside the tube significantly where it reached 142% and 167% higher than the smooth tube for the straight and the twisted fens respectively. This enhancement leads to significant reduction in the tube materials and total heat exchanger size.
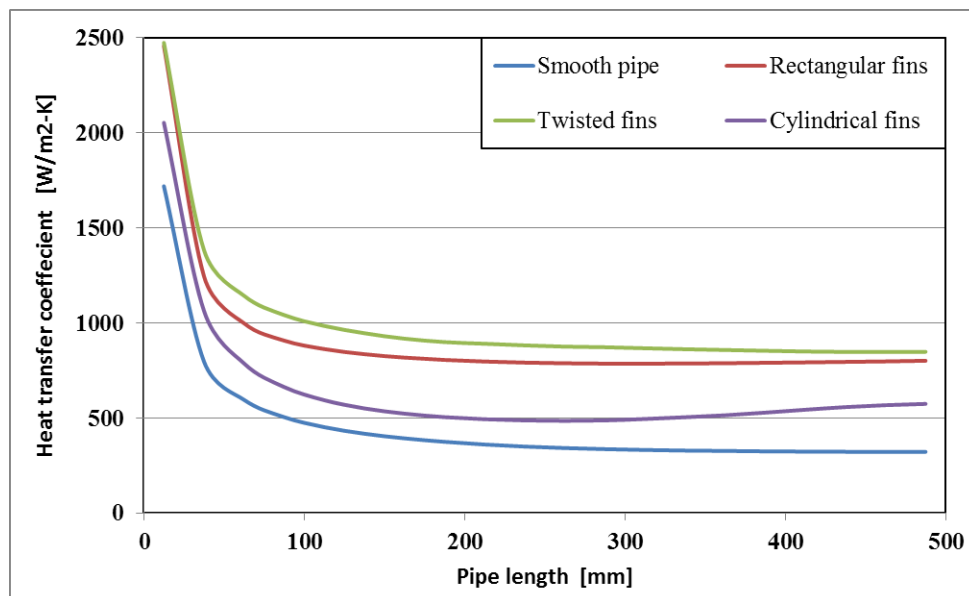
Figure 4-11: Variation of heat transfer coefficient along the tube of each case

A natural heat convection of air was applied on the tube outer surface with an ambient temperature of 293 K which means the wall is heated by air at room temperature. Due to the boiling process the wall temperature will drop down depending on the liquid boiling temperature and the heat transfer coefficient of the fluid inside the tube. The wall heat flux is also affected by heat transfer coefficient. Figure 4-12 and Figure 4-13 show the wall heat flux and temperature along the four pipes. It is clearly seen that, the wall heat flux follows the same trend as that of the heat transfer coefficient. The highest wall heat flux values is at the tube inlet where two phase flow is taken place and as the fluid goes further down and

becomes gas the heat flux is reducing due to low heat transfer in the gas region. The cylindrical finned tube has slightly different trend where the heat flux starts increasing in the second half and this probably due to the flow pattern in the gas region where the flow turbulence increases. In contrast the wall temperature along the four tubes increases while the heat transfer coefficient and heat flux decrease.
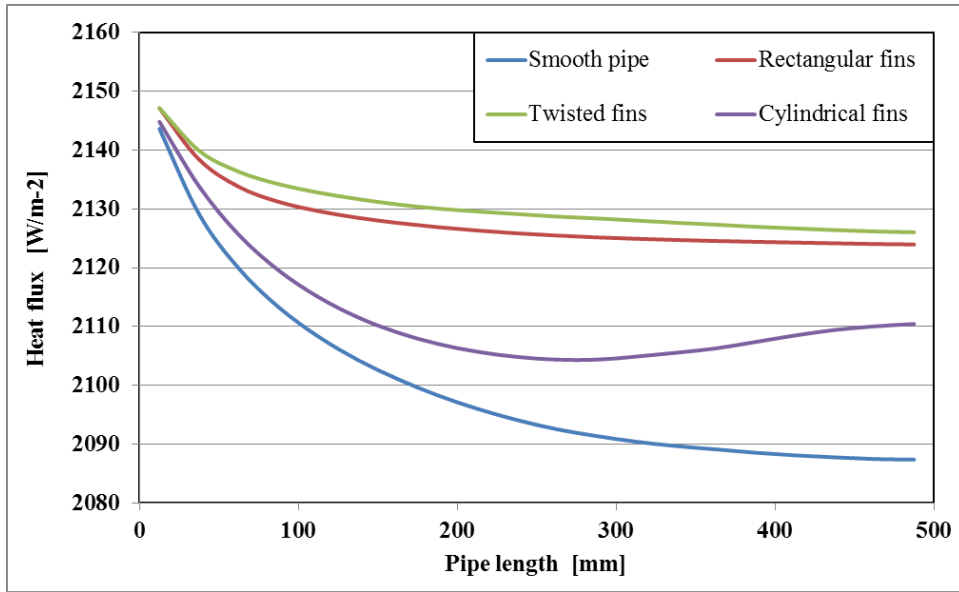
Figure 4-12: Heat flux along the tube wall
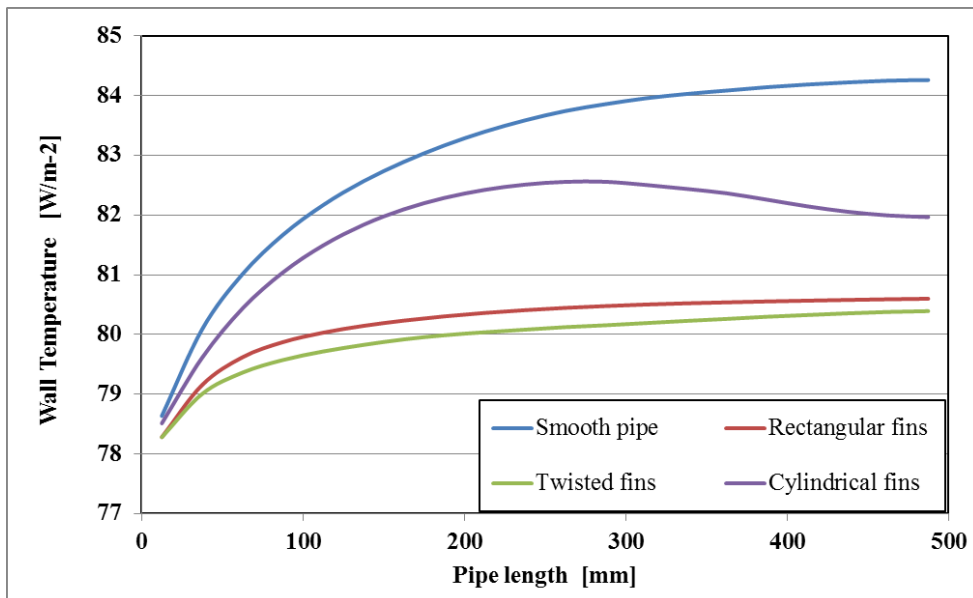
Figure 4-13: Temperature distributions along the tube wall

Figure 4-14, present the temperature and the volume fraction contours along the tubes with the rectangular fins, respectively. The figure represents the previous results presented in Figure 4-13 and shows the temperature and the liquid volume fraction gradient inside the tube. Where the maximum wall temperature reached 80.55 K.
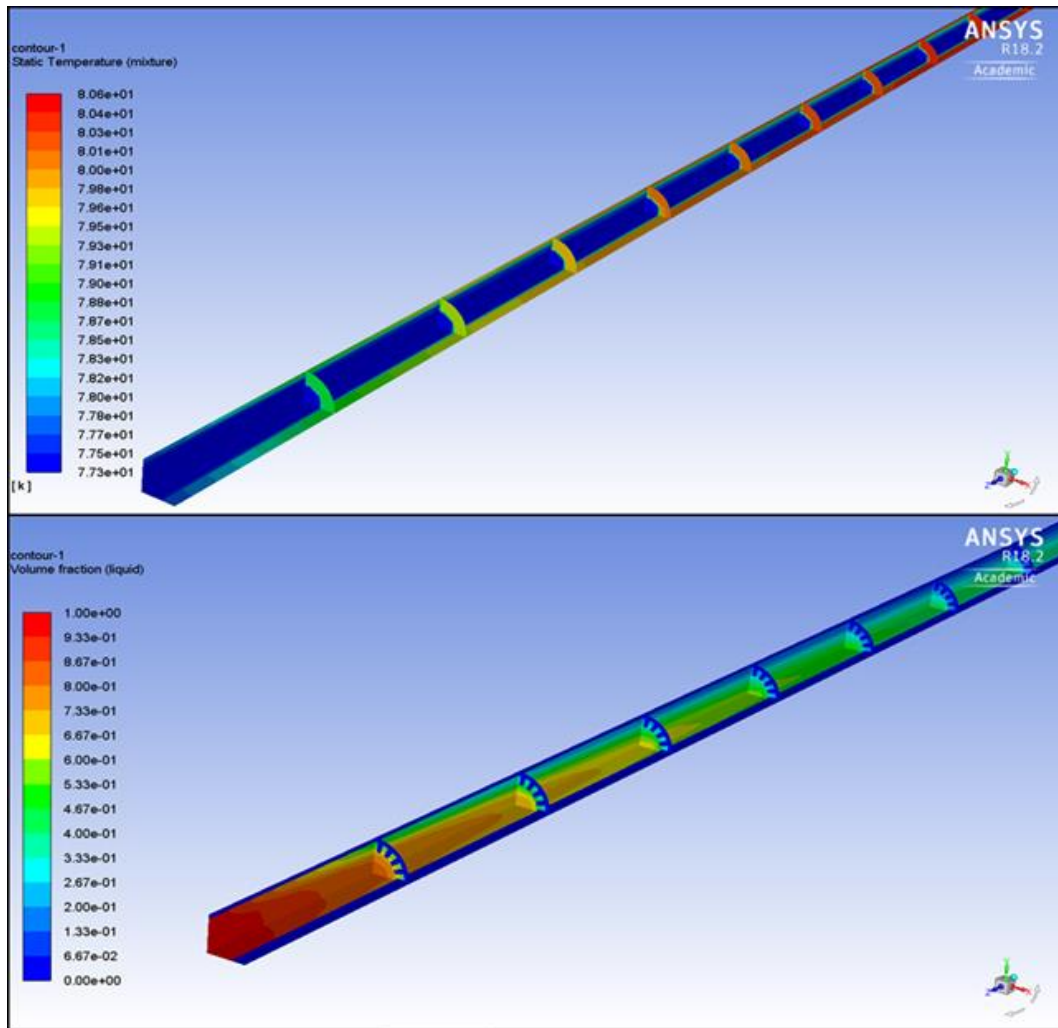
Figure 4-14: Temperature and the volume fraction contours of the rectangular shape fins case

Figure **4**-**15** presents the temperature and the liquid volume fraction contours along the tubes with the twisted fins tube, respectively. The figure represents the previous results presented in Figure 4-13 and shows the temperature and the liquid volume fraction gradient inside the tube. Where the maximum wall temperature reached 80 K.
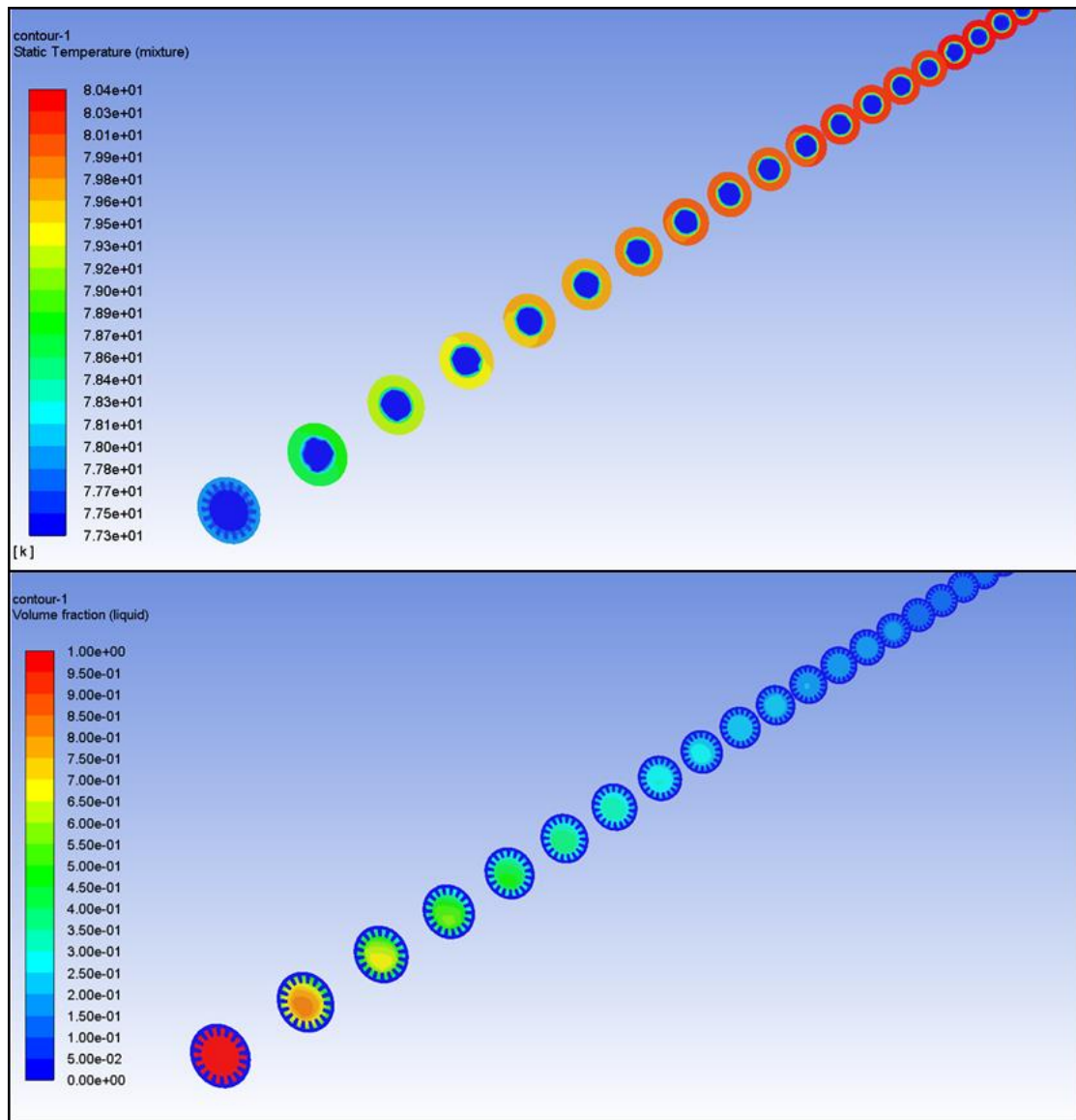
Figure 4-15: Temperature and the volume fraction contours of the twisted fins case

Figure **4**-**16** presents the liquid volume fraction and temperature contours along the tubes with the cylindrical finned tube, respectively. The figure represents the previous results presented in Figure 4-13 and shows the temperature and the liquid volume fraction gradient inside the tube. Where the maximum wall temperature reached 82.6 K at the end of tube.
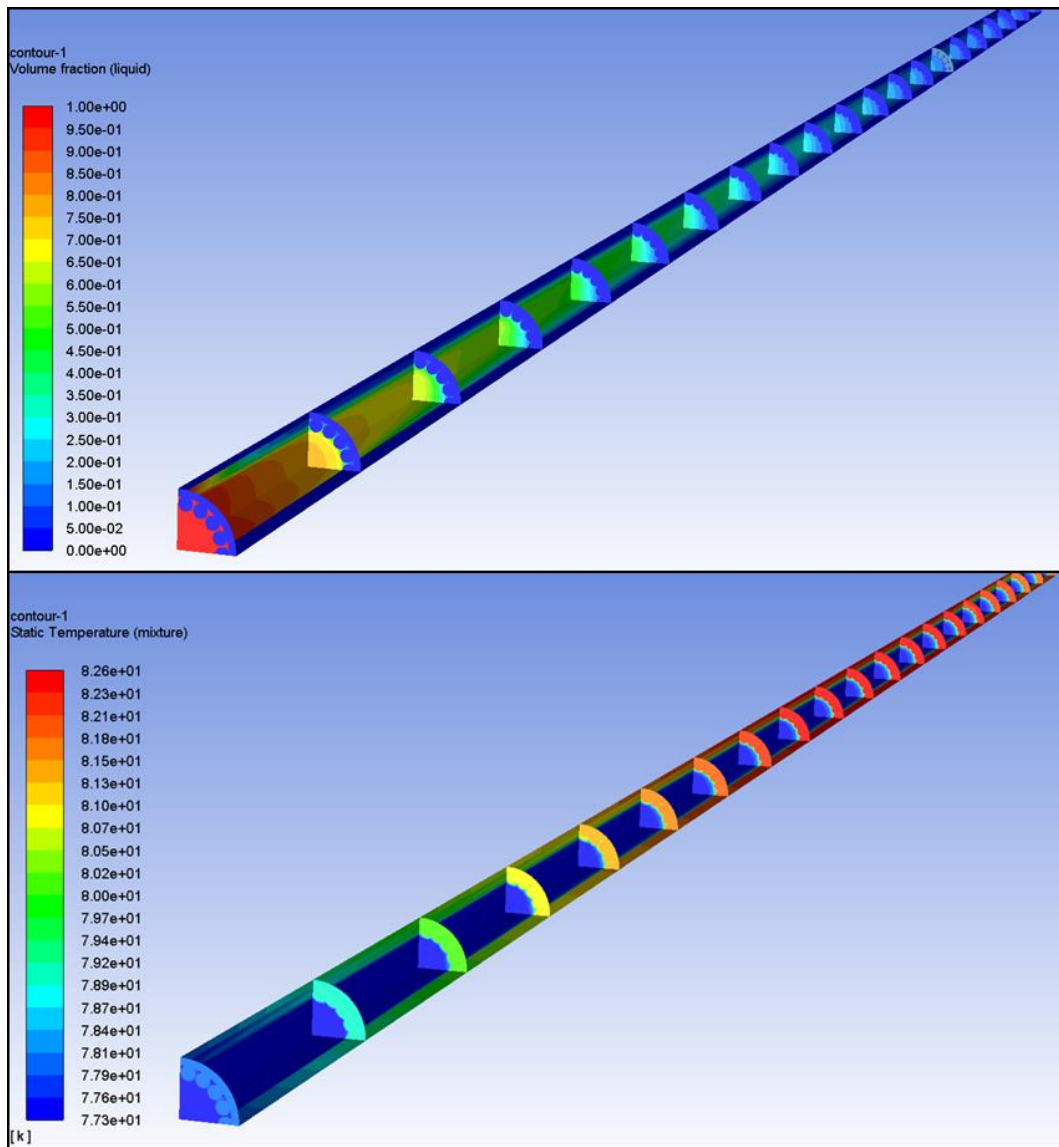
Figure 4-16: Temperature and the volume fraction contours of the cylindrical fins cases

Regarding the pressure drop results shown in Figure 4-17, the smooth tube showed the lowest pressure drop. For both rectangular finned configurations, the pressure drop has increased to almost double that of the smooth tube. The twisted rectangular finned tube showed slightly higher pressure drop than the straight one by approximately 8%, while the cylindrical fins configuration showed the highest pressure drop where it exceeded three times that of the smooth tube. The proposed systems use pumps to increase the LN2/LAir pressure therefore the slight increase in the pressure drop will not cause a significant impact on the whole system.
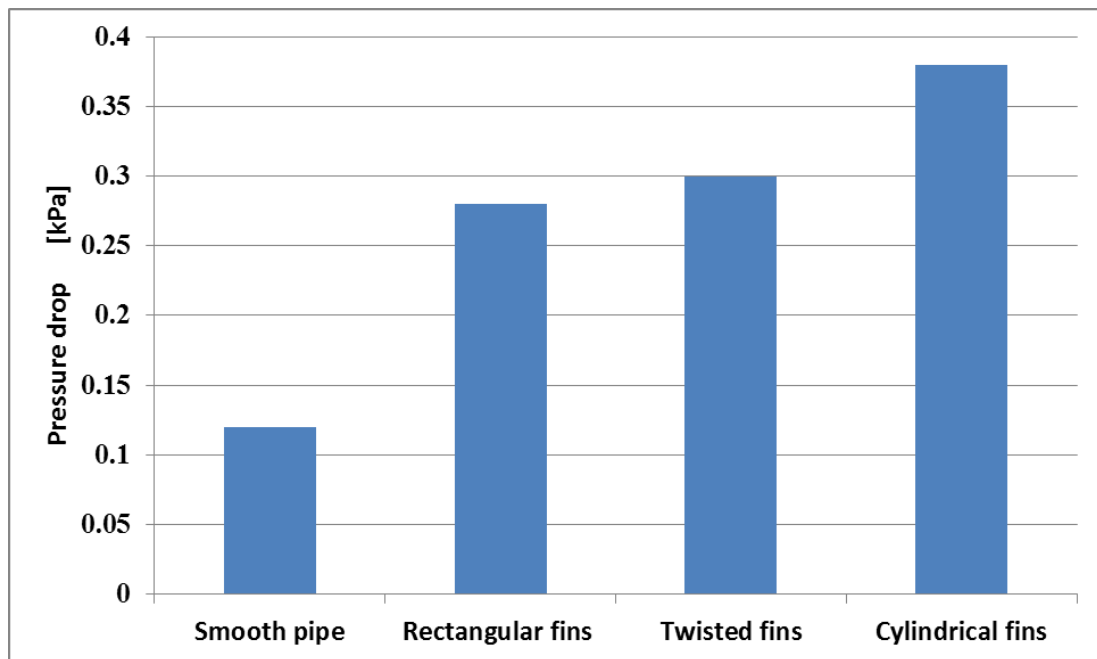
Figure 4-17: Pressure drop in each configuration

4.2.3 CFD model of LN2/LAir heat exchanger

Figure 4-18 shows 3D geometry of concentric pipe heat exchange where the two pipes are made of copper with outer diameters of 6 mm and 15 mm respectively for the inner and outer tubes. The length of the heat exchanger was 500 mm and LN2 flows inside the inner while the secondary warmer fluid flows in the annular gap between the two tubes. The heat exchanger has a symmetrical geometry so only half of the geometry was modelled to reduce the computational time. Figure **4**-**19** shows the flow direction in the heat exchanger where both fluids have the same flow direction from the right hand side to the left hand side (parallel flow) in order to reduce the risk of freezing the secondary fluid.

The secondary fluid was carefully selected considering the possibility of freezing around the LN2 carrier tube (in the annular space) which can restrict the flow. An investigation of substances that have low melting/freezing temperature and are in liquid form at room

temperature was carried out and the results summarized in Table **4**-**1**. Ethanol with melting

temperature of -114 °C and boiling temperature of 78.5 °C was used in this work.
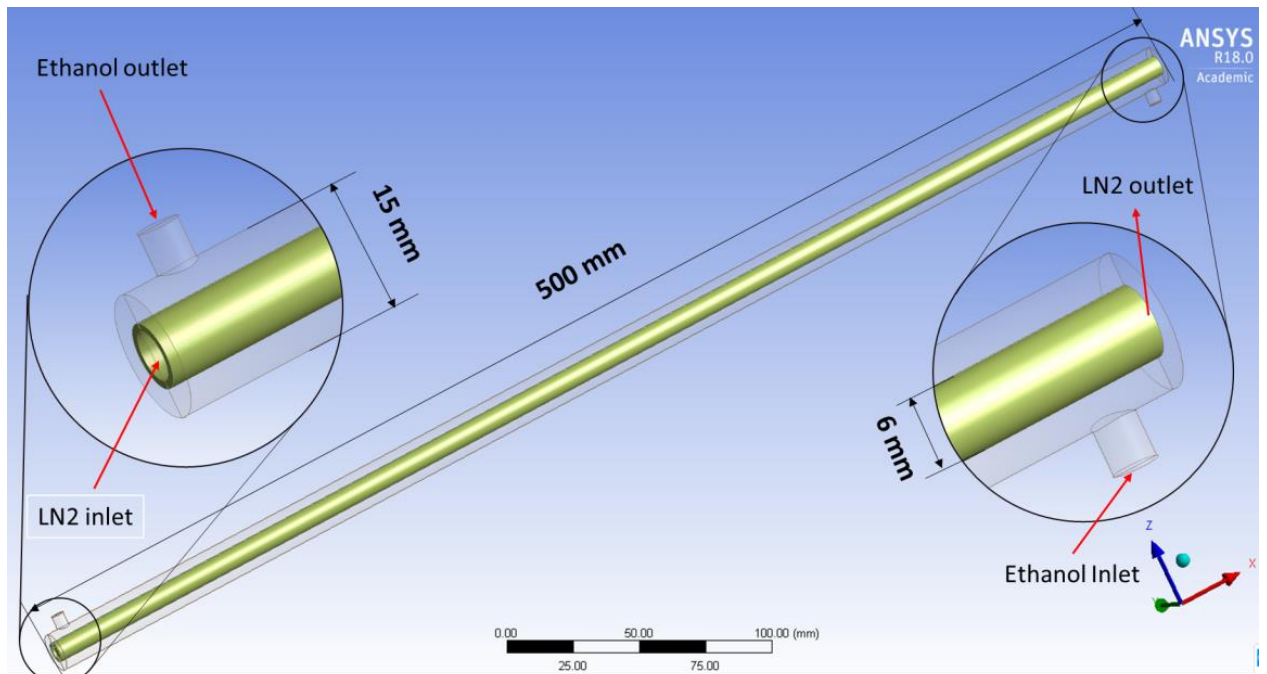
Figure 4-18: Heat exchanger geometry
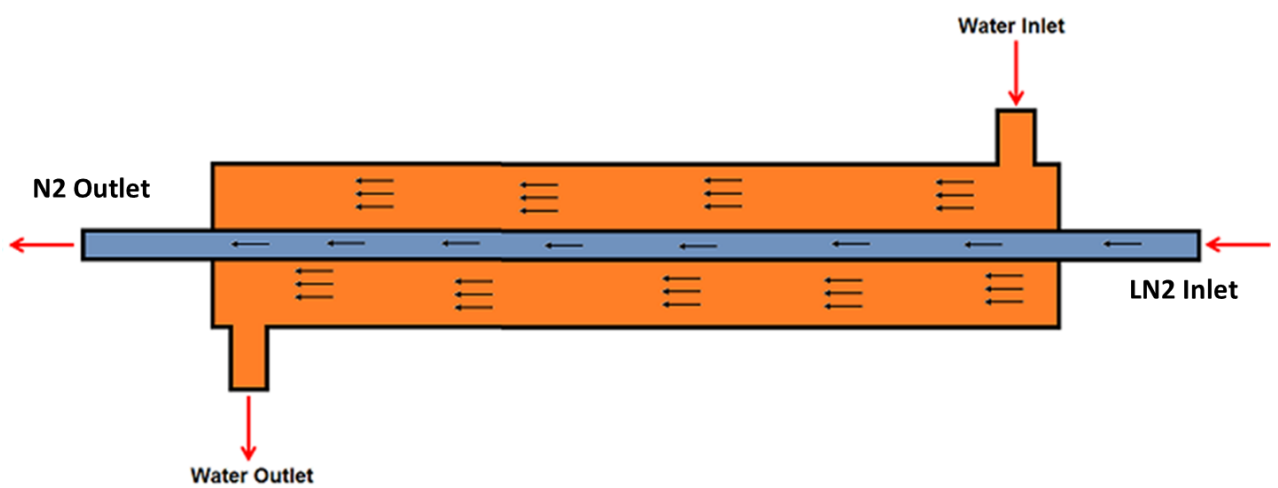
Figure 4-19: Flow direction in the heat exchanger

Table 4-1 Substances have low boiling temperature

Common Name	IUPAC Name	Melting Point (°C)	Boiling Point (°C)
Refrigerant 123	-	-107.2	27.82
Refrigerant 11	-	-111.1	23.8
Refrigerant 611	-	-98.9	31.7
Methyl alcohol	Methanol	-97.8	65.0
Ethyl alcohol	Ethanol	-114.7	78.5
Ethyl chloride	Chloroethane	-136.4	12.3
Propyl alcohol	1-Propanol	-126.5	97.4
Butyl alcohol	1-Butanol	-89.5	117.3
Pentyl alcohol	1-Pentanol	-79	138

Figure 4-20 shows the mesh where a high quality mesh with a total number of 532258 elements were used.
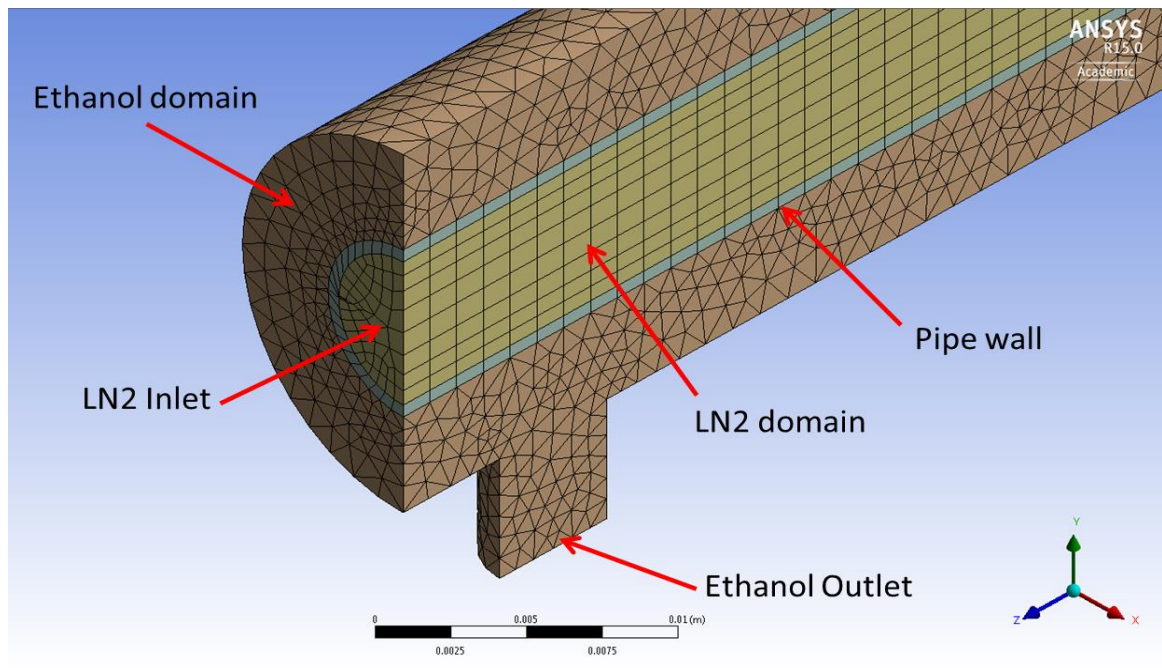
Figure 4-20: Heat exchanger mesh

Regarding the model setup, a steady state, pressure-based solver was used, and for the multiphase model Mixture Model was used due to the difficulties of using Eulerian Model with multi domains. Energy solver and turbulence viscous (k-ε) were also enabled for Nitrogen and Ethanol domains. To consider the LN2 mass transfer, Condensation-Evaporation model was used and the evaporating temperature was set as 77.35 K. In the heat exchange there were three phases LN2, N_2 and Ethanol. In the model, LN2 was set as the

primary phase while the nitrogen gas and ethanol were set as secondary phases. The model solves Continuity, Momentum, Energy, the Secondary Phases Volume Fraction and Mass Transfer equations which are briefly described in the following section. The properties of the liquid phase were assumed as function of temperature only, while the properties of nitrogen gas were varied with pressure and temperature according to ASHERA hand book (see appendix A, C) [87].

Regarding the boundary conditions, velocity inlet with different values (0.1-0.4 m/s) was applied at inlets of LN2 and ethanol fluids. This range was carefully selected reducing the LN2 inlet velocity below the value of 0.1 m/s will reduce the LN2 mass flow rate as result the cooling rate will be too small and hard to compare the cases. Increasing the inlet velocity higher than 0.4 leads to reduce the LN2 vapour volume fraction at the outlet indicating there is a limitation of increasing the inlet velocity with the current inner tube length. Several cases were simulated to investigate the effect of inlet mass flow rates on the LN2 outlet conditions (temperature, liquid volume fraction and vapour volume fraction), the ethanol outlet temperature, and the temperature of the outer surface of the inner tube. Table **4-2** shows the inlet condition (velocity and temperature) of each case, while the outlet pressure with a value of 1 atm was set for LN2 and ethanol outlets.

Table 4-2 Inlet condition of each case

Case No	LN2		Ethanol	
	Velocity [m/s]	Temperature [K]	Velocity [m/s]	Temperature [K]
Case 1	0.1		0.1	
Case 2	0.2		0.1	
Case 3	0.3		0.1	
Case 4	0.4	77.3	0.1	323
Case 5	0.1		0.2	
Case 6	0.1		0.3	
Case 7	0.1		0.4	

A high performance central computing in University of Birmingham (BlueBear) was used and each case took about 7 days to converge. The convergence criteria was based on monitoring different parameters including; the energy balance between the two fluids (i.e. comparing the absorbed energy by LN2 to the energy loss by ethanol), inlet/outlet mass flow rate of each fluid and outlet temperature of each fluid. Figure **4**-**21** shows LN2 and ethanol outlet temperature at the convergence time where it is clear that the outlet temperature of both fluids is no longer changed and this happen after a number of iteration of 1.5 million.
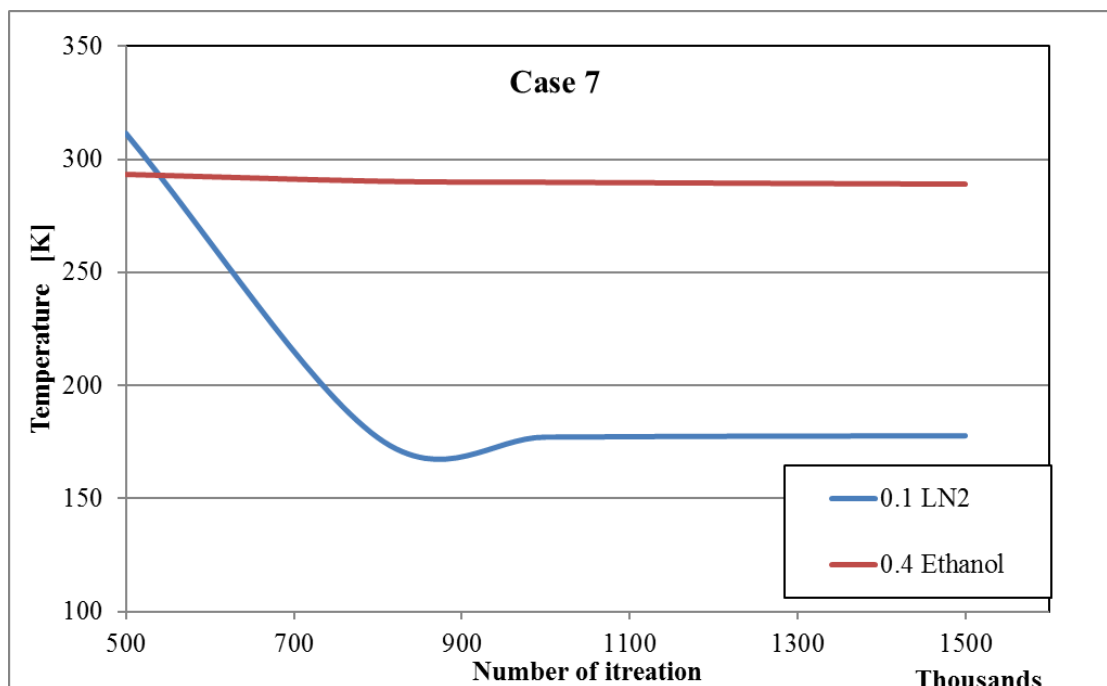
Figure 4-21: LN2 and ethanol outlet temperature at the convergence time

Figure 4-22 shows the nitrogen outlet temperature where it is clearly seen that, as the LN2 inlet velocity increases (cases 1-4) the outlet temperature decreases, however, when the ethanol inlet velocity increases there is no significant change in the nitrogen outlet temperature (cases 5-7). Figure 4-23 shows similar trend of the outlet vapour volume fraction where it decreases with increasing the LN2 inlet velocity however there is no significant change where the ethanol inlet velocity changes. The figure also presents the nitrogen liquid volume fraction which increases with increasing the LN2 inlet velocity indicating the LN2 did

not fully evaporate. The first column in this figure shows the inlet liquid volume fraction LVF where it is equal to 1 indicating LN2 entered to the domain as single phase. Figure 4-24 shows the variation of the LN2 vapour volume fraction along the tube and near to the wall for cases 5-7, with higher ethanol inlet velocity, where a high vapour volume fraction (≈ 1) indicating full evaporation of LN2. Figure 4-25 shows the LN2 vapour volume fraction contours.
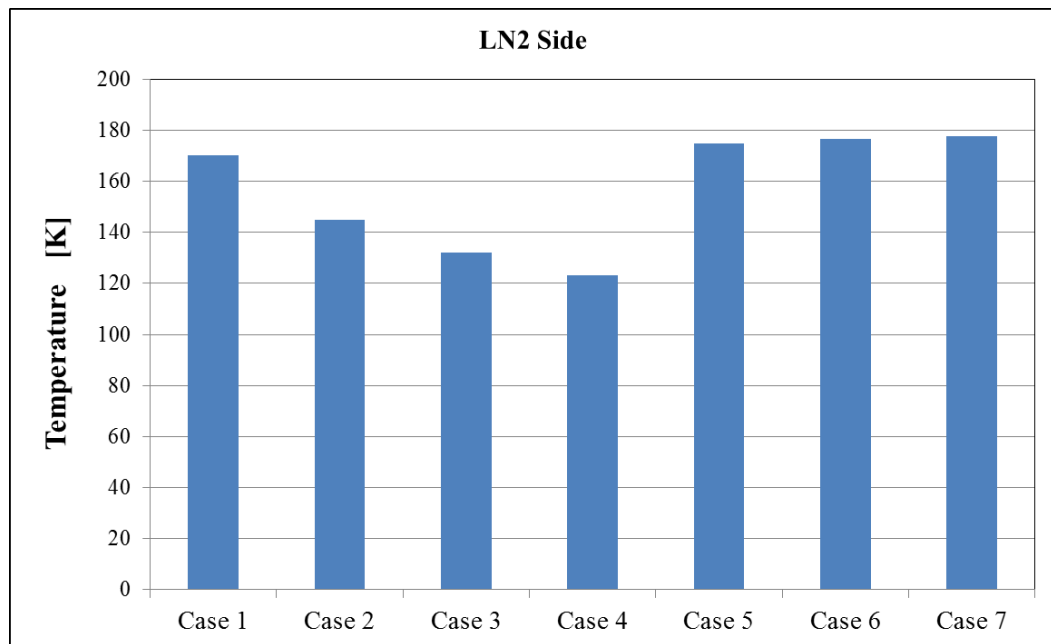
Figure 4-22: Nitrogen outlet temperatures
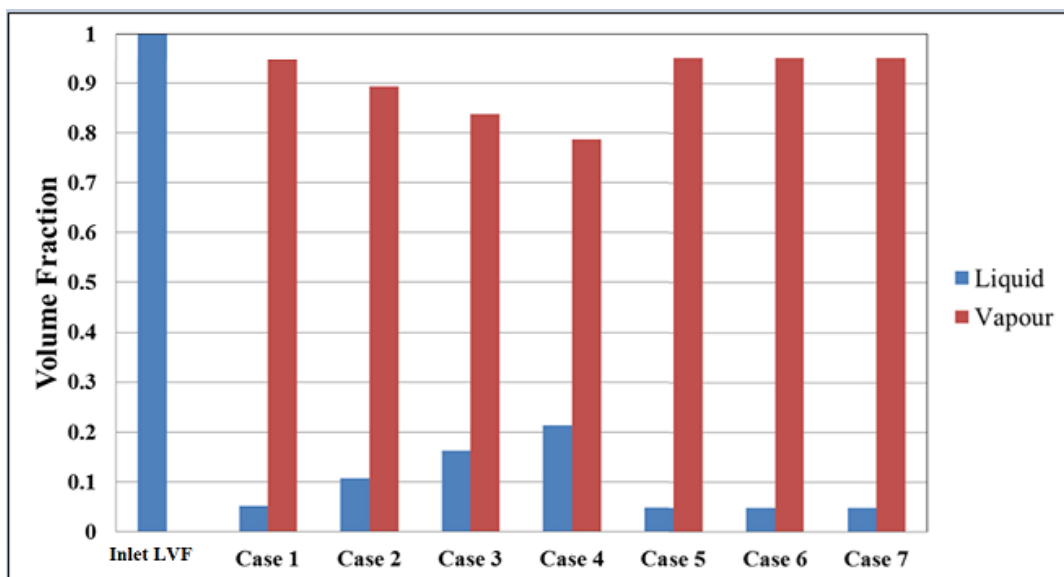
Figure 4-23: Average inlet and outlet volume fractions
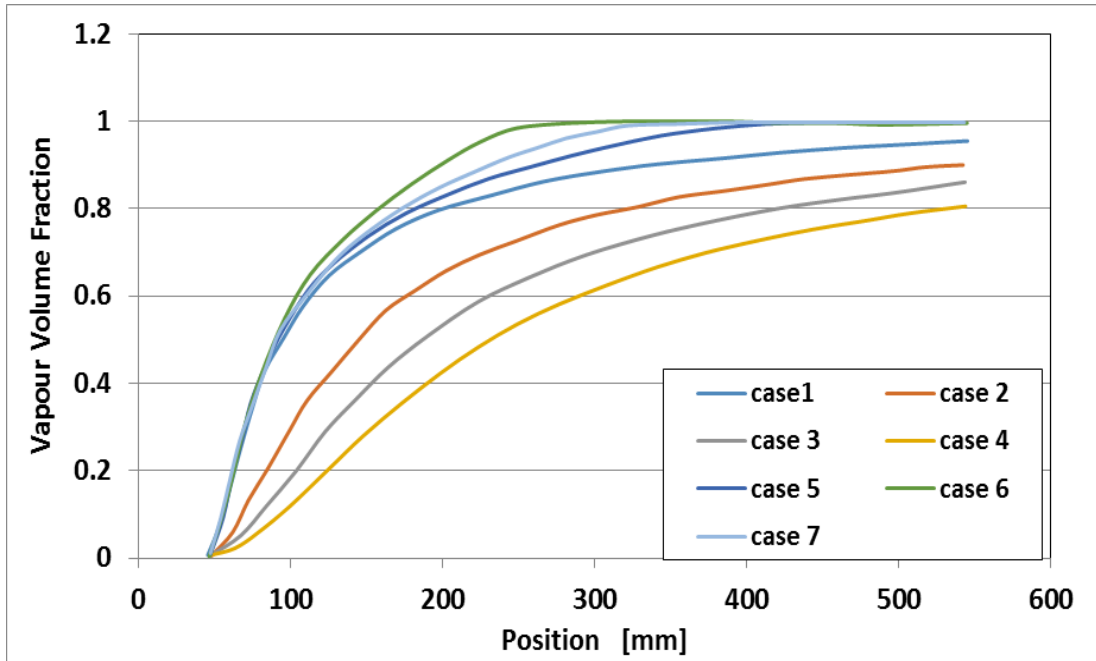
Figure 4-24: Variation of the LN2 vapour volume fraction along the tube

Regarding the ethanol side Figure 4-26 shows the outlet temperature where it decreases with increasing the LN2 inlet velocity (cases 1-4), however, increasing the ethanol inlet velocity (cases 5-7) shows no significant change in the ethanol outlet temperature. This indicates that increasing the ethanol mass flow rate has no significant change on the outlet condition. This is due to the low heat transfer coefficient of N_2 gas.
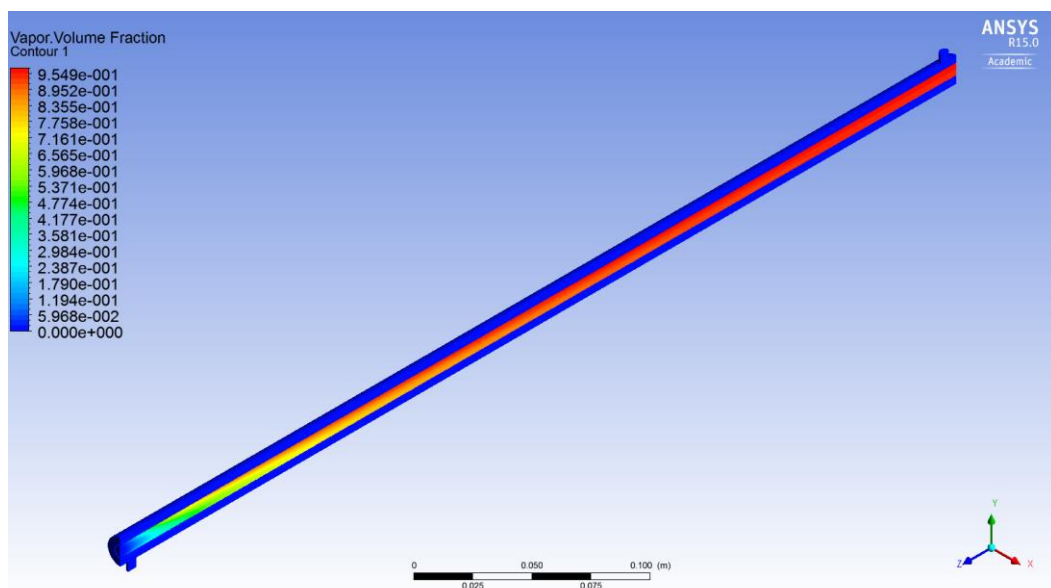
Figure 4-25; LN2 vapour volume fraction contours
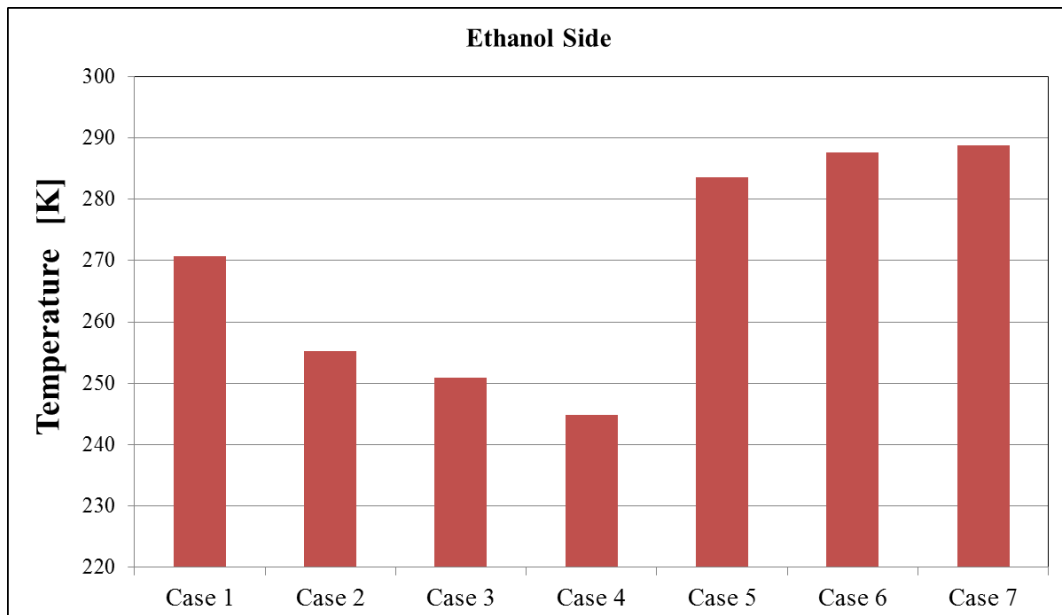
Figure 4-26: Ethanol outlet temperatures

Figure 4-27 shows the temperature distribution along the outer surface of the LN2 carrier tube, and the dash line in the figure refers to the freezing temperature of ethanol. At the highest LN2 flow rate only about 5 cm shows the possibility of the ethanol freezing around the inner tube. Figure 4-28 shows the whole heat exchanger temperature contours.
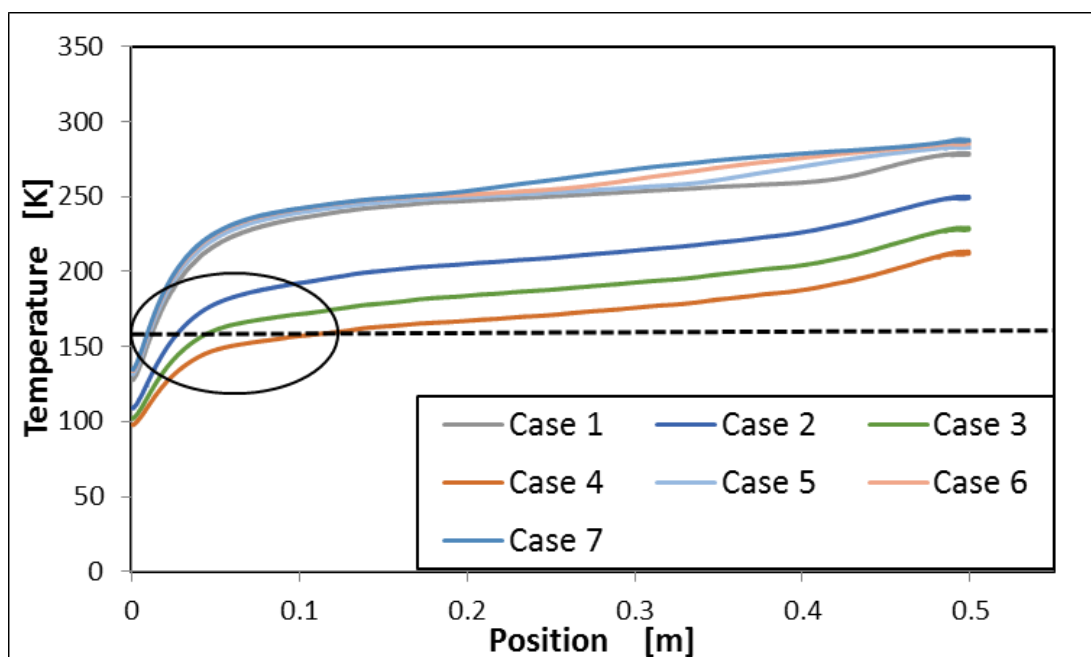
Figure 4-27: Temperature distributions along the LN2 tube
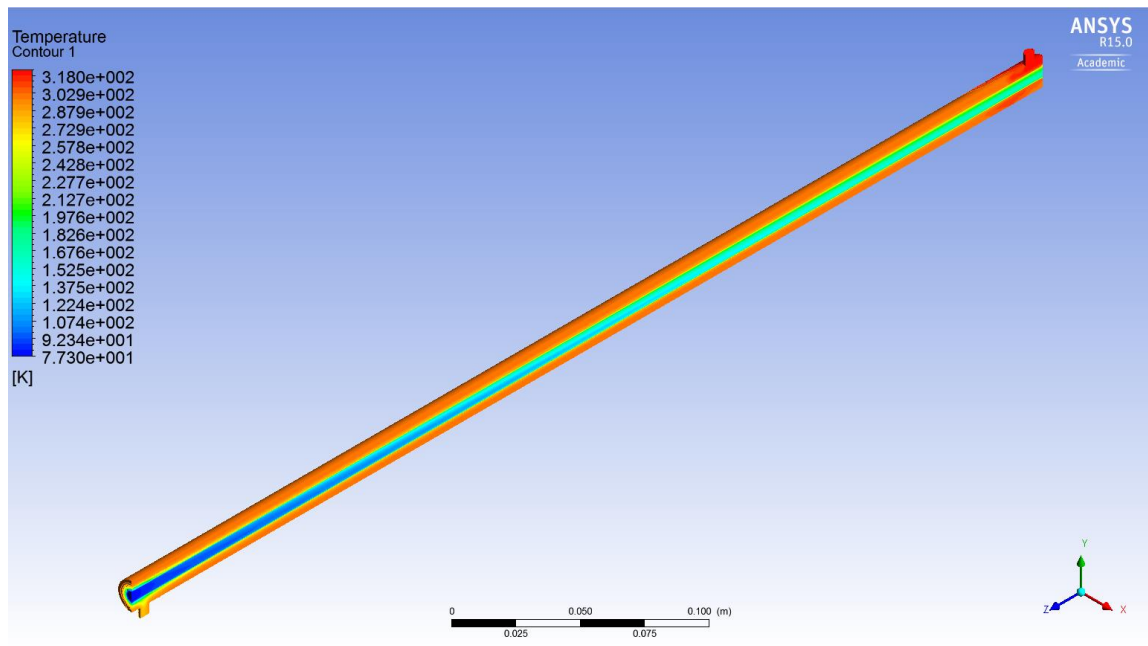
Figure 4-28: Temperature contours of whole heat exchanger

4.2.4 Effect of inner tube configuration (geometry)

To assess the impact of LN2 carrier tube geometry on the outlet conditions from the heat exchanger several pipe geometries were built. Figure 4-29 shows case 1 which is the original geometry (smooth tube with 500 mm length, 6 mm ID and 0.5 mm thickness). Figure 4-30 shows Case 2 where the tube was modified by adding external fins with 1mm height. The tube thickness and diameters were kept the same as the original one. Figure 4-31 shows the Case 3 where 1 mm high external helical fins were added to the original geometry. Figure **4**-**32** shows cases 4 and 5 where the tube was finned internally with different fin heights of 1 mm and 1.5 mm respectively. In Case 4 the wall thickness was 1 mm which is double the original one to investigate its effect on the outer surface temperature. In the last case (Case 6) the tube was finned internally and externally as shown in Figure 4-33, the fins have 0.5 mm height in both sides. Description of each case and their dimensions are summarized in Table **4**-**3**.
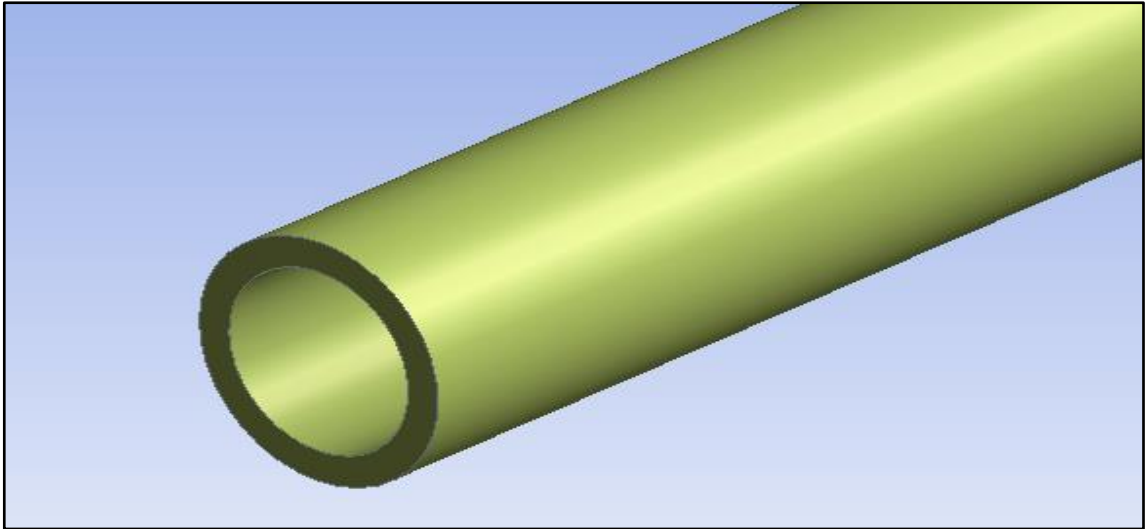
Figure 4-29: Case 1, smooth tube
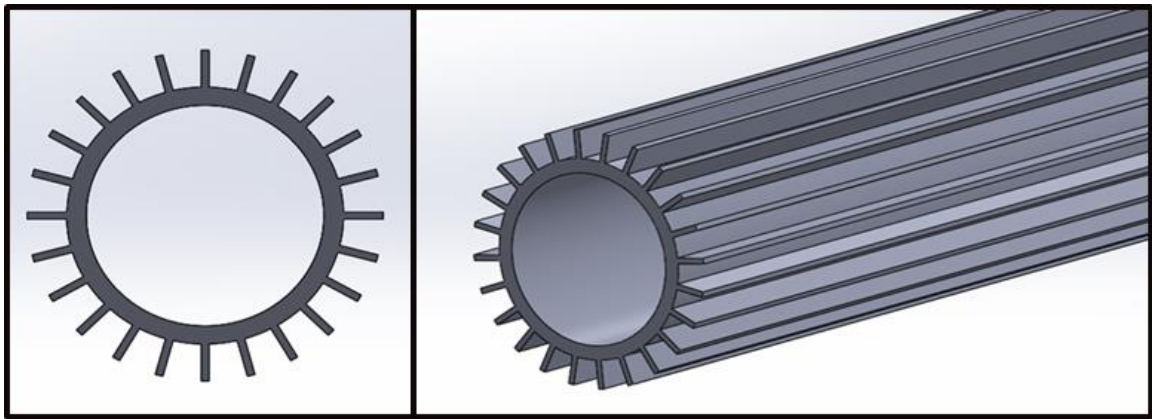
Figure 4-30: Case 2, external straight fins with 1mm height
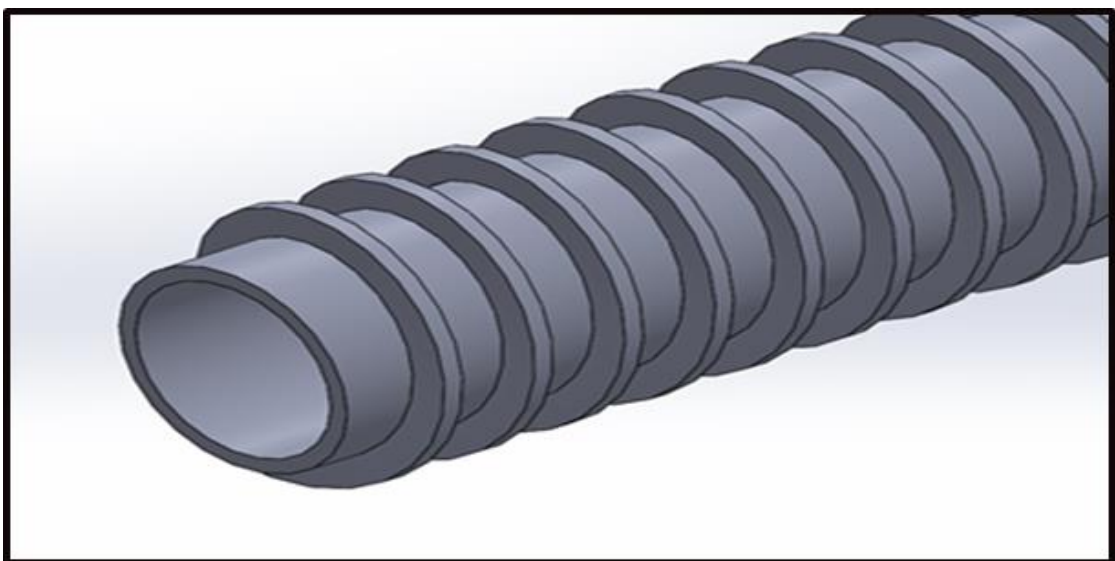
Figure 4-31: Case 3, external helical fin with 1 mm height
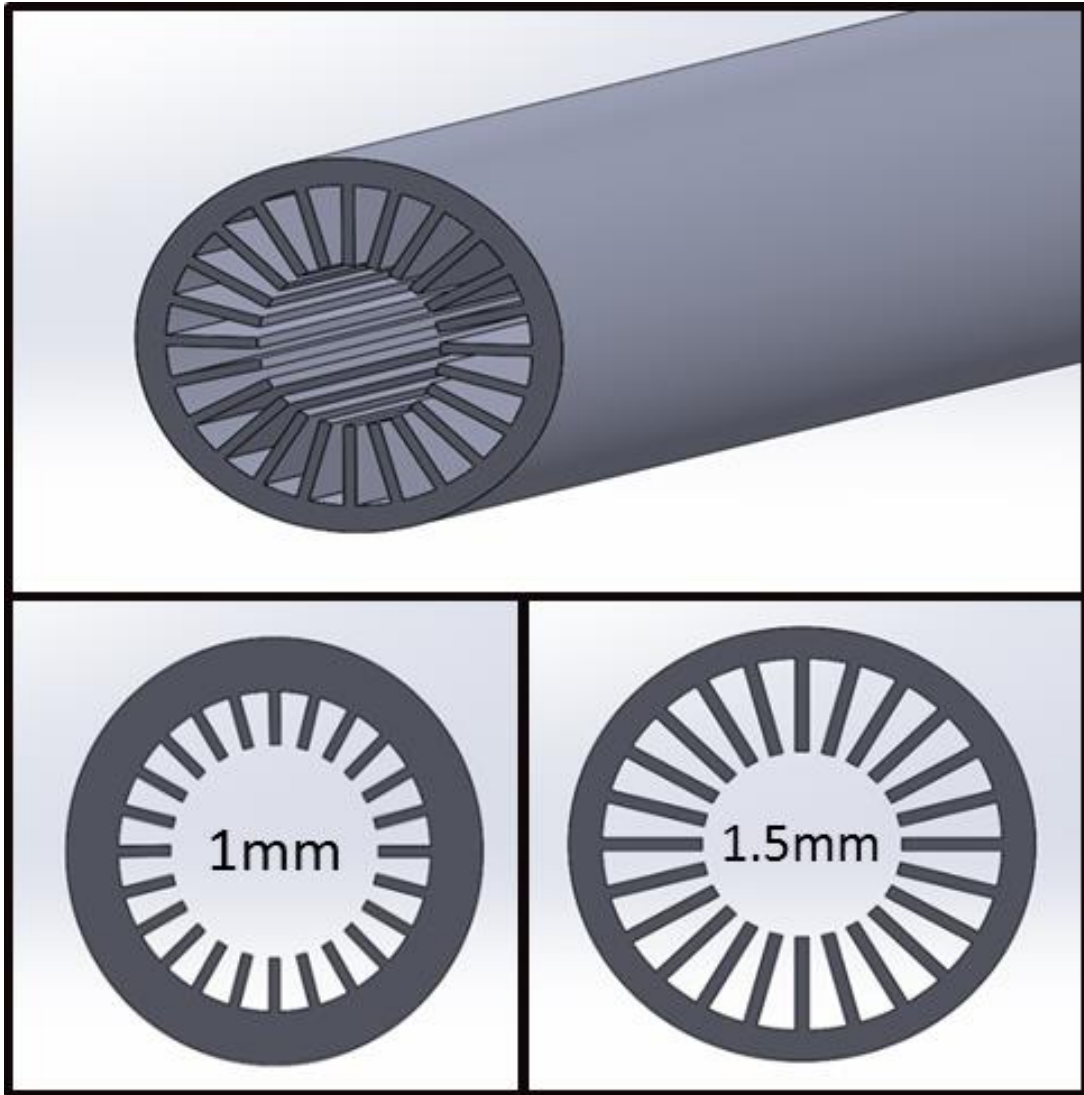
Figure 4-32: Cases 4 and 5 internal fins with a height of 1 mm and 1.5 mm respectively
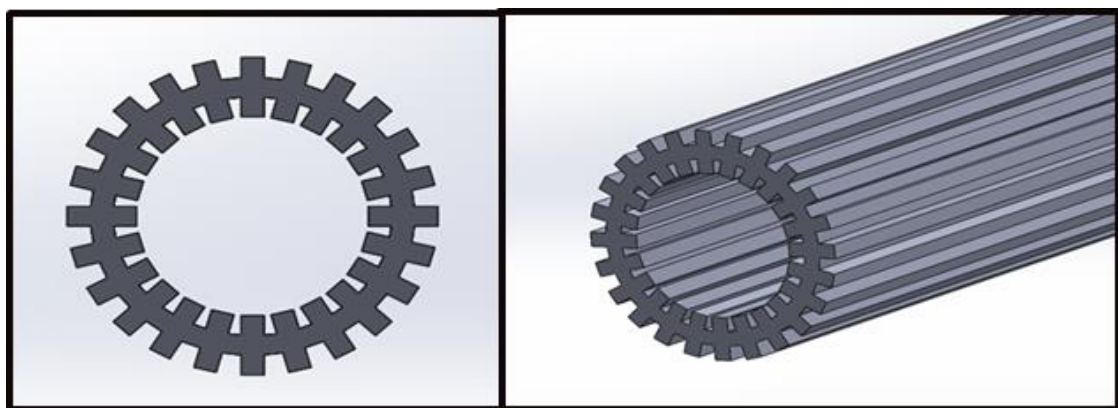
Figure 4-33: Case 6 internally and externally finned tube

Table 4-3 Fins height and location of each case

Case No	Discretion
Case 1	Smooth pipe and 0.5 mm pipe's thickness
Case 2	External Straight fins 1 mm height and 0.5 mm pipe's thickness
Case 3	External helical fins 1 mm height and 0.5 mm pipe's thickness
Case 4	Internal fins 1 mm high and 1 mm pipe's thickness
Case 5	Internal fins 1.5 mm high and 0.5 mm pipe's thickness
Case 6	External and internal fins, 0.5 mm high and 0.5 mm pipe's thickness

Figure 4-34 shows the LN2 outlet temperatures of each case where it is clear that the smooth pipe has the lowest value indicating low heat transfer between the two domains. The figure also shows that the externally finned tubes (cases 2 and 3) have increased the heat transfer but not significantly, while the internally finned tubes (cases 4 and 5) showed higher values of LN2 outlet temperature indicating better improvement in the heat transfer. The last configuration (cases 6) where the tube has fins on both sides (internal and external) the outlet temperature was slightly higher than that of cases 2 and 3 but lower than that of case 4. This is due to the internal fins height where it was 0.5 mm. while in cases 4 and 5 the fins height were 1 mm and 1.5 mm respectively. Case 5 has the highest fins height thus it showed the highest outlet temperature indicating higher heat transfer and its temperature contours are presented in Figure 4-35.
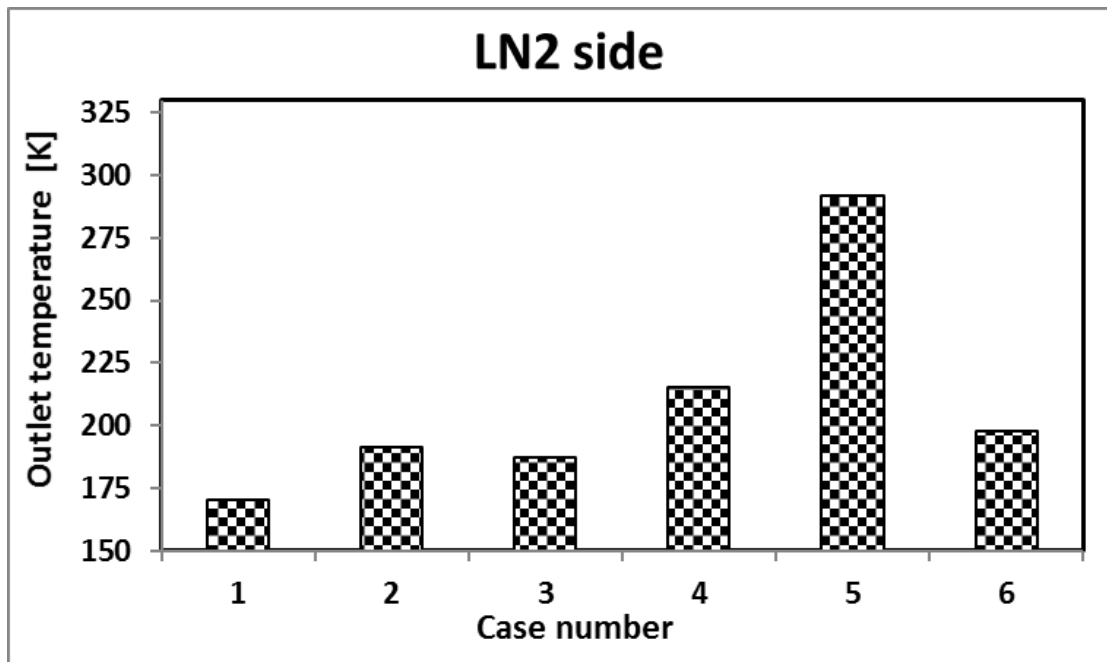
Figure 4-34: LN2 outlet temperatures of each case
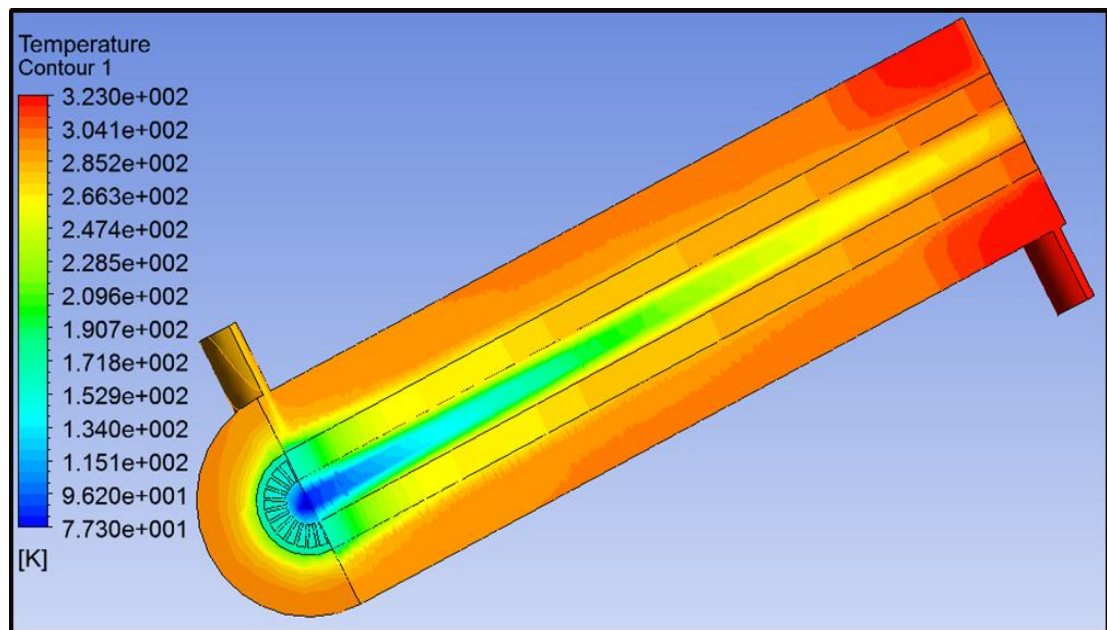
Figure 4-35: The fifth case temperature contour

Figure 4-36 shows the nitrogen outlet vapour volume fraction VVF where similar pattern to the LN2 outlet temperature can be observed. Case 5 with the largest internal fins height showed the highest VVF value while the smooth pipe showed the lowest VVF value. The vapour volume fraction contours for case 5 are shown in Figure 4-37.
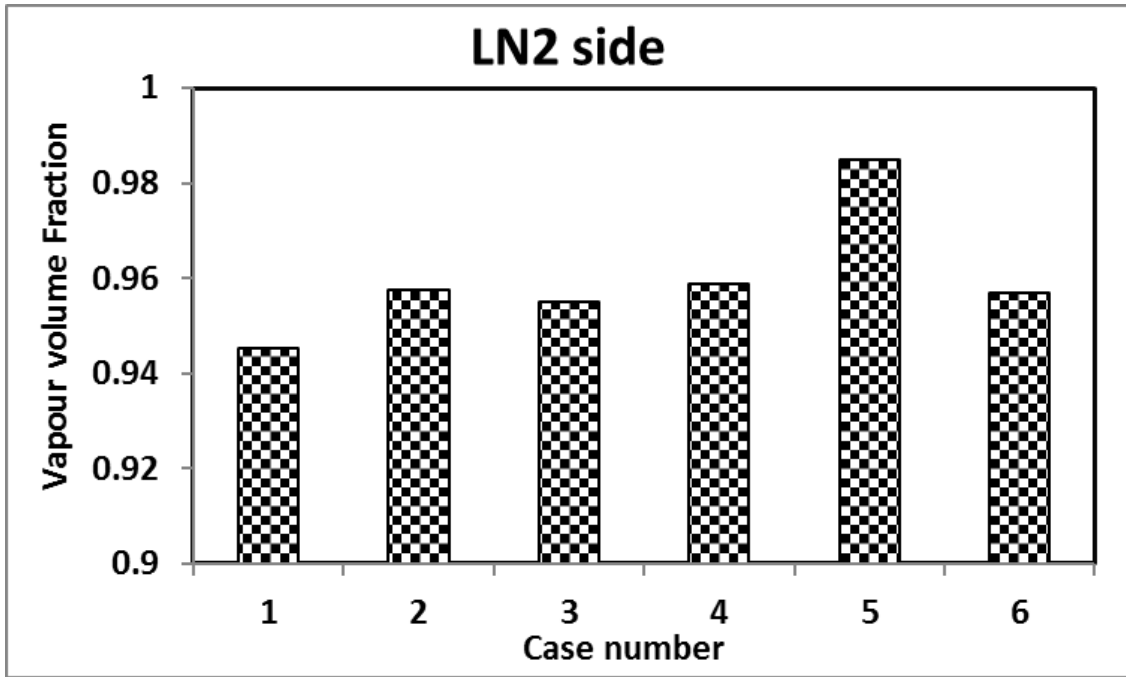
Figure 4-36: Nitrogen outlet vapour volume fraction
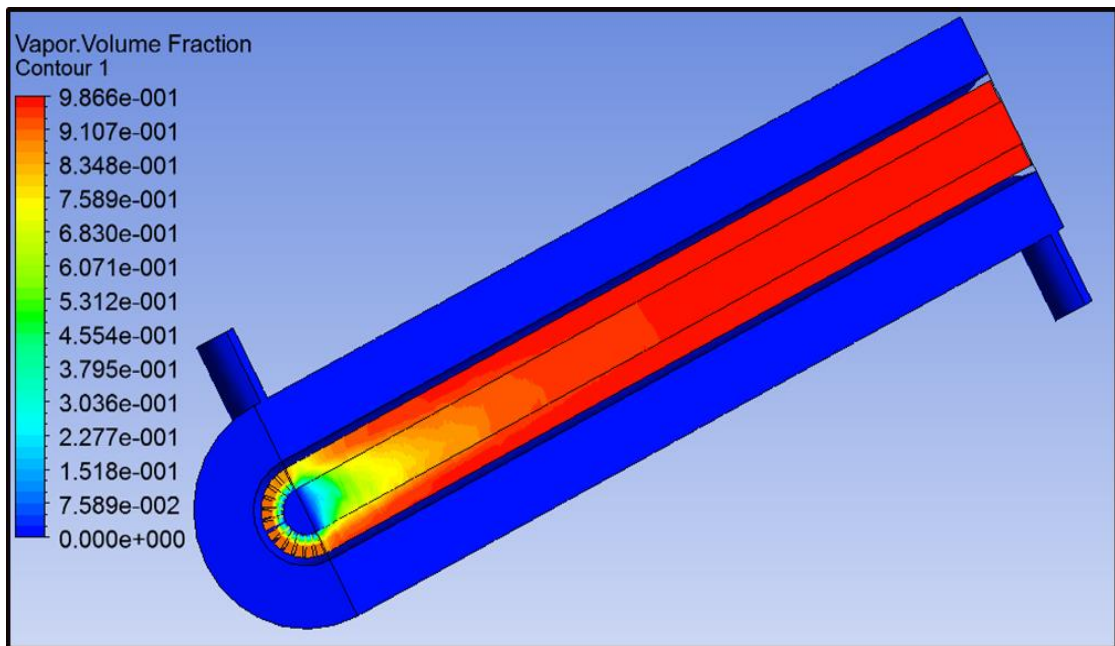
Figure 4-37: Vapour volume fraction contours for case 5

Figure 4-38 shows the ethanol outlet temperatures of all cases (1-6) where the pattern looks opposite to the other LN2 outlet temperature. The smooth pipe showed the highest value whereas the fifth case showed the lowest value indicating the highest heat transfer between the two fluids.
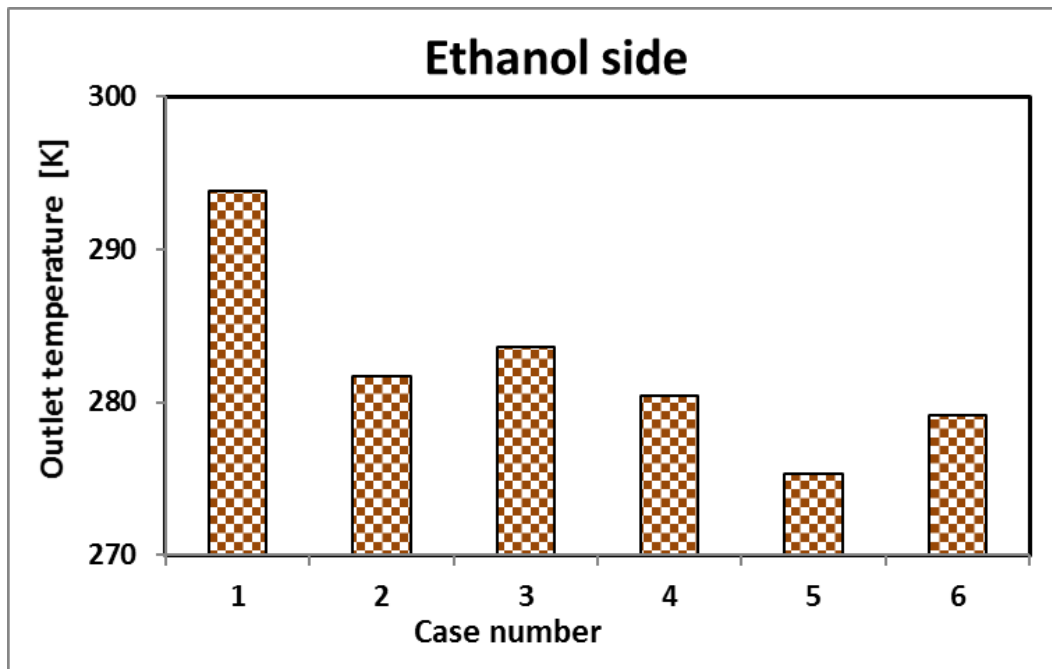
Figure 4-38: Ethanol outlet temperatures of all cases

Figure **4-39** shows the generated cooling for each case where it is clear that the fifth case with the highest internal fins height showing the highest value of generated cooling (88 W) while the first case with the smooth tube showing the lowest cooling capacity (54 W). These low values of the generated cooling are due to the low mass flow rates of the LN2 and ethanol which were 0.08 and 0.05 LPM, respectively.
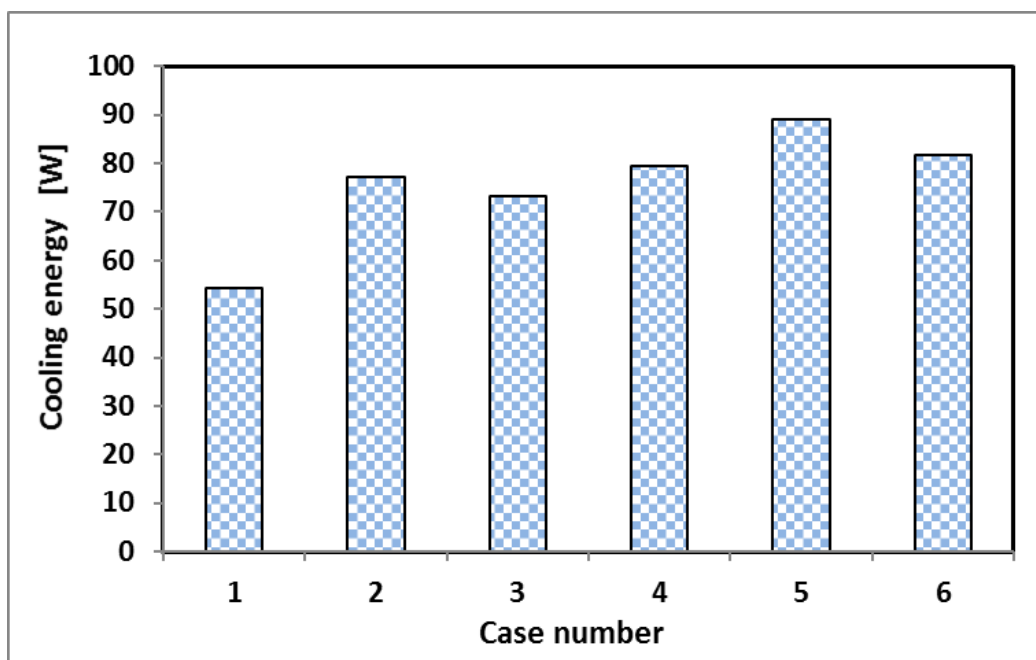
Figure 4-39: Generated cooling of each case

Figure 4-40 shows the temperature distribution along the outer surface on the inner tube. This is an important parameter to predict the possibility of freezing the ethanol in the annular gap which might block the flow. The figure shows that in all cases only about 50 mm of the whole tube length (500 mm) have temperature less than the freezing point of ethanol indicating there is a possibility of freezing the secondary fluid in this region.
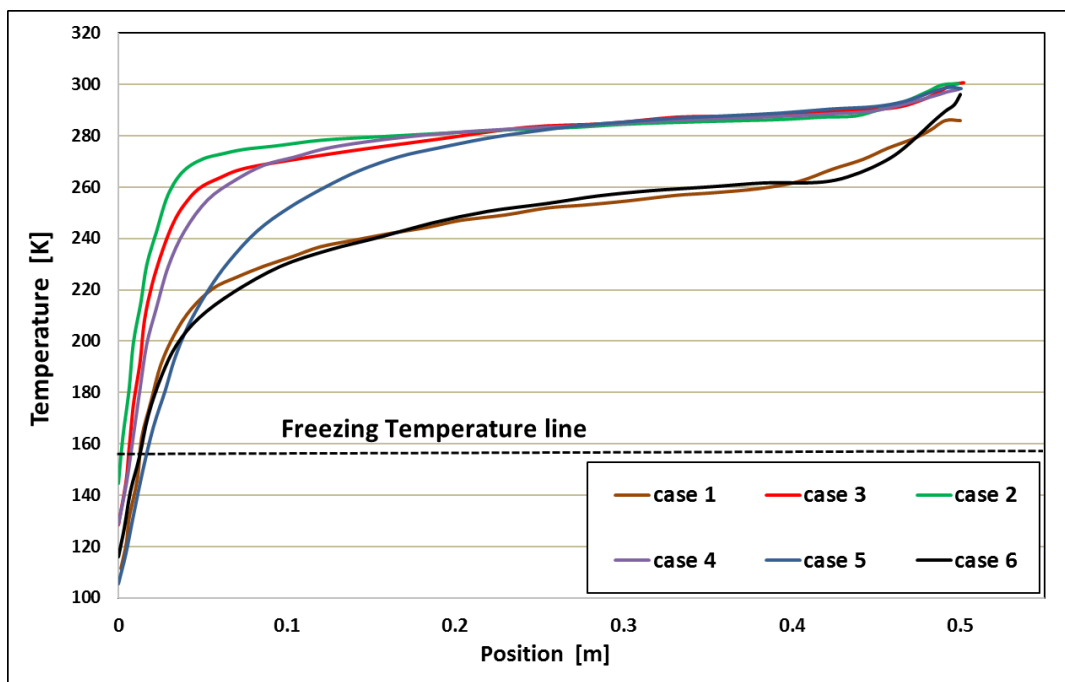
Figure 4-40: Temperature distributions along the outer surface on the inner tube

4.2.5 CFD modelling of solidification process

The previous results showed that there is a possibility of freezing the secondary fluid in the annular space. There were areas (around 10%) where the temperature dropped below the freezing temperature while the remaining 90% of the surface was at much higher temperature than the freezing point. This means that the formed ice might not grow to block the flow due to being melted by the high temperature flow.

Therefore CFD modeling of solidification process was developed to predict if there is any restriction of the ethanol flow due to the ethanol solidification caused by low surface temperature. Ansys fluent was used in this model and case 1 which showed the worst wall temperature as shown in Figure 4-40 was used. The same geometry was used and only the ethanol domain was simulated to reduce the computational time. This means the LN2 evaporation was not modeled with the solidification process and instead the wall temperature distribution obtained from the previous section for case 1 was used.

Ansys Fluent uses Enthalpy-porosity method for modeling melting/solidification process. In this method each cell in the domain is associated with a quantity called Liquid Fraction and an enthalpy balance is used to compute this value. The model solves Energy and Momentum equations, and involves solving the turbulence, species and Pull velocity for the continuity equations.

The energy equation for solidification/melting model can be written as:

$$\frac{\partial}{\partial t}(\rho H) + \nabla.(\rho H \vec{v}) = \nabla.(k\nabla T) + S$$

4.51

Where H is fluid enthalpy, ρ is density, $\vec{v}$ is fluid velocity and S is the source term.

The model calculates the enthalpy of the fluid as the summation of the sensible enthalpy and the latent heat as in Equation (**4.52**).

$$H = h + \Delta H$$

4.52

Where h is the sensible enthalpy which can be calculated using equation **4.53** and ΔH is the latent heat.

$$h = h_{ref} + \int_{T_{ref}}^{T} C_p dT$$

4.53

Where h_{ref} is the material reference enthalpy, T_{ref} is the reference temperature and C_p is specific heat.

The material liquid fraction can be calculated as shown in equation (**4.54**) and it varies from 0 to 1.

$$\beta = \begin{cases} 0 & if\ T < T_{solidus} \\ 1 & if\ T > T_{liquidus} \\ \frac{T-T_{solidus}}{T_{liquidus}-T_{solidus}} & if\quad T_{solidus} < T < T_{liquidus} \end{cases}$$

4.54

The latent heat ΔH can be calculated based on the liquid fraction β as shown in equation (**4.55**).

$$\Delta H\ =\ \beta L$$

4.55

Where L is latent heat of solidification.

Regarding the boundary conditions, the same boundary conditions that were applied on the ethanol side, in the previous section (4.2.1.4) were used in this model. The wall temperature of the inner tube computed in the previous simulation (see Figure 4-40) was applied on the inner surface of the ethanol domain.

Figure 4-41 shows the contours of mass fraction which has value between 0-1. The value 1 means pure liquid while 0 means pure solid. It can be seen that the minimum value of the mass fraction is 0.53 indicating there is no pure ice forming at the surface where the lowest temperature occurred at the inlet of LN2. Figure 4-42 shows the temperature contours.
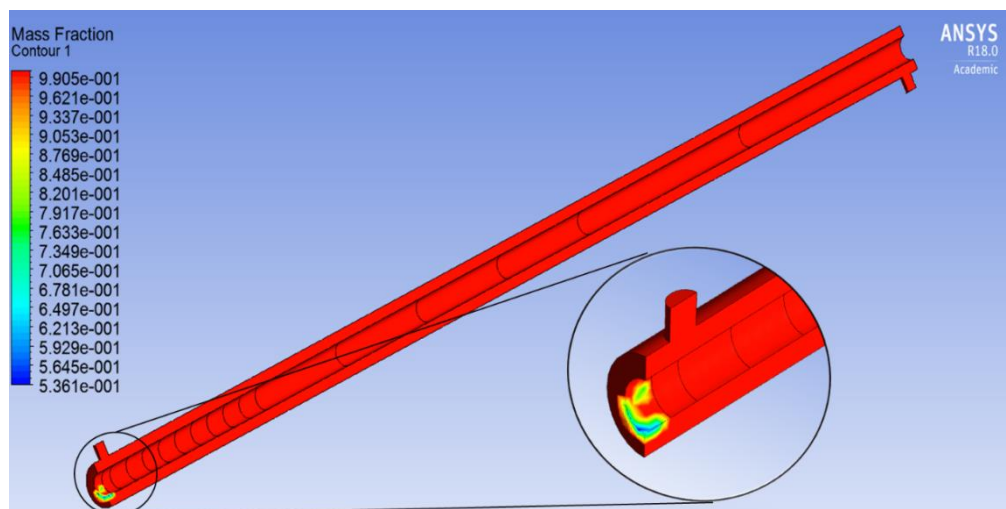
Figure 4-41: Mass fraction Contours
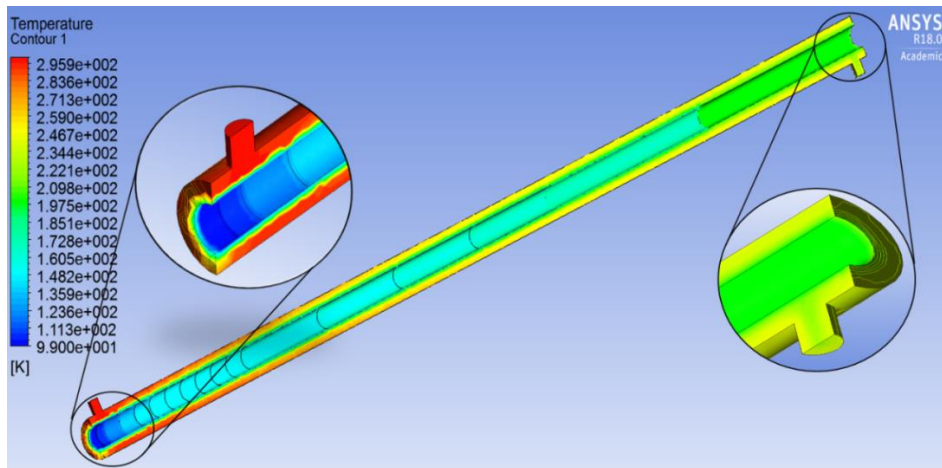
Figure 4-42: Solidification model temperature contour

4.3 CFD model of cryogenic engine

The proposed systems described in chapter three for recovering the stored cold energy in LN2/Air are open systems where LN2 will not be circulated and the output power is affected significantly by the expander inlet pressure. As reported in the literature and in chapter three, increasing the expander inlet pressure leads to reduction in the LN2 consumption. Designing an efficient turbine with these conditions (high pressure ratio and low mass flow rate) is difficult due to high friction losses and supersonic speed [124]. Thus reciprocating engine driven by high pressure of superheated N2/Air is developed using CFD and presented in this section [85].

Figure 4-43 shows the engine geometry and its main components including (a 50 mm piston sets at the Top Dead Center TDC, 50 mm cylinder bore, intake valve and exit valve). Figure 4-44 illustrates the working principle of the engine which consists of two strokes; (a) the power stroke which starts when the piston at the TDC, and the intake valve had already started opening at time of 1/16 of the total cycle time (allowing a high pressure N2/Air to enter the engine cylinder) and will close after the same time. The high pressure N2/Air will push the piston down to expand and generate power. (b) The second stroke is the exhaust

stroke where the exit valve starts opening at a time of 0.5/16 of the total cycle time before the piston reaches the Bottom Dead Center BDC to avoid any compression. The Exit valve will remain open until the piston reaches the TDC again. This to avoid generating negative work while the piston is going up and this is one of the main advantage of this engine. A specific user define function UDF was written using C programming language to simulate these two strokes with their piston movement and valve timing [85].
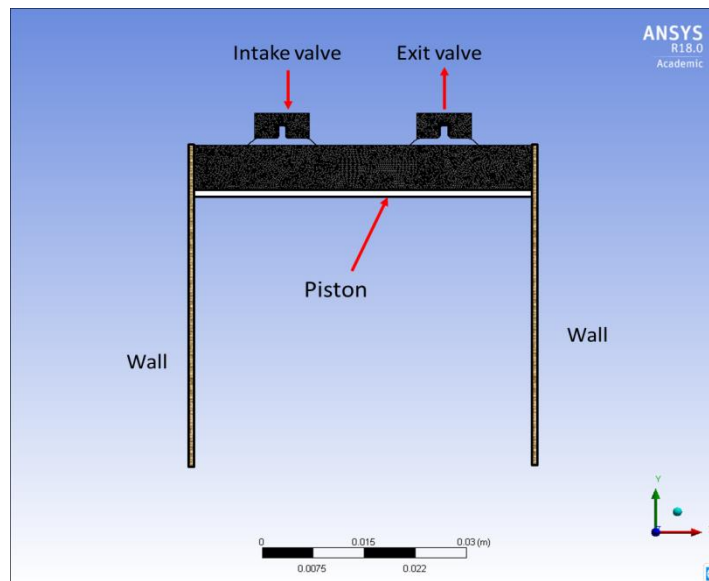
Figure 4-43: LN2/LAir engine geometry [85]
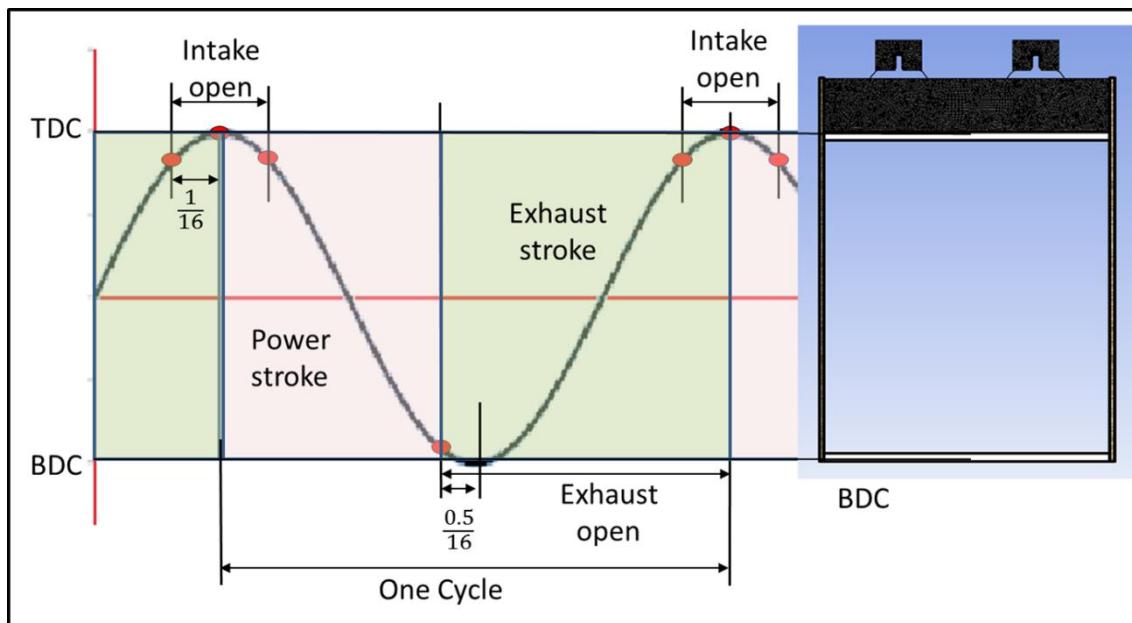
Figure 4-44: The engine working principle [85]

In this model air was selected as working fluid and various inlet pressures were used (4, 6, 8, 10 and 20 Bar) to investigate the effect of charge pressure on the engine output power. Figure 4-45 shows the engine P-V diagram for each inlet pressure which was used to compute the engine output power. The optimum rotational speed that gives the maximum output power was also varied depending on the inlet pressures. For example, at inlet pressure of 4 Bar, the rotational speed was 1500 rpm while at 10 Bar it was 3000 rpm. This optimum rotational speed was determined at each investigated pressure by fixing the inlet pressure and running the engine at various speed to achieve the highest power output. The high pressure air inlet temperature was 300 K and all walls are assumed to be adiabatic [85].
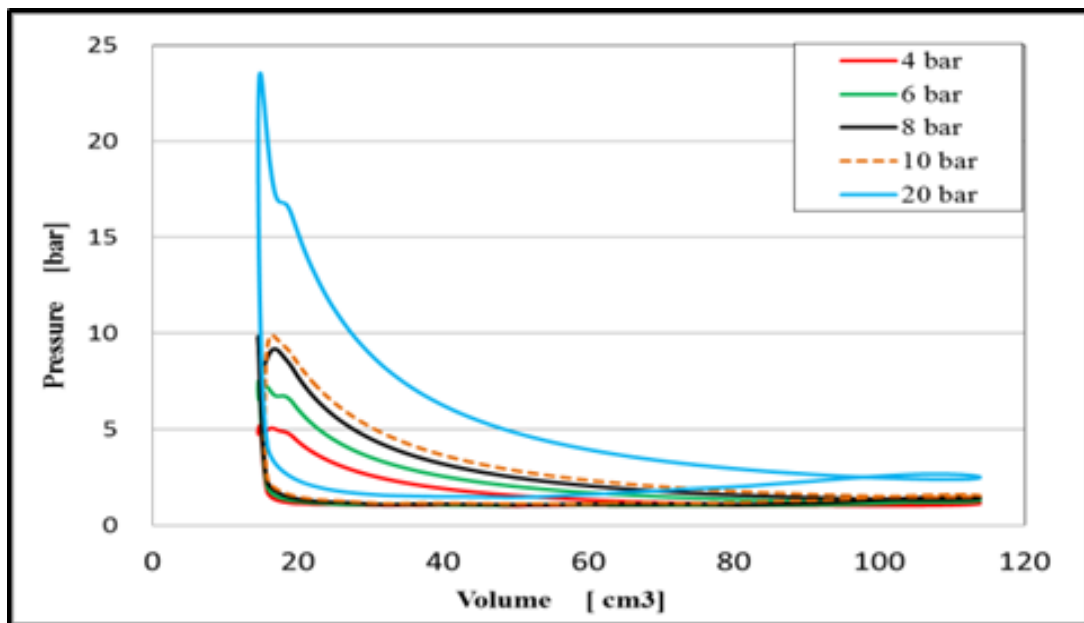
Figure 4-45: The engine P-V diagram at various inlet pressure [85]

Figure 4-46 and Figure 4-47 show the variation of pressure and temperature inside the engine, respectively, versus the crankshaft angle where both of them have increased higher than the inlet conditions. This is due to the rapid change of pressure inside the engine cylinder while the piston is moving up to the TDC (90-100 degree of crank angle). Although the inlet

temperature was 300 K, the engine temperature decreased by about 50 degree during the expansion process as shown in Figure 4-47 [85].
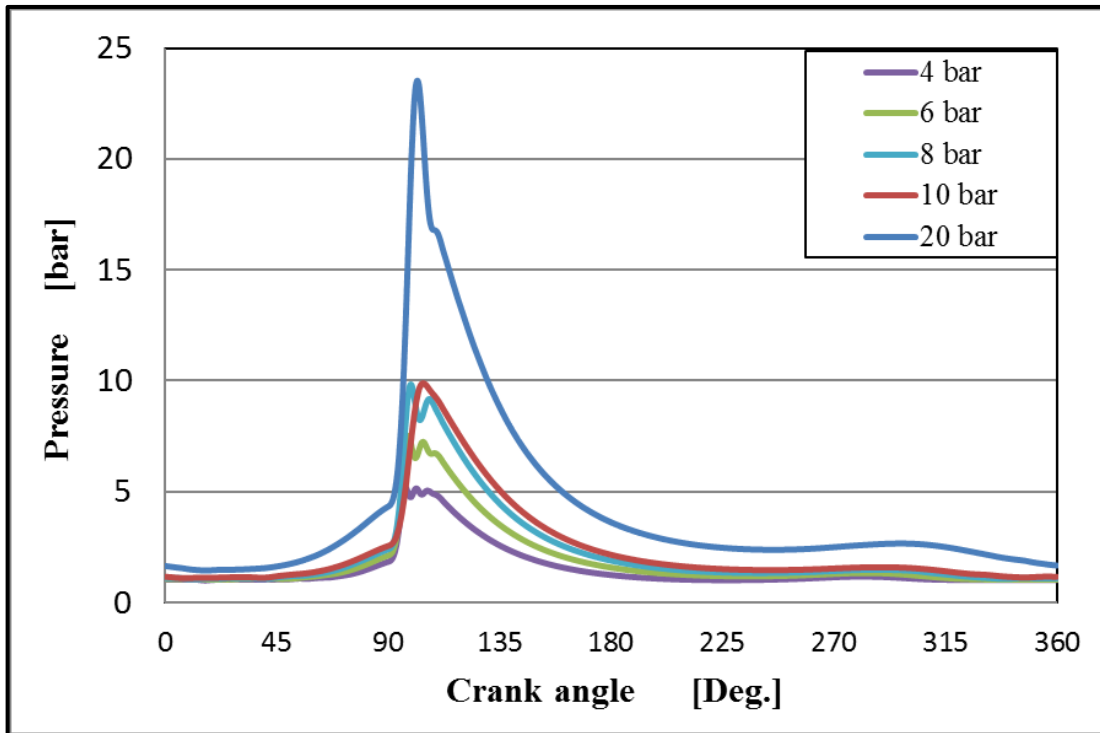
Figure 4-46: Variation of engine pressure and temperature versus the crankshaft angle [85]
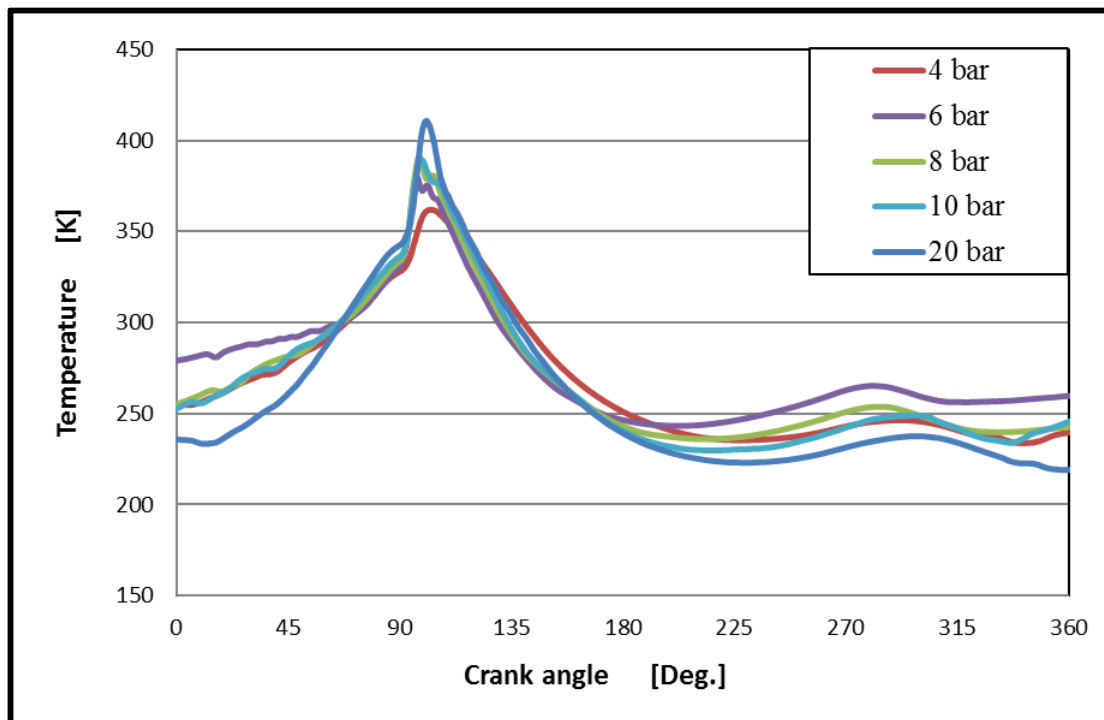
Figure 4-47: Variation of engine temperature versus the crankshaft angle [85]

The output power from the engine and the mass flow rate at each charge pressure is presented in Table **4**-**4**. The proposed systems generate cooling and electric power and the cooling power from the LAir (based on engine mass flow rate) was also calculated in the table. Equivalent electrical power which provides the same amount of cooling was calculated using COP value of 3.5 in order to calculate the total generated power in the form of electricity. At the charge pressure of 20 Bar the total output power reached 5.1 kW which is enough to cool and power a normal domestic house.

Table 4-4 Output power and the mass flow rate at various inlet pressure [85]

Inlet pressure [bar]	LAir mass flow rate [kg/s]	Power output [kW]		Equivalent electrical power	Total power [kW]
		Electric	Cooling		
4	0.0018	0.160	0.7485	0.2994	0.3739
6	0.0036	0.368	1.4975	0.5990	0.7959
8	0.0060	0.641	2.4971	0.9988	1.3544
10	0.0089	0.902	3.7477	1.4991	1.9728
20	0.0239	2.245	10.0176	4.0070	5.1072

4.4 Summary

This chapter presented various CFD simulations that have been carried out (i) including the modeling boiling process of flow of LN2; (ii) enhancing the heat transfer coefficient during and after the the evaporation process using different finned tube; (iii) modeling evaporation process of LN2 using a secondary fluid in cryogenic heat exchanger; (iv) investigating the effect of the tube geometry on the heat exchanger performance using various tube configuration and (v) modeling LN2/LAir reciprocating engine.

The CFD modeling of the evaporation process of LN2 using Eularian and Mixture methods was carried out and results were compared with an experimental data available in the literature showing good with maximum deviation less than 10%.

To investigate the effect of the geometry shape on the evaporating process, four different pipe configurations were used. The first configuration was smooth tube with 0.5 mm wall thickness and while the second configuration was a finned tube where the fins are of a rectangular shape with 1 mm height. The third configuration has also a rectangular shaped fins but instead of straight fins along the pipe length, the fins were twisted. The last configuration has cylindrical shape fins with 1 mm thickness. To evaluate the performance of these configurations the results were compared in terms of heat transfer coefficient, heat flux on the outer wall and the pressure drop. The liquid region in all cases (which were only about 10 cm) showed a high heat transfer due to the effect of the bubbles. In the N_2 gas region which covered about 80% of the tube length, the smooth tube showed the lowest heat transfer due to its lowest contact area between the wall and the fluid domain. The cylindrical finned tube showed lower heat transfer enhancement compared to the rectangular finned tube where it reached 79% higher heat transfer coefficient than that of the smooth tube. The rectangular fins enhanced the heat transfer coefficient inside the tube significantly with value reaching 142% and 167% higher than that of the smooth tube for the straight and the twisted fins respectively. This enhancement leads to significant reduction in the tube materials and total heat exchanger size.

Mixture model was used to model the whole heat exchanger due to its less computational time and better conversion compared with Eulerian model. Parametric studies were carried out using different LN2 and ethanol inlet mass flow rates. The result showed that as the LN2 mass flow rate increased the outlet temperature of nitrogen and ethanol decreased, also the N_2 vapour volume fraction decreased. However when the ethanol flow rate increased the nitrogen and the ethanol outlet temperature increased up to certain value then remained almost constant due to the low heat transfer through the gas. As there is limited published work on CFD

modelling an experimental testing of cryogenic heat exchangers, experimental test facility was developed and will be used in the next chapter.

To evaluate the effect of LN2 carrier tube geometry on the outlet conditions from the heat exchanger different cases with different inner tube configuration were modeled. The first case used a smooth tube with 0.5 mm wall thickness while the second case used externally finned tube with rectangular fins of 1mm height. The third case also used external fins but in helical shape with 1 mm height. The fourth and the fifth cases used an internally finned tube with different fin heights of 1 mm and 1.5 mm respectively. The last case used an internally and externally finned tube. The results showed that the internally finned tube cases have better heat transfer due to the increase of the contact surface in the gas N2/Air region.

All cases showed that less than 10% of the whole copper tube length have a temperature below the freezing temperature of ethanol. The solidification model showed that there is no significant solid formed around the copper tube even in the area where the temperature is significantly below that the freezing point of ethanol. This is due to solid ethanol being melted by the circulated relatively hot ethanol.

A reciprocating engine driven by pressurized superheated N2/Air was developed using CFD modeling. The engine bore and stroke were 50 mm. A specific user define function UDF was written using C programming language to simulate piston movement and valve timing. Air was selected as working fluids with inlet temperature of 300K and various inlet pressures (4, 6, 8, 10 and 20 Bar) and rotational speed were investigated.

At LAir mass flow rate of 0.0239 kg/s and inlet pressure of 20 Bar the system generated 10 kW of cooling and 2.2 kW of electricity which is enough to provide the cooling and power demand of a domestic house. Therefore, using of 0.0239 kg/s of liquid air in cryogenic heat

exchanger and a reciprocating engine like those simulated in this work (case 5) have the

potential of providing the cooling and power demand of a domestic house in Libya.

CHAPTER FIVE

EXPERIMENTAL WORK OF LIQUID NITROGEN

EVAPORATION

5.1   Introduction:

This chapter describes the developed liquid nitrogen evaporator test rig facilities with detailed description of each component and the measuring devices. The main objectives of this experimental work were to study the evaporation process of LN2 and to develop a method that increases the heat transfer in the gas region after the evaporation process of LN2, to maximise the recovery of the cold energy stored in LN2 and to validate the CFD model.

5.2   Test Facility Layout

Figure 5-1shows a schematic diagram of the developed test rig consisting of two main circuits which connected through a heat exchanger. The first circuit is an open circuit for circulating liquid nitrogen where the LN2 flow rate, temperature and pressure are measured before and after entering the heat exchanger using a cryogenic flow meter, cryogenic thermocouples and cryogenic pressure transducers. The second circuit is a close loop for circulating a secondary fluid to be cooled by liquid nitrogen. This circuit consists of a water tank with a heater connected to a temperature controller to maintain the tank temperature at a certain value and a pump to circulate the water between the tank and the heat exchanger. The water inlet and outlet temperature from the heat exchanger are measured using thermocouple probes while the flow rate was measured using Platon NGX flow meter. The heat exchanger is a concentric tube in tube heat exchanger where the hot water flows in the annular space while the LN2 flows in the inner tube. Water was selected as the working fluid of the second circuit for many

reasons; firstly to validate the results from the CFD model that showed the water will not freeze during the circulating process; secondly its availability and safe to use. The outer tube is made of glass to observe any freezing that happen during testing while inner tube and all LN2 carrier tubes were made of copper. Surface thermocouples were fitted on the outer surface of the inner tube to measure the surface temperature.
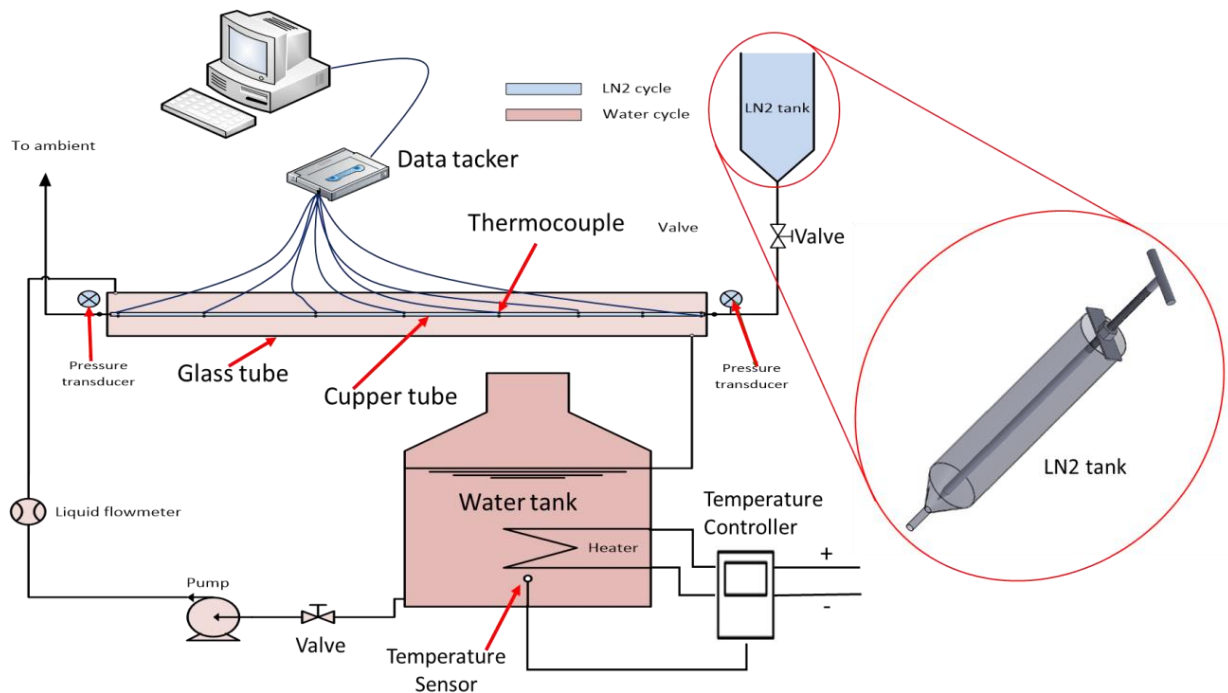
Figure 5-1: Schematic diagram of LN2 evaporation test rig

In this test rig, the LN2 is drawn from a small insulated tank and passed through 8mm copper tube to the heat exchanger. Pressure transducer and a thermocouple are fitted at the heat exchanger inlet to measure inlet pressure and temperature respectively. The LN2 tank, connecting copper tube, fittings and measuring devices were all insulated using insulation sheet. Then LN2 is passes through the inner tube of the heat exchanger to be evaporated and to leave as gas at relatively high temperature. Different metal meshes as shown in Figure **5-2**, were installed inside the inner tube to enhance the heat transfer inside the copper tube. Pressure and temperature sensors were also installed at the heat exchanger outlet.

Figure 5-3 shows a picture of the developed experimental test rig facilities with its all components.
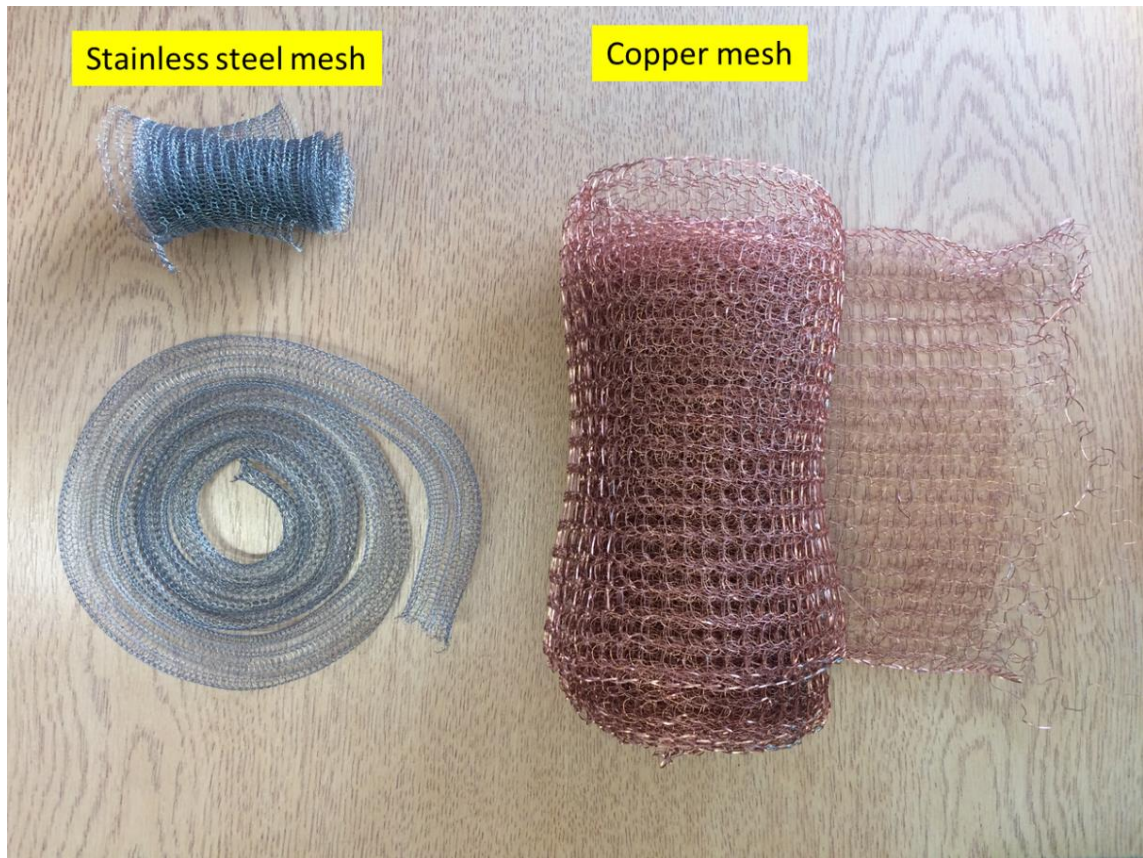
Figure 5-2: Metal mesh

Regarding the water circuit a special insulated tank was used which was filled with water to a certain level (about 10 cm above the heater). To control the water temperature inside the tank a 3 kW electric heater was fitted at the bottom of the tank and connected to a temperature control system. The control system measures the water temperature inside the tank and turns on/off the heater when the required temperature is reached. The water flow rate and the water inlet/outlet temperatures to the heat exchanger were also measured. All the pressure and the temperature sensors on both the LN2 and water circuits were connected to data loggers that is connected to a PC to monitor and record all measurement.
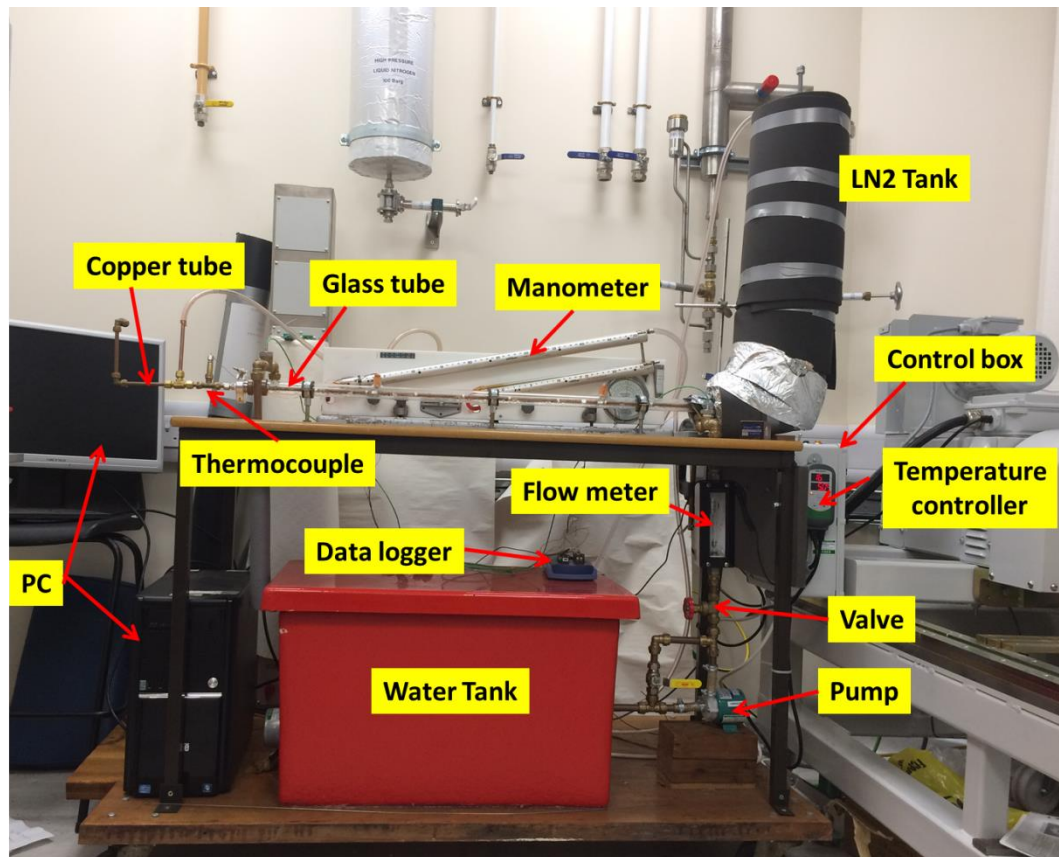
Figure 5-3: Experimental work test facility

5.3 Heat Exchanger

Parallel flow cryogenic concentric heat exchanger was designed and manufactured. The inner tube is made of copper tube with 8 mm OD and 0.5 mm wall thickness while the outer tube was made of a special glass to observe any ice forming around the copper tube during experiment at testing. The glass tube was designed to handle cryogenic temperature and it has dimensions of 28 mm OD and 3 mm thickness. The heat exchanger total length was 1000 mm. Figure 5-4 shows a detailed drawing of the heat exchanger assembly where a push copper fittings with rubber sealing were connected to both ends of the glass tube. Stainless steel KF fittings were connected to the other side of the copper fittings and tube feed through fittings with plastic sealing that allows the copper tube shrinking or expanding without leakage during operation. The low temperature of LN2 could lead to significant shrinking of

the copper fittings compared to the shrinking of the glass tube which can lead to damaging the glass tube. Therefore thermal and structural analysis of the whole heat exchange was carried out to predict the effect of the operating conditions on the mechanical reliability of the heat exchanger connections.
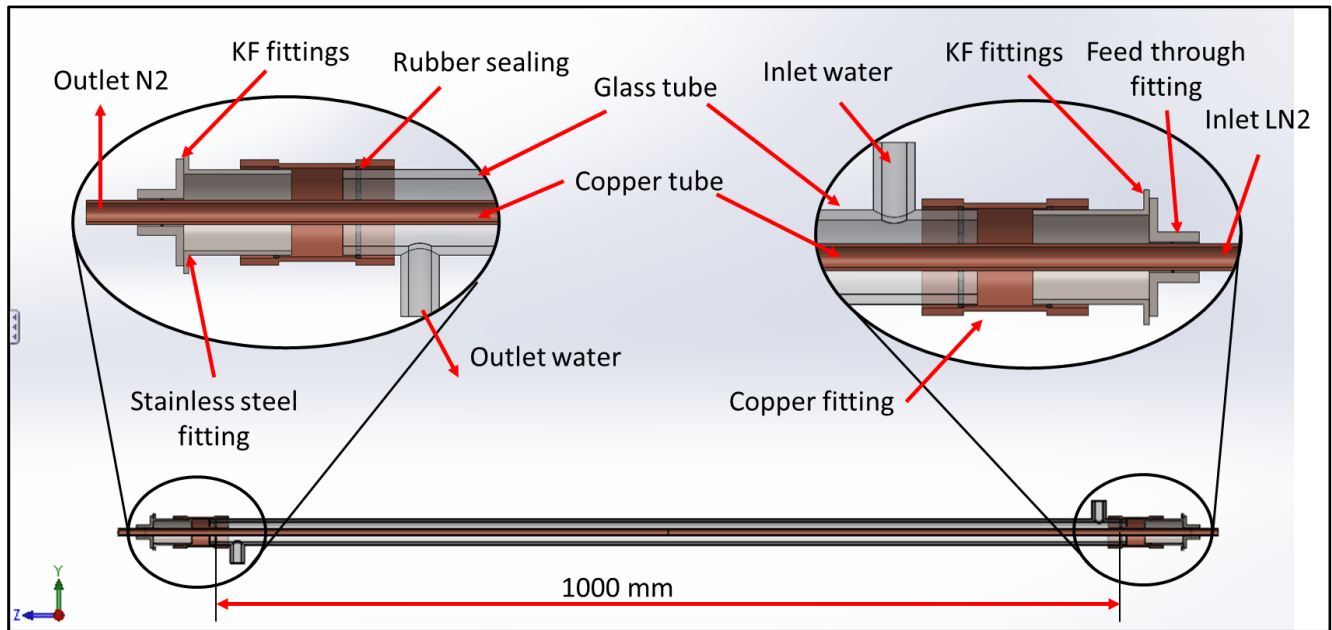
Figure 5-4: Detailed drawing of the heat exchanger

5.4   Thermal and Structural Analysis

To predict the temperature distribution along the heat exchanger and its effect on the glass tube and its connection, a thermal and structure analysis were carried out using Steady-State Thermal and Static Structural models in the Ansys software. Figure 5-5 shows the detailed heat exchanger geometry developed in Ansys workbench and the material properties used. A very fine tetrahedron mesh was used.

In this analysis a worst scenario where the whole inner tube filled with LN2 at 77 K was assumed. Heat convection with a value of 15 W/m^2.K and ambient temperature of 15 °C were applied on the outer surface of the glass tube and other fittings.
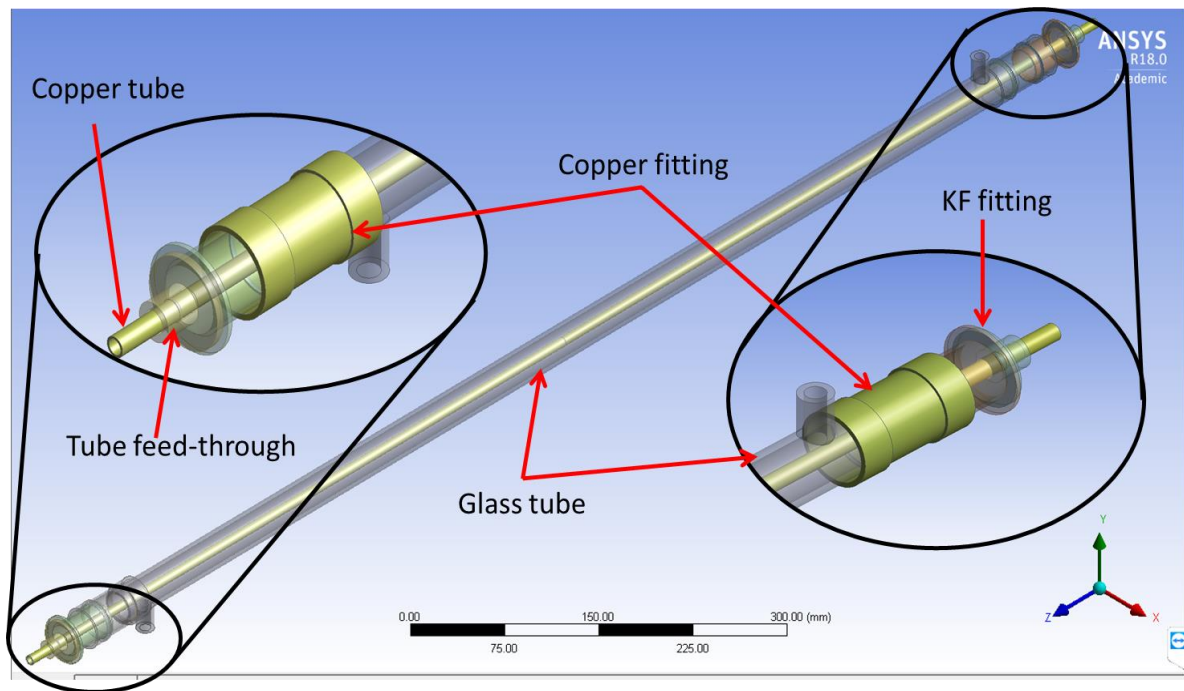
Figure 5-5: Heat exchanger geometry

Figure 5-6 shows the results of the thermal analysis of the heat exchanger where it is clear that the temperature of the copper fittings connected to the glass tube is about one degree below the ambient temperature indicating that there will be no significant contraction of the metal part that could damage the glass tube. The figure shows clearly the temperature gradient where the temperature of the fittings that is very close to the copper tube (LN2 carrier) reached -124 °C while near the copper fittings the temperature reached -5 °C. The other side of the copper fitting where it connected to the glass tube the temperature is only one degree below the water temperature which is 18 °C.

Regarding the static structural analysis, the results of the thermal analysis were applied as the main load and the glass tube was assumed to be fixed as in the real test rig. Figure 5-7 shows the results of the heat exchanger total deformation which is in the order of 10^{-6} m. This is significantly lower than the clearance of the connection parts (0.5 mm). The maximum deformation was at the ends of the copper tube which have the maximum thermal expansion

and maximum length of the heat exchanger. Therefore the risk of damaging the fittings used seems to be very low.
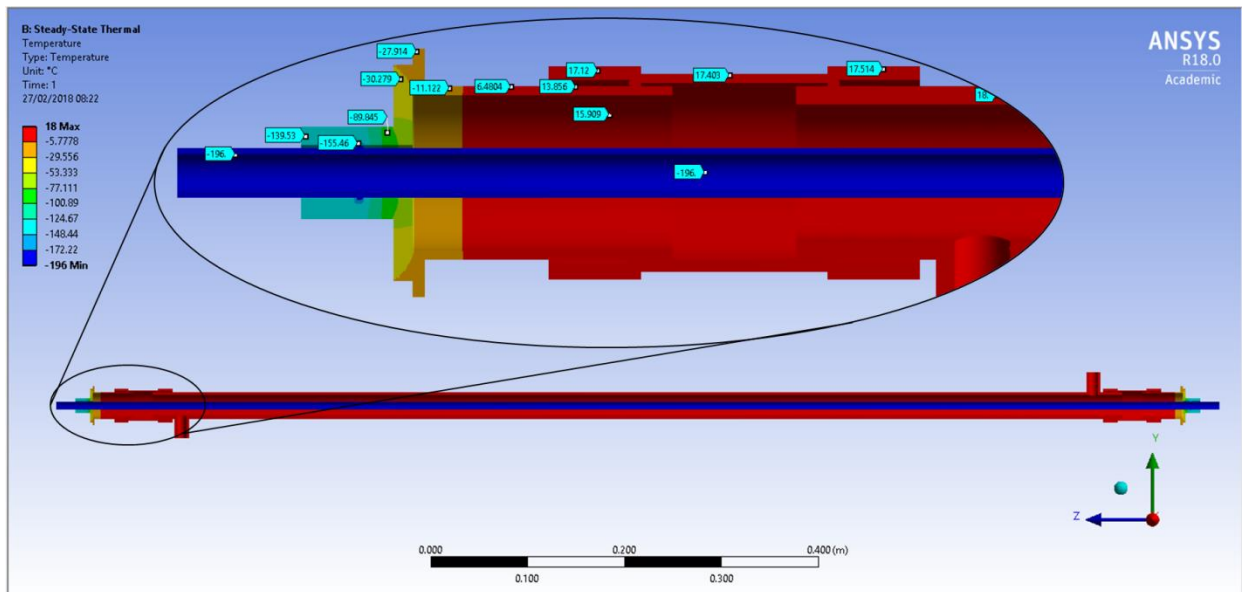
Figure 5-6: Thermal analysis of the heat exchanger
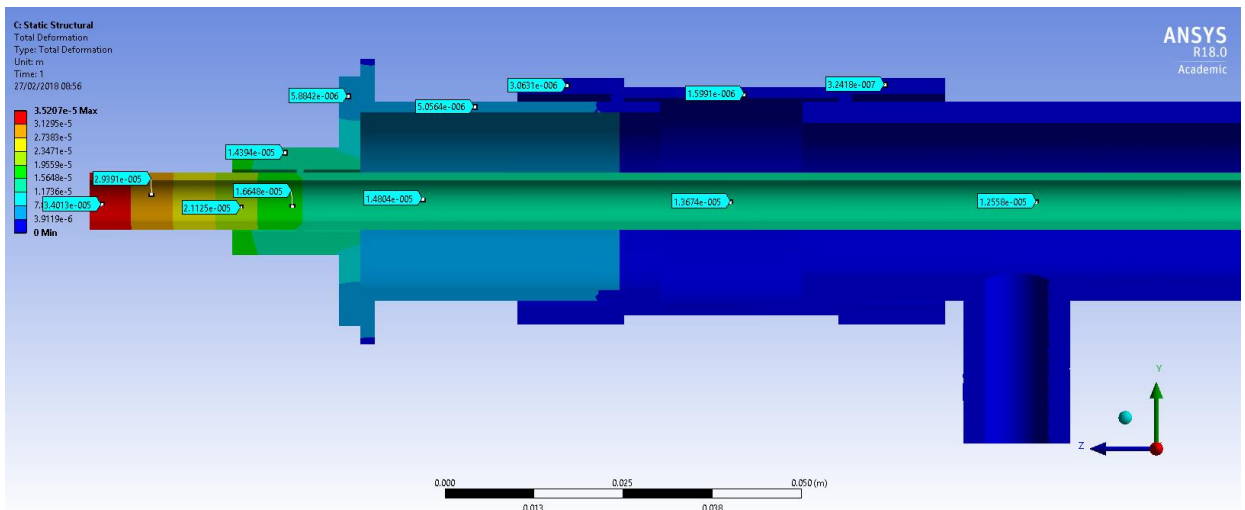
Figure 5-7: Total deformation of the heat exchanger

5.5 Cryogenic tank

Figure 5-8 shows the cryogenic tank manufactured to store the liquid nitrogen. It consists of 200 mm long copper tube with a diameter of 54 mm connected to reducer (54 to 15 mm)

using a copper push fitting, welded to another reducer from 15 mm to 8mm. The tank overall capacity is 0.517 L. The figure also shows the tank insulation where 23 layers of an insulation sheet with thickness of 3 mm and thermal conductivity of 0.035 W/m.K were wrapped around the tank. An Aluminium foil was also used between each two layers to reduce the radiation heat transfer. Considering the insulation, the tank total diameter became 220 mm. To control the flow of LN2 from the tank, an adjustable bar was installed inside the tank.

Figure **5-9** shows the adjustable bar connected to the LN2 tank lid. It is like a long screw with needled head. The lid fitted on the top of the LN2 tank and the bar can be adjusted by rotating it clockwise or anticlockwise. The lid has many holes to avoid pressure building in the system due to continuous evaporation of LN2.
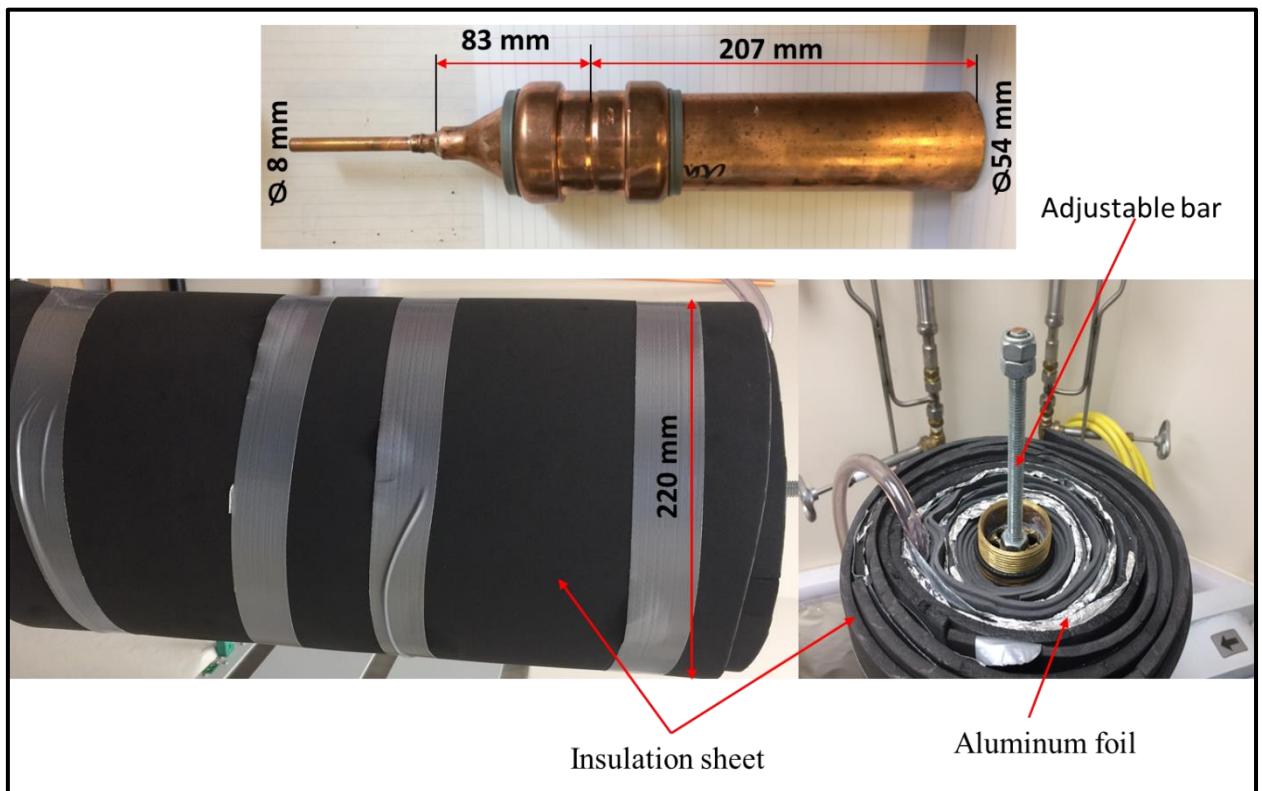
Figure 5-8: Test rig LN2 tank
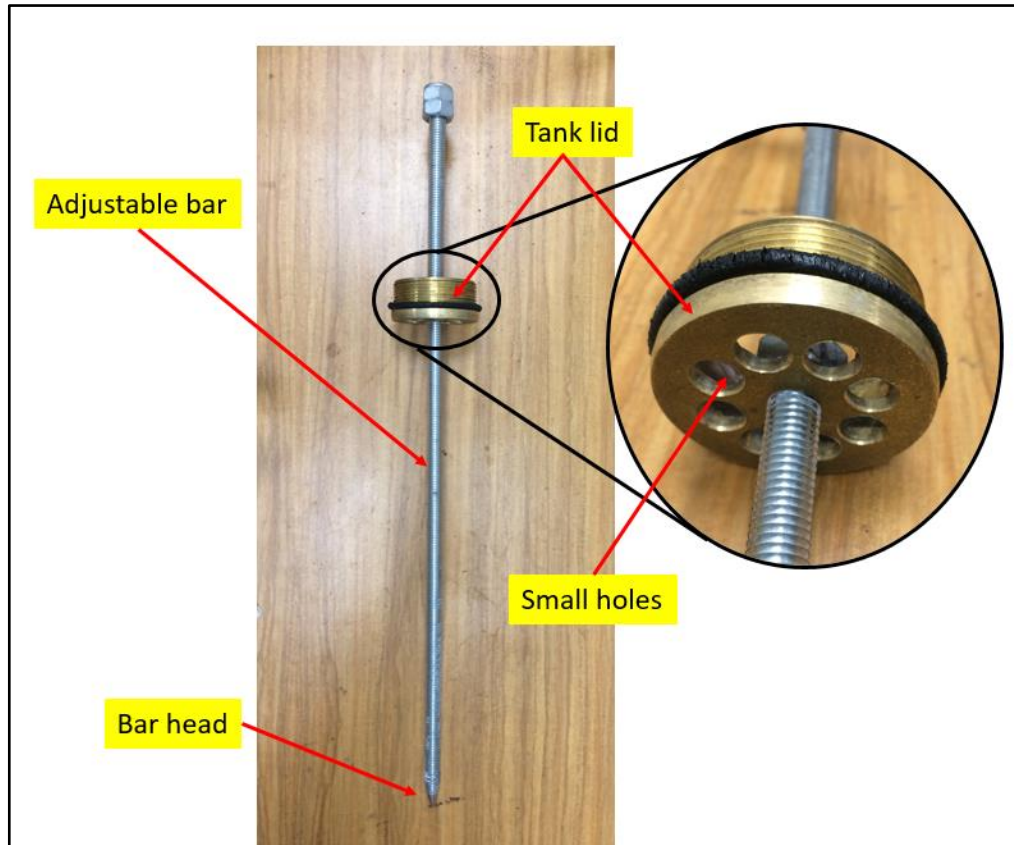
Figure 5-9: Adjustable bar

5.6 Water tank

An insulated tank was designed and manufactured by Precolor Tank Division Company. The tank has a nominal capacity of 68 Litters with internal dimensions of (610 X 305 X 396 mm) and insulation thickness of 50 mm. The tank insulation is made of expanded CFC free polyurethane encapsulated foam. The tank has three small ½ inch ports; one at the bottom of the tank connected to the circulating pump and the other two ports at the top for returning the cold water and installing measuring instruments in the tank. Also there is another 2 ¼ inches port for fitting a 3 kW electrical heater. The tank can be used for various working fluids such as pure water or glycol or mixture of both, also the operating temperature can be as low as -50 °C.

5.7 Pump

A Chemical-Resistance Centrifugal Pump made of Polypropylene was used to circulate the secondary fluid. The pump maximum flow rate is 8.7 LPM and its operating temperature is -50 ^{o}C. It is suitable for wide range of working fluids including water, glycol and mixture of both. Figure 5-10 shows the pump and how it is connected in the test rig. A bypass line with valve was fitted between the pump intake and exit lines to control the water flow rate without increasing the pressure after the pump.
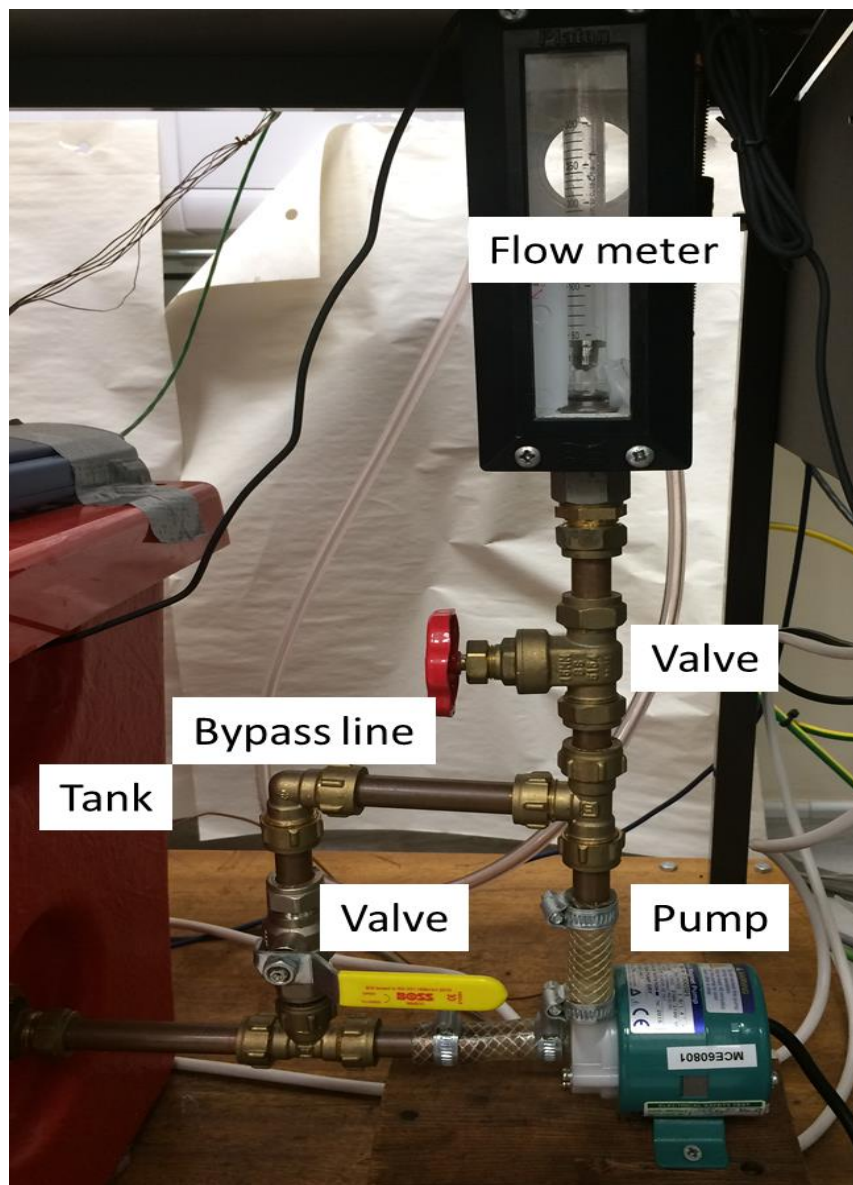
Figure 5-10: The circulation pump installation

5.8   Measuring Devices

To evaluate the system performance, several measuring devices were installed in the test rig. These measuring instrumentations include thermocouples, manometer and flow meter which are described in more details in the following sections.

5.8.1   Thermocouples

For measuring the temperature two different types of temperature sensors were used: the first type was for measuring the outer surface temperature of the inner tube where Cement-On Surface Thermocouples were selected. They are K-type thermocouple that can go to -200 C and self-adhesive. Ten of these thermocouples were stuck on the outer surface of the copper tube at equal distances from each other. A very thin aluminium tape was wrapped around the copper tube at sensor tip to ensure that the sensor have good contact with the tube and does not fall due to the flow of water. The thermocouples were wired outside the glass tube through two small holes with rubber sealing to prevent water leakage. The second type of temperature sensors was thermocouple probes which were also type-K. They were installed at the inlet and outlet of the heat exchanger from both the LN2 and the water sides.

5.8.2   Flow Meter

A water flow meter (Platon NGX) with capacity of 300 cm^3/min and accuracy of $\pm$ 1.25% was installed after the pump to measure the flow rate of circulating water in the system. The water flow rate was controlled using a globe valve as shown in Figure 5-10 and various water flow rates were investigated. Regarding the LN2 side, the flow rate was measured by calculating the average time that needs to empty the LN2 tank where an adjustable metal bar was used to control the flow rates.

5.8.3 Pressure Gauge

There was no high pressure in the test rig so an inclined differential manometer was used to measure the pressure drop of the LN2 flow in the heat exchanger. The manometer ends were connected to the 8 mm copper tube at the heat exchange inlet and outlet as shown in Figure 5-3. The manometer fluid relative density was 0.748 and the inclination angle was 49°. The pressure drop was calculated using the following formula:

$$\Delta P = \rho g l \, sin(\theta)$$

5.1

Where θ is the incline angle, l is the fluid level reading on the inclined scale, ρ is the fluid relative density and g is the gravity acceleration.

5.8.4 Temperature controller

A digital temperature controller (Inkbird ITC-308) was used to maintain the water temperature at specific values during the experimental test. Figure 5-11 shows the controller and its electrical circuit. The temperature controller consists of a sensor that was installed inside the water tank and its input power was plugged to the main power line through the main switch in the control box. The temperature in the controller panel can be set at a specific value and once the temperature in the tank decreases below this temperature by specified value (which can be as low as 0.1 degree) the controller turns on the heater that was connected to the controller output power via contactor.
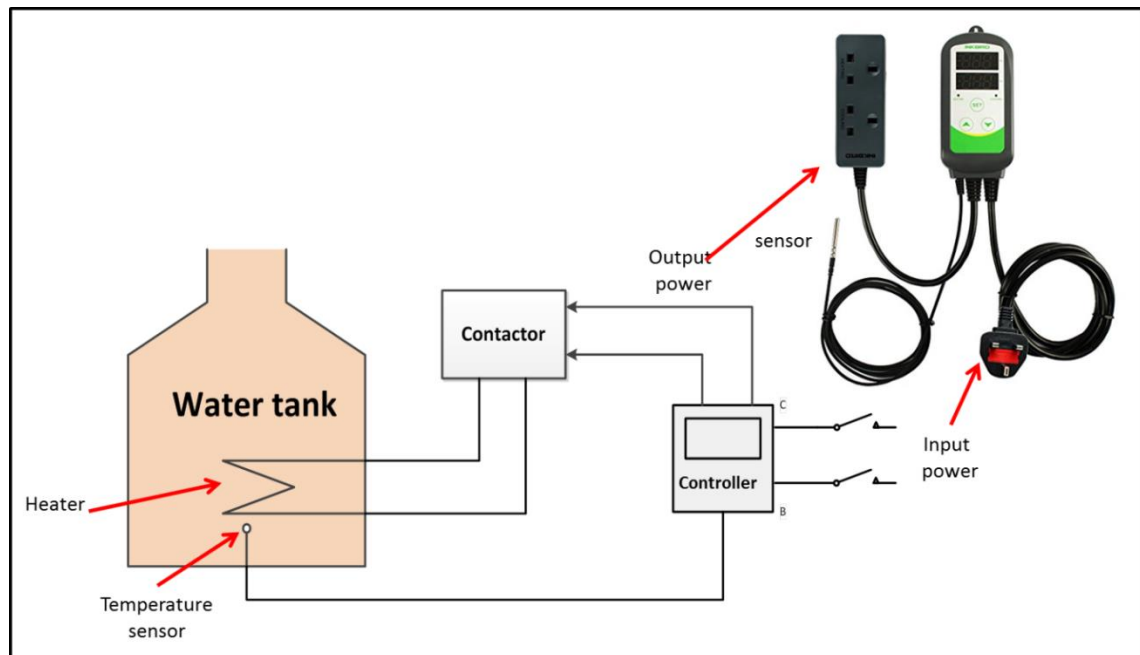
Figure 5-11: Electrical heater and its control system

5.8.5 Data acquisition System

All the surface thermocouples and probes were connected to two data loggers which were connected directly to a computer to read and record the measured data during testing. The used data logger was Pico TC-8 which has eight channels.

5.9 Measuring Devices Calibration

The used surface thermocouples, probes and flow meter were calibrated to evaluate the accuracy of their measurement. The objective of the calibration process is to find a relation between the real value and the measured value. To achieve this, a comparison between the measured value and standard instrument measurements was made.

5.9.1 Thermocouples Calibration

Type K surface thermocouples were used to measure the outer surface temperature of the inner tube of the heat exchanger and another type K thermocouple probes were used to measure the temperature at the heat exchanger inlet and outlet for the LN2 and water sides. All these thermocouples were calibrated versus RTD type thermocouple using a water

container bath fitted with controlled heater as shown in Figure 5-12. The RTD thermocouple

and the K-type thermocouples were installed at the same level in the water container. The

heater input power was controlled by a thermostat which allowed setting the water

temperature at certain values. The starting temperature was 0 °C and increased gradually to

100 °C. Data loggers connected to PC was used to read and record the temperatures.

Figure 5-13 shows the calibration results of one surface thermocouple and one probe versus

the RTD reading. Equations 5.2 and 5.3 give the linear curve fitting equations of the surface

and the probe with R-squared value of 0.9999 and 0.9998 respectively used to find the value

of curve fit parameter (y) in equation (5.3) as:

$$y = 1.0013x + 0.356 \qquad\qquad 5.2$$

$$y = 0.9954x + 0.0087 \qquad\qquad 5.3$$
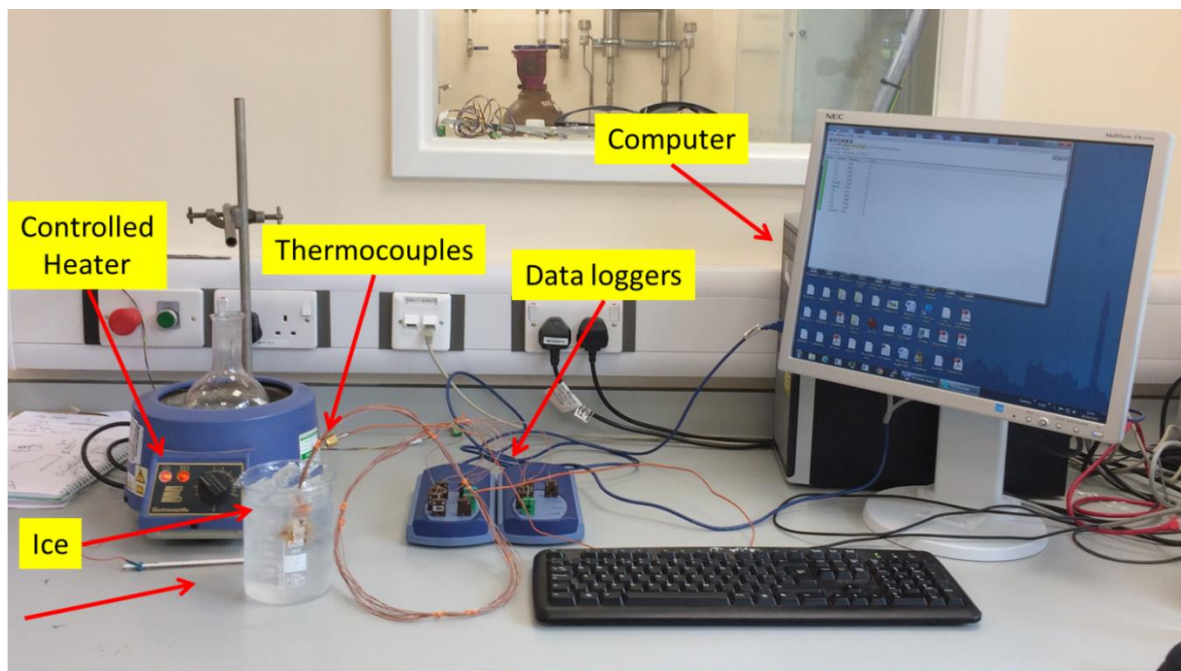
Figure 5-12: Thermocouple calibration process
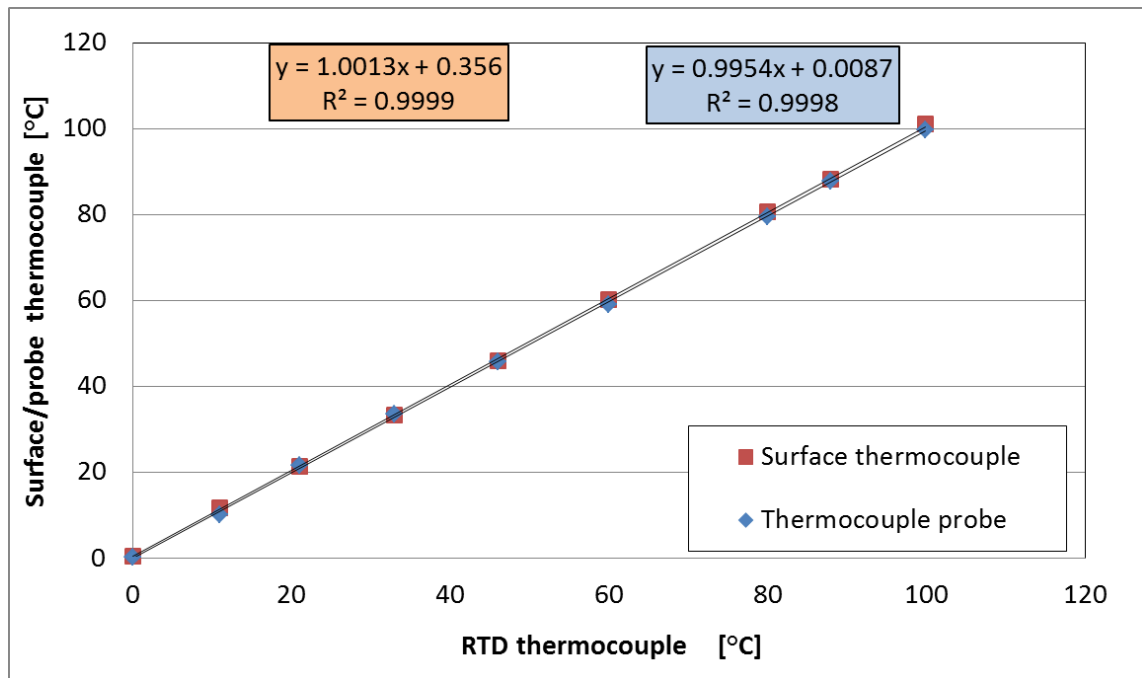
Figure 5-13: Calibration curve of thermocouple No1

5.9.2 Flow Meter Calibration

A labelled standard container with a capacity of 2L and stop watch were used to calibrate the flow meter as shown in Figure 5-14. A globe valve was used to control the inlet water flow rate while the stop watch was used to measure the time needed to fill the container. The process was repeated using different flow rates. Figure 5-15 shows the relation between the measured flow rate and the reading from the flow meter where the R^2 value of the linear fitting was 0.999 using equation 5.4.

$$y = 1.0013x + 0.356 \qquad\qquad 5.4$$
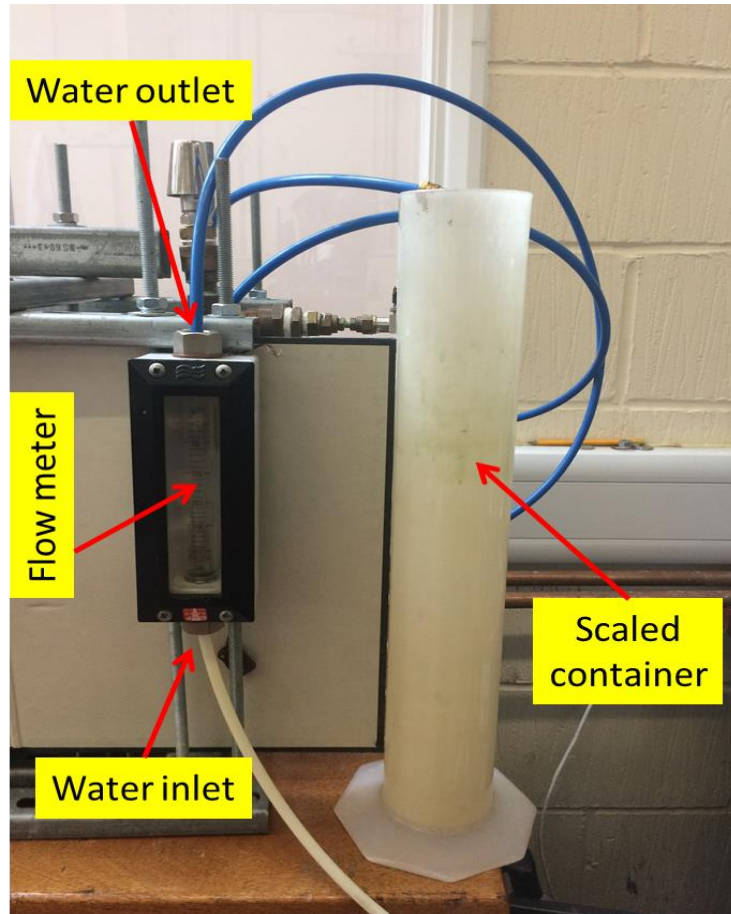
Figure 5-14: Flow meter calibration set up
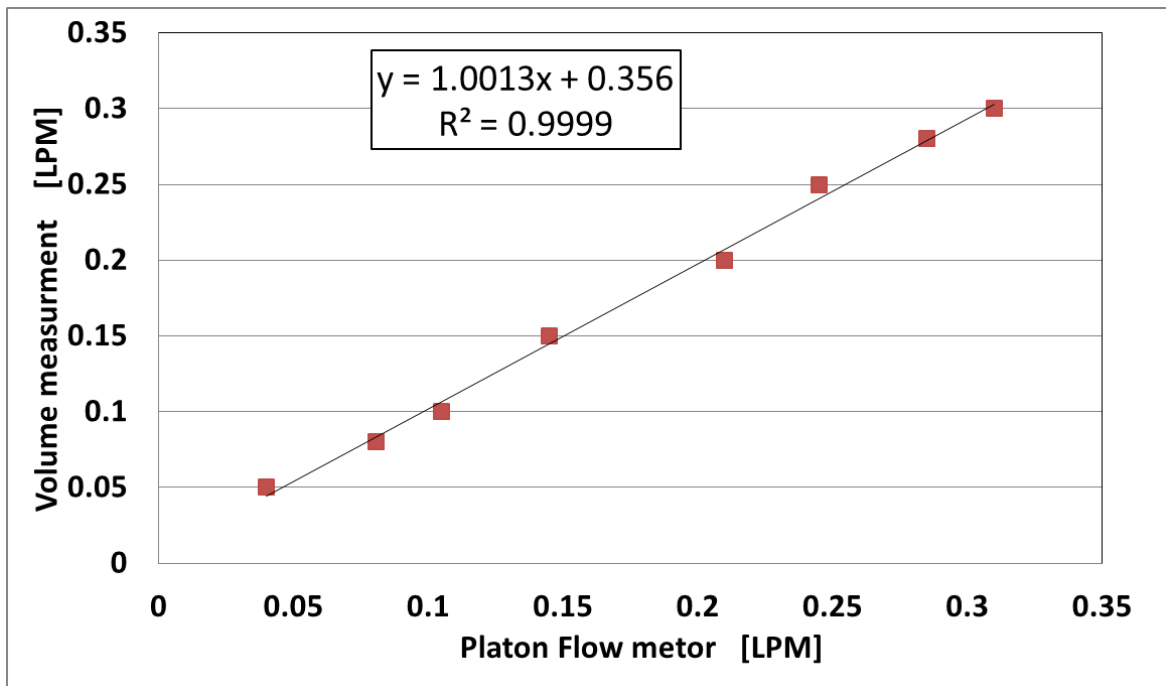
Figure 5-15: Calibration curve of the water flow meter

5.9 Uncertainty Analysis

The experimentally obtained results (R) are affected by the devices used to measure the various parameters (X_i). Errors in measuring these parameters cause deviation of the results from the true values. These errors are classified into two categories; systematic or fixed errors and random errors. The first one (fixed errors) refers to lack of measurement accuracy because of poor calibration, faulty installation and user faults in taking measurements. These errors can be eliminated by devices calibration and appropriate installation [125, 126]. The second errors (random errors) can be defined as fluctuations of the results below and above the actual values. These errors can be statistically analysed using the mean square deviation approach which can achieve a 95% confidence level [97].

$$R = f(X_1, X_2, \ldots . . X_n)$$

5.5

Uncertainty analysis is a method to estimate the error value (U) and the commonly used approach to estimate the overall uncertainty $(U_{Overall})$ is standard mean square summation of the systematic (U_{sys}) and the random (U_{random}) errors as in equation 5.6.

$$U_{Overall} = \pm\sqrt{U_{sys}^2 + U_{random}^2}$$

5.6

For a number M of fixed error sources, the systematic errors can be computed using equation 5.7.

$$U_{sys} = \sqrt{\sum_{i=1}^{M} U_{i,sys}^2}$$

5.7

While the random errors (U_{random}) can be estimated using the standard mean deviation approach with a confidence level of 95% using equation (5.8).

$$U_{random} = t_{N-1,95\%}\sigma_{\bar{S}}$$
<div align="right">5.8</div>

Where: $t_{N-1,95\%}$ is the student distribution coefficient with N-1 degree of freedom, N is the number of samples, and $\sigma_{\bar{S}}$ is the mean deviation calculated using equation 5.9.

$$\sigma_{\bar{S}} = \frac{1}{\sqrt{N}} \sqrt{\frac{\sum_{i=1}^{N}(X_i-\bar{X})^2}{N-1}}$$
<div align="right">5.9</div>

Table **5**-**1** shows the calculation method of uncertainty of one thermocouple while Table **5**-**2** summarise the uncertainty of all other thermocouples.

Table 5-1 An example of uncertainty calculations of one thermocouple

Data point (N)	RTD reading (X_i)	Thermocouple reading	Curve fit equation ($\bar{X}$) $\bar{X}$= 1.0013x + 0.356	Deviation $(X_i - \bar{X})^2$
1	0.01	0.5	0.366013	0.1267
2	11	11.6	11.3703	0.1371
3	21	21.45	21.3833	0.1469
4	33	33.35	33.3989	0.1591
5	46	46	46.4158	0.1728
6	60	60.2	60.434	0.1883
7	80	80.5	80.46	0.2116
8	88	88.1	88.4704	0.2212
9	99.9	101	100.3859	0.2361
Summation of deviation points ($\sum_{i=1}^{N}(X_i - \bar{X})^2$) = 1.6001				
Degree of freedom ($N - 1$) = 8				
Standard deviation ($\sigma_{\bar{S}}$) =0.149076				
student distribution coefficient with N-1 degree of freedom ($t_{N-1,95\%}$)=2.306004				
random errors (U_{random}) = 0.343769K				
Uncertainty of the thermocouple=$\mp$ 0.344677				

Table 5-2 Calibration and uncertainty of surface thermocouples and probes

Thermocouple	Location on the test rig	Curve fit equation	Uncertainty (˚C)
T1	On the inner tube surface	$\bar{x} = 1.0013x + 0.356$	±0.3446
T2	On the inner tube surface	$\bar{x} = 0.9974x + 0.4172$	±0.3020
T3	On the inner tube surface	$\bar{x} = 0.9988x + 0.2502$	±0.1979
T4	On the inner tube surface	$\bar{x} = 0.9965x + 0.2327$	±0.1377
T5	On the inner tube surface	$\bar{x} = 1.0013x - 0.3302$	±0.3980
T6	On the inner tube surface	$\bar{x} = 1x + 0.3406$	±0.4083
T7	On the inner tube surface	$\bar{x} = 1.0013x + 0.0704$	±0.1447
T8	On the inner tube surface	$\bar{x} = 1.0037x - 0.0217$	±0.2446
T9	On the inner tube surface	$\bar{x} = 1.0032x - 0.5259$	±0.6944
T10	On the inner tube surface	$\bar{x} = 1.0029x - 0.5457$	±0.6930
Probe 1	LN2 inlet	$\bar{x} = 0.9985x - 0.0363$	±0.0697
Probe 2	LN2 outlet	$\bar{x} = 0.9984x - 0.2121$	±0.1456

5.10 Test Procedure

An experimental test facility was developed to assess the potential of using liquid nitrogen to generate cooling for air conditioning and to evaluate the performance of the secondary fluid flow in the annular space during indirect contact with LN2. Also the experimental work was carried out to validate the CFD modelling. The tests were carried out using different flow rates of the secondary fluid and the LN2, and with and without heat transfer enhancement using metal mesh.

The testing procedure is summarized as following:

1- The water tank was filled with water up to 10 cm above the heater to avoid increasing the heater surface temperature and to achieve good temperature distribution of the water inside the tank.

2- All thermocouples were connected to data loggers and PC to monitor and record the temperature at the heat exchanger inlets and outlets and the outer surface of the inner tube.

3- The water temperature in the tank was set at a specific value using the temperature controller.

4- The circulating pump was switched on to circulate the water between the tank and the heat exchanger, and its flow rate set at a certain value using the globe valve installed after the pump and the bypass valve.

5- Once the temperature in all system became steady and all thermocouples show similar readings, LN2 tank was filled slowly with liquid nitrogen. Due to the relatively high initial temperature of the LN2 tank and the piping system, the boiling process of LN2 is very fast and strong at the beginning until the tank, walls and the insulation temperature become close to LN2 saturated temperature at atmospheric pressure then the boiling process decreases gradually.

6- Once the system temperature became steady, the LN2 tank was filled again and the data was recorded. In order to calculate the LN2 flow rate a stop watch was used to measure the required time to empty the LN2 tank.

7- The top surface of the LN2 tank should be always open during the test time to avoid pressure build up in the system.

5.11   Results of the experimental work

Four different cases were experimentally tested and their results are presented in this section. In the first and second cases, a smooth copper tube was used as the inner tube of the heat exchanger while in the third and fourth cases stainless steel mesh was installed inside the smooth tube in order to enhance the heat transfer. The experimental work was carried out

using different LN2 and water flow rates. During experiments, the heat exchanger inlet and outlet temperatures and flow rates of water and LN2 sides were monitored. Also the inner tube outer surface temperature was measured using ten surface thermocouples that were pasted on the surface at equal distance from each other. The following figures present the heat exchanger inlet/outlet conditions and the inner tube temperature of four each case, and a comparison between them was also made.

Figure 5-16 and Figure 5-17 show the heat exchanger inlet and outlet temperature of both sides for the case of smooth tube (first case) where the LN2 and water flow rates were 0.103 LPM and 0.300 LPM, respectively. The LN2 inlet temperature was about -194 C while the a average outlet temperature was about -70 °C indicating a great amount of cold energy was wasted and rejected to the ambient. The water inlet temperature was about 18.5 °C and it dropped by 5.9 degree at the outlet as shown in Figure 5-17.
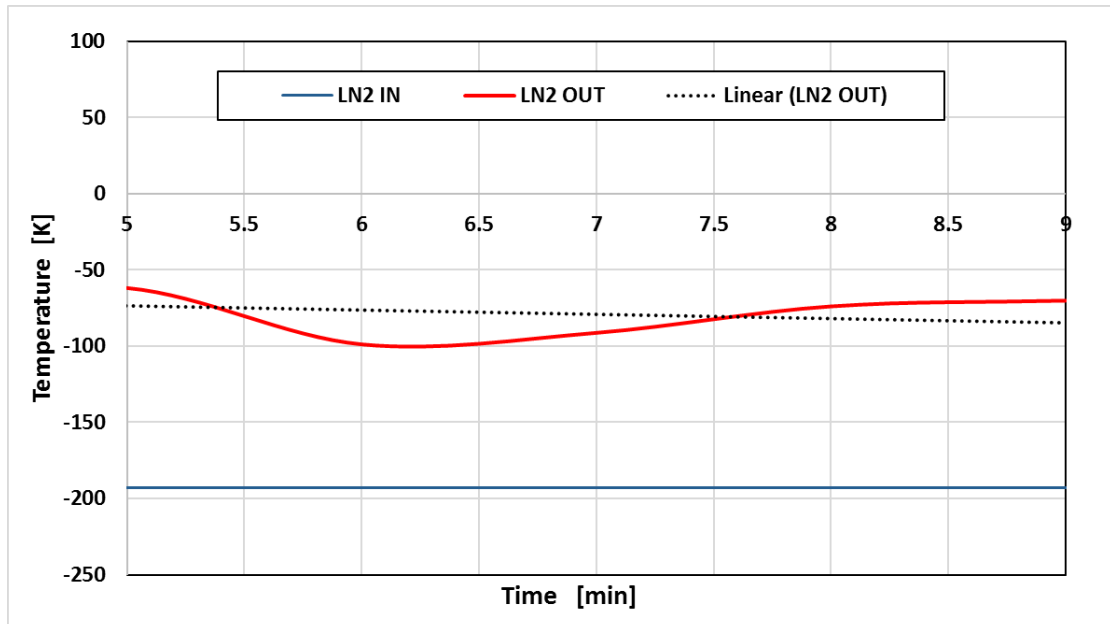
Figure 5-16: LN2 inlet and outlet temperature for the first case
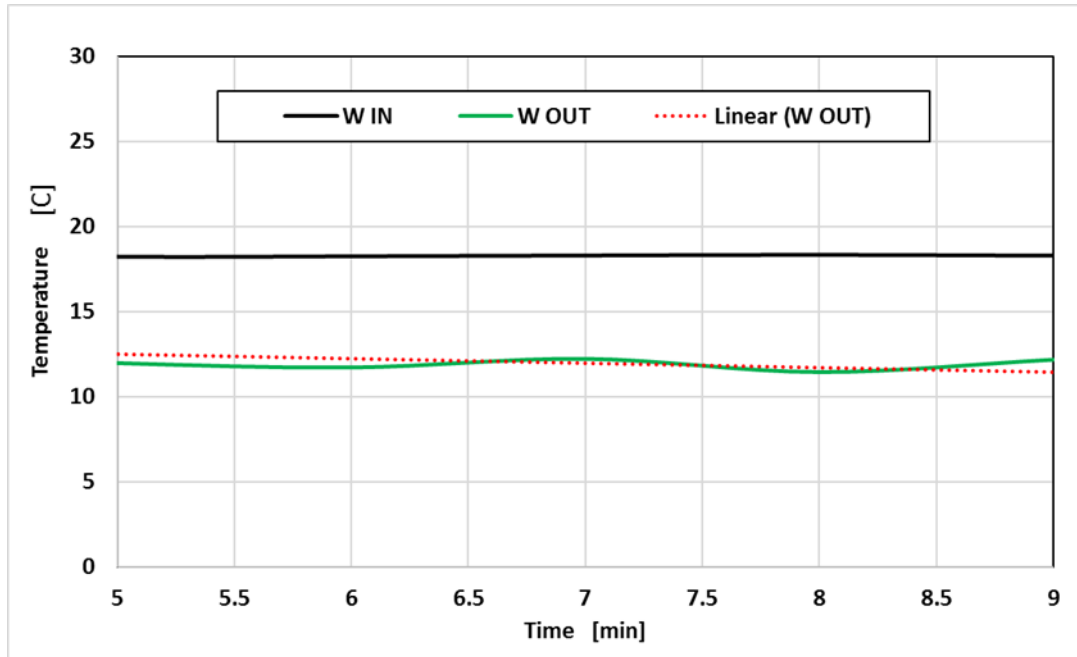
Figure 5-17: Water inlet and outlet temperature for the first case

Figure 5-18 shows the inner tube temperature gradient at ten different locations where T1 is the closest point to the heat exchanger LN2 and Water inlets while T10 was closest point to the outlets. Although the tempperature of LN2 flow inside the tube was extremelly low, the outer surface temperatures were closer to the water temperature, and the trend shows that as the water temperature decreases the wall temperature, reduce. The average wall temperature was 5 °C.

The energy loss was calculated using the energy balance of the two fluids in the heat exchanger using equation (**5.10**), and the resuls showed that the required heat to bring LN2 from the inlet conditions to the room temperature was 270 W while only 124 W was absorbed by water which means about 54% of the cold energy stored in LN2 was lost.

$$Q = \dot{m}\,(C_{p2}T_2 - C_{p1}T_1) \hspace{4cm} 5.10$$

Where $\dot{m}$ is the mass flow rate. T_1 and T_2 are inlet and outlet temperatures, respictively. C_{p1} and C_{p2} are the specific heat capacity of water at the inlet and outlet, respectively .
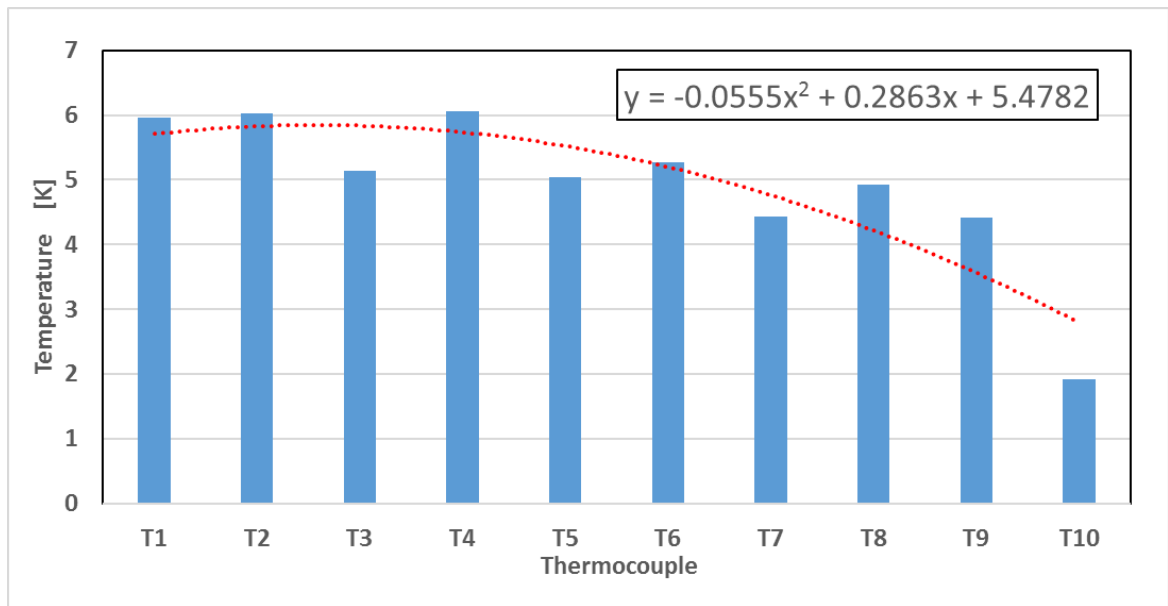
Figure 5-18: The inner tube temperature gradient for the first case

In the second case, also a smooth copper tube was used in the heat exchanger for the LN2 and the LN2 flow rate was controlled using the adjustable bar. The flow rates of the LN2 and water were 0.026 LPM and 0.300 LPM respectively. The heat exchanger inlet and outlet temperatures for the water and the LN2 sides are respectively shown in Figure 5-19 and Figure 5-20 where for the water side they were 18.6 °C and 16.8 °C respectively as shown in Figure 5-19, and for the LN2 they were about -196 °C and 9 °C, respectively as shown in Figure 5-20.
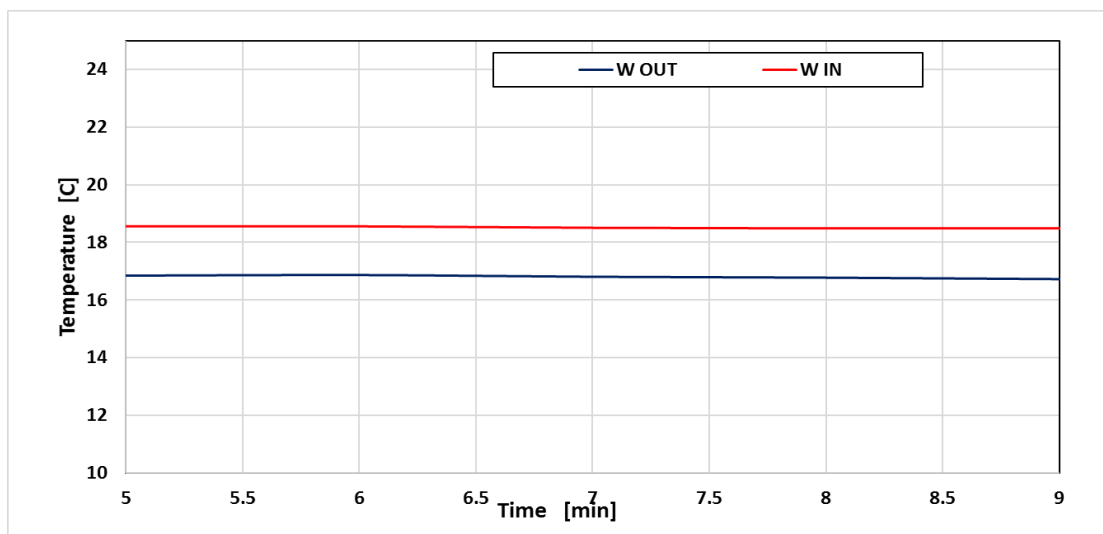
Figure 5-19: Water inlet and outlet temperature for the second case
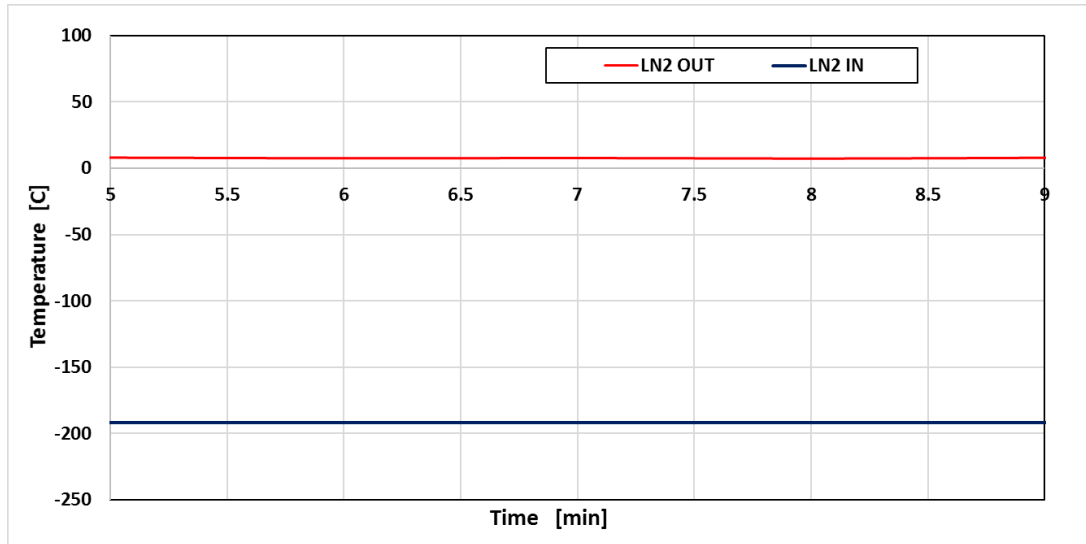
Figure 5-20: LN2 inlet and outlet temperature for the second case

Figure 5-21 shows the temperature of the outer surface of the inner tube. The trend differs from that of the first case due to the significant reduction of the LN2 flow rate, and the average wall temperature was 15.7 °C which is about ten degrees higher than the first case.

Compared with the first case this case showed better preformance where the water absorbs 74% of the cold energy stored in LN2, however the total heat trasfer rate between the fluids was only 37 W.
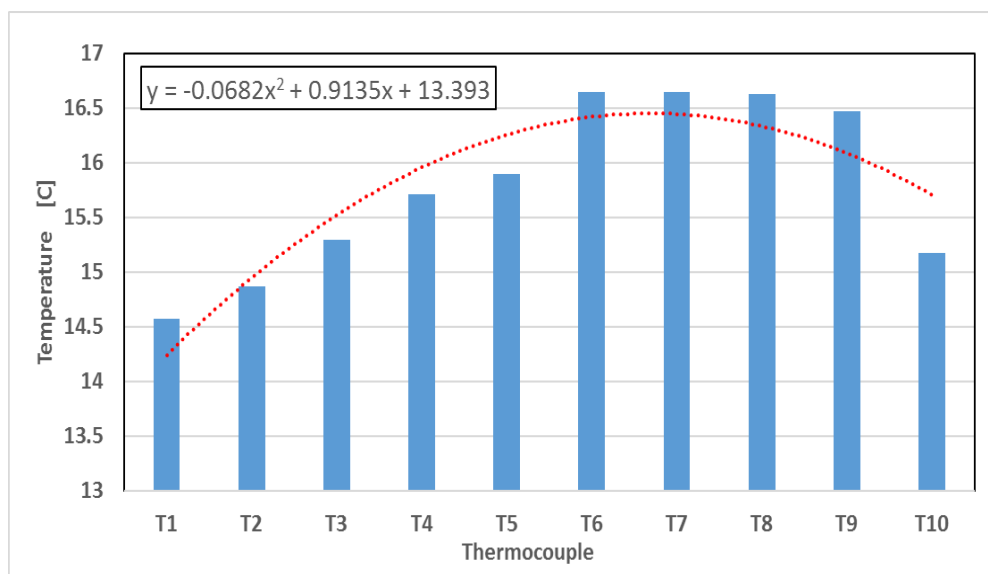
Figure 5-21: The inner tube temperature gradient for the second case

In the third case a stainless steel mesh was installed inside the inner tube to enhance the heat transfer coefficient. The LN2 and water flow rates were 0.032 LPM and 0.200 LPM respectively. Figure 5-22 and Figure 5-23 show the heat exchanger inlet and outlet average temperatures during the experiment where for the LN2 side they are -194 °C and 12 °C respectively, while for the water side they are 18.3 °C and 14.6 °C respectively.
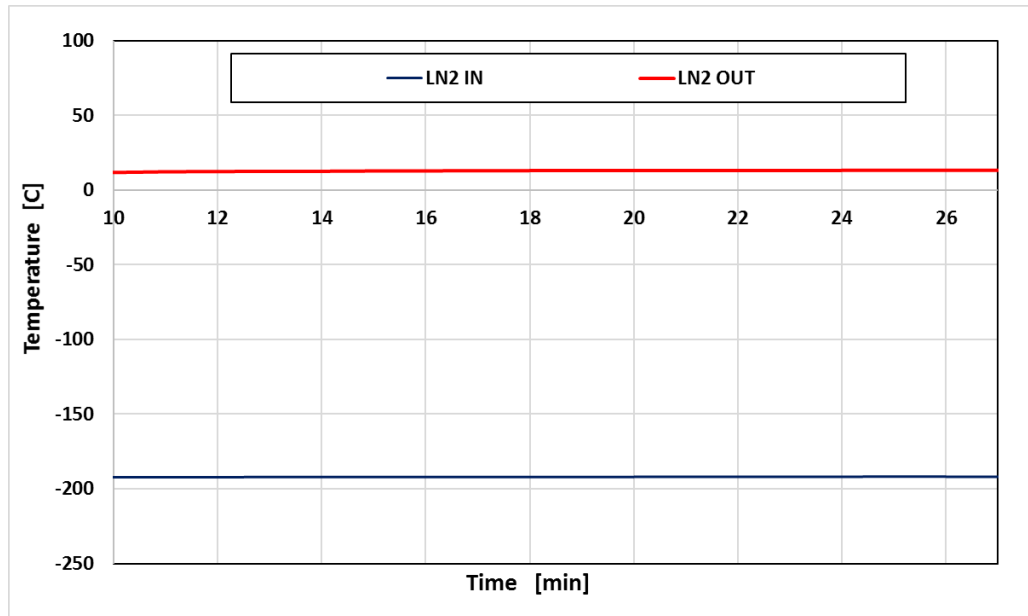
Figure 5-22: LN2 inlet and outlet temperature for the third case
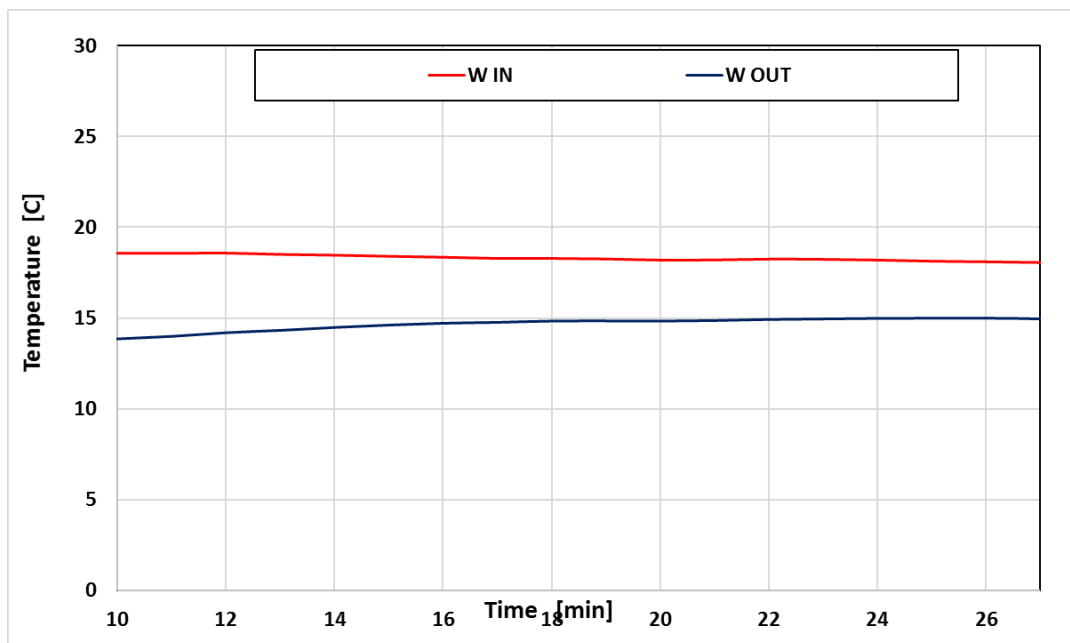
Figure 5-23: Water inlet and outlet temperature for the third case

Figure 5-24 shows the temperature variation along the inner tube outer surface where there is no significant difference along the pipe except for the first position where the temperature reached 5 °C. The whole pipe average surface temperature is 12.3 °C.

Compared with the previous cases, this case showed better heat exchange performance where the water side absorbed 85% of the cold energy in the LN2 side. The heat transfer rate of the water and LN2 sides were 57 W and 67 W respectively.
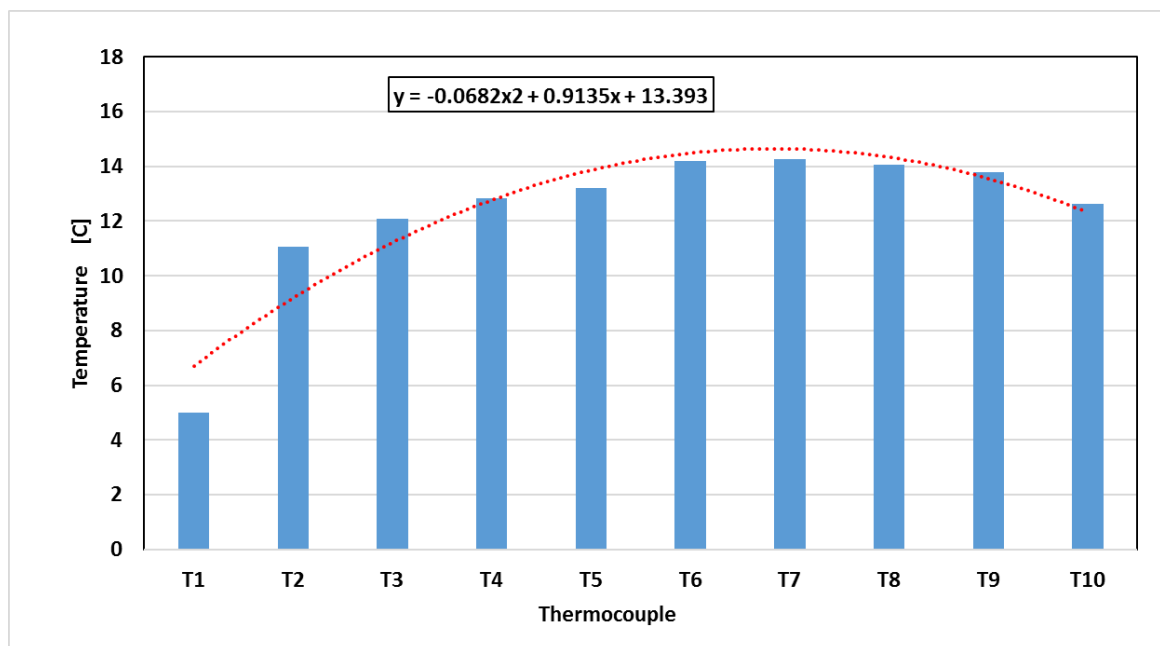
Figure 5-24: The inner tube temperature gradient for the third case

Stainless steel mesh was also used in the fourth case however the LN2 and water flow rates were increased by 37.5% and 50%, respectively. Figure 5-25 and Figure 5-26 show the heat exchanger inlet and outlet average temperatures during the testing where for the LN2 side they are -194 °C and 0 °C respectively, while for the water side they are 15 °C and 9.2 °C respectively.
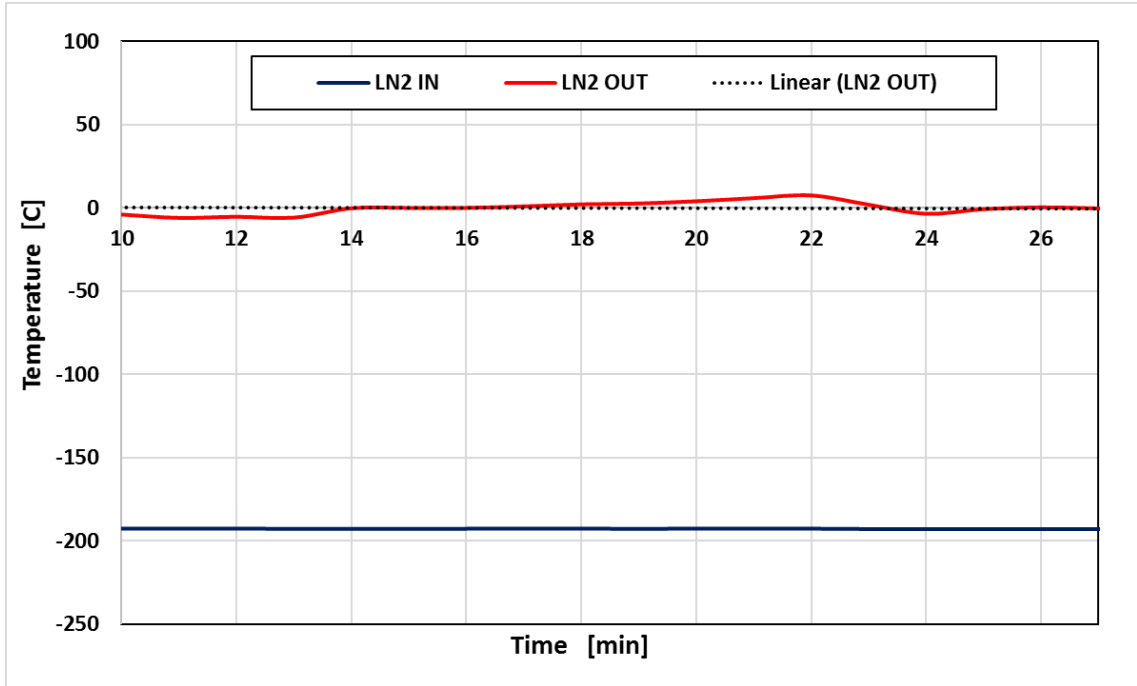
Figure 5-25: LN2 inlet and outlet temperature for the fourth case
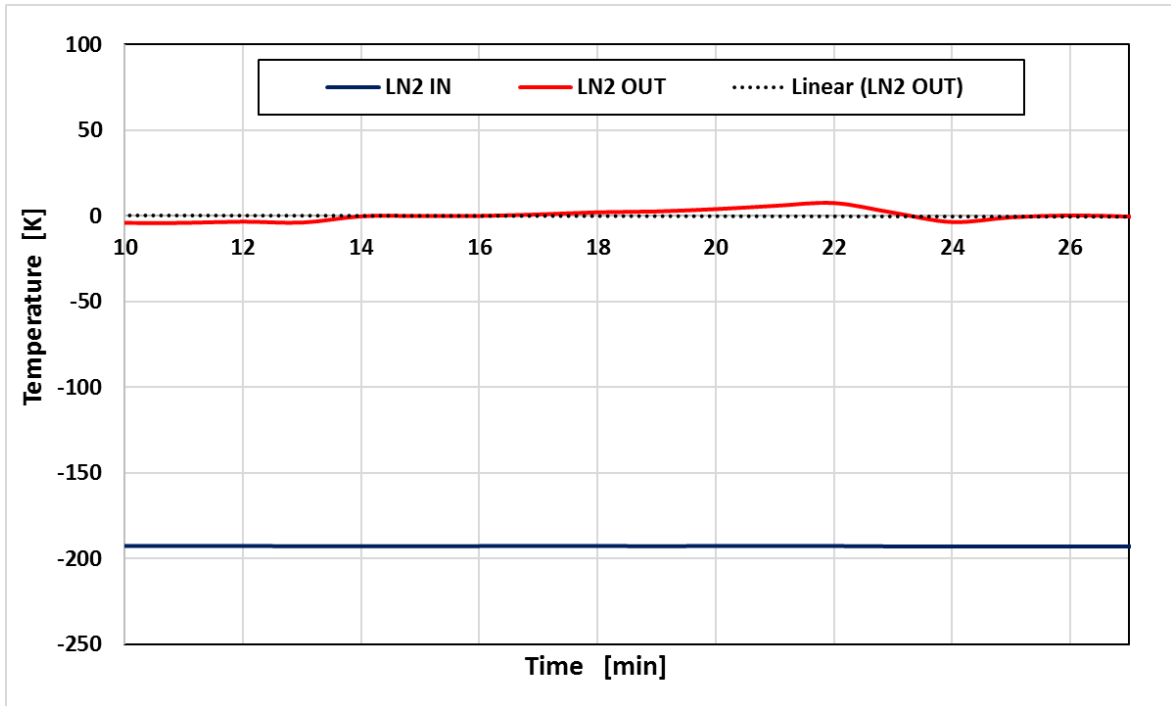
Figure 5-26: Water inlet and outlet temperature for the fourth case

Figure 5-27 shows the temperature distribution along the inner tube outer surface where it is about 1.5 °C at the first point near the water inlet then decreases until it reaches its peak of about -4 °C at the fourth point, then increases until it reaches its maximum value of 3 °C at measuring point nine. This fluctuation in the first half of the tube probably due to the unstable

flow in this region where the boiling and the turbulence flow taken place. The whole tube average temperature was 0.23 °C.

Compared with the third case this case showed higher heat transfer rate for both sides due to the increase in the flow rates which were 123 W and 150 W respectively for the LN2 and water sides. However it showed less performance in terms of cold energy recovery where the water side absorbed 82% of the cold energy stored in the LN2 side.

In first case, where a smooth copper tube was used for carrying LN2, the results showed that; compared to other cases this case was having the highest LN2 flow rate and it was flowing from the LN2 tank level to the heat exchanger level naturally by the effect of gravity acceleration without any restriction.

The equation shown in the figure:

$$y = 0.0036x^5 - 0.102x^4 + 0.9917x^3 - 3.6015x^2 + 3.0246x + 1.1834$$
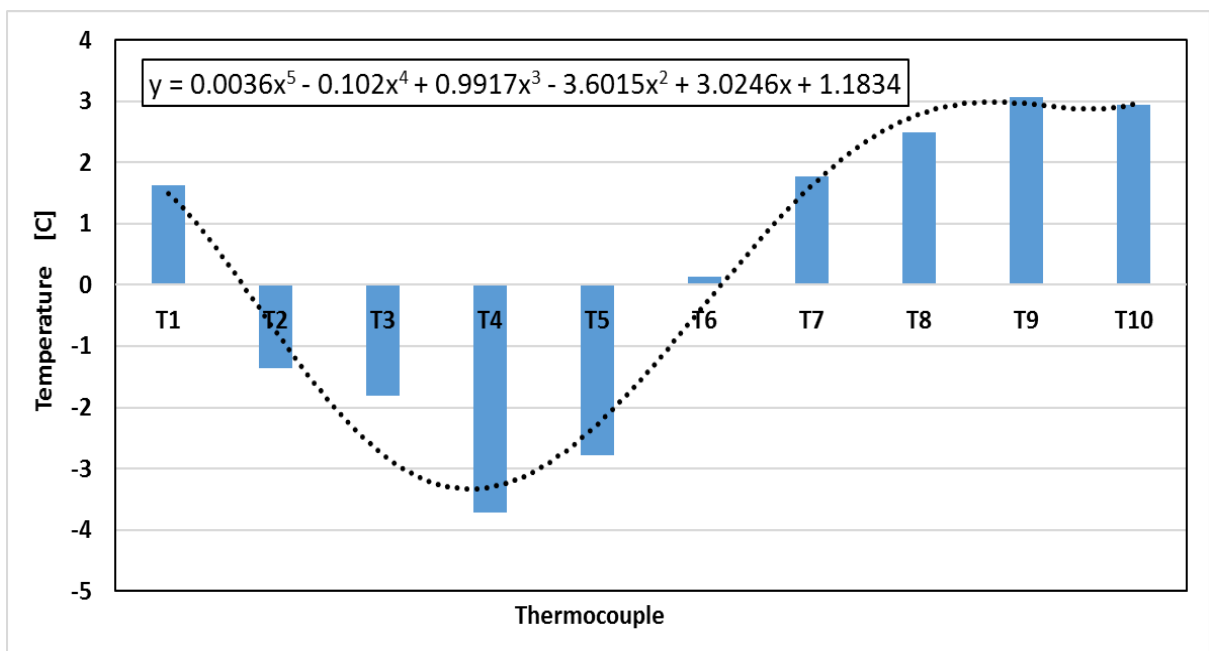
Figure 5-27: The inner tube temperature gradient for the fourth case

Figure **5-28** shows the cold energy absorbed by water for each case. This presents the percentage of the cold energy recovered from the LN2 by the water. This figure shows clearly that the enhanced cases where a metal mesh was installed in the copper pipe (cases three and four) have higher energy absorbed compared to the smooth pipe. The third case showed

slightly higher percentage of the cold energy recovery than the fourth case however the heat transfer rate for the fourth case was more than double that of case three.
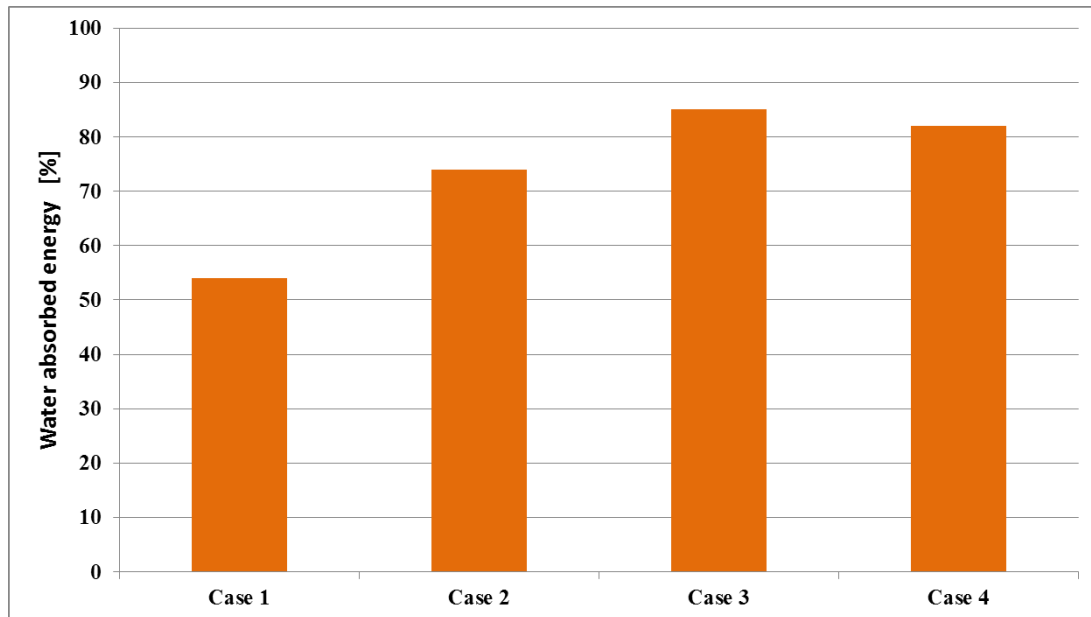
Figure 5-28: Cold energy absorbed by water for each case

The effectiveness of cryogenic heat exchangers is normally very high above 95% [127]. Gifford et al. [128] experimentally measured a liquid nitrogen heat exchanger and their results showed that the effectiveness varied from 97 to 99.5%.

In this work for all cases heat exchanger effectiveness ε were calculated using Logarithmic Mean Temperature Difference (LMTD) using equation (**5.11**) and the Number of Transfer Units NTU approaches using equation (**5.14**) [98, 129].

$$\Delta T_{lm} = \frac{\Delta T_2 - \Delta T_1}{ln\frac{\Delta T_2}{\Delta T_1}}$$

5.11

Where ΔT_1 and ΔT_2 were calculated using equations (**5.12**) and (**5.13**) for parallel flow heat exchanger.

$$\Delta T_2 = T_{h1} - T_{c1} \qquad\qquad 5.12$$

$$\Delta T_2 = T_{h2} - T_{c2} \qquad\qquad 5.13$$

Where T_{c1} and T_{c2} are nitrogen side inlet and outlet temperature while T_{h1} and T_{h2} for the water side.

$$NTU = \frac{UA}{(\dot{m}C_p)_{min}} \qquad\qquad 5.14$$

Where U is the overall heat transfer coefficient which can be calculated using equation (**5.15**), A is the copper tube area surface and $(\dot{m}C_p)_{min}$ is the smaller magnitude of $(\dot{m}C_p)$ of the hot and the cold side of the heat exchanger.

$$U = \frac{\dot{Q}}{A\Delta T_{lm}} \qquad\qquad 5.15$$

Where $\dot{Q}$ is the heat transfer rate calculated by equation (**5.10**).

Knowing the inlet/outlet temperatures, mass flow rates, the surface area, the heat exchanger effectiveness can be calculated using equation (**5.16**).

$$\varepsilon = 1\dot{-}\, e^{-NTU} \qquad\qquad 5.16$$

Figure **5-29** shows the heat exchanger effectiveness for the four stated cases where it is clear that the first case (Case 1) has the lowest value (51%) indicating a high energy loss in this case, while the last case (Case 4) showed the highest effectiveness where it reached 98%. The second and the third cases showed heat exchanger effectiveness values of 89% and 94% respectively
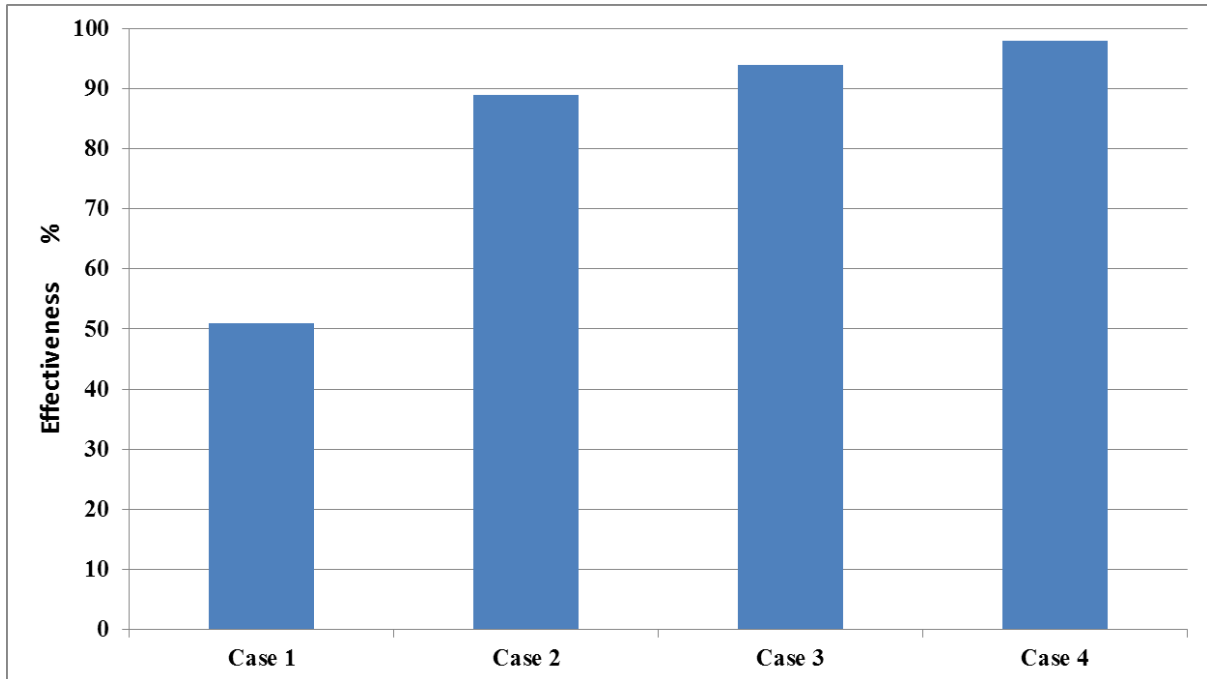
Figure 5-29: Heat exchanger effectiveness

5.12 Validation of the CFD modelling

The experimental work results were used to validate the CFD modelling where the heat exchanger geometry was built in Ansys workbench and the experimental operating conditions were applied as boundary conditions. Due to the difficulties to include the metal mesh in the CFD model due to the high computational time, only the first and the second cases with smooth tube were used in the validation. For the CFD model similar steps as these described in chapter four were followed. The measured temperature of the outer surface of the inner tube and outlets from both sides were used for validation.

For the first case where the LN2 and water flow rates were 0.103 LPM and 0.300 LPM respectively, Figure 5-30 compares the measured inner tube outer wall surface temperatures to these predicted by the CFD model where maximum difference of 4 degree at the first and the last point were observed. This means the CFD model deviates only by a maximum of 1.5% from the experimental work. The wall average temperature obtained from the experimental

and CFD modelling were 277.9K and 276.6 indicating good agreement. The LN2 outlet temperature from the experimental work was fluctuating between -85 to -55 °C but the average was about 203K, while from the CFD model the LN2 predicted outlet temperature was constant at 185 K. The water outlet temperature from the experimental work and the CFD were 285.6 K and 286.6 K respectively with difference of 1 degree only.
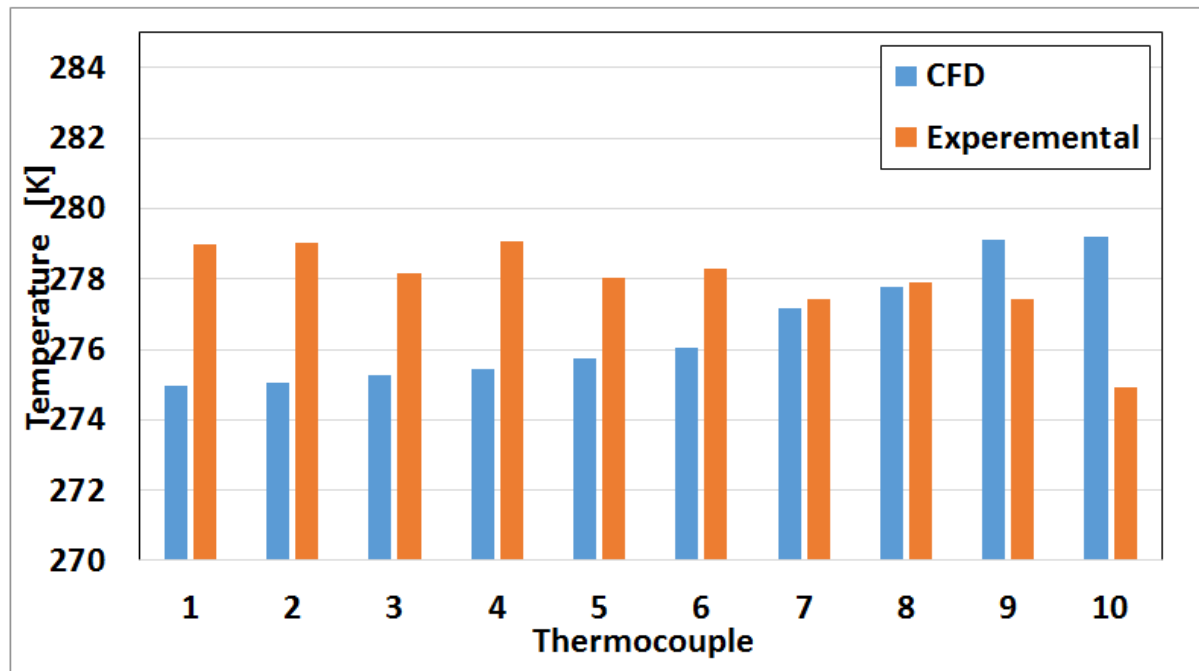
Figure 5-30: The inner tube wall temperature of the experimental work and the CFD model

For the second case where the LN2 and water flow rate were 0.026 LPM and 0.300 LPM, Figure **5-31** shows the measured inner tube outer wall temperature and those predicted by the CFD model. The CFD model showed a very good agreement with the experimental work with only 1-1.5 degree difference in all measured points apart from the first one that showed about 20 degree difference with 7.5% deviation. Again this probably due to unstable or the bubble flow in this region. The average wall temperature from the experimental and CFD modelling were 288.78 K and 285.55 K. The LN2 outlet temperature from the experimental and the CFD

modelling were 281and 265 K respectively; while for the water they were 289.8 K and 287.99 K, respectively.
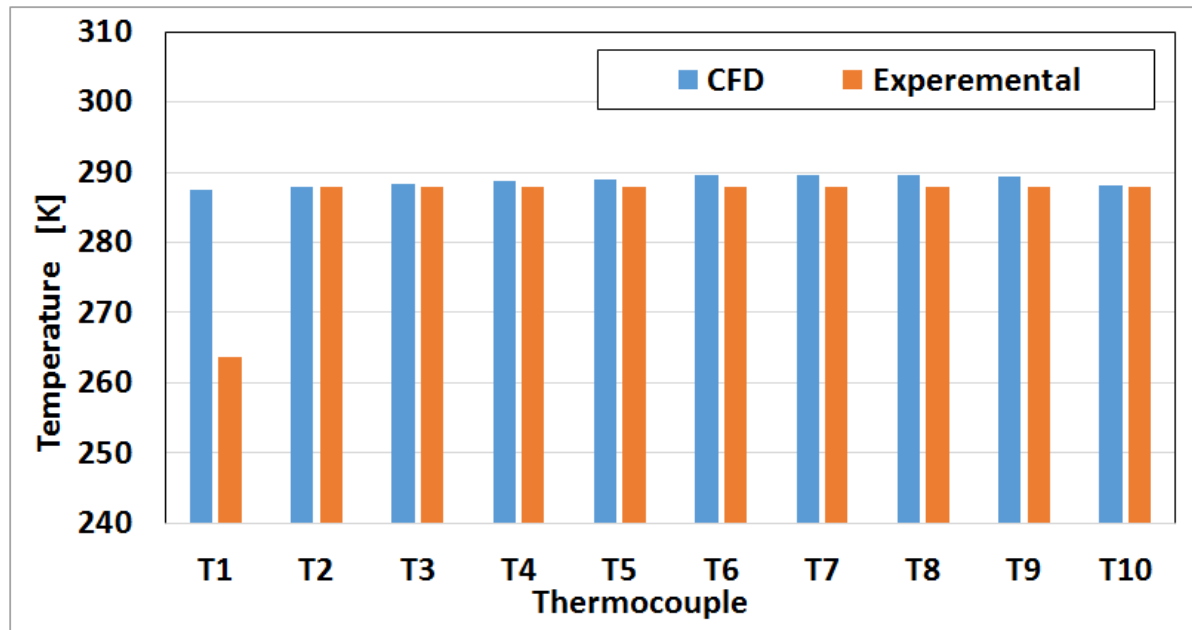
Figure 5-31: The inner tube wall temperature of the experimental work and the CFD model

5.13 Summary

This chapter described the development of liquid nitrogen heat exchanger test facility to investigate the potential of using LN2 to generate cooling for domestic air conditioning and to validate the CFD modelling. Components, fittings, control system, data acquisition system and measuring devices were individually described. Calibrations of the measuring devices and uncertainty analysis were also carried out.

Experiments were carried out using smooth tube with LN2 flow rates of 0.1034 LPM to 0.1034 LPM and using smooth tube with two types of stainless steel and copper mesh inserted inside the tube.

The results showed that there is a potential of using LN2 to generate cooling however using a smooth tube without any enhancement will lead to significant loss of the stored cold energy

where the high expansion ratio due to the phase change will vent the LN2 droplets outside the heat exchanger leading to inefficient use of LN2.

The enhancement was made by installing a metal mesh inside the smooth tube which improved the heat exchanger effectiveness for the third and the fourth cases by 5% and 10% respectively compared with second case and by 84% and 92% respectively compared with first case.

Installing a metal mesh in the LN2 side of the heat exchanger not only enhances the heat transfer in the gas region but also stops the LN2 droplets from leaving the heat exchanger without evaporation and extraction of its stored cold.

In all studied cases the temperature of the outer surface of the LN2 carrier tube in the heat exchanger was close to water temperature thus reducing the risk of freezing the secondary fluid.

The CFD model and experimental results were in good agreement with maximum deviation of 7.6%.

CHAPTER SIX

CONCLUSIONS AND RECOMMENDATIONS

6.1 Introduction

Global demands for residential air conditioning systems have increased significantly during the last few decades and most of this growth occurred in the developing countries. Market forecasts showed that this growth will continue at the same rate until the end of this century. Currently used air conditioning systems contribute to significant amount of power consumption and CO2 emissions particularly during the electricity peak time where most of electricity suppliers face difficulties to meet the user's demands and to cope with this significant growth. Thus there is a need to enhance the current commonly used air conditioning systems (vapour compression system) that forms a major part of electricity consumption in the residential sector particularly during the summer season. This enhancement can reduce energy consumption and shift the cooling load to off peak times (night-time) where the electricity generating plants operate more efficiently leading to better electricity network balance.

6.2 Conclusions

This research described research work carried out to develop an efficient air conditioning technology that exploits cold energy storage to reduce energy consumption and CO_2 emissions and shift the cooling load to off peak times to achieve better national electricity grid stability. The investigation includes the use of cold storage materials (ice, Phase Change Materials PCM) to enhance the current air conditioning systems through mathematical modelling using MATLAB software. Also using cryogenic fluids such as liquid nitrogen/air

(which are produced using surplus electricity or renewable energy sources) were thermodynamically investigated to provide air conditioning for domestic and office buildings using MATLAB and REFPROP software. This thermodynamic investigation was through five different cycle configurations; the 1st cycle for providing cooling only; 2nd cycle for providing cooling and power using expander; 3rd cycle integrating the 2nd cycle with Brayton cycle; 4th cycle integrating the 2nd cycle with Rankine cycle and 5th integrating the 2nd cycle with two cascade Rankine cycle. CFD modelling of the two main components in the proposed cryogenic systems namely, cryogenic heat exchanger and expander were also carried out. An experimental work to assess the potential of using LN2/LAir cryogenic fluids to provide cooling and to validate the CFD model was also carried out. The main outcome from this work can be summarized in the following points:

- Integrating the existing A/C units with cold storage tank is a promising technique which can lead to energy saving and shifting the cooling load to off peak times.

- Several materials can be used as cold storage medium but PCMs are the most recommended materials due to their advantages such as; higher storage capacity reaching about 5-14 times that of sensible heat storage mediums; wide range of materials giving flexibility to choose the phase change temperature according to A/C requirements and low temperature variation. However some disadvantages of these materials were also reported such as low thermal conductivity, density variation, unstable under long term cycling and phase segregation.

- The energy saving of the A/C integrated with cold storage tank is highly dependent on the storage medium and its phase change temperature. For example, when Hydrate (HC-290) which has phase change temperature of 5.6 °C was used the system showed an energy saving of up to 26% compared with conventional A/C system depending on the operating strategy. But when ice the most commercially available PCM is used,

the chiller capacity was reduced by 30-40% leading to higher power consumption compared to the conventional system with no storage.

- Regarding the use of cryogenic fluids, liquid air/nitrogen are identified as the most attractive energy carriers due to their high energy density (770 kJ/kg), availability and environment friendly.

- From the investigated cryogenic cooling and power cycles, the fifth configuration showed the highest system performance, and it recovered up to 94% of the energy stored in LAir and up to 78% of the energy stored in LN2. Also it showed cost saving of the energy consumption of up to 73% when LAir is used and 67% when LN2 is used compared to conventional A/C system.

- Using LN2 system showed slightly higher (less than 4%) specific power output and specific cooling capacity than LAir, however, LAir showed 21-25% higher Recovery Efficiency and COP than LN2 due to its lower production energy demand.

- Compared to the conventional A/C system, the cost saving of using the LN2/Lair systems depends on the LN2/LAir prices. At the price of 3.5 pence per kg the 1st, 2nd, 3rd and 4th cycles showed cost energy saving up to 15%, 24%, 31% and 37.5%, respectively, when LAir is used, and -3%, 5%, 16% and 24%, consecutively, when LN2 is used.

- Extensive use of this technology can lead to further reduction in the LAir and LN2 prices, and results showed that, at price level of 1.5 pence per kg-LAir/kg-LN2 the 1st, 2nd, 3rd and 4th cycles saved up to 63%, 67%, 70% and 72%, respectively when LAir is used, and 55%, 59%, 63% and 67%, consecutively when LN2 is used. Therefore using even the simplest cycle can result in significant cost saving.

- CFD modelling of evaporation/boiling process of LN2 showed good agreement with experimental data with deviation of less than 10%.

- The tube heat transfer can be significantly enhanced using finned tubes and the enhancement will vary depending on the fins shape and height. The CFD investigated fin configurations showed enhancement by 79%-167% compared with the smooth tube.

- The CFD model showed that although LN2 enters the heat exchanger at extremely low temperature, less than 20% of the LN2 carrier tube showed a temperature less than the freezing temperature of the secondary fluid. However, even at these regions with low temperatures, the secondary fluid did not freeze due to being melted by the circulated secondary fluid.

- The temperature of the gas region in the remaining tube (which is about 80% of its whole length) is relatively low but the heat transfer is limited duo to the low thermal properties of the N_2 gas therefore enhancing the heat transfer in this region will lead to significant reduction in the heat exchanger size.

- The experimental work showed that, enhancing the heat transfer in the gas region in the LN2 carrier tube using metal mesh increases the heat exchanger effectiveness and the heat transfer rate by more than 10%.

- Using the same experimental boundary conditions, the CFD modelling of the cryogenic heat exchanger showed good agreement with the experimental results with maximum deviation of 7.6%.

- The research showed that, there is a potential of using cryogenic fluids such as LN2/LAir to provide cooling and power for domestic applications where a mass flow rate of 0.0239 kg/s of LAir at inlet pressure of 20 Bar can generate 10 kW of cooling and 2.2 kW of electricity which is enough to meet the cooling and power demand of a domestic house.

6.3   Recommendations for future work

Based on the work carried out regarding development of an efficient air conditioning system for domestic and office buildings there are further recommendation to enhance the methods described in this thesis as following:

- Using CFD tools to develop a heat exchanger that enhances the low thermal conductivity of the phase change materials.

- Develop a test facility for integrating the current air conditioning system with cold storage system that uses PCMs as storage medium.

- The current liquefaction plants require great amount of energy therefore there is a need to develop new technique that leads to reducing the required energy to produce LN2/LAir. This will further reduce the cost of LN2/LAir and facilitate the wide spread usage of the developed cryogenic energy storage based technology for cooling and power applications.

REFERENCES:

[1]   I. E. Agency, "Air conditioning demand set to grow rapidly over the coming decades," 2016.

[2]   L. W. Davis and P. J. Gertler, "Contribution of air conditioning adoption to future energy use under global warming," *Proceedings of the National Academy of Sciences of the United States of America,* vol. 112, pp. 5962-5967, May 12 2015.

[3]   A. Ahmad, R. Al-Dadah, and S. Mahmoud, "Liquid nitrogen energy storage for air conditioning and power generation in domestic applications," *Energy conversion and management,* vol. 128, pp. 34-43, 2016.

[4]   M. A. McNeil and V. E. Letschert, "Future air conditioning energy consumption in developing countries and what can be done about it: the potential of efficiency in the residential sector," 2008.

[5]   T. guardian, "World set to use more energy for cooling than heating," 2017.

[6]   M. Isaac and D. P. Van Vuuren, "Modeling global residential sector energy demand for heating and air conditioning in the context of climate change," *Energy policy,* vol. 37, pp. 507-521, 2009.

[7]   I. Dincer, *Refrigeration systems and applications*: John Wiley & Sons, 2017.

[8]   M.-J. Hsiao, C.-H. Cheng, M.-C. Huang, and S.-L. Chen, "Performance enhancement of a subcooled cold storage air conditioning system," *Energy Conversion and Management,* vol. 50, pp. 2992-2998, 2009.

[9]   M. Hosoz and A. Kilicarslan, "Performance evaluations of refrigeration systems with air-cooled, water-cooled and evaporative condensers," *International journal of energy research,* vol. 28, pp. 683-696, 2004.

[10]   M. Youbi-Idrissi, H. Macchi-Tejeda, L. Fournaison, and J. Guilpart, "Numerical model of sprayed air cooled condenser coupled to refrigerating system," *Energy conversion and management,* vol. 48, pp. 1943-1951, 2007.

[11]   S.-C. Hu and R.-H. Yang, "Development and testing of a multi-type air conditioner without using AC inverters," *Energy Conversion and Management,* vol. 46, pp. 373-383, 2005.

[12]   C. Aprea, R. Mastrullo, and C. Renno, "Determination of the compressor optimal working conditions," *Applied Thermal Engineering,* vol. 29, pp. 1991-1997, 2009.

[13]   F. KITANI, "Inverter-mounted multi-package type air conditioners," *Hitachi review,* vol. 39, pp. 141-148, 1990.

[14]   X. Zhai, X. Wang, T. Wang, and R. Wang, "A review on phase change cold storage in air-conditioning system: materials and applications," *Renewable and Sustainable Energy Reviews,* vol. 22, pp. 108-120, 2013.

[15]   A. Sharma, V. V. Tyagi, C. Chen, and D. Buddhi, "Review on thermal energy storage with phase change materials and applications," *Renewable and Sustainable energy reviews,* vol. 13, pp. 318-345, 2009.

[16]   B. Rismanchi, R. Saidur, H. Masjuki, and T. Mahlia, "Thermodynamic evaluation of utilizing different ice thermal energy storage systems for cooling application in office buildings in Malaysia," *Energy and Buildings,* vol. 53, pp. 117-126, 2012.

[17]   S. Hasnain, "Review on sustainable thermal energy storage technologies, Part II: cool thermal storage," *Energy conversion and management,* vol. 39, pp. 1139-1153, 1998.

[18]   Y. Sun, S. Wang, F. Xiao, and D. Gao, "Peak load shifting control using different cold thermal energy storage facilities in commercial buildings: a review," *Energy conversion and management,* vol. 71, pp. 101-114, 2013.

[19]   S. M. Hasnain and N. M. Alabbadi, "Need for thermal-storage air-conditioning in Saudi Arabia," *Applied energy,* vol. 65, pp. 153-164, 2000.

REFERENCES

[20]   B. Rismanchi, R. Saidur, H. Masjuki, and T. Mahlia, "Modeling and simulation to determine the potential energy savings by implementing cold thermal energy storage system in office buildings," *Energy conversion and management,* vol. 75, pp. 152-161, 2013.

[21]   B. Rismanchi, R. Saidur, G. BoroumandJazi, and S. Ahmed, "Energy, exergy and environmental analysis of cold thermal energy storage (CTES) systems," *Renewable and sustainable energy reviews,* vol. 16, pp. 5741-5746, 2012.

[22]   C. V. Dellino, *Cold and chilled storage technology*: Springer Science & Business Media, 2012.

[23]   C. E. Dorgan and J. S. Elleson, *Design guide for cool thermal storage*: ASHRAE Atlanta, USA, 1993.

[24]   M. M. Farid, A. M. Khudhair, S. A. K. Razack, and S. Al-Hallaj, "A review on phase change energy storage: materials and applications," *Energy conversion and management,* vol. 45, pp. 1597-1615, 2004.

[25]   R. Parameshwaran, S. Harikrishnan, and S. Kalaiselvam, "Energy efficient PCM-based variable air volume air conditioning system for modern buildings," *Energy and Buildings,* vol. 42, pp. 1353-1360, 2010.

[26]   R. Parameshwaran and S. Kalaiselvam, "Energy conservative air conditioning system using silver nano-based PCM thermal storage for modern buildings," *Energy and Buildings,* vol. 69, pp. 202-212, 2014.

[27]   R. Parameshwaran and S. Kalaiselvam, "Energy efficient hybrid nanocomposite-based cool thermal storage air conditioning system for sustainable buildings," *Energy,* vol. 59, pp. 194-214, 2013.

[28]   I. Dincer, "On thermal energy storage systems and applications in buildings," *Energy and buildings,* vol. 34, pp. 377-388, 2002.

[29]   I. Dincer and M. Rosen, *Thermal energy storage: systems and applications*: John Wiley & Sons, 2002.

[30]   Y. Liu and K. Guo, "A novel cryogenic power cycle for LNG cold energy recovery," *Energy,* vol. 36, pp. 2828-2833, 2011.

[31]   C. Dispenza, G. Dispenza, V. La Rocca, and G. Panno, "Exergy recovery during LNG regasification: Electric energy production–Part one," *Applied Thermal Engineering,* vol. 29, pp. 380-387, 2009.

[32]   S. Deng, H. Jin, R. Cai, and R. Lin, "Novel cogeneration power system with liquefied natural gas (LNG) cryogenic exergy utilization," *Energy,* vol. 29, pp. 497-512, 2004.

[33]   Y. Lim, M. Al-Atabi, and R. A. Williams, "Liquid air as an energy storage: a review," *J Eng Sci Technol,* vol. 11, pp. 496-515, 2016.

[34]   M. Antonelli, U. Desideri, R. Giglioli, F. Paganucci, and G. Pasini, "Liquid air energy storage: a potential low emissions and efficient storage system," *Energy Procedia,* vol. 88, pp. 693-697, 2016.

[35]   Y. Li, X. Wang, and Y. Ding, "A cryogen-based peak-shaving technology: systematic approach and techno-economic analysis," *International Journal of Energy Research,* vol. 37, pp. 547-557, 2013.

[36]   R. M. Skobel and D. Davey, "Liquid nitrogen cooled beverage dispenser," ed: Google Patents, 2012.

[37]   F. Dakhil, "Air conditioning apparatus using liquid nitrogen," ed: Google Patents, 1999.

[38]   Y. Li, H. Chen, and Y. Ding, "Fundamentals and applications of cryogen as a thermal energy carrier: A critical assessment," *International Journal of Thermal Sciences,* vol. 49, pp. 941-949, 2010.

[39]   C. Knowlen, A. Mattick, A. P. Bruckner, and A. Hertzberg, "High efficiency energy conversion systems for liquid nitrogen automobiles," SAE Technical Paper 0148-7191, 1998.

[40]   R. Morgan, S. Nelmes, E. Gibson, and G. Brett, "Liquid air energy storage–analysis and first results from a pilot scale demonstration plant," *Applied energy,* vol. 137, pp. 845-853, 2015.

REFERENCES

[41]   M. Magnini, "CFD modeling of two-phase boiling flows in the slug flow regime with an interface capturing technique," alma, 2012.

[42]   J. A. Clark, "Cryogenic heat transfer," in *Advances in heat transfer*. vol. 5, ed: Elsevier, 1969, pp. 325-517.

[43]   Y. Liu, T. Olewski, L. Vechot, X. Gao, and S. Mannan, "Modelling of a cryogenic liquid pool boiling using CFD code," in *14th Annual Symposium, Mary Kay O'Connor Process Safety Center "Beyond Regulatory Compliance: Making Safety Second Nature*, 2011, pp. 512-524.

[44]   V. Klimenko and A. Sudarchikov, "Investigation of forced flow boiling of nitrogen in a long vertical tube," *Cryogenics,* vol. 23, pp. 379-385, 1983.

[45]   D. Steiner, "Heat transfer during flow boiling of cryogenic fluids in vertical and horizontal tubes," *Cryogenics,* vol. 26, pp. 309-318, 1986.

[46]   H. Umekawa, M. Hirayama, T. Kitajima, M. Ozawa, K. Mishima, and Y. Saito, "HEAT TRANSFER AND FLOW CHARACTERISTICS OF A NON-UNIFORMLY HEATED TUBE UNDER LOW PRESSURE AND LOW MASS FLUX CONDITION," *Multiphase Science and Technology,* vol. 18, 2006.

[47]   E. Polomik, S. Levy, and S. Sawochka, "Film boiling of steam-water mixtures in annular flow at 800, 1100, and 1400 psi," *Journal of Heat Transfer,* vol. 86, pp. 81-87, 1964.

[48]   H. Umekawa, M. Ozawa, and T. Yano, "Boiling two-phase heat transfer of LN2 downward flow in pipe," *Experimental thermal and fluid science,* vol. 26, pp. 627-633, 2002.

[49]   W. Simin, W. Jian, L. Yamei, Y. Huizhu, L. Yanzhong, and J. Tu, "Numerical prediction for subcooled boiling flow of liquid nitrogen in a vertical tube with MUSIG model," *Chinese Journal of Chemical Engineering,* vol. 21, pp. 1195-1205, 2013.

[50]   S. R. Darr, H. Hu, R. Shaeffer, J. Chung, J. W. Hartwig, and A. K. Majumdar, "Numerical simulation of the liquid nitrogen chilldown of a vertical tube," in *53rd AIAA Aerospace Sciences Meeting*, 2015, p. 0468.

[51]   D. Deng, S.-w. Xie, and R.-s. Wang, "Two-phase flow pressure drop of liquid nitrogen boiling in the straight section downstream of U-bend," *Journal of Shanghai Jiaotong University (Science),* vol. 19, pp. 495-501, 2014.

[52]   J. Chung and K. Yuan, "Recent Progress on Experimental Research of Cryogenic Transport Line Chilldown Process," *Frontiers in Heat and Mass Transfer (FHMT),* vol. 6, 2015.

[53]   J. Hartwig, H. Hu, J. Styborski, and J. Chung, "Comparison of cryogenic flow boiling in liquid nitrogen and liquid hydrogen chilldown experiments," *International Journal of Heat and Mass Transfer,* vol. 88, pp. 662-673, 2015.

[54]   K. Yuan, "Cryogenic boiling and two-phase chilldown process under terrestrial and microgravity Conditions," University of Florida, 2006.

[55]   H. Hu, J. N. Chung, and S. H. Amber, "An experimental study on flow patterns and heat transfer characteristics during cryogenic chilldown in a vertical pipe," *Cryogenics,* vol. 52, pp. 268-277, 2012.

[56]   A. Chandra, "Refrigeration and air conditioning: PHI Learning Pvt," ed: Ltd, 2010.

[57]   A. S. o. Heating, Refrigerating, and A.-C. Engineers, *Heating, Ventilating, and Air-Conditioning: Systems and Equipment: 2000 Ashrae Handbook: Inch-Pound*: Amer Society of Heating, 2012.

[58]   H. Ogoshi and S. Takao, "Air-conditioning system using clathrate hydrate slurry," *JFE Tech. Rep,* vol. 3, pp. 1-5, 2004.

[59]   M. Sebzali and P. Rubini, "The impact of using chilled water storage systems on the performance of air cooled chillers in Kuwait," *Energy and Buildings,* vol. 39, pp. 975-984, 2007.

[60]   N. Nassif, C. Hall, and D. Freelnad, "Optimization of Ice Thermal Storage Systems Design for HVAC Systems," 2013.

[61]   M. Sebzali, "Assessment of cool thermal storage strategies in Kuwait," 2006.

[62]   M. Sebzali and P. Rubini, "Analysis of ice cool thermal storage for a clinic building in Kuwait," *Energy Conversion and Management,* vol. 47, pp. 3417-3434, 2006.

REFERENCES

[63]   C. Chaichana, W. W. Charters, and L. Aye, "An ice thermal storage computer model," *Applied Thermal Engineering,* vol. 21, pp. 1769-1778, 2001.

[64]   H. Yang and S. You, "Partial ice-storage: Application to air conditioning systems in Hong Kong," *Building Services Engineering Research and Technology,* vol. 20, pp. 201-203, 1999.

[65]   J. Szargut and I. Szczygiel, "Utilization of the cryogenic exergy of liquid natural gas (LNG) for the production of electricity," *Energy,* vol. 34, pp. 827-837, 2009.

[66]   C. Dispenza, G. Dispenza, V. La Rocca, and G. Panno, "Exergy recovery during LNG regasification: electric energy production–part two," *Applied thermal engineering,* vol. 29, pp. 388-399, 2009.

[67]   W. Qiang, L. Yanzhong, and C. Xi, "Exergy analysis of liquefied natural gas cold energy recovering cycles," *International journal of energy research,* vol. 29, pp. 65-78, 2005.

[68]   R. Harold, "Air conditioning system," ed: Google Patents, 1960.

[69]   M. Watanabe, H. Yumura, H. Hirota, T. Masuda, M. Shimoda, R. Ohno*, et al.*, "Recent progress of liquid nitrogen cooling system (LINCS) for Yokohama HTS cable project," *Physics Procedia,* vol. 36, pp. 1313-1318, 2012.

[70]   R. Garlov, V. Saveliev, K. Gavrylov, L. Golovin, and H. Pedolsky, "Refrigeration of a food transport vehicle utilizing liquid nitrogen," ed: Google Patents, 2002.

[71]   L. P. Saia III and C. S. Wilbrandt, "Portable self-contained cooler/freezer apparatus for use on airplanes, common carrier type unrefrigerated truck lines, and the like," ed: Google Patents, 1994.

[72]   J. F. Place, "Apparatus for cooling and preserving foods, &c., by liquid air," ed: Google Patents, 1909.

[73]   H. Chen, Y. Ding, Y. Li, X. Zhang, and C. Tan, "Air fuelled zero emission road transportation: a comparative study," *Applied Energy,* vol. 88, pp. 337-342, 2011.

[74]   C. Knowlen, J. Williams, A. Mattick, H. Deparis, and A. Hertzberg, "Quasi-isothermal expansion engines for liquid nitrogen automotive propulsion," SAE Technical Paper 0148-7191, 1997.

[75]   C. Ordonez, M. Plummer, and R. Reidy, "Cryogenic heat engines for powering zero emission vehicles," in *Proceedings of 2001 ASME international mechanical engineering congress and exposition, US, IMECE*, 2001, pp. 67-75.

[76]   C. Ordonez and M. Plummer, "Cold thermal storage and cryogenic heat engines for energy storage applications," *Energy Sources,* vol. 19, pp. 389-396, 1997.

[77]   R. Schneider and L. Manning, "Nitrogen vapor engine," ed: Google Patents, 1974.

[78]   J. Wang, W. Xu, S. Ding, Y. Shi, M. Cai, and A. Rehman, "Liquid air fueled open-closed cycle Stirling engine and its exergy analysis," *Energy,* vol. 90, pp. 187-201, 2015.

[79]   W. Xu, J. Wang, M. Cai, and Y. Shi, "Liquid air fueled open–closed cycle Stirling engine," *Energy Conversion and Management,* vol. 94, pp. 210-220, 2015.

[80]   M. D. Newman and S. A. McCormick, "LNG (liquefied natural gas) and LIN (liquid nitrogen) in transit refrigeration heat exchange system," ed: Google Patents, 2014.

[81]   B. Ameel, C. T'Joen, K. De Kerpel, P. De Jaeger, H. Huisseune, M. Van Belleghem*, et al.*, "Thermodynamic analysis of energy storage with a liquid air Rankine cycle," *Applied Thermal Engineering,* vol. 52, pp. 130-140, 2013.

[82]   Dearman, "Liquid Air on the European Highway, The economic and environmental impact of zero-emission transport refrigeration. ," 2015.

[83]   M. Akhurst, I. Arbon, M. Ayres, N. Brandon, R. Bruges, S. Cooper*, et al.*, "Liquid Air in the energy and transport systems: Opportunities for industry and innovation in the UK," 2013.

[84]   C. Ordonez, "Liquid nitrogen fueled, closed Brayton cycle cryogenic heat engine," *Energy Conversion and Management,* vol. 41, pp. 331-341, 2000.

[85]   A. Ahmad, R. Al-Dadah, and S. Mahmoud, "CFD modelling of a novel liquid Nitrogen/Air engine and cryogenic heat exchanger for small scale applications," *Energy Procedia,* vol. 142, pp. 3654-3660, 2017.

REFERENCES

[86]   A. M. Mohamed, A. Al-Habaibeh, H. Abdo, and M. J. R. Abdunnabi, "The significance of utilizing renewable energy options into the Libyan Energy Mix," *Energy Research Journal,* vol. 4, pp. 15-23, 2013.

[87]   G. A. Sayah, "The use of renewable energy technologies in the Libyan energy system," 2017.

[88]   K. M. Khalil, A. Ahmad, S. Mahmoud, and R. Al-Dadah, "Liquid air/nitrogen energy storage and power generation system for micro-grid applications," *Journal of cleaner production,* vol. 164, pp. 606-617, 2017.

[89]   A. Ahmad, R. Al-Dadah, and S. Mahmoud, "Liquid air utilization in air conditioning and power generating in a commercial building," *Journal of Cleaner Production,* vol. 149, pp. 773-783, 2017.

[90]   A. Ahmad, R. Al-Dadah, and S. Mahmoud, "energy and exergy analysis of using liquid air for generating air conditioning and power for domestic buildings," 2017.

[91]   A. Y. Ahmad, A.-D. Raya, and S. Mahmoud, "Liquid nitrogen air conditioning system for domestic application," in *Students on Applied Engineering (ICSAE), International Conference for*, 2016, pp. 291-296.

[92]   A. Ahmad, R. Al-Dadah, and S. Mahmoud, "Air conditioning and power generation for residential applications using liquid nitrogen," *Applied energy,* vol. 184, pp. 630-640, 2016.

[93]   Mohamed A. and G. A., "Effect of some types of building materials on the thermal load for a residential house in Sebha area," 2016.

[94]   M. Navidbakhsh, A. Shirazi, and S. Sanaye, "Four E analysis and multi-objective optimization of an ice storage system incorporating PCM as the partial cold storage for air-conditioning applications," *Applied Thermal Engineering,* vol. 58, pp. 30-41, 2013.

[95]   P. Naphon and S. Wongwises, "A review of flow and heat transfer characteristics in curved tubes," *Renewable and sustainable energy reviews,* vol. 10, pp. 463-490, 2006.

[96]   H. Gao, L. Guo, and X. Zhang, "Liquid–solid separation phenomena of two-phase turbulent flow in curved pipes," *International Journal of Heat and Mass Transfer,* vol. 45, pp. 4995-5005, 2002.

[97]   A. M. Elsayed, "Heat transfer in helically coiled small diameter tubes for miniature cooling systems," University of Birmingham, 2011.

[98]   S. Kakac, H. Liu, and A. Pramuanjaroenkij, *Heat exchangers: selection, rating, and thermal design*: CRC press, 2012.

[99]   M. Panjeshahi and A. Ataei, "Application of an environmentally optimum cooling water system design in water and energy conservation," *International Journal of Environmental Science & Technology,* vol. 5, pp. 251-262, 2008.

[100]   G. Wall, "Optimization of refrigeration machinery," *International Journal of Refrigeration,* vol. 14, pp. 336-340, 1991.

[101]   R. Selbaş, Ö. Kızılkan, and A. Şencan, "Thermoeconomic optimization of subcooled and superheated vapor compression refrigeration cycle," *Energy,* vol. 31, pp. 2108-2128, 2006.

[102]   P. Roosen, S. Uhlenbruck, and K. Lucas, "Pareto optimization of a combined cycle power system as a decision support tool for trading off investment vs. operating costs," *International Journal of Thermal Sciences,* vol. 42, pp. 553-560, 2003.

[103]   A. Bejan and G. Tsatsaronis, *Thermal design and optimization*: John Wiley & Sons, 1996.

[104]   D. MacPhee and I. Dincer, "Performance assessment of some ice TES systems," *International Journal of Thermal Sciences,* vol. 48, pp. 2288-2299, 2009.

[105]   G. Li, Y. Hwang, and R. Radermacher, "Review of cold storage materials for air conditioning application," *International journal of refrigeration,* vol. 35, pp. 2053-2077, 2012.

[106]   E. Oró, A. De Gracia, A. Castell, M. Farid, and L. Cabeza, "Review on phase change materials (PCMs) for cold thermal energy storage applications," *Applied Energy,* vol. 99, pp. 513-533, 2012.

REFERENCES

[107] B. M. Diaconu, S. Varga, and A. C. Oliveira, "Experimental assessment of heat storage properties and heat transfer characteristics of a phase change material slurry for air conditioning applications," *Applied Energy,* vol. 87, pp. 620-628, 2010.

[108] H.-T. Gao, "Investigation on organic phase transition materials in Energy Storage Air Conditioning system," in *Materials for Renewable Energy & Environment (ICMREE), 2011 International Conference on*, 2011, pp. 669-672.

[109] E. W. Lemmon, M. L. Huber, and M. O. McLinden, "NIST Standard ReferenceDatabase 23: Reference Fluid Thermodynamic and Transport Properties-REFPROP. 9.0," 2010.

[110] T. MATLAB, "version 7.7. 0 (R2008b)," *The MathWorks Inc., Natick, Massachusetts,* 2008.

[111] P. D. Vitt, "Operational characteristics of a liquid nitrogen powered automobile," Washington Univ Seattle Dept Of Aeronautics And Astronautics1998.

[112] T. B. North, *Liquid nitrogen propulsion systems for automotive applications: calculation of the mechanical efficiency of a dual, double-acting piston propulsion system*: University of North Texas, 2008.

[113] B. Gas, "British Gas," 2016.

[114] D. E. Company, "Cold and Power – UKES 201," 2016.

[115] ANSYS, "Fluent, A. N. S. Y. S. "Ansys fluent." Academic Research. Release 18.2 (2017)." 2017.

[116] ANSYS, "Fluent,A.N.S.Y.S.,Release 18.2, User Guide. ANSYS Inc," 2017.

[117] F. Ansys, "Fluent, A.N.S.Y.S., Release 18.2, Theory Guide. ," 2017.

[118] D. A. D. a. R. T. Lahey, " In Particulate Two-Phase Flow," 1993.

[119] T. Frank, J. Shi, and A. D. Burns, "Validation of Eulerian multiphase flow models for nuclear safety application," in *Proceeding of the Third International Symposium on Two-Phase Modelling and Experimentation, Pisa, Italy*, 2004.

[120] J. Lavieville, E. Quemerais, S. Mimouni, M. Boucker, and N. Mechitoua, "NEPTUNE CFD V1. 0 theory manual," *NEPTUNE report Nept_2004_L1,* vol. 2, 2006.

[121] A. Tentner, S. Lo, A. Ioilev, V. Melnikov, M. Samigulin, V. Ustinenko*, et al.*, "Advances in computational fluid dynamics modeling of two phase flow in a boiling water reactor fuel assembly," in *14th International Conference on Nuclear Engineering*, 2006, pp. 65-72.

[122] H. Ünal, "Maximum bubble diameter, maximum bubble-growth time and bubble-growth rate during the subcooled nucleate flow boiling of water up to 17.7 MN/m2," *International Journal of Heat and Mass Transfer,* vol. 19, pp. 643-649, 1976.

[123] A. Handbook, "Fundamentals, SI ed," *American Society of Heating, Refrigerating and Air Conditioning Engineers: Atlanta, GA, USA,* 2009.

[124] B. VARGA, G. ÓVÁRI, and L. KAVAS, "The Turbine Inlet Temperature And Compressor Pressure Ratio, The Siamese Twins Of The Gas Turbine Engines," in *International Conference Scientific Research And Education In The Air Force-AFASES 2016*, 2016, pp. 393-398.

[125] R. Moffat, "Contributions to the theory of single-sample uncertainty analysis," *Journal of Fluids Engineering,* vol. 104, pp. 250-258, 1982.

[126] A. Bahr Ennil, "Optimization of small-scale axial turbine for distributed compressed air energy storage system," University of Birmingham, 2017.

[127] R. S. Meher, S. S. Murthy, and G. Venkatarathnam, "Measurement of the performance of very high effectiveness heat exchangers," in *Thermal Issues in Emerging Technologies Theory and Applications (ThETA), 2010 3rd International Conference on*, 2010, pp. 157-162.

[128] W. Gifford, A. Acharya, and R. Ackermann, "Compact cryogenic thermal regenerator performance," in *Advances in Cryogenic Engineering*, ed: Springer, 1969, pp. 353-360.

[129] R. F. Barron and G. F. Nellis, *Cryogenic heat transfer*: CRC press, 2017.

APPENDIX A: Thermophysical Properties of Nitrogen [123]

Refrigerant 728 (Nitrogen) Properties of Saturated Liquid and Saturated Vapor

Temp.,* K	Absolute Pressure, MPa	Density, kg/m³ Liquid	Volume, m³/kg Vapor	Enthalpy, kJ/kg Liquid	Vapor	Entropy, kJ/(kg·K) Liquid	Vapor	Specific Heat c_p, kJ/(kg·K) Liquid	Vapor	c_p/c_v Vapor	Velocity of Sound, m/s Liquid	Vapor	Viscosity, μPa·s Liquid	Vapor	Thermal Cond., mW/(m·K) Liquid	Vapor	Surface Tension, mN/m	Temp.,* K
63.15[a]	0.01252	867.2	1.48310	−150.73	64.78	2.4257	5.8383	2.000	1.058	1.411	995	161.1	311.6	4.38	173.2	5.62	12.24	63.15
64	0.01460	863.7	1.28720	−149.03	65.59	2.4524	5.8059	2.002	1.061	1.413	987	162.1	297.5	4.44	171.5	5.71	12.03	64
66	0.02062	855.4	0.93698	−145.02	67.47	2.5140	5.7336	2.005	1.066	1.417	966	164.3	267.8	4.59	167.5	5.92	11.55	66
68	0.02848	847.0	0.69642	−141.00	69.31	2.5739	5.6667	2.010	1.073	1.421	946	166.4	242.3	4.73	163.5	6.14	11.07	68
70	0.03854	838.5	0.52743	−136.97	71.10	2.6321	5.6045	2.014	1.082	1.427	926	168.4	220.2	4.88	159.5	6.35	10.59	70
72	0.05121	829.9	0.40625	−132.93	72.83	2.6889	5.5466	2.020	1.091	1.433	906	170.3	201.1	5.03	155.5	6.58	10.12	72
74	0.06691	821.1	0.31772	−128.87	74.50	2.7442	5.4925	2.027	1.102	1.441	885	172.1	184.3	5.19	151.5	6.80	9.65	74
76	0.08610	812.2	0.25192	−124.79	76.11	2.7983	5.4417	2.035	1.114	1.450	865	173.8	169.6	5.34	147.5	7.03	9.19	76
77.35[b]	0.10132	806.1	0.21682	−122.02	77.16	2.8342	5.4090	2.041	1.124	1.457	851	174.8	160.7	5.44	144.8	7.19	8.87	77.35
78	0.10926	803.1	0.20226	−120.70	77.64	2.8511	5.3939	2.045	1.129	1.461	845	175.3	156.6	5.49	143.5	7.26	8.73	78
80	0.13687	793.9	0.16422	−116.58	79.10	2.9028	5.3487	2.056	1.145	1.473	824	176.7	145.1	5.65	139.5	7.51	8.27	80
82	0.16947	784.6	0.13470	−112.43	80.47	2.9534	5.3059	2.068	1.163	1.487	804	178.0	134.8	5.81	135.6	7.76	7.83	82
84	0.20757	775.0	0.11152	−108.26	81.75	3.0031	5.2651	2.083	1.184	1.503	783	179.2	125.6	5.97	131.6	8.01	7.38	84
86	0.25174	765.2	0.09310	−104.05	82.93	3.0520	5.2262	2.099	1.208	1.521	762	180.2	117.2	6.14	127.7	8.29	6.94	86
88	0.30251	755.2	0.07831	−99.81	84.01	3.1000	5.1888	2.119	1.235	1.542	741	181.0	109.7	6.31	123.7	8.57	6.51	88
90	0.36046	745.0	0.06632	−95.52	84.97	3.1473	5.1527	2.141	1.266	1.567	719	181.8	102.8	6.48	119.8	8.87	6.09	90
92	0.42616	734.5	0.05651	−91.18	85.81	3.1940	5.1178	2.166	1.300	1.594	697	182.4	96.5	6.66	115.9	9.19	5.67	92
94	0.50020	723.8	0.04842	−86.79	86.52	3.2401	5.0839	2.196	1.341	1.626	675	182.8	90.7	6.84	111.9	9.53	5.25	94
96	0.58316	712.7	0.04169	−82.34	87.10	3.2858	5.0507	2.231	1.387	1.664	652	183.1	85.4	7.03	108.0	9.89	4.84	96
98	0.67565	701.2	0.03605	−77.81	87.51	3.3311	5.0181	2.271	1.440	1.707	629	183.3	80.4	7.23	104.0	10.29	4.44	98
100	0.77827	689.4	0.03129	−73.21	87.77	3.3761	4.9858	2.318	1.503	1.758	605	183.3	75.8	7.43	100.1	10.73	4.05	100
105	1.08330	657.5	0.02224	−61.27	87.56	3.4882	4.9055	2.479	1.714	1.931	543	182.5	65.3	7.98	90.3	12.04	3.10	105
110	1.46580	621.5	0.01598	−48.49	85.84	3.6015	4.8226	2.743	2.062	2.221	476	180.8	56.0	8.63	80.4	13.83	2.21	110
115	1.93700	578.7	0.01146	−34.39	81.91	3.7198	4.7311	3.240	2.749	2.778	403	177.7	47.3	9.44	70.6	16.58	1.39	115
120	2.51060	523.4	0.00799	−17.87	74.17	3.8514	4.6185	4.508	4.631	4.216	317	172.6	38.4	10.62	61.0	21.72	0.66	120
125	3.20690	426.1	0.00487	6.40	55.03	4.0373	4.4263	16.720	23.740	16.930	195	160.3	26.9	13.33	56.4	41.54	0.08	125
126.19[c]	3.39580	313.3	0.00319	29.23	29.23	4.2149	4.2149	∞	∞	∞	0	0.0	—	—	∞	∞	0.00	126.19

*Temperatures on ITS-90 scale   [a]Triple point   [b]Normal boiling point   [c]Critical point

Refrigerant 728 (Nitrogen) Properties of Gas at 0.101 325 MPa (one standard atmosphere)

Temp., °C	Density, kg/m³	Enthalpy, kJ/kg	Entropy, kJ/(kg·K)	c_p, kJ/(kg·K)	c_p/c_v	Vel. of Sound, m/s	Visc., μPa·s	Thermal Cond., mW/(m·K)	Temp., °C	Density, kg/m³	Enthalpy, kJ/kg	Entropy, kJ/(kg·K)	c_p, kJ/(kg·K)	c_p/c_v	Vel. of Sound, m/s	Visc., μPa·s	Thermal Cond., mW/(m·K)
−195.8[b]	4.6121	77.16	5.4090	1.124	1.457	174.8	5.44	7.19	150	0.8065	439.66	7.2005	1.047	1.397	419.0	23.14	34.30
−180	3.7571	94.51	5.6133	1.081	1.432	194.0	6.51	8.72	160	0.7879	450.14	7.2249	1.048	1.396	423.8	23.53	34.93
−160	3.0593	115.90	5.8213	1.061	1.419	215.2	7.81	10.63	170	0.7701	460.62	7.2489	1.049	1.396	428.6	23.92	35.56
−140	2.5858	137.02	5.9932	1.052	1.412	234.2	9.06	12.49	180	0.7531	471.12	7.2723	1.050	1.395	433.3	24.31	36.18
−120	2.2414	158.02	6.1402	1.048	1.409	251.6	10.27	14.28	190	0.7368	481.62	7.2952	1.051	1.394	438.0	24.69	36.80
−100	1.9789	178.95	6.2687	1.045	1.406	267.9	11.42	16.03	200	0.7212	492.14	7.3177	1.053	1.394	442.6	25.07	37.42
−90	1.8696	189.40	6.3273	1.045	1.405	275.6	11.99	16.88	210	0.7063	502.67	7.3397	1.054	1.393	447.1	25.44	38.03
−80	1.7719	199.85	6.3829	1.044	1.405	283.1	12.54	17.71	220	0.6920	513.22	7.3613	1.055	1.392	451.6	25.81	38.63
−70	1.6839	210.28	6.4355	1.043	1.404	290.4	13.08	18.54	230	0.6782	523.78	7.3825	1.057	1.391	456.0	26.18	39.23
−60	1.6043	220.71	6.4857	1.043	1.404	297.5	13.61	19.35	240	0.6650	534.36	7.4033	1.059	1.390	460.4	26.54	39.83
−50	1.5320	231.14	6.5335	1.042	1.403	304.4	14.14	20.15	250	0.6523	544.95	7.4238	1.060	1.389	464.7	26.90	40.42
−40	1.4659	241.56	6.5791	1.042	1.403	311.2	14.65	20.94	260	0.6401	555.56	7.4439	1.062	1.389	468.9	27.26	41.01
−30	1.4053	251.98	6.6229	1.042	1.403	317.9	15.16	21.72	270	0.6283	566.19	7.4636	1.064	1.388	473.2	27.62	41.59
−20	1.3496	262.40	6.6649	1.042	1.402	324.4	15.66	22.49	280	0.6169	576.84	7.4831	1.066	1.387	477.3	27.97	42.17
−10	1.2981	272.82	6.7053	1.042	1.402	330.7	16.15	23.25	290	0.6060	587.50	7.5022	1.068	1.386	481.5	28.32	42.75
0	1.2504	283.23	6.7441	1.041	1.402	337.0	16.63	24.00	300	0.5954	598.19	7.5210	1.070	1.385	485.5	28.66	43.32
10	1.2061	293.65	6.7815	1.041	1.402	343.1	17.10	24.74	310	0.5852	608.90	7.5395	1.072	1.384	489.6	29.00	43.89
20	1.1648	304.06	6.8177	1.041	1.401	349.1	17.57	25.47	320	0.5753	619.62	7.5577	1.074	1.383	493.6	29.35	44.46
30	1.1263	314.47	6.8526	1.041	1.401	355.0	18.03	26.20	330	0.5658	630.37	7.5757	1.076	1.381	497.5	29.68	45.02
40	1.0903	324.89	6.8864	1.041	1.401	360.8	18.49	26.91	340	0.5565	641.14	7.5934	1.078	1.380	501.4	30.02	45.58
50	1.0565	335.30	6.9191	1.042	1.401	366.5	18.94	27.62	350	0.5476	651.93	7.6109	1.080	1.379	505.3	30.35	46.13
60	1.0247	345.72	6.9509	1.042	1.400	372.1	19.38	28.32	360	0.5390	662.74	7.6281	1.082	1.378	509.1	30.68	46.69
70	0.9948	356.14	6.9817	1.042	1.400	377.7	19.82	29.01	370	0.5306	673.58	7.6451	1.085	1.377	512.9	31.01	47.23
80	0.9666	366.56	7.0117	1.042	1.400	383.1	20.25	29.69	380	0.5225	684.44	7.6618	1.087	1.376	516.7	31.34	47.78
90	0.9399	376.99	7.0408	1.043	1.400	388.5	20.68	30.37	390	0.5146	695.32	7.6783	1.089	1.375	520.4	31.66	48.33
100	0.9147	387.42	7.0691	1.043	1.399	393.7	21.10	31.04	400	0.5069	706.22	7.6947	1.092	1.374	524.1	31.98	48.87
110	0.8908	397.85	7.0967	1.044	1.399	398.9	21.52	31.70	420	0.4923	728.10	7.7267	1.096	1.371	531.4	32.62	49.94
120	0.8681	408.30	7.1236	1.044	1.398	404.0	21.93	32.36	440	0.4785	750.08	7.7580	1.101	1.369	538.6	33.24	51.00
130	0.8466	418.74	7.1498	1.045	1.398	409.1	22.34	33.01	460	0.4655	772.15	7.7885	1.106	1.367	545.6	33.87	52.06
140	0.8261	429.20	7.1755	1.046	1.397	414.1	22.74	33.66	480	0.4531	794.32	7.8183	1.111	1.365	552.6	34.48	53.10
									500	0.4414	816.59	7.8475	1.116	1.363	559.4	35.08	54.14

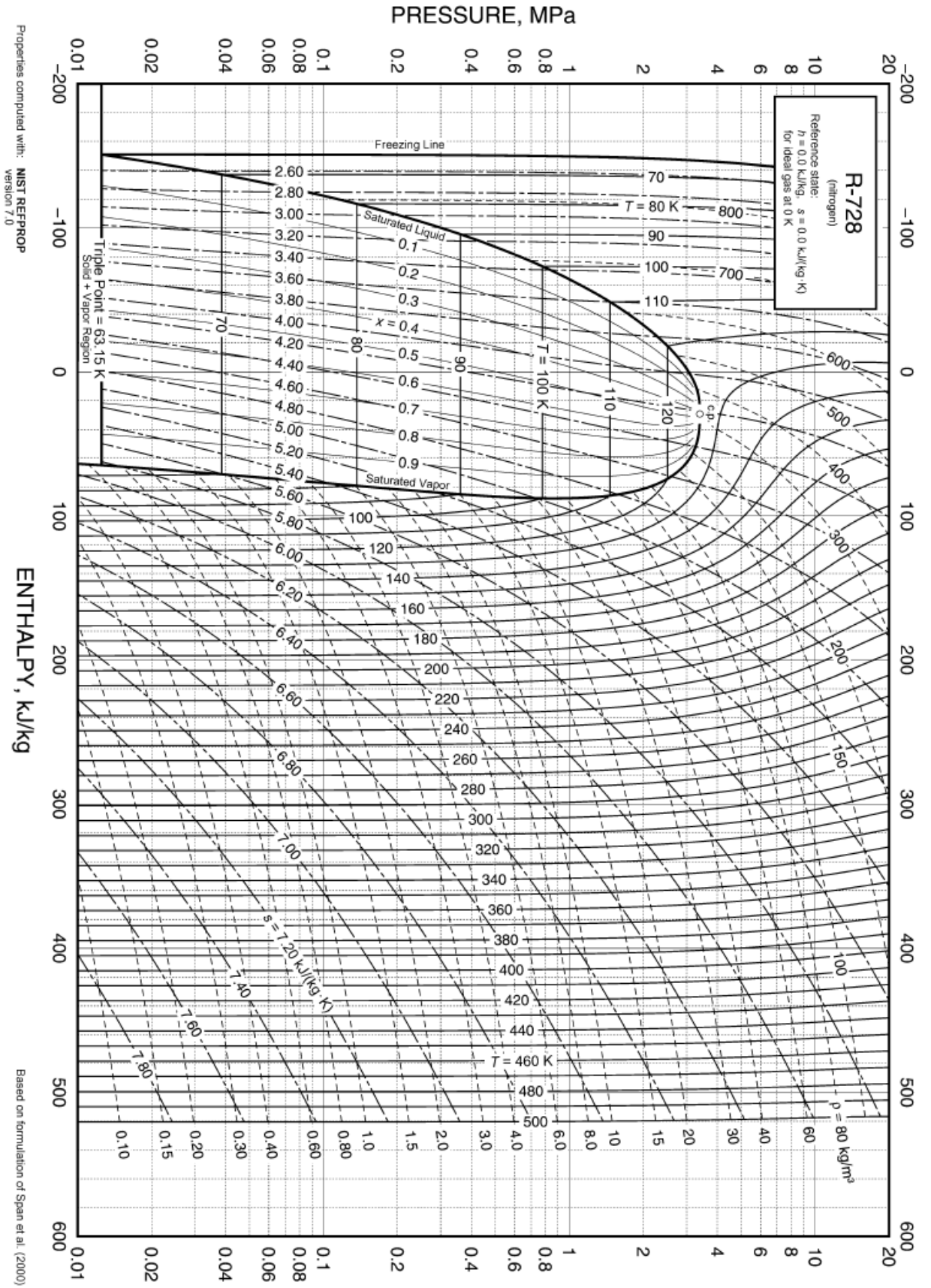[b]Saturated vapor at normal boiling point

Fig. 29   Pressure-Enthalpy Diagram for Refrigerant 728 (Nitrogen)

APPENDIX

APPENDIX B: Thermophysical Properties of Air [123]

Refrigerant 729 (Air) Properties of Liquid on the Bubble Line and Vapor on the Dew Line

Absolute Pressure, MPa	Temperature,* K Bubble	Temperature,* K Dew	Density, kg/m³ Liquid	Volume, m³/kg Vapor	Enthalpy, kJ/kg Liquid	Enthalpy, kJ/kg Vapor	Entropy, kJ/(kg·K) Liquid	Entropy, kJ/(kg·K) Vapor	Specific Heat c_p, kJ/(kg·K) Liquid	Specific Heat c_p, kJ/(kg·K) Vapor	c_p/c_v Vapor	Velocity of Sound, m/s Liquid	Velocity of Sound, m/s Vapor	Viscosity, μPa·s Liquid	Viscosity, μPa·s Vapor	Thermal Cond., mW/(m·K) Liquid	Thermal Cond., mW/(m·K) Vapor	Surface Tension, mN/m
0.00526	59.75	63.09	957.8	3.42745	−162.40	62.73	2.4517	6.1507	1.895	1.014	1.405	1056	158.9	424.8	4.47	185.2	5.83	14.95
0.008	61.83	65.12	949.2	2.32401	−158.45	64.67	2.5165	6.0614	1.897	1.017	1.407	1035	161.3	377.9	4.62	181.2	6.04	14.41
0.01	63.00	66.27	944.4	1.88990	−156.22	65.75	2.5522	6.0142	1.899	1.019	1.408	1023	162.6	354.6	4.70	179.0	6.16	14.11
0.015	65.27	68.47	934.9	1.29870	−151.92	67.82	2.6193	5.9293	1.902	1.023	1.411	1001	165.0	315.3	4.87	174.7	6.38	13.54
0.02	66.99	70.15	927.6	0.99558	−148.64	69.35	2.6687	5.8697	1.904	1.026	1.414	984	166.8	289.6	4.99	171.4	6.55	13.11
0.03	69.58	72.68	916.5	0.68481	−143.68	71.62	2.7412	5.7866	1.909	1.033	1.420	959	169.4	256.4	5.18	166.5	6.80	12.46
0.04	71.57	74.61	907.9	0.52523	−139.88	73.30	2.7948	5.7282	1.913	1.039	1.425	940	171.3	234.8	5.33	162.7	7.00	11.97
0.05	73.19	76.19	900.8	0.42756	−136.77	74.63	2.8378	5.6832	1.917	1.044	1.430	925	172.8	219.0	5.45	159.7	7.16	11.57
0.06	74.58	77.53	894.7	0.36139	−134.10	75.75	2.8738	5.6467	1.921	1.050	1.434	911	174.0	206.8	5.55	157.0	7.29	11.24
0.08	76.89	79.78	884.3	0.27713	−129.64	77.55	2.9323	5.5893	1.928	1.060	1.443	889	175.9	188.7	5.72	152.7	7.52	10.68
0.1	78.79	81.62	875.7	0.22550	−125.95	78.96	2.9794	5.5450	1.936	1.070	1.452	871	177.3	175.6	5.86	149.1	7.71	10.22
0.10132[b]	78.90	81.73	875.1	0.22277	−125.73	78.96	2.9822	5.5424	1.936	1.071	1.452	869	177.4	174.8	5.87	148.9	7.72	10.20
0.15	82.51	85.23	858.4	0.15488	−118.68	81.55	3.0688	5.4648	1.953	1.094	1.471	834	179.9	153.5	6.15	142.1	8.07	9.35
0.2	85.39	88.02	844.6	0.11849	−113.01	83.38	3.1357	5.4079	1.969	1.117	1.409	806	181.6	139.3	6.37	136.8	8.37	8.68
0.3	89.82	92.32	822.7	0.08100	−104.17	85.84	3.2353	5.3272	2.002	1.162	1.527	762	183.7	120.9	6.72	128.5	8.88	7.67
0.4	93.26	95.65	805.0	0.06165	−97.17	87.42	3.3104	5.2691	2.034	1.207	1.564	727	184.9	108.9	7.00	122.1	9.37	6.90
0.5	96.12	98.42	789.7	0.04977	−91.26	88.49	3.3715	5.2231	2.068	1.253	1.601	697	185.6	100.1	7.25	116.8	9.82	6.28
0.6	98.59	100.80	776.0	0.04169	−86.07	89.22	3.4235	5.1848	2.102	1.299	1.639	670	186.0	93.3	7.47	112.2	10.24	5.75
0.8	102.76	104.83	751.9	0.03136	−77.12	89.99	3.5098	5.1221	2.176	1.398	1.721	625	186.3	83.0	7.86	104.4	11.03	4.88
1	106.23	108.18	730.4	0.02500	−69.40	90.12	3.5811	5.0708	2.258	1.506	1.813	585	186.0	75.3	8.21	98.0	11.81	4.18
1.5	113.15	114.83	682.6	0.01623	−53.12	88.65	3.7230	4.9678	2.515	1.844	2.101	500	184.2	61.9	9.00	85.2	13.87	2.85
2	118.58	120.02	638.2	0.01162	−39.06	85.27	3.8379	4.8805	2.899	2.359	2.538	427	181.4	52.5	9.79	75.2	16.31	1.89
2.5	123.11	124.32	592.9	0.00869	−25.82	80.04	3.9407	4.7966	3.558	3.27	3.286	359	177.8	44.8	10.68	66.9	19.55	1.16
3	127.03	127.99	541.8	0.00658	−12.26	72.34	4.0419	4.7056	5.008	5.303	4.895	290	173.4	37.7	11.82	60.0	24.56	0.59
3.78781[c]	132.53	132.53	342.6	0.00292	29.38	29.38	4.3479	4.3479	—	—	—	—	—	—	—	—	—	0.00

*Temperatures on ITS-90 scale   [b]Bubble and dew points at one standard atmosphere   [c]Critical point

Refrigerant 729 (Air) Properties of Gas at 0.101 325 MPa (one standard atmosphere)

Temp., °C	Density, kg/m³	Enthalpy, kJ/kg	Entropy, kJ/(kg·K)	c_p, kJ/(kg·K)	c_p/c_v	Vel. of Sound, m/s	Visc., μPa·s	Thermal Cond., mW/(m·K)	Temp., °C	Density, kg/m³	Enthalpy, kJ/kg	Entropy, kJ/(kg·K)	c_p, kJ/(kg·K)	c_p/c_v	Vel. of Sound, m/s	Visc., μPa·s	Thermal Cond., mW/(m·K)
−191.4[d]	4.4889	79.05	5.5424	1.071	1.452	177.4	5.87	7.72	150	0.8338	424.81	7.2142	1.017	1.394	411.7	24.11	34.75
−180	3.8887	91.09	5.6804	1.044	1.435	190.8	6.68	8.84	160	0.8145	434.99	7.2379	1.019	1.394	416.4	24.52	35.39
−160	3.1648	111.75	5.8814	1.025	1.421	211.7	8.04	10.76	170	0.7961	445.18	7.2612	1.020	1.393	421.1	24.93	36.04
−140	2.6744	132.15	6.0474	1.016	1.414	230.4	9.35	12.63	180	0.7785	455.39	7.2840	1.022	1.392	425.7	25.34	36.67
−120	2.3178	152.43	6.1893	1.012	1.410	247.6	10.61	14.45	190	0.7617	465.62	7.3063	1.023	1.391	430.2	25.74	37.31
−100	2.0462	172.63	6.3133	1.009	1.408	263.5	11.82	16.20	200	0.7456	475.86	7.3282	1.025	1.390	434.7	26.13	37.93
−90	1.9332	182.71	6.3699	1.008	1.407	271.1	12.41	17.06	210	0.7302	486.12	7.3497	1.027	1.389	439.1	26.53	38.56
−80	1.8321	192.79	6.4235	1.007	1.406	278.5	12.99	17.91	220	0.7154	496.40	7.3707	1.029	1.388	443.5	26.92	39.17
−70	1.7411	202.86	6.4743	1.007	1.406	285.7	13.55	18.74	230	0.7011	506.70	7.3914	1.031	1.387	447.8	27.30	39.79
−60	1.6588	212.93	6.5227	1.007	1.405	292.7	14.11	19.56	240	0.6875	517.02	7.4117	1.033	1.386	452.0	27.69	40.40
−50	1.5840	222.99	6.5688	1.006	1.405	299.5	14.66	20.37	250	0.6743	527.35	7.4317	1.035	1.385	456.2	28.06	41.00
−40	1.5156	233.06	6.6130	1.006	1.404	306.2	15.20	21.17	260	0.6617	537.71	7.4513	1.037	1.384	460.4	28.44	41.60
−30	1.4530	243.11	6.6552	1.006	1.404	312.7	15.73	21.96	270	0.6495	548.09	7.4705	1.039	1.383	464.5	28.81	42.20
−20	1.3953	253.17	6.6957	1.006	1.404	319.1	16.25	22.74	280	0.6378	558.49	7.4895	1.041	1.381	468.6	29.18	42.80
−10	1.3421	263.23	6.7347	1.006	1.403	325.4	16.76	23.51	290	0.6264	568.91	7.5082	1.043	1.380	472.6	29.55	43.39
0	1.2927	273.29	6.7722	1.006	1.403	331.5	17.27	24.27	300	0.6155	579.35	7.5266	1.045	1.379	476.6	29.91	43.97
10	1.2469	283.35	6.8084	1.006	1.402	337.5	17.77	25.02	310	0.6049	589.82	7.5447	1.048	1.378	480.5	30.27	44.56
20	1.2043	293.41	6.8433	1.006	1.402	343.4	18.26	25.77	320	0.5947	600.30	7.5625	1.050	1.377	484.4	30.63	45.14
30	1.1644	303.48	6.8771	1.007	1.402	349.2	18.75	26.50	330	0.5849	610.81	7.5801	1.052	1.376	488.3	30.98	45.71
40	1.1272	313.55	6.9098	1.007	1.401	354.9	19.22	27.22	340	0.5753	621.35	7.5974	1.055	1.375	492.1	31.34	46.29
50	1.0922	323.62	6.9414	1.008	1.401	360.5	19.70	27.94	350	0.5661	631.90	7.6145	1.057	1.373	495.9	31.69	46.86
60	1.0594	333.70	6.9721	1.008	1.400	366.0	20.16	28.65	360	0.5572	642.48	7.6313	1.059	1.372	499.7	32.03	47.42
70	1.0284	343.79	7.0020	1.009	1.400	371.4	20.62	29.36	370	0.5485	653.09	7.6479	1.062	1.371	503.4	32.38	47.99
80	0.9993	353.88	7.0310	1.010	1.399	376.7	21.08	30.05	380	0.5401	663.71	7.6643	1.064	1.370	507.1	32.72	48.55
90	0.9717	363.98	7.0592	1.011	1.399	381.9	21.52	30.74	390	0.5320	674.37	7.6805	1.066	1.369	510.7	33.06	49.11
100	0.9456	374.09	7.0866	1.011	1.398	387.1	21.97	31.42	400	0.5241	685.04	7.6965	1.069	1.368	514.3	33.40	49.66
110	0.9209	384.21	7.1134	1.012	1.397	392.1	22.41	32.10	420	0.5089	706.47	7.7279	1.074	1.365	521.5	34.06	50.76
120	0.8975	394.34	7.1395	1.014	1.397	397.1	22.84	32.77	440	0.4947	727.98	7.7585	1.078	1.363	528.5	34.72	51.86
130	0.8752	404.49	7.1650	1.015	1.396	402.1	23.27	33.43	460	0.4812	749.60	7.7884	1.083	1.361	535.4	35.37	52.94
140	0.8540	414.64	7.1899	1.016	1.395	406.9	23.69	34.09	480	0.4684	771.31	7.8176	1.088	1.359	542.3	36.02	54.01
									500	0.4563	793.12	7.8461	1.093	1.357	549.0	36.65	55.08

[d]Saturated vapor at dew-point temperature

PRESSURE, MPa

R-729
(dry air)

Reference state:
h = 0.0 kJ/kg, s = 0.0 kJ/(kg·K)
for ideal gas at 0 K

ENTHALPY, kJ/kg
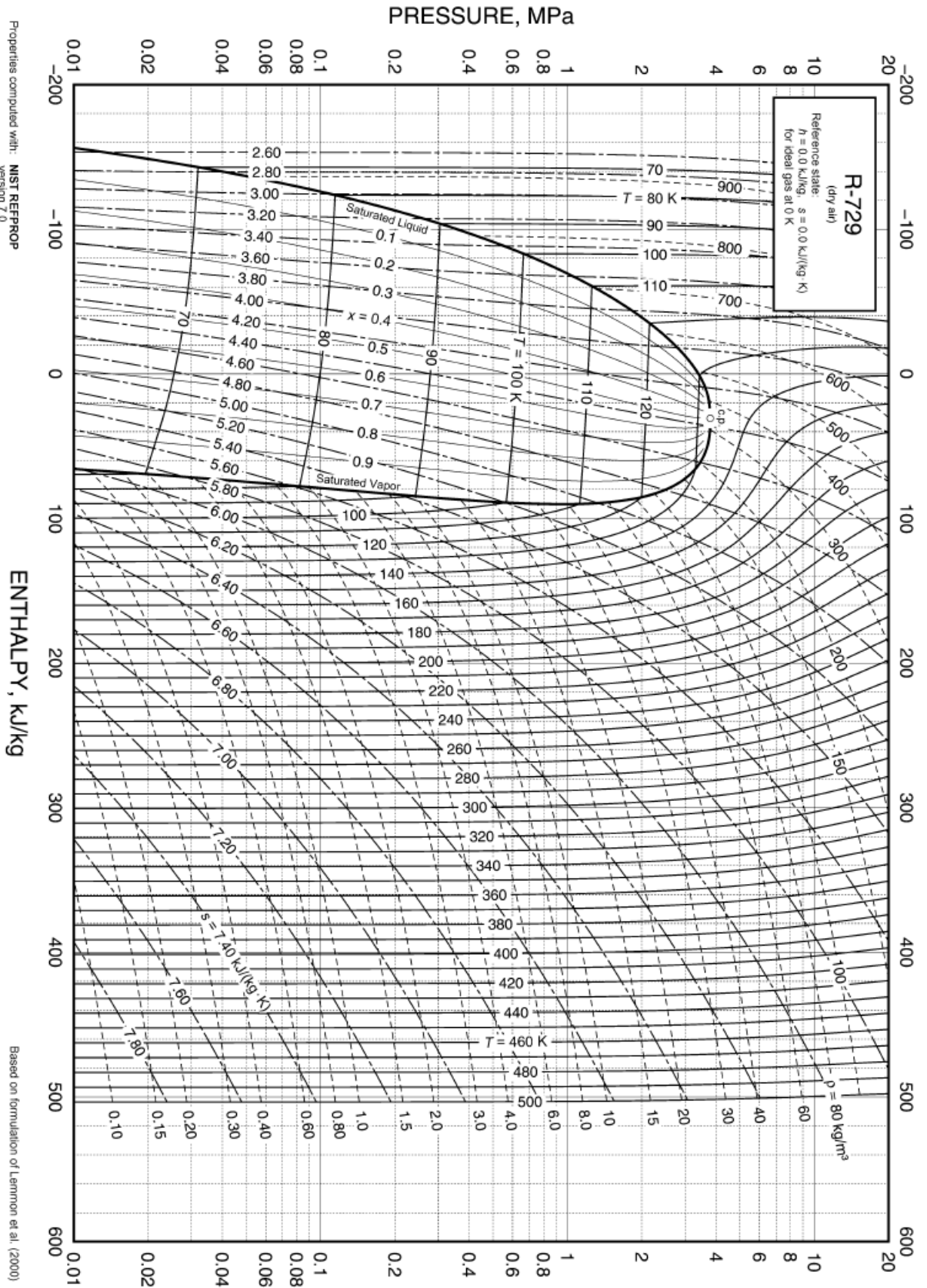
Fig. 30   Pressure-Enthalpy Diagram for Refrigerant 729 (Air)

Based on formulation of Lemmon et al. (2000)

APPENDIX

Appendix C: Thermophysical Properties of Water [123]

Refrigerant 718 (Water/Steam) Properties of Saturated Liquid and Saturated Vapor

Temp.,* °C	Pres- sure, MPa	Density, kg/m³ Liquid	Volume, m³/kg Vapor	Enthalpy, kJ/kg Liquid	Vapor	Entropy, kJ/(kg·K) Liquid	Vapor	Specific Heat cp, kJ/(kg·K) Liquid	Vapor	cp/cv Vapor	Velocity of Sound, m/s Liquid	Vapor	Viscosity, μPa·s Liquid	Vapor	Thermal Cond., mW/(m·K) Liquid	Vapor	Surface Tension, mN/m	Temp.,* °C
0.01ᵃ	0.00061	999.8	205.990	0.00	2500.92	0.0000	9.1555	4.220	1.884	1.329	1402	409.0	1791.2	9.22	561.0	17.07	75.65	0.01
5	0.00087	999.9	147.010	21.02	2510.06	0.0763	9.0248	4.205	1.889	1.328	1426	412.6	1518.3	9.34	570.5	17.34	74.94	5
10	0.00123	999.7	106.300	42.02	2519.21	0.1511	8.8998	4.196	1.895	1.328	1447	416.2	1306.0	9.46	580.0	17.62	74.22	10
15	0.00171	999.1	77.8750	62.98	2528.33	0.2245	8.7803	4.189	1.900	1.328	1466	419.7	1137.6	9.59	589.3	17.92	73.49	15
20	0.00234	998.2	57.7570	83.91	2537.43	0.2965	8.6660	4.184	1.906	1.327	1482	423.2	1001.6	9.73	598.4	18.23	72.74	20
25	0.00317	997.0	43.3370	104.83	2546.51	0.3672	8.5566	4.182	1.912	1.327	1497	426.6	890.1	9.87	607.2	18.55	71.97	25
30	0.00425	995.6	32.8780	125.73	2555.55	0.4368	8.4520	4.180	1.918	1.327	1509	430.0	797.4	10.01	615.5	18.89	71.19	30
35	0.00563	994.0	25.2050	146.63	2564.55	0.5051	8.3517	4.180	1.925	1.327	1520	433.4	719.3	10.16	623.3	19.24	70.40	35
40	0.00738	992.2	19.5150	167.53	2573.51	0.5724	8.2555	4.180	1.931	1.327	1529	436.7	653.0	10.31	630.6	19.60	69.60	40
45	0.00959	990.2	15.2520	188.43	2582.43	0.6386	8.1633	4.180	1.939	1.327	1536	440.0	596.1	10.46	637.3	19.97	68.78	45
50	0.01235	988.0	12.0270	209.34	2591.29	0.7038	8.0748	4.182	1.947	1.328	1542	443.2	546.8	10.62	643.6	20.36	67.94	50
55	0.01576	985.7	9.5643	230.26	2600.09	0.7680	7.9898	4.183	1.955	1.328	1547	446.4	504.0	10.77	649.2	20.77	67.10	55
60	0.01995	983.2	7.6672	251.18	2608.83	0.8313	7.9081	4.185	1.965	1.328	1551	449.5	466.4	10.93	654.3	21.19	66.24	60
65	0.02504	980.5	6.1935	272.12	2617.50	0.8937	7.8296	4.187	1.975	1.329	1553	452.6	433.2	11.10	659.0	21.62	65.37	65
70	0.03120	977.7	5.0395	293.07	2626.10	0.9551	7.7540	4.190	1.986	1.330	1555	455.6	403.9	11.26	663.1	22.07	64.48	70
75	0.03860	974.8	4.1289	314.03	2634.60	1.0158	7.6812	4.193	1.999	1.331	1555	458.5	377.7	11.43	666.8	22.53	63.58	75
80	0.04741	971.8	3.4052	335.01	2643.02	1.0756	7.6111	4.197	2.012	1.332	1554	461.4	354.3	11.59	670.0	23.01	62.67	80
85	0.05787	968.6	2.8258	356.01	2651.33	1.1346	7.5434	4.201	2.027	1.333	1553	464.2	333.3	11.76	672.8	23.51	61.75	85
90	0.07018	965.3	2.3591	377.04	2659.53	1.1929	7.4781	4.205	2.043	1.334	1550	466.9	314.4	11.93	675.3	24.02	60.82	90
95	0.08461	961.9	1.9806	398.09	2667.61	1.2504	7.4151	4.210	2.061	1.335	1547	469.6	297.3	12.10	677.3	24.55	59.87	95
99.97ᵇ	0.10133	958.4	1.6732	419.06	2675.53	1.3069	7.3544	4.216	2.080	1.337	1543	472.2	281.8	12.27	679.1	25.09	58.92	99.97
100	0.10142	958.3	1.6718	419.17	2675.57	1.3072	7.3541	4.216	2.080	1.337	1543	472.2	281.7	12.27	679.1	25.10	58.91	100
105	0.12090	954.7	1.4184	440.27	2683.39	1.3633	7.2952	4.222	2.101	1.339	1538	474.7	267.6	12.44	680.5	25.66	57.94	105
110	0.14338	950.9	1.2093	461.42	2691.06	1.4188	7.2381	4.228	2.124	1.341	1533	477.1	254.7	12.61	681.7	26.24	56.96	110
115	0.16918	947.1	1.0358	482.59	2698.58	1.4737	7.1828	4.236	2.150	1.343	1527	479.5	242.9	12.78	682.6	26.85	55.97	115
120	0.19867	943.1	0.89121	503.81	2705.93	1.5279	7.1291	4.244	2.177	1.346	1520	481.7	232.1	12.96	683.2	27.47	54.97	120
125	0.23224	939.0	0.77003	525.07	2713.10	1.5816	7.0770	4.252	2.207	1.349	1512	483.9	222.1	13.13	683.6	28.11	53.96	125
130	0.27028	934.8	0.66800	546.38	2720.08	1.6346	7.0264	4.261	2.239	1.352	1504	486.0	212.9	13.30	683.7	28.76	52.93	130
135	0.31323	930.5	0.58173	567.74	2726.87	1.6872	6.9772	4.272	2.274	1.355	1496	487.9	204.4	13.47	683.6	29.44	51.90	135
140	0.36154	926.1	0.50845	589.16	2733.44	1.7392	6.9293	4.283	2.311	1.359	1486	489.8	196.5	13.65	683.3	30.14	50.86	140
145	0.41568	921.6	0.44596	610.64	2739.80	1.7907	6.8826	4.294	2.351	1.363	1476	491.6	189.2	13.82	682.8	30.86	49.80	145
150	0.47616	917.0	0.39245	632.18	2745.93	1.8418	6.8371	4.307	2.394	1.368	1466	493.3	182.5	13.99	682.0	31.60	48.74	150
155	0.54350	912.3	0.34646	653.79	2751.81	1.8924	6.7926	4.321	2.440	1.373	1455	494.8	176.1	14.16	681.1	32.35	47.67	155
160	0.61823	907.4	0.30678	675.47	2757.44	1.9426	6.7491	4.335	2.488	1.379	1443	496.3	170.2	14.34	680.0	33.13	46.59	160
165	0.70093	902.5	0.27243	697.24	2762.81	1.9923	6.7066	4.351	2.540	1.385	1431	497.6	164.7	14.51	678.6	33.93	45.50	165
170	0.79219	897.5	0.24259	719.08	2767.90	2.0417	6.6650	4.368	2.594	1.392	1419	498.9	159.6	14.68	677.0	34.75	44.41	170
175	0.89260	892.3	0.21658	741.02	2772.71	2.0906	6.6241	4.386	2.652	1.399	1405	500.0	154.7	14.85	675.3	35.59	43.30	175
180	1.00280	887.0	0.19384	763.05	2777.21	2.1392	6.5840	4.405	2.713	1.407	1392	501.0	150.1	15.03	673.3	36.45	42.19	180
185	1.12350	881.6	0.17390	785.19	2781.41	2.1875	6.5447	4.425	2.777	1.416	1378	501.9	145.8	15.20	671.1	37.33	41.07	185
190	1.25520	876.1	0.15636	807.43	2785.28	2.2355	6.5059	4.447	2.844	1.425	1363	502.7	141.8	15.37	668.8	38.24	39.95	190
195	1.39880	870.4	0.14089	829.79	2788.82	2.2832	6.4678	4.471	2.915	1.436	1348	503.4	137.9	15.54	666.1	39.16	38.81	195
200	1.55490	864.7	0.12721	852.27	2792.01	2.3305	6.4302	4.496	2.990	1.447	1332	503.9	134.3	15.71	663.3	40.11	37.67	200
205	1.72430	858.8	0.11508	874.88	2794.83	2.3777	6.3930	4.523	3.068	1.459	1316	504.3	130.9	15.89	660.3	41.09	36.53	205
210	1.90770	852.7	0.10429	897.63	2797.27	2.4245	6.3563	4.551	3.150	1.472	1299	504.6	127.6	16.06	657.0	42.09	35.38	210
215	2.10580	846.5	0.09468	920.53	2799.32	2.4712	6.3200	4.582	3.237	1.486	1282	504.8	124.5	16.24	653.4	43.11	34.23	215
220	2.31960	840.2	0.08609	943.58	2800.95	2.5177	6.2840	4.615	3.329	1.501	1264	504.8	121.5	16.41	649.7	44.17	33.07	220
225	2.54970	833.7	0.07840	966.80	2802.15	2.5640	6.2483	4.650	3.426	1.518	1246	504.6	118.7	16.59	645.6	45.26	31.90	225
230	2.79710	827.1	0.07150	990.19	2802.90	2.6101	6.2128	4.688	3.528	1.536	1228	504.4	116.0	16.76	641.3	46.38	30.74	230
235	3.06250	820.3	0.06530	1013.77	2803.17	2.6561	6.1775	4.728	3.638	1.556	1209	503.9	113.4	16.94	636.7	47.53	29.57	235
240	3.34690	813.4	0.05970	1037.55	2802.96	2.7020	6.1423	4.772	3.754	1.578	1189	503.3	110.9	17.12	631.8	48.73	28.39	240
245	3.65120	806.2	0.05465	1061.55	2802.22	2.7478	6.1072	4.819	3.878	1.601	1169	502.6	108.4	17.31	626.7	49.97	27.22	245
250	3.97620	798.9	0.05008	1085.77	2800.93	2.7935	6.0721	4.870	4.011	1.627	1148	501.6	106.1	17.49	621.2	51.26	26.04	250
255	4.32290	791.4	0.04594	1110.23	2799.07	2.8392	6.0369	4.925	4.153	1.655	1127	500.5	103.9	17.68	615.4	52.61	24.87	255
260	4.69230	783.6	0.04217	1134.96	2796.60	2.8849	6.0016	4.986	4.308	1.686	1105	499.2	101.7	17.88	609.2	54.03	23.69	260
265	5.08530	775.7	0.03875	1159.96	2793.49	2.9307	5.9661	5.051	4.475	1.720	1083	497.7	99.6	18.07	602.8	55.53	22.51	265
270	5.50300	767.5	0.03562	1185.27	2789.69	2.9765	5.9304	5.123	4.656	1.757	1060	496.0	97.5	18.28	595.9	57.11	21.34	270
275	5.94640	759.0	0.03277	1210.90	2785.17	3.0224	5.8944	5.202	4.855	1.798	1037	494.1	95.5	18.48	588.7	58.80	20.16	275
280	6.41660	750.3	0.03015	1236.88	2779.87	3.0685	5.8579	5.289	5.073	1.845	1013	491.9	93.5	18.70	581.1	60.61	18.99	280
285	6.91470	741.3	0.02776	1263.25	2773.73	3.1147	5.8209	5.385	5.314	1.896	988	489.5	91.6	18.92	573.2	62.57	17.83	285
290	7.44180	731.9	0.02555	1290.03	2766.70	3.1612	5.7834	5.493	5.582	1.954	962	486.9	89.7	19.15	565.0	64.71	16.66	290
295	7.99910	722.2	0.02353	1317.27	2758.70	3.2080	5.7451	5.614	5.882	2.019	936	483.9	87.8	19.40	556.3	67.05	15.51	295
300	8.58790	712.1	0.02166	1345.01	2749.64	3.2552	5.7059	5.750	6.220	2.094	909	480.7	85.9	19.65	547.4	69.65	14.36	300
310	9.86510	690.7	0.01833	1402.22	2727.95	3.3510	5.6244	6.085	7.045	2.277	853	473.3	82.2	20.21	528.7	75.84	12.09	310
320	11.28430	667.1	0.01547	1462.22	2700.59	3.4494	5.5372	6.537	8.159	2.528	793	464.4	78.4	20.85	509.2	83.91	9.86	320
330	12.85810	640.8	0.01298	1525.87	2666.03	3.5518	5.4422	7.186	9.753	2.889	729	453.7	74.5	21.61	489.1	94.94	7.70	330
340	14.60070	610.7	0.01078	1594.53	2621.85	3.6601	5.3356	8.210	12.24	3.45	658	440.7	70.4	22.55	468.5	110.91	5.63	340
350	16.52940	574.7	0.00880	1670.89	2563.64	3.7784	5.2110	10.120	16.69	4.46	578	424.4	65.9	23.82	447.4	135.95	3.67	350
360	18.66600	527.6	0.00695	1761.66	2481.49	3.9167	5.0536	15.000	27.36	6.83	480	402.4	60.3	25.72	425.7	181.51	1.88	360
370	21.04360	451.4	0.00495	1890.69	2334.52	4.1112	4.8012	45.160	96.60	21.15	360	362.8	52.1	29.68	425.0	323.84	0.39	370
373.95ᶜ	22.06400	322.0	0.00311	2084.26	2084.26	4.4070	4.4070	∞	∞	∞	0	0.0	—	—	∞	∞	0.00	373.95

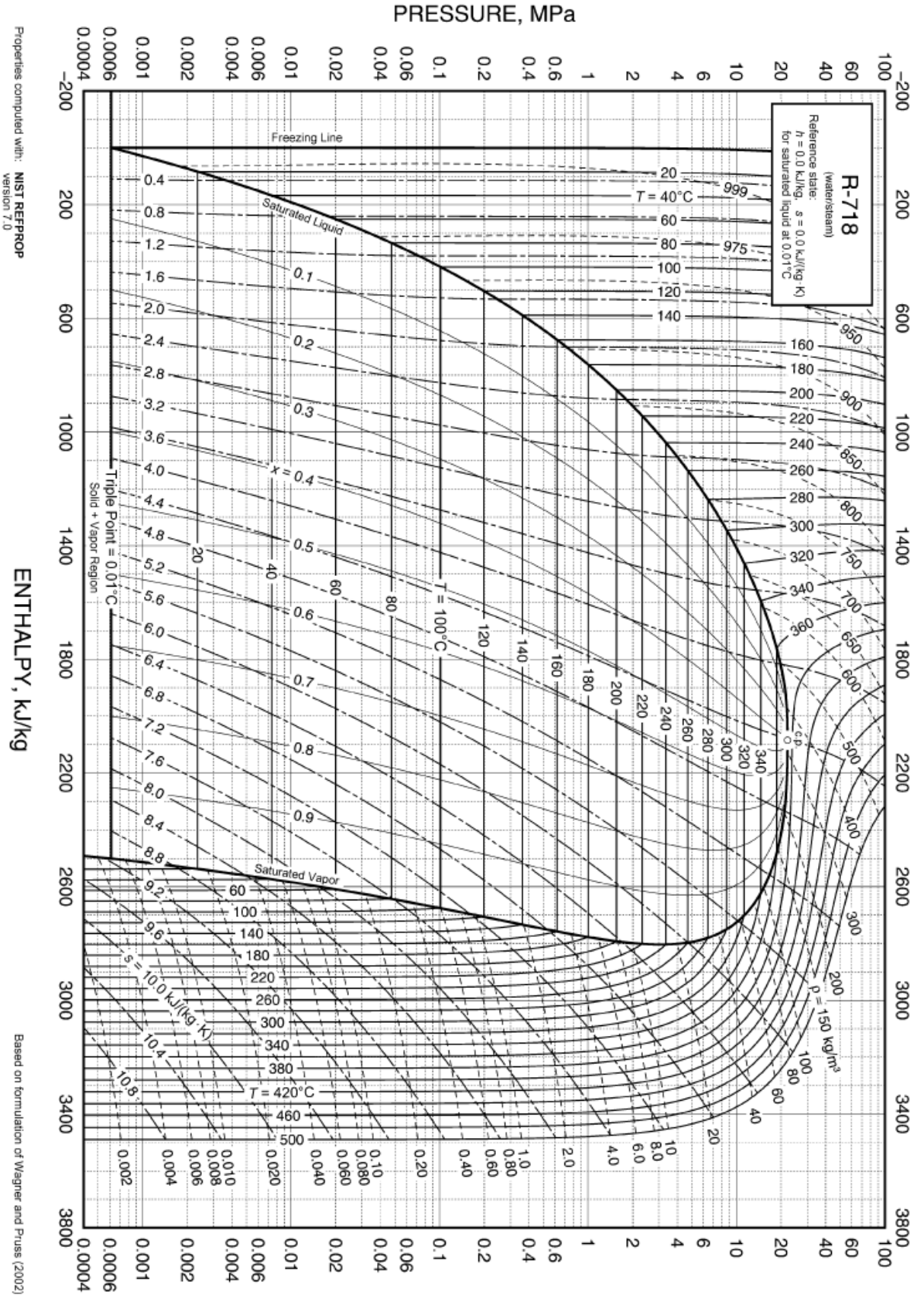*Temperatures on ITS-90 scale   ᵃTriple point   ᵇNormal boiling point   ᶜCritical point
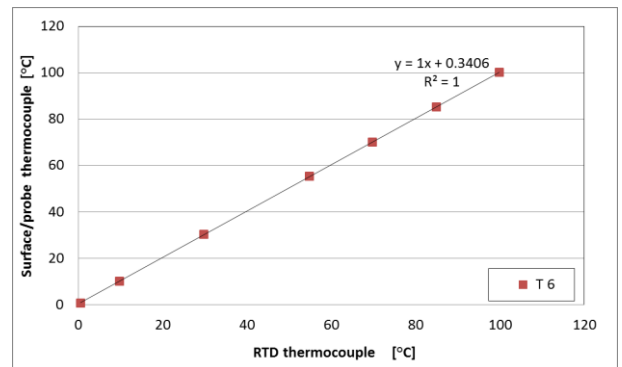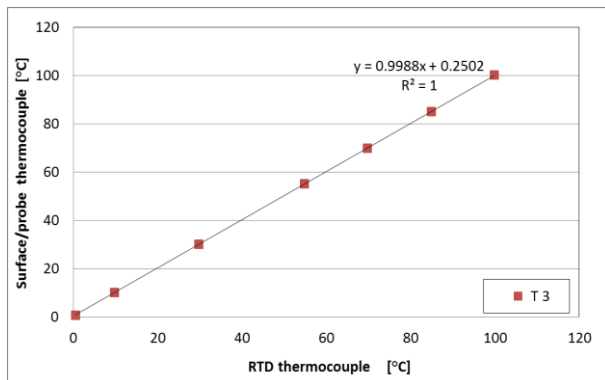
Fig. 17 Pressure-Enthalpy Diagram for Refrigerant 718 (Water/Steam)

APPENDIX

Appendix D: Thermocouple calibration

Appendix B presents the calibration procedure for the remaining thermocouples used in experimental work where figures show the temperature readings for 11 thermocouples versus TRD sensor which are part of the calibration procedure presented in chapter five, section 5.9.1.

APPENDIX